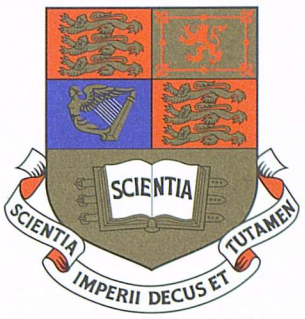
Imperial College
London



REUSE OF SILICATE WASTES: PROCESS DEVELOPMENT AND PROPERTY MEASUREMENTS OF DENSE AND POROUS GLASS-CERAMICS

Jeremy Po-Wei Wu

A thesis submitted in fulfilment of the requirements for the degree of
Doctor of Philosophy and the Diploma of Imperial College London

September 2006

Abstract

Vitrification is a well-established waste treatment method that has been used for silicate based wastes to achieve waste volume reduction and improve chemical stability before further use. However, the poor mechanical strength of the vitrified products has led to a low commercial value and thus an unjustifiable use of energy-intensive thermal technology over the cheaper, although environmentally unsatisfactory, land disposal option. To overcome this issue, the emphasis of this work lies in demonstrating the feasibility of fabricating dense glass-ceramics from several types of waste and combination of wastes, which are generally superior to their parent glasses in their mechanical performance, as well as highly porous glass-ceramics to be used in building industries as an alternative to conventional waste disposal.

The first part of the research work demonstrated the ease of production of an array of relatively dense glass-ceramic material from coal ash from thermal power plants using powder sintering technology. These products had robust physical and mechanical properties suitable to compete against commercially available building materials such as granite and marble for the floor and wall covering applications.

A fully-dense, fine-grained, high-strength glass-ceramic was also fabricated from Fe-slag using an economically viable single-stage melt heat-treatment route. The iron-slag derived glass-ceramic material had a unique composition, with an associated microstructure containing a high content of titanium-rich compounds, and has the potential for non-critical load-bearing applications.

Finally, the thesis provides the results of an experimental study concerning with the production of highly porous glass-ceramic foams from a mixture of coal ash and waste glass with the addition of an inorganic foaming agent. The correlations between physical, thermal, and mechanical properties were carried out based on results from practical experiments, physical model studies and numerical simulations using X-ray microtomography and finite element analysis.

It was concluded that, these waste-derived materials have the potential to be used in building applications where there can be a large demand to meet the large volumes of wastes available.

Table of Contents

Abstract *2*

Table of Contents *3*

List of Figures *6*

List of Tables *10*

Dedication *11*

Acknowledgements *12*

Chapter 1 Introduction *13*

Chapter 2 The Glass-Ceramic Process *16*

2.1 Introduction **16**

2.2 Conventional Method (Two-Stage) **16**

2.3 Modified Conventional Method (Single-Stage) **17**

2.4 Petrurgic Method **18**

2.5 Powder Methods **19**

2.6 Sol-Gel Precursor Glass **20**

Chapter 3 Glass-ceramic from Wastes *21*

3.1 Slag from iron and steel production **21**

3.1.1 Melting and Subsequent Heat Treatment – Conventional Two-Stage Method 21

3.1.2 Melting and Subsequent Heat-Treatment – Modified One-Stage Method 23

3.1.3 Petrurgic Method 26

3.1.4 Powder Technology and Sintering 26

3.2 Coal Ash from Power Stations **30**

3.2.1 Melting and Subsequent Heat Treatment 32

3.2.2 Powder Technology: monolithic material and composites 37

3.2.3 Petrurgic Method 39

3.3 Other Silicate Wastes **40**

3.3.1 Residues from Urban Incinerators 40

3.3.2 Other Metallurgical Slag Wastes 42

3.3.3 Electric Arc Furnace Dust (Steel Fly Ash) 42

3.3.4 Sewage Sludge 43

3.3.5 Zinc-Hydrometallurgy Wastes 44

3.4 Concluding Remarks **46**

Chapter 4 Processing Techniques for Porous Materials *48*

4.1 Use of Hollow Microspheres **48**

4.2 Use of Foaming Agents **49**

4.3 Inclusion of Secondary Organic Solids **51**

4.4 Burn-out of Polymeric Preforms **51**

4.5 Introduction of Gas during Processing **52**

4.6 Loose-Packed Powder Sintering **52**

4.7 Sol-Gel Technique **53**

4.8 Chemical Leaching 53
4.9 Plasma-Spraying 54
4.10 Microwave Processing 54
4.11 Summary 55
Chapter 5 Experimental 56
5.1 Materials 56
5.1.1 Milling 56
5.1.2 Powder Compaction 57
5.1.3 Melting / Glass Frit Making 58
5.1.4 Heat-treatments 58
5.1.5 Sample Preparation 58
5.2 Characterisation of Materials 59
5.2.1 Chemical Analysis 59
5.2.2 Laser Particle Size Analyser 59
5.2.3 Microscopy 60
5.2.4 X-Ray Diffraction Analysis (XRD) 60
5.2.5 Thermal Analysis 61
5.2.6 Dilatometry 61
5.2.7 X-ray Microtomography (XMT) 62
5.2.8 Density Measurement 66
5.2.9 Water Uptake 67
5.3 Determination of Mechanical and Thermal Properties 67
5.3.1 Modulus of Elasticity 67
5.3.2 Microhardness and Indentation Fracture Toughness 68
5.3.3 K_{IC}, Chevron Notched Beams and Elevated Temperature Tests 68
5.3.4 Bending Strength 69
5.3.5 Compressive Strength Test 70
5.3.6 Thermal Conductivity 70
5.3.7 Thermal Shock Resistance 73
5.3.8 Chemical Resistance Test 74
Chapter 6 Characterisation of Raw Materials 75
6.1 Chemical Composition 75
6.2 Particle Size Distribution 76
6.3 Phase Identification 77
6.4 Thermal Analysis 80
6.5 Preliminary Sintering Experiment 83
6.5.1 Coal Fly Ash 83
6.5.2 Coal Pond Ash 85
6.5.3 Melter Slag 86
6.5.4 KOBM Slag 88
6.6 Chapter Conclusions 90
Chapter 7 Coal Ash-based Glass-Ceramics by the Sintering Route 91
7.1 Sintering studies – Linear Shrinkage 92
7.2 Phase Identification 95
7.3 Coefficient of Linear Thermal Expansion 97
7.4 Mechanical Properties 101
7.5 Thermal Shock Resistance 104

7.6 Chemical Resistance **110**

7.7 Conclusion **111**

Chapter 8 Dense Slag-based Glass-Ceramics via Melting Route ***112***

8.1 Preparation of Precursor Glass **113**

8.2 Thermal Analysis **116**

8.3 X-Ray Diffraction and Microstructural Analysis **118**

8.4 Coefficient of Linear Thermal Expansion **121**

8.5 Mechanical Properties **123**

8.5.1 Fracture Toughness at Elevated Temperatures 125

8.5.2 Thermal Shock Resistance 129

8.6 Chemical Resistance **130**

8.7 Conclusion **132**

Chapter 9 Waste-derived Glass-ceramic Foams ***133***

9.1 Introduction **133**

9.2 Process Optimisation **134**

9.2.1 $CaCO_3$ as a Foaming Agent 134

9.2.2 SiC as a Foaming Agent 135

9.3 Phase Identification **140**

9.4 Microstructural analysis **142**

9.4.1 Conventional Microscopy 142

9.4.2 X-ray Microtomography 144

9.5 Coefficient of Linear Thermal Expansion **150**

9.6 Thermal conductivity **154**

9.6.1 Experimental – Lee's Disc 154

9.6.2 Models for Heat Conduction 156

9.6.3 Simulation – Finite Element Analysis 158

9.7 Mechanical Properties **164**

9.7.1 Vickers Hardness 165

9.7.2 Modulus of Elasticity 165

9.7.3 Flexural and Compressive Strengths 169

9.7.4 Effect of Thermal Shock on Compressive Strength 176

9.8 Density-Graded Glass-Ceramic Foam **178**

9.9 Applications **183**

Chapter 10 Conclusions ***184***

Chapter 11 Further work ***190***

References ***193***

List of Figures

Figure 2-1: Crystallisation of a glass to form a glass-ceramic. (a) Temperature dependence of the nucleation and growth rates with negligible overlap (b) two-stage heat treatment. 17
Figure 2-2: Crystallisation of a glass to form a glass-ceramic by a single-stage heat treatment. (a) Temperature dependence of the nucleation and growth rates with significant overlap (b) single-stage heat treatment. 18
Figure 2-3: Production of slag-based "Silceram" glass-ceramic by direct cooling and a single-stage heat treatment (a) temperature dependence of the nucleation and growth rates with significant overlap of the secondary nuclei rate and the growth rate curves (b) direct cooling/heat treatment 19
Figure 3-1: Microstructure of (a) pure constituents-based and (b) slag-based "Silceram" glass-ceramics [44] 25
Figure 3-2: Scanning electron microscopy (SEM) micrograph showing surface and bulk crystallisation in sintered "Silceram" glass-ceramic [48] 27
Figure 3-3: SEM micrograph of a sample made of a 1/1 mixture of Fe-containing coal ash and showing crystalline microstructure consisting of cristobalite (dark grains) and titanium bearing ferrite (bright phase), embedded in a glassy phase [59]. 38
Figure 3-4: Dendritic microstructure of magnetic glass-ceramic produced using the petrurgic method from Fe-containing coal ash [17] 40
Figure 3-5: Photo of the pilot plant for production of glass-ceramic tiles from industrial wastes, situated in Iglesias, Italy [127]. (Photo courtesy Prof. M. Pelino, University of L'Aquila, Italy) 46
Figure 4-1: From left to right, as-pressed compact, 5.5MPa, and 41.4MPa-saturated samples [164] 52
Figure 4-2: SEM illustrating surface of a sintered sample from loose-packed coal ash 53
Figure 5-1: Graphical representation of the milling components (sectioned view) 57
Figure 5-2: Irradiated by the same X-ray intensity, the higher density object A absorbs more radiation than the object B which is of lower attenuation coefficient. Object B absorbs more radiation than the thinner object C 63
Figure 5-3: Comparison between X-ray sources with different focal spot sizes, illustrating the relationship between spot size and geometric unsharpness (grey areas). 64
Figure 5-4: Schematic diagram of the Lee's Disc setup for determination of thermal conductivity (3 digital voltmeters for temperature measurement, one heater, and 3 steel discs) 70
Figure 5-5: Illustration of the setup of the apparatus used for measuring thermal conductivity 73
Figure 6-1: Illustration of the particle size distribution of milled PA 77
Figure 6-2: Morphology of a) as-received FA; b) milled PA; c) milled MS; and d) milled KS 77
Figure 6-3: XRD patterns on as-received coal ash samples (FA and PA) 78
Figure 6-4: XRD pattern of MS – iron-making melter slag 79
Figure 6-5: XRD pattern of KS – steel-making KOBM slag 80
Figure 6-6: DTA/TGA curve for PA (heating rate = 10°C/min) 81
Figure 6-7: DTA/TGA curve for as-received FA (heating rate = 10°C/min) 81
Figure 6-8: DTA/TGA curve for MS (heating rate = 10°C/min) 82
Figure 6-9: DTA/TGA curves of KS (as-received, heating rate = 10°C/min) 82
Figure 6-10: Illustrations of the various sintered specimen in different sizes and shapes produced in the course of the study 83
Figure 6-11: XRD patterns of FA50G samples sintered at different temperatures 85
Figure 6-12: MS50G sintered at 10°C min^{-1} up to 1000 °C for 1h: (a) secondary image; (b) backscattered image; (c) and (d) higher magnification images showing the complex heterogeneous microstructure and residual porosity 88

Figure 6-13: High-lime steel-making (KOBM) slag-based glass-ceramics produced by powder sintering, 50/50 KOBM slag and glass cullet. 90
Figure 7-1: Linear shrinkage of as-received coal pond ash as a green compact 92
Figure 7-2: XRD patterns showing the phase formation and crystallization during different stages of the sintering study: as-received (bottom), at 810 ℃ (middle), and at 1031 ℃ (top). 93
Figure 7-3: Isothermal shrinkage of the PA as-received specimen at set temperature of 1105 ℃ for 1 hour 94
Figure 7-4: Secondary electron micrograph and backscattered electron micrographs of coal pond ash with 10wt% waste glass heated at 2 ℃/min and sintered at 1075 ℃ for 1h 95
Figure 7-5: XRD plot: Illustration of crystalline phase present with changes with glass content 96
Figure 7-6: XRD plots of the sintered vitrified pond ash and sintered as-received pond ash. 97
Figure 7-7: Change in length with temperature, where the gradient of each slope is the CTE of that particular material 98
Figure 7-8: Increasing CTE with increasing additional glass content in the pond ash mixture 98
Figure 7-9: An example of XRD pattern treatment – where 4 individual patterns from the PA glass sample were highlighted. 100
Figure 7-10: Summary of amount of various crystalline phases (relative to 10wt% MgO) present in sintered PA-based samples, showing the relationship with additional glass content. 101
Figure 7-11: PA30G quenched from (top) 200°C; (middle) 340°C; and (bottom) 600°C. Cracks initiated from quenching were highlighted in white using a computer drawing package. 105
Figure 7-12: Crack density, number of cracks per unit area, versus the quenching temperature 106
Figure 7-13: Average crack length measured from the cross-section of each quenched bar 107
Figure 7-14: Critical thermal shock resistance temperature for glass-ceramic PA10G 108
Figure 7-15: Critical thermal shock resistance temperature for glass-ceramic PA30G 108
Figure 7-16: Secondary electron micrographs illustrating the corrosion of wollastonite crystals present in the sintered PA30G material; (top) before leaching, (bottom) after leaching 111
Figure 8-1: XRD patterns of the as-quenched melter slag after melting at 1480 ℃. 114
Figure 8-2: XRD patterns of MS40G as-quenched glass after melting at 1450 ℃ in (a) alumina and (b) zirconia crucibles 114
Figure 8-3: Combined DTA plot of MS40G glass in bulk and powder form, each sample weighed about 35mg. 116
Figure 8-4: DTA plots showing consistency over 3 individual runs of powder samples each weighed about 15mg 117
Figure 8-5: Corresponding XRD patterns (bottom to top) to the DTA peaks of results from previous figure (left to right) 118
Figure 8-6: XRD pattern of powdered samples from bulk specimens heat-treated at 850, 900, 1000, 1100°C for 2h. ▲perovskite ■ armalcolite ○ nepheline × diopside ◊ loveringite ... 119
Figure 8-7: HT-XRD of MS40G showing the precipitation and dissolution of ▲perovskite ■ armalcolite ○ pyroxene (nepheline and diopside) and ◊ loveringite 120
Figure 8-8: SEM images of (a) MS40G heat-treated at 900 ℃ for 2h; (b) MS40G annealed at 1100 ℃ for 2h; (c) and (d) magnified area of the matrix under secondary electron and back-scattered electron modes, respectively 121
Figure 8-9: Linear thermal expansion (change in length versus temperature) of MS40G samples in the form of as-cast glass, glass-ceramics heat-treated at 900°C and 1100°C (L_o = ~25mm). 122
Figure 8-10: Micrographs showing (a) fracture surface of MS40G glass-ceramic annealed 1100°C for 2h; (b) microscopic crack deflection across the material. 125

Figure 8-11: Summary plot of fracture toughness values of MS40G glass-ceramics heat-treated at 1100°C for 2 hours with testing temperature, showing the range from the minimum to the maximum of each dataset as vertical lines, and the mean K_{IC} values as the solid horizontal lines 126
Figure 8-12: A typical force-displacement plot of high temperature (500°C) 3-point bending test with Chevron notched MS40G glass-ceramic bars. 127
Figure 8-13: SEM images of fracture surfaces of MS40G glass-ceramic specimens at point of failure at (a) ambient temperature, (b) 500°C, (c) 650°C, and (d) 730°C. 128
Figure 8-14: Residual flexural strength versus quenching temperature difference for slag-based glass-ceramic materials heat-treated at 1100°C. 130
Figure 8-15: Corroded surface of MS40G samples as (a) as-cast glass, (b) heat-treated at 900°C, and (c) heat-treated at 1100°C, after immersing in 1N HCl for 15 hours at 50°C. ... 131
Figure 9-1: Soda-lime glass + 5wt%$CaCO_3$ sintered at 700°C for 15min. 135
Figure 9-2: PA80G glass-ceramics with 0, 2, and 5wt%SiC, heat-treated at 1050°C for 5min 136
Figure 9-3: XRD plots illustrating the crystalline phases present in samples containing different amounts of SiC after heat-treatment at 1025°C for 5 minutes 137
Figure 9-4: SEM micrograph showing the cross section of the glass-ceramic foam made by mixing 2wt% SiC powder with PA80G glass powder 138
Figure 9-5: DTA/TG plots of silicon carbide powder of different particle size (5-25μm and 200μm) 138
Figure 9-6: XRD spectra showing the synergetic effect of pond ash on reaction of SiC and glass oxides 140
Figure 9-7: XRD analysis illustrates the crystalline phases present in PA80G glass-ceramic with and without foaming agent at different sintering temperatures 141
Figure 9-8: Relative degree of crystallinity of PA80G foams with 2%SiC and dense PA80G solid at various heat-treatment temperatures. 142
Figure 9-9: Scanning electron micrographs showing the pore morphology of glass-ceramic foams of composition PA80G +2wt%SiC heat-treated at (a) 975°C, (b) 1000°C, (c) 1050°C, (d) 1100°C. 144
Figure 9-10: 2D and cropped 3D representations of PA80G + 2wt%SiC foamed at 1050°C for 6min 145
Figure 9-11: XMT reconstruction showing a cropped section (the inner core) of a waste-derived porous glass-ceramic material PA80G with 2wt%SiC sintered at 1050°C for 5min 145
Figure 9-12: From left to right: Original axial (xy) slice of PA80G 2wt%SiC 1100°C; processed using less aggressive convolution operation (3 iterations); processed using more aggressive operation (9 iterations). 146
Figure 9-13: Example of a 3D defect analysis conducted on a small volume of PA80G foam using VGStudio; (left) porous sample; (right) volumes representing the defects/pores 146
Figure 9-14: Effect of heat-treatment temperature on density and level of porosity of PA80G glass-ceramic foams 147
Figure 9-15: Effect of heat-treatment temperature on pore morphology (roundness, pore size, and wall thickness) 149
Figure 9-16: Schematic representation of the effect of increasing pore size on wall thickness at constant porosity 149
Figure 9-17: Pore size distribution (post-convolution) of PA80G foams heat-treated at 4 different temperatures 150
Figure 9-18: Change in length versus temperature plot, showing the linear CTEs of bulk solid and foams of the same composition (PA80G). (L_o = ~25mm) 151
Figure 9-19: SEM images of a PA80G + 2wt% SiC bar foamed at 1050°C (left) before and (right) after subjected to a thermal treatment up to 700°C in a dilatometer 152
Figure 9-20: Change in degree of crystallinity after further heat-treatment of glass-ceramic foams and bulk sample at 750°C at 10°C/min 152

Figure 9-21: Photograph showing a specimen of glass-ceramic foam for Lee's disc measurement 154
Figure 9-22: Thermal conductivity values versus actual density of PA80G foams 155
Figure 9-23: Thermal conductivity versus actual porosity of PA80G foams 155
Figure 9-24: Thermal conductivity versus Median Pore Size of PA80G glass-ceramic foams 156
Figure 9-25: Comparison between the experimental data and Leach model 158
Figure 9-26: A mesh of tetrahedral elements of a sample of PA80G + 2wt%SiC heat-treated at 1050°C 159
Figure 9-27: Temperature profile of a sample of foam at steady state 160
Figure 9-28: Comparisons between the simulated thermal conductivity values and experimental values 160
Figure 9-29: Plots of actual density versus actual porosity and XMT porosity 161
Figure 9-30: Computer generated volume of PA80G glass-ceramic with 2wt%SiC (1050°C), (a) matrix, (b) pores, (c) combination of the two phases, and (d) meshed volume 163
Figure 9-31: Simulated thermal conductivity values showing good agreement with the experimental values obtained from Lee's Disc. 164
Figure 9-32: Comparison between the modulus of elasticity values obtained experimentally and mathematically. 166
Figure 9-33: Young's modulus values of low-density glass-ceramic foams and its corresponding fit curves derived from a Gibson & Ashby model using different Φ values... 167
Figure 9-34: Illustration of a closed unit cell with cell edges and cell walls 168
Figure 9-35: Flexural strength versus relative density shows a trend following a polynomial equation to the degree of 2 169
Figure 9-36: Flexural strength values of PA80G glass-ceramic foams with relative densities of 0.05 to 0.20 170
Figure 9-37: Stress versus strain curves of PA80G glass-ceramic foams of different relative density showing typical behaviour of a brittle foam under compression 171
Figure 9-38: Fracture surfaces of PA80G glass-ceramic foams heated treated at (a) 1000°C, (b) and (c) 1050°C 172
Figure 9-39: Comparison between experimental compressive strength and values determined theoretically 174
Figure 9-40: Illustration of foam fragments building up in pores on the contact surface, and generating tension and thus cracks parallel to the compressive loading. 175
Figure 9-41: Specific stiffness versus specific strength chart [217] for generic materials, materials investigated during the study, and reference materials from literature 176
Figure 9-42: Specimens of PA80G with 2wt% SiC used for compressive strength test 177
Figure 9-43: Compressive strength of PA80G + 2 wt% SiC 1000°C foams as-sintered, and quenched from various temperatures 178
Figure 9-44: Cross-sections of the density-graded foams (PA80G 2wt%SiC) produced at 950°C 178
Figure 9-45: XRD spectrums showing the crystalline phases present in the core and shell of the density graded glass-ceramic foam 179
Figure 9-46: Voigt and Reuss models for predicting the mechanical strength of fibre-reinforced composites 180
Figure 9-47: Prediction of the compressive strength with respect to the loading configuration and fraction of porous core 182
Figure 9-48: Indications of an improvement in compressive strength with the presence of dense shell; however, negligible difference in mechanical performance between different configurations 183

List of Tables

Table 3-1: Comparison of the mechanical properties of "Silceram" glass-ceramics produced by various methods (HP and CP are hot pressed and cold pressed and heat treated respectively) 28
Table 3-2: Summary of properties of glass-ceramics and composites made from metallurgical slag by different routes 29
Table 3-3: Typical coal fly ash compositions (wt%) from various sources 31
Table 3-4: Properties of glass-ceramic materials made from coal ash with and without additives using various processing methods 35
Table 4-1: Advantages and disadvantages of different processing methods for porous materials 55
Table 5-1: Uniaxial pressure (MPa) used for various compaction moulds 57
Table 5-2: Lens Specification of Malvern Mastersizer 60
Table 6-1: Starting raw waste materials with their code names 75
Table 6-2: Typical compositions of the waste materials (wt%) 75
Table 6-3: Density and particle size distribution of the waste materials 76
Table 6-4: Relative densities of sintered samples containing calcined coal fly ash 84
Table 6-5: Relative densities of sintered samples containing coal pond ash 86
Table 6-6: Relative densities of sintered samples containing melter slag 87
Table 6-7: Relative densities of sintered samples containing KOBM slag 89
Table 7-1: Effect of heating rate on percentage of theoretical density of various sintered PA specimens 94
Table 7-2: Typical linear CTE values of individual crystalline phases present in the investigated materials 99
Table 7-3: Relative percentage of crystallisation of each sintered material 99
Table 7-4: Physical and mechanical properties of coal pond ash based sintered glass-ceramics, compared with relevant values of other materials from the literature 103
Table 7-5: Percentage weight loss of gehlenite based glass-ceramics after exposing to acid and alkali solutions 110
Table 8-1: Chemical composition of waste materials and slag-based glass-ceramics 115
Table 8-2: Typical linear CTE values of individual crystalline phases present in the investigated materials 123
Table 8-3: Effect of heat-treatment on the properties of MS40G glass and glass-ceramics (properties of 'Silceram' are given for comparison purposes 124
Table 9-1: Effect of heat-treatment temperature on pore morphology of glass-ceramic foams as measured by XMT 147
Table 9-2: Comparison of the properties of PA80G foams, Corning Foamglas®, and Saint-Gobain NORFOAM™A 165
Table 9-3: Volume fraction of solids in cell edges of different PA80G glass-ceramic foams, calculated using Gibson & Ashby model 168
Table 9-4: Comparison between the experimental compressive strength and predicted value 181

Dedication

This is dedicated to my parents Richard (Chung-Er) and Sheree (Sheau-Ling) and my brother Kevin (Su-Wei) for their constant caring and support over the three busy but wonderful years at Imperial College London. I would also like to thank my grandparents for their confidence in me. Thank you all for always believing in me and for lending an ear when I complained about things that seem insignificant right now.

Acknowledgements

First of all, it has been an honour and pleasure to work under the guidance of my supervisors: Prof. Rees Rawlings and Dr. Aldo Boccaccini. I have always enjoyed the weekly meetings and discussions. It is something that many of my fellow colleagues envy. Thank you both for inserting and building up that confidence in me.

Thanks to Prof. Jim Williamson and Dr. Chris Cheeseman for participating in my transfer examination. I really believe that was the turning point of my PhD where I started to look at this experience differently.

Special thanks to Prof. Peter Lee and his group of researchers. Without their contribution, especially allowing me to make use of the X-ray Microtomography facility and finite element software packages, we would not be able to carry out a series of successful modelling work and any publication would be impossible.

As for Richard Sweeney, Matt Kershaw, Dr. Mahmoud Ardakani, Nick Royall, Gary Gregg, Tim Mellor, Jim Wright, Stephen Fay, Alan Willis, and Bob Rudkin (in no particular order), they have all been important to my research as they have helped me in different technical aspects of my work. Many of them are delightful to work with and to talk to.

I also enjoyed the casual chats as well as exchanges in ideas with Prof. Robert Hill, Dr. Jane Minay, and Dr. Ambrose Taylor from Mechanical Engineering.

Thanks to Dr. Anne Staton-Bevan, Norma Hikel, Dawn Araim, Keith Tritton, Ashley Perris and Darakshan Khan for making the administrative and personal side of my life at Imperial easy.

With the forewarnings and other advice from former PhD students, Andy Carr and Jonny Blaker, I was very fortunate to be motivated and organised in order to progress my research in 3 years without much trouble.

I have been very fortunate to have this group of people as well as numerous friends in the college I made along the way during the past 3 years, making the experience of working at Imperial College an exciting and memorable one. All the best to each and one of them for their futures.

Finally, I would like to thank TEC of New Zealand government for financial support of this study, and the companies (Genesis - Huntly power station, SteelServ Ltd, and RMF) for supplying the waste materials.

Chapter 1 Introduction

Zero-waste is an unrealistic goal for many manufacturing or energy conversion processes. For solid waste by-products, landfilling and special dumpsites seem to be the most convenient solution to their disposal. However, with the stringent government regulations around the world, landfilling disposal is becoming less environmentally acceptable and thus less economically viable. On the other hand, reuse of these wastes can help minimise the environmental impact, and despite being costly in terms of processing, it is a much more sustainable solution. Reuse is the processing of waste to produce a useful product different from the material whose manufacture produced the waste. The aim of this thesis is to demonstrate the production of glass-ceramics as a feasible method to reuse silicate wastes by optimising economical fabrication processes for dense as well as porous glass-ceramics for the building industry and potentially other specialised applications. This is achieved by using a range of conventional fabrication techniques and advanced technologies in materials science for characterisation.

Glass-ceramics are fine-grained polycrystalline inorganic materials formed when glasses of suitable compositions are heat treated and thus undergo controlled crystallisation to the lower energy, crystalline state [1, 2]. It has to be noted that only specific glass compositions are suitable precursors for glass-ceramics; some glasses are too stable and difficult to crystallise, such as ordinary window glass, whereas others crystallise too readily in an uncontrollable manner resulting in undesirable microstructures. The heat treatment is also critical to the attainment of an acceptable and reproducible product. As will be discussed later, a range of generic heat-treatment procedures have been used, each of which has to be carefully developed and modified for a specific glass composition [1-3].

Fortunately, most of the silicate-based wastes have compositions that are potentially suitable as raw materials for glass-making and also glass-ceramic process. This is enhanced by additives that are often incorporated to adjust the chemical composition of the parent glass. Waste glass cullet was frequently used in this project as a source of glass forming oxides and/or network modifying oxides. The majority of the earlier research work on waste-derived glass-ceramics has been centred on energy-intensive and thus costly methods. Therefore, one of the objectives concerning process development is using powder technology (e.g. sintering) as well as a modified melting

routes to produce dense materials with lower energy consumption and thus lower production costs when compared to the conventional glass-ceramic heat-treatment method which has two stages.

A key advantage of glass-ceramics over their parent glasses is their superior physical and mechanical properties. This is usually the case and is the direct result of their polycrystalline structure. Usually a glass-ceramic is not fully crystalline; typically the microstructure is partially crystalline (up to 95vol%) with the remainder being residual glass. One or more crystalline phases may form during heat treatment and as their composition is normally different from the precursor (parent) glass, it follows that the composition of the residual glass is also different to the parent glass. In addition, glass-ceramics may exhibit other distinct properties which are beneficial for particular applications, as exemplified by the extremely small coefficient of thermal expansion of certain compositions in the Li_2O-Al_2O_3-SiO_2 system which consequently are suitable for thermal shock resistant applications [2-4]. A wide range of glass-ceramics with tailored properties have been developed and several comprehensive review articles and dedicated books on their production, properties and applications, have been published [1-7].

The format of the thesis is such that the literature survey is divided into three chapters, covering the main subjects: (1) glass-ceramics from various industrial silicate wastes, (2) different techniques to produce porous materials, and (3) X-ray microtomography and its use in examination of composite (or multiphase) materials. The background information is followed by the description of experimental procedures used during the research. There are four main chapters on experimental work in the area of (1) characterisation of raw materials and optimisation of material mixes; (2) dense glass-ceramics from coal ash via powder sintering route; (3) dense high-titania containing glass-ceramic from iron-making slag via a modified melt heat-treatment route, and (4) glass-ceramic foams by powder sintering coal ash with the incorporation of a foaming agent, and their characterisation using X-ray microtomography.

The objective for (1) the optimisation work is to find the best composition(s) for different mixture of wastes, which leads to the production of dense glass-ceramic materials. The objectives of (2) and (3) both emphasise the characterisation and specification of mechanical properties as well as thermal properties for comparisons against existing products. Finally, the objective for (4) is to show highly porous foams as an alternative form for waste-derived glass-ceramics, in this case, as

potential thermal insulation or lightweight filler material for building applications. Apart from characterising and specifying material properties of glass-ceramic foams using conventional techniques, X-ray microtomography was used as the preferred non-destructive characterisation technique to examine these porous materials. The conclusion chapter draws the main points from the three main aspects of the project, and the thesis concludes with recommendations for the future.

Please note that the following chapters 2 and 3 are mostly based on the recent publication by the authors (including the author of this thesis). This is to clarify the similarities between the article and the thesis.

R.D. Rawlings, J.P. Wu, A.R. Boccaccini
Glass-ceramic: Their production from wastes – A Review
Journal of Materials Science
Volume 40 Issue 3, 2006, 733-761

The review paper will be cited towards the end of Chapter 3 as a reference for further reading.

Chapter 2 The Glass-Ceramic Process

2.1 Introduction

The crystallisation, or devitrification, of glass to form a glass-ceramic is a heterogeneous transformation and as such consists of two stages, namely a nucleation stage and a growth stage. In the nucleation stage small, stable volumes of a crystalline phase are formed, usually at preferred sites in the parent glass. The preferred sites are interfaces within the parent glass or the free surface. The latter is usually undesirable as the resulting glass-ceramic microstructure often consists of large oriented crystals that are detrimental to mechanical properties. However, in a few instances an oriented structure is beneficial, e.g., glass-ceramics for piezoelectric and pyroelectric devices [8] and machinable glass-ceramics [9]. In most cases internal nucleation, also known as bulk nucleation, is required and the parent glass composition is chosen to contain species that enhance this form of nucleation. These species are termed nucleating agents and may be metallic (e.g., Au, Ag, Pt, and Pd) or non-metallic (e.g., TiO_2, P_2O_5 and fluorides). The rate of nucleation is very temperature dependent as illustrated in Figure 2-1(a).

Once a stable nucleus has been formed the crystal growth stage commences. Growth involves the movement of atoms/molecules from the glass, across the glass-crystal interface, and to the crystal. The driving force for this process is the difference in volume or chemical free energy, ΔG_v, between the glass and crystalline states. The transport of atom/molecules across the interface is thermally activated with an associated activation energy ΔG_a. Models, involving the terms ΔG_v and ΔG_a, have been developed for the temperature dependence of the growth rate and the form of the resulting curve is given in Figure 2-1(a). Further in-depth treatment of the glass crystallisation process can be found in the previous cited works [1, 3].

2.2 Conventional Method (Two-Stage)

The conventional method for producing a glass-ceramic is to devitrify a glass by a two-stage heat treatment (Figure 2-1 (b)). The first stage takes place at a relatively low temperature that gives a high nucleation rate (around T_N in Figure 2-1 (a)) thus forming a high density of nuclei throughout the interior of the glass. A high density of

nuclei is important as it leads to a desirable microstructure consisting of a large number of small crystals. The second stage is a higher temperature heat treatment at around temperature T_C to produce growth of the nuclei at a reasonable rate.

The parent glass may be shaped prior to crystallisation employing any of the well-established, traditional glass shaping methods such as casting and forming [1-4] or more special methods such as extrusion [10-14]. Glass production and the subsequent heat treatments are in general energy intensive and therefore expensive.

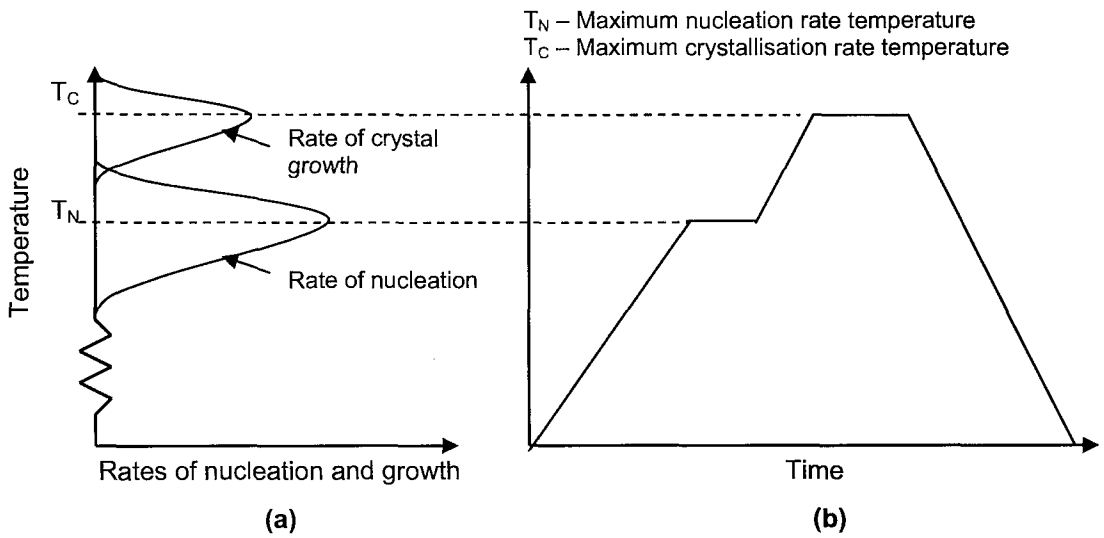


Figure 2-1: Crystallisation of a glass to form a glass-ceramic. (a) Temperature dependence of the nucleation and growth rates with negligible overlap (b) two-stage heat treatment.

2.3 Modified Conventional Method (Single-Stage)

The reason for the two-stage heat treatment of the glass is a consequence of the limited overlap between the nucleation and growth rate curves (Figure 2-1 (a)). If there is extensive overlap of the rate curves then nucleation and growth can take place during a single-stage heat treatment at temperature T_{NG} as indicated in Figure 2-2. The rate curves, particularly the nucleation rate curve, is sensitive to composition and hence by optimising the glass composition it is, in some cases, possible to obtain the necessary overlap. By judicious choice of nucleating agents, this was first achieved for the glass-ceramic system known as "Silceram" [15], as will be discussed later.

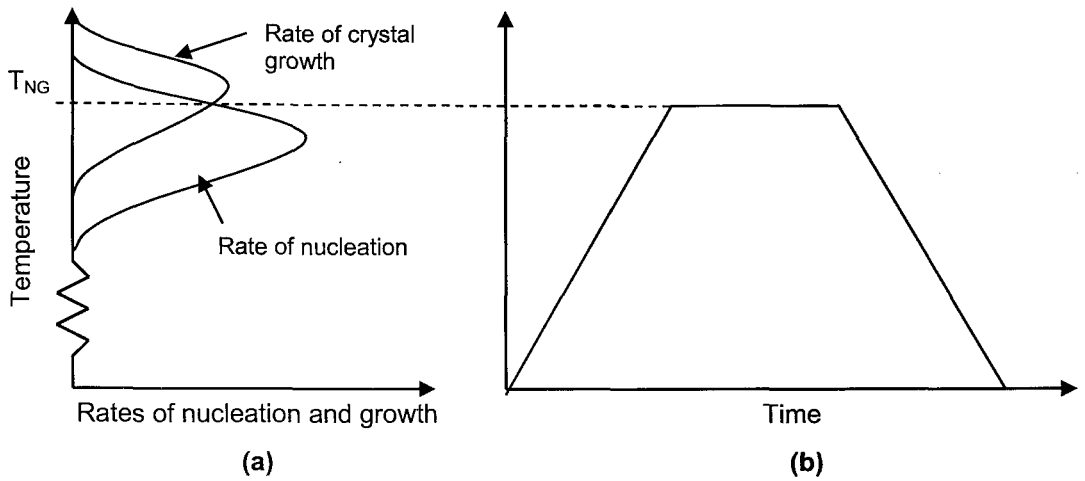


Figure 2-2: Crystallisation of a glass to form a glass-ceramic by a single-stage heat treatment. (a) Temperature dependence of the nucleation and growth rates with significant overlap (b) single-stage heat treatment.

2.4 Petrurgic Method

It was found with "Silceram" that it made little difference whether the glass was heated up to T_{NG} from room temperature or the molten glass was cooled to T_{NG} [15]. This led to the development of the production of certain glass-ceramics by a controlled, usually very slow, cooling of the parent glass from the molten state without a hold at an intermediate temperature. With this method, referred to in the recent literature as the petrurgic method [16, 17], both nucleation and crystal growth can take place during the cooling. Both the modified conventional (single-stage) and the petrurgic methods are more economical that the conventional method (two-stage).

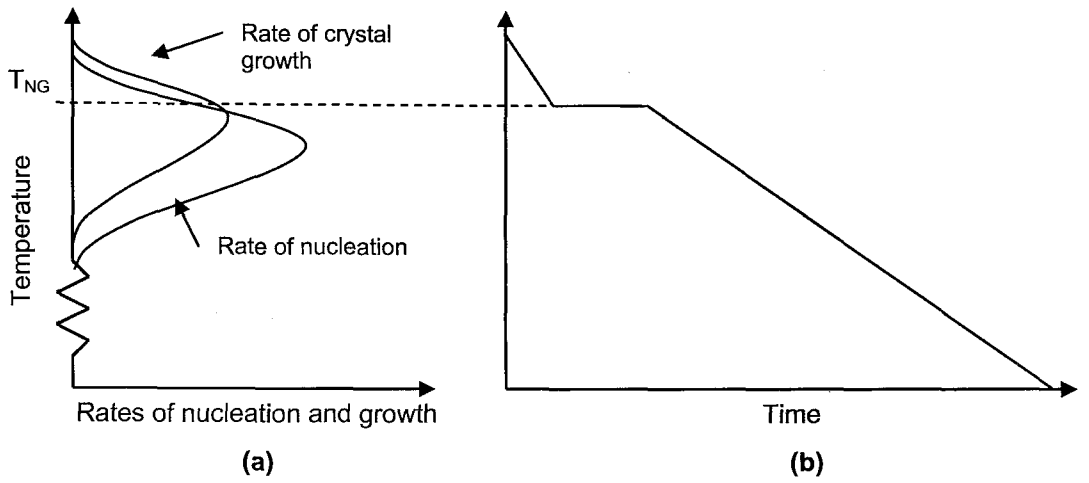


Figure 2-3: Production of slag-based "Silceram" glass-ceramic by direct cooling and a single-stage heat treatment (a) temperature dependence of the nucleation and growth rates with significant overlap of the secondary nuclei rate and the growth rate curves (b) direct cooling/heat treatment

2.5 Powder Methods

The shaping by cold-compacting a powder followed by a high temperature heat treatment to sinter the compact is a common route for the fabrication of ceramics and it has been also employed for glass-ceramic production [18-22]. As there are limitations on the size and shape of components that may be cold compacted, and also a cost in producing a powder, this method is only used if an obvious benefit is identified. In most cases there is little advantage in compacting and sintering a glass-ceramic powder because a high sintering temperature is required and the properties of the final product do not differ significantly from those of glass-ceramics produced by the other routes. It is more attractive to sinter a parent glass powder, which sinters by a viscous flow mechanism at lower temperatures [23]. It is important to consider the rates of viscous flow sintering and crystallisation and the interaction of these processes. If crystallisation is too rapid the resulting high degree of crystallinity will hinder the low temperature sintering leading to an unacceptable amount of porosity [24, 25]. On the other hand, if sintering is fully completed before crystallisation, then the final product is unlikely to differ significantly from those fabricated by other methods. With appropriate rates it is possible in some cases to fabricate dense glass-ceramics by a sintering process in which both densification and crystallisation take place simultaneously at the same temperature. The technological significance of this

process as well as the theoretical complexities of its kinetics have been discussed in the literature [26-28].

Optimisation of composition and sintering temperature can lead to different microstructures, and even different crystalline phases, compared to those from the conventional method, and hence different properties of the product. Pressure assisted densification methods such as hot pressing and HIPping have also been successfully applied for production of glass-ceramics from powders. Although these methods give improved products and near full densification, they are more expensive than cold pressing and sintering and thus unlikely to be employed for processing wastes into monolithic glass-ceramics.

Powder technology facilitates the production of dispersion reinforced glass-ceramic matrix composites [29]. Fabrication of these particle-reinforced composites involves intimately mixing the powdered parent glass with the reinforcement in the required proportions. The mixture is then shaped, sintered and crystallised. Hard and rigid inclusions used as reinforcement hinder the sintering process. The production of continuous fibre reinforced glass-ceramics is more complex and requires dedicated apparatus [30]. For both particulate- and fibre-reinforced glass-ceramics the densification is usually carried out by hot pressing and a final heat treatment is required to achieve crystallisation of the glass matrix.

2.6 Sol-Gel Precursor Glass

So far only glasses produced from the molten state have been considered but in the last decades there has been considerable interest in using sol-gel and colloidal techniques to obtain the precursor glass in either powder or bulk form [31]. Thus all the methods for glass-ceramic production discussed previously may be used with glass produced by this route. However, the sol-gel method will not be discussed further in this review as it is obviously not applicable for the production of glass-ceramics from waste materials.

Chapter 3 Glass-ceramic from Wastes

3.1 Slag from iron and steel production

Blast-furnace slag was the first silicate waste to be thoroughly investigated as a source material for glass-ceramics as discussed further below. These slags typically consist of CaO, SiO_2 and MgO in decreasing amounts as the main constituents, together with minor constituents such as MnO, Fe_2O_3 and S.

3.1.1 Melting and Subsequent Heat Treatment – Conventional Two-Stage Method

The first attempt to commercialise a glass-ceramic from slag was by the British Iron and Steel Research Association (BISRA) in the late 1960s [32]. This glass-ceramic was known as "Slagceram" and it was produced by the conventional, two-stage, heat treatment method [32, 33]. A similar material, "Slag-Sitall", was developed in the former USSR at about the same time [34]. It was widely used in the construction industry for wall claddings and floor coverings because of the inexpensive manufacturing cost in the former USSR. More crystallisation studies were carried out in recent years to investigate the effect of adding nucleating agents to the slag; in particular glass-ceramics with acceptable properties were produced using a two-stage heat treatment and addition of titania [35].

A small percentage of TiO_2 (~1wt%) is usually present in metallurgical slag, but Ovecoglu [35] looked at the effect of adding TiO_2 as a nucleating agent in concentration of 2, 3, and 5wt% of the overall mixture. As in many crystallisation studies thermal analysis was used to assist in the selection of heat treatment schedule. For samples with no additional TiO_2, the shallow exothermic peaks indicated that surface crystallisation was the predominant mechanism of glass-ceramic formation [35]. With extra TiO_2, the exothermic peaks were much better defined suggesting that bulk crystallisation takes over as the main mechanism. This led to grain refinement of the crystallites. A nucleation temperature of 725°C was employed and crystallisation temperatures in the range 950°C- 1100°C investigated. At the low crystallisation temperature of 950°C, crystallisation was incomplete and only small amounts of gehlenite ($Ca_2Al_2SiO_7$) and merwinite ($Ca_3Mg(SiO_4)_2$) were formed. The optimised

crystallisation temperature was found to be 1100°C, and the main crystalline phase was a melilite solid solution, containing gehlenite and akermanite ($Ca_2MgSi_2O_7$). The subsequent mechanical testing results showed the effect of the crystallisation temperature and TiO_2 content. The fracture toughness (5.2MPa.$m^{1/2}$) and bending strength (340MPa) for the 5wt%TiO_2 containing glass-ceramic produced by a 1100°C heat treatment were better than the values of samples with 3wt%TiO_2 crystallised at 1100°C and with 5wt%TiO_2 crystallised at 950°C [35].

Another example of TiO_2 nucleated slag-based glass-ceramics comes from the study of Gomes et al. [36]. A combination of steelwork slag, limestone, sand, bauxite, and ilmenite was used to produce glass-ceramics via the conventional melting followed by two stages of heat treatment. The authors did not disclose the exact quantity of each component used in the raw mixture, but the slag was claimed to be the main component. Sand was used to increase the SiO_2 content, CaO and Al_2O_3 contents were enriched by the inclusion of limestone and bauxite, respectively and ilmenite was used as a source of TiO_2. Through microstructural and thermal analysis, the authors selected 720°C and 883°C for the nucleation temperature and the crystallisation stage respectively and claimed that this heat treatment resulted in bulk crystallisation. The main crystalline phases were diopside ($CaMgSi_2O_6$) and augite $(Ca,Na)(Mg,Fe,Al)(Al,Si)_2O_6$, which are part of a solid solution of the pyroxene group, and these phases were homogeneously distributed in the residual glass matrix. It appears that the presence of a relatively high percentage of TiO_2 helps the nucleation process and favours bulk nucleation as the dominant mechanism, which is suitable for melt-heat-treatment routes.

Ferreira et al. [37] experimented with another type of slag, basic-oxygen-furnace (BOF) slag, and produced glasses and glass-ceramics with good physical and mechanical properties and attractive aesthetics. Glasses from mixtures of BOF slag, sand, and Na_2O in different proportion were produced by melting at 1400-1450°C for 1h in Al_2O_3/ZrO_2 crucibles. The best mixture (in wt%, 60 BOF slag, 35 sand, and 5 Na_2O), i.e. with a relatively good glass-forming ability, gave the most intense exothermic peak and exhibit bulk crystallisation [37]. Samples of this composition were nucleated at 660°C followed by an isothermal crystallisation heat treatment at 775°C. It was found that augite was the main crystalline phase after 5 minutes but a second crystalline phase (wollastonite, $CaSiO_3$) was observed after 50 minutes at

775°C. The bending strength of glass-ceramic samples (~136 MPa) was higher than that of typical marble (~15 MPa) and of soda-lime glass (~50 MPa), indicating the material's potential as floor tiles and in other building applications.

As far as other glass-ceramic systems are concerned, El-Alaily [38] recently investigated some basic physical and chemical properties of lithium silicate glass and glass-ceramics derived from blast furnace slag with additions. The study was based around a 20wt%Li_2O-80wt%SiO_2 glass mixed with slag up to a concentration of 35wt%. It is well documented that an addition of 30wt%Li_2O to SiO_2 reduces the liquidus temperature significantly from 1713 to 1030°C [39]. Thus El-Alaily [38] was able to melt slag-containing mixtures at 1350°C, which is 100°C or more lower than in the previously discussed systems. Heat treatment involved 1 h hold at 500°C and then another 1 h hold at 850°C to complete crystallisation. Surprisingly the hardness of the glass-ceramics was less than that of their parent glasses. This was attributed to microcracking associated with the crystals, although from the text it was not clear whether the microcracking was thought to occur at, or when cooling from, the crystallisation temperature.

3.1.2 Melting and Subsequent Heat-Treatment – Modified One-Stage Method

This approach is designed to simplify the conventional heat-treatment process for glass-ceramic production and thus to reduce the cost of production and maybe process time as well. A recent work on slag glass-ceramics using the modified one-stage method was reported by Francis [40]. The gehlenite/diopside glass-ceramic was the product of a single-stage heat-treatment at 900-1100°C of a glass precursor from blast furnace slag. It was claimed to have good erosion resistance in slurry but no data from the parent glass or other materials were presented for comparison. The material also showed good chemical resistance in a 10% NaOH solution but not in 10% HCl solution [40].

The most comprehensive work on reuse of metallurgical slag using the modified one-stage method has to be the development of 'Silceram' at Imperial College London (UK) in the 1980s [15, 41, 42] and will be considered in detail in this section. The composition of the starting batch was adjusted by mixing the blast-furnace slag with

up to 30wt% colliery shale (another waste product) and small amounts of pure oxide components. A typical composition of "Silceram" parent glass (in wt%) is: SiO_2, 48.3; TiO_2, 0.6; Al_2O_3, 13.3; Cr_2O_3, 0.8; Fe_2O_3, 4.0; MnO, 0.4; MgO, 5.7; CaO, 24.7, Na_2O, 1.2; K_2O, 1.1. Of particular significance is the Cr_2O_3 and Fe_2O_3 content, as these oxides are both nucleating agents. Either oxide alone is capable of initiating nucleation but there is a synergistic effect if they are both present. These oxides promote the formation of small crystals of spinel ($MgCr_2O_4$), which in turn act as nucleation sites for the main crystal phase, a pyroxene.

When Cr_2O_3 is used on its own, the spinel nuclei, termed primary nuclei, are formed over a narrow, high temperature range centred at around 1350°C. The primary nuclei are also formed when Cr_2O_3 and Fe_2O_3 are both present but, in addition, secondary nuclei are created. The secondary nucleation occurs over the temperature range 850°C to 1150°C with a maximum at 950°C (refer back to Figure 2-2(a) in Chapter 2). The important feature of this figure is that the growth rate curve overlaps the secondary nucleation rate curve thereby allowing successful crystallisation at a single temperature by the modified conventional method (single stage). The main crystalline phase is a pyroxene of composition close to diopside although small quantities of anorthite ($CaAl_2Si_2O_8$) are found after excessively long heat treatments [43, 44]. Depending on the exact composition and processing parameters the crystals exhibited varying degrees of dendritic morphology, for example some "Silcerams" produced from pure constituents have a more marked dendritic structure than those of slag-based "Silceram", as depicted in Figure 3-1. However, the difference in properties between slag-based and pure constituents-based "Silceram" is not significant and data from both types have been obtained, focusing on potential applications of the materials in structural applications, including thermal shock, erosion, impact and abrasion resistant components [15, 43-49].

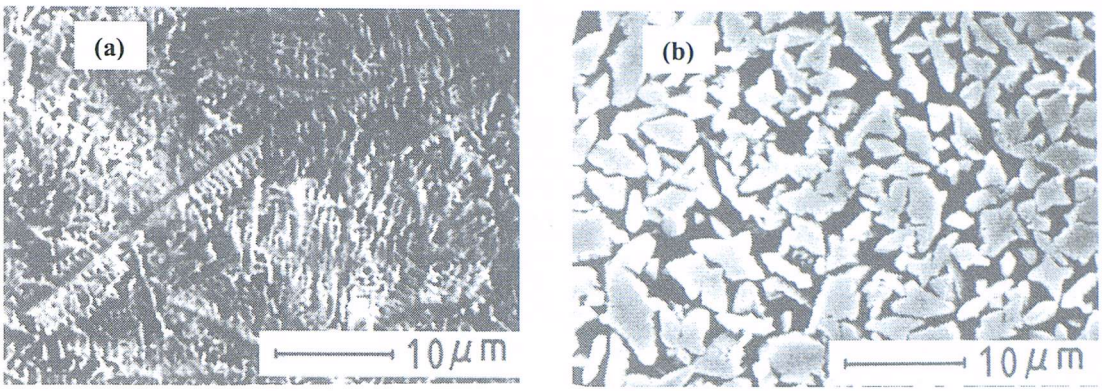


Figure 3-1: Microstructure of (a) pure constituents-based and (b) slag-based "Silceram" glass-ceramics [44]

Preliminary erosion studies demonstrated that "Silceram" had superior erosion resistance to many rival erosion resistant materials such as cast basalt, "Slag-sitall" and alumina (75% purity) although inferior to the more expensive 97.5% purity alumina [46]. It was found that erosion resistance decreased with increasing diopside crystal size but that neither the volume fraction of diopside nor the presence of a second crystalline phase played a major role in determining resistance. Abrasion resistance was found to be even less microstructure sensitive as it was crystal size independent [46]. This insensitivity to microstructure is encouraging as it means that any microstructural variations that may occur during production from wastes on an industrial scale are unlikely to affect performance.

The ballistic resistance of Silceram has been investigated at velocities up to nearly 300m/s using a gas gun and its performance found to be comparable to that of alumina and a glass-ceramic, LZ16, developed for ballistic applications [47]. In view of these encouraging results composite armour with Silceram as the front face was tested in field trials with 5.56mm ball rounds over a velocity range 600-1000m/s. The critical velocity below which the armour was not defeated was 660m/s which is only slightly inferior to the well-established alumina-Kevlar armour system. The armour system used for the field trials was not optimised and it was considered that reducing the thickness of the Silceram front face and increasing the thickness of the laminate backing would further improve the anti-ballistic performance.

3.1.3 Petrurgic Method

As described in Chapter 2, the petrurgic method is an alternative heat-treatment method that can significantly reduce the energy consumption and thus production cost of glass-ceramics. Figure 2-3(a) in Chapter 2 indicates that rather than reheating the parent glass to 950°C it would be feasible to cool it (after shaping) from a high temperature to the heat treatment temperature. This heating schedule is given in Figure 2-3(b) and this particular method has been analysed for production of Silceram [41]. It has been estimated that controlled cooling with a hold at 950°C would result in an energy saving of about 60% when compared to the conventional two-stage heat treatment. Significant additional energy savings could also be made if the production plant was situated at a steel works so that hot slag was used as a raw material [42].

3.1.4 Powder Technology and Sintering

Although it has been established that bulk nucleation can be achieved in parent glasses with a slag component, studies have also been carried out on fabrication of glass-ceramics by the powder route in which surface nucleation usually plays a more important role [48, 49]. For example, the micrograph of Figure 3-2 shows a continuous crystalline layer that was nucleated at the particle surface and also individual crystals in the interior that were bulk nucleated in "Silceram" material [48]. Both cold compacting followed by a single sintering/crystallisation treatment and hot pressing without a post pressing crystallisation treatment have been employed in the case of Silceram glass-ceramics [15, 48]. The main crystalline phase was diopside, as found in the glass-ceramics produced by conventional methods, but there was also a marked increase in the propensity for the formation of anorthite.

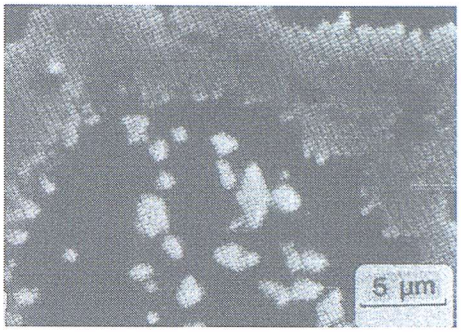


Figure 3-2: Scanning electron microscopy (SEM) micrograph showing surface and bulk crystallisation in sintered "Silceram" glass-ceramic [48]

There are a few recent studies that involved using the sintering route to produce slag-based glass-ceramics. Cimdins et al. [50] used mixtures of metallurgical slag, peat ash and clay as sources of silica, and other glass formers. The addition of clay helped to lower the sintering temperature while maintaining the final density of the glass-ceramic at about 3 g/cm^3. The appropriate sintering temperature was found to be around 1100-1180°C, depending on the starting composition. The best properties (bending strength of 96MPa) were obtained from a specimen with high contents of SiO_2 (60.6wt%) and Al_2O_3 (17.9wt%) produced from 15wt% peat ash; 55wt% metallurgical slag and 30wt% clay mixture. The chemical durability of this glass-ceramic in 0.1N HCl solution was superior to the one without clay. Dana et al. [51] sintered two combinations of clay, feldspar, and a limited amount of slag (20 and 30wt%) from steel plants to produce ceramic floor tiles with superior mechanical properties and similar thermal expansion coefficients to those of commercial products. Compacts were subjected to a single stage firing at a temperature between 1060°C and 1180°C for 30 minutes with the denser samples being obtained at the higher end of this temperature range. Sintering at 1180°C produced the highest Young's modulus and the lowest water absorption, similar to that specified for commercial floor tiles, whereas an 1160°C treatment resulted in a slightly better flexural strength. In general, the mechanical properties become poorer when the content of slag in the overall mixture increases, suggesting there is a trade-off between cost and strength when the more expensive feldspar is replaced by the slag.

As mentioned earlier, hot-pressing may be used to fabricate dense glass-ceramics from slags. In general, the mechanical properties of hot pressed glass-ceramic are superior to the properties of the materials manufactured by the conventional methods

and cold compacting, as shown in Table 3-1 for "Silceram" materials. However, the main benefit of research on hot-press glass-ceramics is that it provides the prerequisite knowledge for the fabrication of glass-ceramic matrix composites [30] where the marked enhancement in mechanical properties can be used to vindicate the additional energy consumption and thus production cost. For more details on glass-ceramic matrix composites made from metallurgical slag, please see the review paper [52].

Table 3-1: Comparison of the mechanical properties of "Silceram" glass-ceramics produced by various methods (HP and CP are hot pressed and cold pressed and heat treated respectively)

Method	**K_{1C} (MPa.m$^{-1/2}$)**	**Bend Strength (MPa)**
Modified conventional	2.1	174
HP (940°C, 90 min)	3.0	186
HP (900°C, 120min)	2.2	262
CP	1.4	90

Table 3-2 presents a summary of mechanical properties of glass-ceramics made from metallurgical slag, summarising the studies described in the proceeding sections and other results in the literature.

Table 3-2: Summary of properties of glass-ceramics and composites made from metallurgical slag by different routes

Starting Material	Method	Main Crystalline Phase	Material Properties					Reference
			Density ($g\ cm^{-3}$)	Thermal Expansion Coefficient ($\times 10^{-6}\ °C^{-1}$)	Bending Strength (MPa)	Young's Modulus (GPa)	Microhardness	
Blast furnace slag + 5wt%TiO_2	Conventional	Solid solution of melilite, i.e. gehlenite and akermanite	2.877 (as-cast glass)	9.1 [250-800°]	340	n/r	1020kg mm^{-2}	Ovecoglu [35]
60wt% BOF slag + 35wt% sand + 5wt%Na_2O	"	Augite/wollastonite	3.3	n/r	136 ± 14	n/r	7.8 ± 0.2GPa	Ferreira et al. [37]
(80wt%SiO_2 + 20wt%Li_2O) + 20wt% blast furnace slag	"	Lithium disilicate ($Li_2O.2SiO_2$), lithium aluminium silicate ($Li_2AlSi_3O_8$), and wollastonite	3.408	n/r	n/r	n/r	590kg mm^{-2}	El-Alaily [38]
Silceram, iron blast-furnace slag based glass-ceramic (SCR25-76)	Conventional / Powder technology / Sintering	Diopside	2.9	7.5	180	122	7GPa	Carter et al. [44]
15wt% peat ash + 55wt% steel plant slag + 30wt% clay	Powder technology / Sintering	n/r	3.04	n/r	96	n/r	n/r	Cimdins et al. [50]
45wt% clay + 35wt% feldspar + 20wt% metallurgical slag	Powder technology/ Sintering	Quartz and feldspar	~2.3	7.08 [up to 1000°C]	56.6	31.2	7 (Mohs' scale)	Dana et al. [51]

n/r not reported;

3.2 Coal Ash from Power Stations

Two types of coal ash are generated from combustion of coal in thermal power stations: fly ash and bottom ash. Fly ash, which accounts for about 80% of the total ash generated, is trapped and recovered from gas flow. The remaining 20% is called bottom ash as it is collected at the bottom of the furnace. Mixtures of these wastes are sometimes stored and weathered in water ponds to give what is known as pond ash. From the study of Benavidez et al. [53] it is clear that the principal difference between fly and bottom ashes is that the former has a much higher proportion of fine, spherical particles and a narrower particle size distribution.

Significant amounts of fly ash (e.g. in the order of 15 million tonnes per annum in an industrialised country such as Germany [54]) are produced continuously as a by-product of coal combustion in power stations. In 2002, approximately 50% of coal fly ash produced by New Zealand coal-fired power plant was sold to local cement company as substitute for cement in concrete mixes [55], and similar percentages were utilised mainly in the building industry or in road construction in other countries [56, 57]. Nevertheless, a large amount of coal ash is still left in storage ponds waiting to be disposed, with China being the major and still-growing force (e.g. 85 million tons p.a. in the early 1990s [58]) in the Asia Pacific region.

Coal ash typically contains more SiO_2 but less CaO than metallurgical slag. There are exceptions, of course, and of particular note is the high Fe_2O_3 content (>40wt%) in an Egyptian ash [59] and the high loss on ignition (thus low SiO_2) content in an Italian ash (Rete) [60]. Chemical compositions of coal fly ash reported from different countries are given in Table 3-3. Given that the composition of coal ash can vary in SiO_2, Al_2O_3 and CaO content, glass cullet and other additives were often used to ensure the stability of the parent glass. Glass-ceramic production provides an alternative to disposal of coal ash, as documented by numerous reports in the literature, which will be discussed in this section.

Table 3-3: Typical coal fly ash compositions (wt%) from various sources

Oxides	Poland [56]	Illinois, USA [61]	Utah, USA [62]	Seyitömer, Turkey [63]	Çayırhan, Turkey [64]	Portugal [65]
SiO_2	61.96	47.6	65.37	44.58	42.82	66.15
Al_2O_3	19.68	29.6	22.14	22.54	13.36	21.63
Fe_2O_3	8.52	15.8	3.61	9.85	7.01	7.20
CaO	2.55	4.2	4.66	6.76	16.38	0.36
MgO	2.32	0.6	1.53	8.98	5.85	0.85
Na_2O	0.65	0.5	0.62	0.22	5.06	0.40
TiO_2	1.01	-	0.96	-	-	0.97
K_2O	2.72	1.7	1.10	0.60	1.83	2.14
MnO	0.27	-	-	-	-	0.05
ZnO	0.06	-	-	-	-	-
P_2O_5	0.12	-	-	-	-	0.18
Cr_2O_3	-	-	-	-	-	-
PbO	0.05	-	-	-	-	-
SO_3	0.08	-	-	-	6.47	-
Total	99.99	100	99.99	93.53	98.78	99.93

Oxides	China [66]	China [67]	Rete, Italy [60]*	Meirama, Spain [60]	Teruel, Spain [60]	Egypt [68]	India [69]
SiO_2	58.30	55.30	15.17	58.88	51.56	31.0	57.00
Al_2O_3	15.36	29.36	7.14	25.50	29.13	11.4	29.3
Fe_2O_3	11.58	5.84	3.76	6.58	4.78	43.5	6.5
CaO	6.84	4.58	23.71	5.64	4.21	4	3.9
MgO	0.35	0.33	1.35	1.12	1.62	1.3	1.1
Na_2O	0.15	0.46	0.90	0.28	0.26	-	0.2
TiO_2	1.25	1.22	0.31	1.24	1.66	2.3	0.13
K_2O	1.23	1.13	0.44	0.49	0.80	-	0.3
MnO	-	-	-	-	-	-	-
ZnO	-	-	-	-	-	1.4	-
P_2O_5	0.56	0.25	-	-	-	-	-
Cr_2O_3	-	-	-	-	-	0.9	-
PbO	-	-	-	-	-	-	-
SO_3	0.95	0.82	-	-	-	-	-
Total	96.57	99.29	52.78*	99.73	94.02	95.8	98.43

* Loss on ignition = 41wt%

3.2.1 Melting and Subsequent Heat Treatment

Glass-ceramics from coal fly ash were produced using the melt quenching / heat treatment method as early as in the 1980s by DeGuire and Risbud [61]. The fly ash was melted at 1500°C without any additives and then cast into graphite moulds. An unusual two stage nucleation treatment was used: 2hrs at 650°C or 700°C followed by 5 or 10 hours at a temperature in the range 800°C to 950°C prior to a crystallisation treatment at 1000°C or 1150°C. It was claimed that the extent of crystallisation was not significantly affected by the different nucleation treatments prior to the crystallisation stage, hence, a single-stage nucleation heat treatment may be feasible. However, as the authors noted, the percentage crystallisation was low (less than 25%) which was attributed to the limited amount of TiO_2 present to act as a nucleating agent [61].

Cumpston et al. [62] used $CaCO_3$ (20wt%) and TiO_2 as additives to fly ash to achieved a 40vol% crystalline glass-ceramic material with anorthite as the main crystalline phase. The addition of $CaCO_3$ lowered the melting temperature and the viscosity of the melt allowing a homogeneous amorphous glass to be obtained with a melting temperature 100°C less than used in the previous study [62]. The small percentage of TiO_2 added made little difference to the final degree of crystallinity and the main crystalline phase remained anorthite. However the crystal morphology and distribution must have been affected as the hardness of the TiO_2-containing glass-ceramic was higher than that of the glass-ceramic without that additive. A decrease in crystallinity was observed with increasing crystallisation temperature, and this can be explained by the fact that the heat-treatment temperature was above the maximum of the crystal growth rate curve. However, since no new crystalline phase was observed, the authors concluded that this occurrence was due to the formation of a metastable amorphous phase with increasing heat-treatment temperature. The glass-ceramic was heat treated for 48 hours at 1000°C, which highlights the energy intensiveness of such a processing method. Technical applications such as high-temperature crucibles or refractory materials were suggested for this glass-ceramic [62].

Similar but more recent studies using two Turkish fly ashes (Table 3-3) and the conventional two-stage method have been carried out by Erol and co-workers [63, 64]. The fly ash powders were melted, crushed and remelted at 1550°C without any additives or nucleating agents. Based on the DTA analysis, nucleation temperature of

680°C and crystallisation temperature of 924°C were employed for the Cayirhan ash [64] whereas the corresponding temperatures for the Seyitőmer ash were 728°C and 980°C, respectively [63]. The main crystalline phase in the glass-ceramics produced was diopside-alumina [$Ca(Mg,Al)(Si,Al)_2O_6$]. An interesting feature of the investigation was the correlation found between heat treatment and microstructure, hardness and wear resistance. Surprisingly, increasing the nucleation time for the Cayirhan ash glass-ceramic, whilst holding the crystallisation time and temperature constant, led to an increase in crystal size. This in turn resulted in a decrease in hardness and wear resistance with increasing nucleation time. For the Seyitőmer ash glass-ceramics increasing the crystallisation time was found, as expected, to increase both crystal size and degree of crystallinity. As a consequence the hardness and wear resistance increased with increasing crystallisation time. The Portuguese ashes investigated by Leroy et al. [65] gave melts that were too viscous to pour at 1520°C and hence 10wt%Na_2O and 10wt%CaO (by adding pure Na_2CO_3 and $CaCO_3$) were added to the ash to lower the viscosity. Pourable melts were obtained which were successfully transformed into glass-ceramics with esseneite ($CaFeAlSiO_6$) as the main crystalline phase formed and nepheline ($NaAlSiO_4$), as secondary phase [65, 70]. The microstructures were notable for their fineness; the crystals being about 0.1μm and 0.2μm after crystallisation treatments at 800°C and 870°C, respectively. The authors mentioned the pleasing aesthetic quality of the glass-ceramics, comparable to that of dark marble and malachite, and concluded that, taken together with the acceptable mechanical properties, thermal expansion coefficient and chemical stability, potential applications for these materials are related to the structural and building industries, such as kitchen and laboratory benches, and wall, roof, and floor tiles. More recently, a group of Chinese researchers [66, 67] produced interesting yet unusual glass-ceramics with nano-sized spherical crystals (<300nm) from both low (~15wt%) and high (~30wt%) alumina containing fly ashes. The crystals were reported to be wollastonite, but the authors made no attempt to explain their fineness and morphology. The optimised glass-ceramics based on the high alumina fly ash had slightly better mechanical properties (Hv: 7.1 GPa; 4-point bending strength: 103 MPa) than those of the low alumina fly ash based glass-ceramic and the glass-ceramics reported by Ferro et al. [70].

Barbieri and co-workers have published a series of papers [60, 71, 72] on glass-ceramics produced from fly ash mixed with other waste materials. The other wastes were mainly float dolomite ($CaMg(CO_3)_2$) from mineral extraction operations, which was used to increase CaO and MgO content, and glass cullet to increase the amount of SiO_2, Na_2O and CaO present in the parent glass. In this way the authors were able to study the crystallisation of parent glasses of a wide range of compositions. Particularly noteworthy was their use of constitutional diagrams to predict suitable parent glasses and the phases resulting from devitrification. The diagrams employed were that due to Ginsberg [73], which indicate the composition of suitable glasses for crystallisation, and those proposed by Raschin-Tschetveritkov [74] and Lebedeva [73], both of which aid in predicting the phase formed on devitrification. By judicious selection of the mixtures of wastes, and hence compositions of parent glasses, and of heat treatment schedules, Barbieri and co-workers were able to produce a series of glass-ceramics containing different phases [60, 71, 72]. For example glass-ceramics from fly ash with only glass cullet as an additive had acicular wollastonite as the crystalline phase whereas, with the further addition of dolomite, this phase was only found after heat treatment in a narrow temperature range around 1000°C and most heat treatments resulted in a microstructure with dendritic pyroxene (diopside) and a small amount of acicular feldspar (anorthite).

These reports are summarised in Table 3-4 which presents the properties of different glass-ceramics produced from coal fly ash using the conventional method with and without additives.

Table 3-4: Properties of glass-ceramic materials made from coal ash with and without additives using various processing methods

Starting Material	Main Crystalline Phase	Material Properties					Reference
		Density ($g\ cm^{-3}$)	Thermal Expansion Coefficient ($\times 10^{-6}\ °C^{-1}$)	Bending Strength (MPa)	Fracture Toughness ($MPa\ m^{-1/2}$)	Microhardness	
Coal fly ash (Two-stage)	Ferroaugite [(Ca, Fe^{2+})(Al, Fe^{3+})$_2SiO_6$] and potassium melilite [$KCaAlSi_2O_7$]	2.73	5.63 ± 0.70 [100-600°C]	n/r	n/r	458.6 ± 45.8kg mm^{-2}	DeGuire et al. [61]
Coal fly ash + 20wt%$CaCO_3$ + 1wt%TiO_2 (Two-stage)	Anorthite	1.69	n/r	n/r	n/r	627.2kg mm^{-2}	Cumpston et al. [62]
Coal fly ash (Two-stage)	Diopside-alumina [Ca(Mg, Al)(Si, Al)$_2O_6$]	3.29	7.31 [100-850°C]	n/r	n/r	2899±135kg mm^{-2}	Erol et al. [63]
Coal fly ash + 10wt%Na_2CO_3 + 10wt%$CaCO_3$ (Single-stage)	Esseneite and nepheline	2.73	10.1 [20-400°C]	67.02 ± 13.3	1.46 ± 0.2	7.18 ± 0.5 GPa	Leroy et al. [65], Ferro et al. [70]
i) Coal fly ash + 8wt%Na_2O and 9.2wt%CaO ii) 9wt%BaO and 9.1wt%CaO	Wollastonite	2.57-2.67	8.8-9.7	63-79	n/r	5.4-6.9	Peng et al. [66]
i) Coal fly ash + 5.7wt%Na_2O, 8.6wt%CaO, and 5wt%B_2O_3 ii) 6wt%Na_2O and 9wt%CaO	Wollastonite and anorthite	2.58-2.72	8.9-9.9	48-103	n/r	5.2-7.1	Peng et al. [67]
40wt% coal fly ash + 30wt% glass cullet + 30wt% dolomite (Single-stage)	Diopside/augite + anorthite/albite + iron spinels (magnetite Fe_3O_4, magnesioferrite $MgFe_2O_4$, and maghemite Fe_2O_3)	n/r	n/r	n/r	3.0	7.3 GPa	Barbieri et al. [60]
50wt% coal fly ash + 50wt% waste glass cullet	Pyroxene (diopside, augite and hedenbergite)	n/r	n/r	90	n/r	4.4	Boccaccini et al. [75]
Coal fly ash + 10wt%CaO (from ark shell) + 7wt%TiO_2 (Petrurgic)	Identified as $(Ca_{0\text{-}05})AlSi_{0.75}P_{0.5}O_{4.5}$ by EDS	2.77-2.81	5.49-6.49	98-176	1.121-3.100	91-100 GPa	Kim et al. [76]

n/r not reported

Unlike fly ash, coal bottom ash has been subjected to limited number of investigations as a viable waste material for producing glass-ceramics. This is simply due to the inhomogeneous nature of bottom ash, containing much coarser particles and sometimes more residual carbon, unfavourable for glass-ceramic production. Nonetheless, Kniess et al. [77] produced glass-ceramics in the Li_2O-Al_2O_3-SiO_2 system using the conventional method. The bottom ash used in the study was submitted to magnetic field separation with the goal of reducing the iron content as the authors had found difficulties with controlling the crystallisation of glasses with high iron content [77]. The magnetic separation reduced the amount of magnetic crystalline phases, which were mainly magnetite and hematite, from 9.96wt% to 5.36wt% Fe_2O_3. After the reduction, the bottom ash was mixed with 2wt% TiO_2 (rutile) and 5wt% Al_2O_3. 85wt% of this mixture and 15wt% Li_2CO_3 was then calcined at 800°C. The addition of Li_2O to aluminosilicate glasses helped to reduce the melt viscosity and to form stable glass [78]. The calcined charge was melted and the viscosity at 1550°C was such that the flow of the melt was satisfactory and a dark glass was readily obtained. Samples of the bulk glass were heat treated at 730°C for 15min for the nucleating stage and at 866°C for up to 20 minutes for the crystallisation stage. As expected the longer the crystallisation treatment the greater the degree of crystallinity but surprisingly the authors claimed that the grain size decreased. The crystalline phases produced after the heat treatments were lithium aluminosilicate ($Li_xAl_xSi_{1-x}O_2$) and virgilite ($Li_xAl_xSi_{3-x}O_6$), as predicted from the ternary phase diagram, and resulted in low values for the coefficient of thermal expansion (($-23.4\times10^{-7}°C^{-1}$ and $2.2\times10^{-7}°C^{-1}$ over the temperature ranges 25-325°C and 25-700°C respectively). Given the low thermal expansion coefficient of these glass-ceramics based on the SiO_2-Al_2O_3-Li_2O system, the commercial application is likely to be mainly kitchen hot plates with relatively low production costs [77]. However, glass-ceramics from this system could find applications also in photolithographic processes, since the thermal expansion coefficient of the glass and of the used metal are compatible [79], and for substrates for telescopes [80].

3.2.2 Powder Technology: monolithic material and composites

Mixtures of coal ash and waste glass have been used in early technological approaches to the fabrication of glass-ceramics and glass matrix composites by powder technology and sintering [54, 75, 81]. However, it is only recently that fundamental studies have appeared focusing specifically on the production of sintered glass-ceramics from coal ash.

For example, powder technology and sintering have been used recently to obtain novel glass-ceramics with magnetic properties from mixtures of coal ash with high iron content and borosilicate glass [59]. Samples containing ash and glass in a 50/50 weight proportion and sintered at 1500°C for 5 hours showed the best results in terms of densification, microstructure and magnetic properties. A typical microstructure of the material is shown in Figure 3-3; the large dark grey grains were identified as being cristobalite, while the small bright particles were found to be enriched in metals, especially iron and titanium, and consequently were assumed to be the ferrite-type phase that was detected by XRD. It is the latter which is responsible for the soft magnetic characteristics of the glass-ceramic. The saturation magnetisation increased with sintering/crystallisation time which was attributed to a concomitant increase in the proportion of the ferrite phase. Comparison of the magnetisation saturation values for an iron-containing ferrite and the glass-ceramic (6emu/g) indicated that about 10% of the ferrite-type phase was present in the latter, which was consistent with the microstructural observations. This work demonstrated a convenient way of dealing with high iron-content ash by transforming it into useful magnetic glass-ceramic products, via a simple and cost-effective powder technology and sintering route [59].

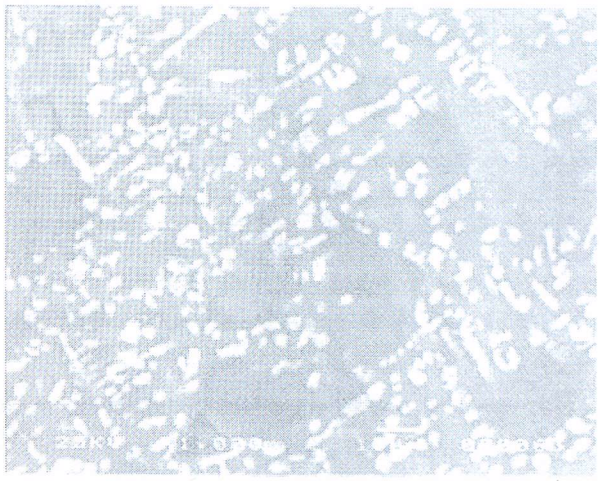


Figure 3-3: SEM micrograph of a sample made of a 1/1 mixture of Fe-containing coal ash and showing crystalline microstructure consisting of cristobalite (dark grains) and titanium bearing ferrite (bright phase), embedded in a glassy phase [59].

Francis et al. [68, 82] also explored the combination of coal fly ash and soda-lime glass using the powder route. In this case parent glasses were produced which were ground and then given a sintering/crystallisation treatment. The microstructural development varied with both the quantity of cullet used and the heat treatment schedule. For the particular treatment at 1000°C for 15 hours, it was deduced that increasing the proportion of glass leads to a decrease in both crystalline phases of SiO_2 (i.e. quartz and cristobalite) and hematite. On the other hand, the propensity for the formation of pyroxenes (diopside and augite) and anorthite increased with glass content. At the higher heat treatment temperature of 1050°C, due to the complete reaction of SiO_2 with other components present in the mixture, another phase ν-Fe_2O_3, known as maghemite, was detected in the sample containing 50wt% soda-lime glass. Most work, e.g. thermal analysis to determine i) heat treatment schedules, ii) activation energy for crystallisation and iii) Avrami exponent, was carried out on a parent glass containing 40wt% coal ash as this exhibited a good combination of ease of melting, good fluidity and controllable sintering/crystallisation. For this composition pyroxene dominated at low heat treatment temperature but was displaced by plagioclase at higher temperatures (950°C).

In the previous section the production of low coefficient expansion glass-ceramics with lithium aluminosilicate and virgilite phases was discussed. Low coefficient glass-ceramics have also been formed via sintering although in this case the main phase is indialite, which is a hexagonal form of cordierite ($2MgO.2Al_2O_3.5SiO_2$) [69].

Mixtures of fly ash, talc and alumina powder were sintered at 1370°C to produce a cordierite-based glass-ceramic with a density of 2.4 g/cm^3, Young's modulus of 100GPa, flexural strength of 78.4 MPa, and a low thermal expansion coefficient (about 1-2×10^{-6}/°C in the 250-650°C range).

In the studies discussed so far in this review, conventional furnaces were used, however it has been shown that coal fly ash can be immobilised into a glass-ceramic material in a much shorter time by microwave processing while improving the physical and mechanical properties compared to those achieved via conventional heating [83]. In addition, there is very little work done on glass-ceramic matrix composites produced from coal ash. For further details, please consult the review paper [52].

3.2.3 Petrurgic Method

Magnetic glass-ceramics have been obtained from mixtures of coal ash and 20-60wt% soda-lime glass by the petrurgic method (see Section 2.4) [17]. The mixtures were melted at 1500°C for 5 hours and then cooled in the furnace at 10°C/min or 1°C/min. At a cooling rate of 1°C/min, there was a greater propensity for the formation of plagioclase with increasing soda-lime glass content as the added glass supplied the Na and Ca required for this crystalline phase. The authors also reported that the glass-ceramics with 20 and 40wt% glass addition had good aesthetic qualities because of their black shiny surfaces [17]. Samples that were cooled at 10°C/min had limited time of residence at temperature to crystallise fully, and therefore, there was an absence of augite and plagioclase phases. However, a dendritic magnetite crystalline phase was formed instead, as shown in Figure 3-4, conferring to the glass-ceramic material interesting magnetic properties.

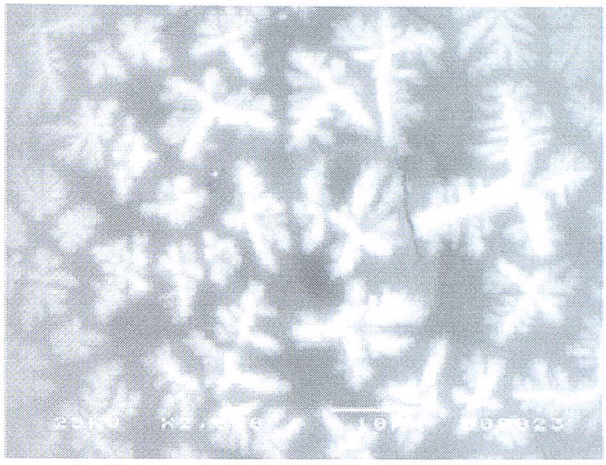


Figure 3-4: Dendritic microstructure of magnetic glass-ceramic produced using the petrurgic method from Fe-containing coal ash [17]

Kim et al. [76] recently published their work on a coal fly ash based glass-ceramic produced via an economic single-stage heat treatment method based on the same principle as the "Silceram" method described in section 3.1.2. Ark shell was added to the coal ash as a source of CaO to reduce the melting temperature of the overall mixture, and TiO_2 was used as the nucleating agent. The molten mixture was cast into a preheated (750°C) mould before being transferred to a furnace for crystallisation. The interruption during cooling makes this process slightly different from the described petrurgic method. The glasses crystallised successfully to produce a new phase, $(Ca_{0.05})AlSi_{0.75}P_{0.5}O_{4.5}$, which has a monoclinic crystal structure. This phase has a rod-like morphology of which the aspect ratio increased with crystallisation time and temperature up to 1000°C. Promising mechanical properties were obtained from this coal fly ash based glass-ceramic, particularly the maximum fracture toughness value of 3.1MPa $m^{-1/2}$ which is associated with the presence of high aspect ratio crystals (Table 3-4).

3.3 Other Silicate Wastes

3.3.1 Residues from Urban Incinerators

Apart from the extensive research effort made on the two main streams of silicate waste considered above, the interest in reusing municipal incinerator wastes has been equally significant as demonstrated by the numerous publications on this topic [52]. The disposal of large quantities of municipal solid waste (MSW) is a major and

growing problem, especially in large cities in developed countries. Only 15% of MSW were recycled in England during 2002/03, leaving a major issue of the disposal of the remaining wastes [84]. One of the options for the disposal of the non-recyclable fraction is incineration with energy recovery [85]. Unfortunately the incineration process itself also results in waste. About 10 to 25wt% of the solid waste after incineration remain as solid residues, such as bottom ash, electrofilter fly ash and slag [85, 86]. The magnitude of the problem is illustrated by the following facts: (1) a single large European urban incinerator may produce fly ash at the rate of 10,000 to 60,000 tonnes per year [87] and (2) the estimated total incinerator fly ash rate for a country like Taiwan for 2003 was 2,000,000 tonnes per year [88]. Filter ashes (fly ash), collected in the air pollution control systems of incinerators, are particularly problematic because they contain significant concentrations of undesirable elements and heavy metals (e.g. As, Pb, Sb, Sn, Sr) as well as trace amounts of organic pollutants (e.g. polychlordibenzo-dioxins and -furanes). Due to increasingly stringent environmental regulations, these residues are regarded as hazardous in most countries [89-91].

Thermal treatment of problematic wastes by vitrification has been well-documented regarding its effectiveness in immobilising the toxic contents in inert glass-matrices [92]. Vitrification technologies used around the world for treatment of incinerator residues vary from the conventional electric furnaces to the more recent plasma arc technology [93-97]. The end product in all cases is a glassy slag, which encapsulates the toxic elements and heavy metal residues present in the incinerated ash. Often the vitrified product has adequate and satisfactory technical properties to compete against conventional materials for some building applications. However, an end-product with better physical, mechanical, and, perhaps, aesthetic properties may be needed to overcome the perception of it being inferior because of the waste origin. Hence, investigations are being carried out aiming at producing glass-ceramic materials with superior properties to glassy slag from incinerator wastes. The feasibility of developing novel glass-ceramics from incinerator fly ash has been an active area of research over the last few years [98-108], with first developments reported in Germany in 1994 [109]. It is important to note that concurrent with the studies into producing glass-ceramics to recycle incinerator wastes, other ceramic-based end applications have been under investigation with reasonable success, for example,

fabrication of construction bricks [110, 111] and porcelainised stoneware tiles [112, 113].

3.3.2 Other Metallurgical Slag Wastes

Fabrication of glass-ceramics using slag-type wastes from non-ferrous metal production, although not as common as iron and steel slag, has been reported, e.g. wastes from copper production [114, 115] and phosphorus metal refinement [116]. Up to 40wt% of copper slag was incorporated into a base glass composition to produce tiles via the powder sintering method [114]. The corresponding glass-ceramic possessed the best properties after sintering at 1025°C for 1 hour and phases were hematite, maghemite, and amorphous silica. The tiles have a bending strength of 57 MPa, 2wt% water absorption, and a Vickers microhardness value (load of 200g) of 750 kg mm^{-2} (7.4 GPa). The material also showed excellent resistance to mineral acids. These properties make the material suitable for production of chemical resistant floor tiles.

Phosphorus slag is generated during the refining of elemental phosphorus. The refinement involves separation of elemental phosphorus from the phosphate-bearing rock in an electric arc furnace. Silica and carbon are added as flux materials to remove impurities during the slagging process. Murat et al. [116] demonstrated that devitrification of the phosphorous slag in the $CaO\text{-}SiO_2\text{-}CaF_2$ system at temperatures between 700°C and 830°C led to nucleation and crystallisation of cuspidine ($3CaO.2SiO_2.CaF_2$) as well as α- (metastable) and β-wollastonite. The study also highlighted that it was not necessary to heat-treat the glass via the conventional two-step heat-treatment, but the adoption of a single heating step up to 1000°C was sufficient to obtain glass-ceramics with optimised mechanical strength.

3.3.3 Electric Arc Furnace Dust (Steel Fly Ash)

Electric Arc Furnace (EAF) dust (or steel fly ash) is a waste by-product of the steel-making process. About 650-700 kilotons per year of EAF dust are produced in the USA and 1 million tons per year in Europe [117]. The dust contains a lot of heavy elements such as Pb, Cr, Zn, Cd, and Cu, whose solubility in leaching media exceeds the environmental regulatory limits in EU and USA. Hence, vitrification and

subsequent heat-treatment to devitrify the glass have been investigated as a process to immobilise the hazardous elements in the waste [117, 118].

EAF dusts from two sources (carbon steel making and stainless steel making process) were mixed with glass cullet and sand in varying proportions and examined after vitrification and heat-treatment [118]. The results showed that it is important to have a high Si/O ratio to ensure stable glass network and thus impart chemical resistance to the glass. It was found that a mixture containing stainless steel EAF dust and 50wt% glass cullet had poor chemical resistance but showed the highest tendency to crystallise. The main crystalline phases for this mixture were chromite-magnetite spinels and pyroxene. In commercial glass-ceramics, the stable crystal phases formed from crystallisation usually improves the chemical durability compared to their parent glasses [2]. The glass-ceramic made from 50% EAF dust, however, exhibited a poorer chemical durability than its parent glass. Similar results were obtained from the carbon steel EAF dust, where a glass-ceramic was produced from 45wt% dust, 35wt% glass cullet, and 20wt% sand. The poor leaching characteristics of the glass-ceramics were attributed to spinel and pyroxene phases being more prone to leaching than the parent glass coupled with no improvement in the performance of the residual glass as its SiO_2 content had not significantly increased with respect to that of the parent glass.

3.3.4 Sewage Sludge

Fly ash from the incineration of sewage sludge has been studied by Endo et al. [119], Suzuki et al. [120] and Park et al. [121] regarding the production of glass and glass-ceramics to reduce the environmental impact of such waste. Endo et al. [119] focused mainly on the feasibility of crystallising the glass obtained from melting of the fly ash. The work was successful considering the slag was crystallised into 80% anorthite crystals with mechanical properties meeting the requirement for construction and civil works materials. Suzuki et al. [120] and Park et al. [121] added limestone or CaO to lower the melting point of the parent glass and to obtain anorthite or diopside as the crystalline phases using a conventional two-stage heat-treatment of the molten glass. Suzuki et al. only worked with one temperature (1100°C) and obtained an anorthite-based glass-ceramic [120], whereas Park et al. [121] investigated a range of temperatures (1050°C to 1200°C) and found that diopside dominated at lower

temperature and anorthite at the higher temperature. Both groups pointed out that some of the relevant properties of these glass-ceramics were superior to construction materials, such as granite and marble.

3.3.5 Zinc-Hydrometallurgy Wastes

Reusing jarosite and goethite from hydrometallurgical processes to obtain glass and glass-ceramic materials has been reported in several papers [16, 122-127]. Jarosite (red mud) comes from electrolytic zinc hydrometallurgy. Goethite is the other type of zinc hydrometallurgy waste produced depending on the type of treatment used to remove the iron content.

Rincon and co-workers have studied the formation and crystallisation kinetics of glasses [122] and production of glass-ceramics [16, 123] from goethite. Because of the high iron oxide and zinc oxide content in goethite, it was common to add glass cullet, dolomite, and granite to adjust the glass composition. In the glass-ceramic production, the starting mixture of calcined goethite, granite, glass cullet and 2.0wt%TiO_2 was melted to produce a glass with a chemical composition of (wt%): 44.6SiO_2, 3.3Al_2O_3, 25.5Fe_2O_3, 1.6MgO, 4.5CaO, 5.9Na_2O, 3.1PbO, 6.5ZnO, 1.0K_2O, 2.0TiO_2, and 2wt% of other elements in trace amounts. A conventional two-stage heat treatment (670°C and 860°C) method was employed to give a high crystalline volume fraction of 0.80-0.85 [123]. The main crystalline phase was pyroxene, which occurred on the magnetite crystals nucleated at the first heat treatment step. Minor phases were residual magnetite crystals and zinc ferrite. It has been suggested that the zinc ferrite ($ZnFe_{2.5}O_4$, franklinite) was nucleated on the magnetite by the incorporation of zinc oxide in the glass matrix associated with the magnetite phase [16, 124]. There is also one interesting observation in that longer nucleation times produced an adverse effect on the crystalline volume fraction. This is thought to be caused by the coalescence of the magnetite with time thereby leaving fewer nucleation sites. However, as normal, a longer crystallisation time increased the volume fraction of the crystalline phase. The fracture toughness was found to be dependent on the volume fraction of crystalline phase, as the extended network of dendritic pyroxene matrix and magnetite microcrystals improve the crack propagation resistance.

The production of glass-ceramics from jarosite has been reported by Karamanov et al. [125] who sintered vitreous glass frits made from a molten mixture of jarosite, granite, quartz sand, limestone, and Na_2CO_3. From the thermal analysis of powder and bulk samples, it was found that formation of hematite occurs on the surface, whereas magnetite was formed via bulk crystallisation. A complex three stage heat treatment was developed consisting of a nucleation step at 700°C for the formation of hematite, a crystallisation step at 1029°C and finally another crystallisation stage at 750-800°C to give pyroxene in the bulk of the material. Although crystallisation was easily controlled here, the three-stage process is relatively more energy-intensive than the conventional two-stage process and thus costly. Fortunately, the study has also showed that crystallisation can be achieved by slow controlled cooling, i.e. petrurgic method. This would be the preferred fabrication route from an economic point of view.

It has been demonstrated that pyroxene glass-ceramics can be made from both types of zinc hydrometallurgy wastes via different processing routes, namely conventional melting and heat treatment, petrurgic method and sintering. These glass-ceramics also showed potential for applications in environments exposed to chemicals, as their chemical durability is comparable to commercial soda-lime glasses, basaltic glasses and glass-ceramics [126]. The next obvious step, an industrial- scale pilot plant, was made available in Italy [127]. The scale-up was tested using the custom-made pilot plant shown in Figure 3-5. Based on results from pilot runs, this plant is capable of continuously processing and producing 1 ton of glass frit per day, or discontinuously making 250-300kg of frit per batch. Glass-ceramics tiles made from a two-stage heat treatment (630-650°C and 750-800°C) of these glass frits had a crystal volume fraction of 0.40-0.55 of fine magnetite-pyroxene crystals. These tiles showed good fracture toughness (as high as 2.0 $MPa.m^{1/2}$) and relatively low thermal expansion coefficient for both the parent glass and the glass-ceramic (5.21×10^{-6} $°C^{-1}$ and 6.08×10^{-6} $°C^{-1}$, respectively). The main reason for not aiming for a higher degree of crystallisation was to avoid a too high concentration of heavy metal, such as Pb in the glass matrix, leading to a possible high leaching rate of this element.

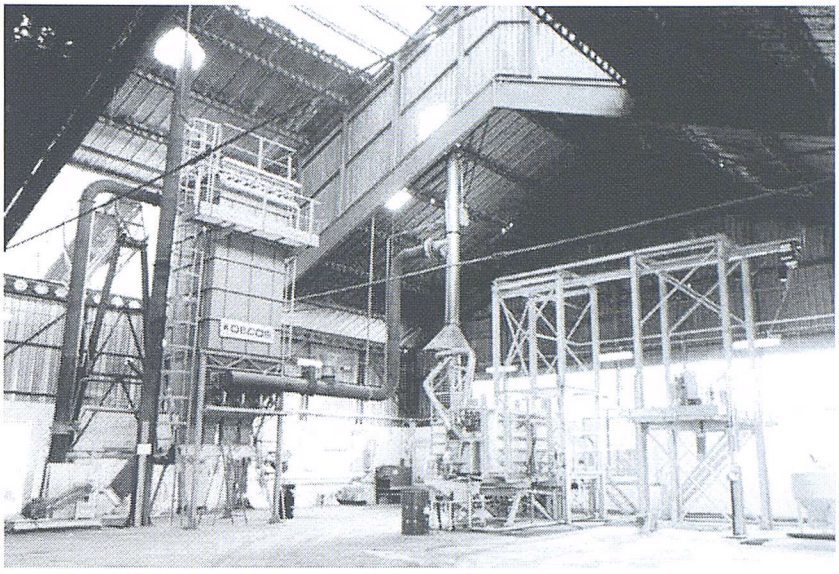


Figure 3-5: Photo of the pilot plant for production of glass-ceramic tiles from industrial wastes, situated in Iglesias, Italy [127]. (Photo courtesy Prof. M. Pelino, University of L'Aquila, Italy).

The plant showed flexibility as various combinations of waste streams were processed, including jarosite, goethite, granite mud, and lead foundry slag, along with additives such as sand, limestone, and Na_2CO_3. Problems of scaling up laboratory based experiments were identified and tackled. For example, dusts and gaseous products, such as SO_2, SO_3, zinc and lead vapours, generated during vitrification, were trapped and collected via filters and condensers, respectively. These streams can be recovered or recycled back into the process.

3.4 Concluding Remarks

Apart from the above mentioned types of silicate waste, there have been many efforts made in reusing wastes from other sources for production of glass-ceramic materials, e.g. IGCC (Induction Gasification Combined Cycle) slag [128], galvanising and anodising plant wastes [129], ore-refinement wastes [130], clay-refining wastes [131], and waste fluorescent glass [132]. For further reading on the array of work done on glass-ceramics derived from silicate wastes, please see the review paper by Rawlings et al. [52].

The key to producing glass-ceramics from silicate wastes is the correct chemical composition. Fortunately, the range of chemical composition fit for glass formation can be extremely vast, and these glass systems can be stabilised for controlled

crystallisation with the presence of network modifying oxides (nucleating agents) that are often already present in silicate wastes. Hence, by controlling heat-treatment parameters such as time, temperature, and heating rate, there are endless possibilities of producing glass-ceramics with desired material properties that can be utilised in place of current commercial products from pure constituents.

Chapter 4 Processing Techniques for Porous Materials

The comprehensive literature survey in the last chapter has demonstrated the huge effort made by researchers from all over the world to develop glass-ceramics from different types of silicate wastes. However, there is a relative lack of information on fabricating porous glass-ceramic materials from wastes. As a rule of thumb, porous materials have at least one of the following qualities: low density, low thermal conductivity, high permeability, high surface area, high thermal shock resistance (low elastic modulus) and high specific strength. Hence, they are suitable for thermal and sound insulators, lightweight structural components, filters, absorbents, gas sensors, and heat exchangers. There are, of course, porous materials used as surgical medical implants; porous ceramics, such as hydroxyapatite (HA), have been used in prostheses. Like HA, some special glass-ceramics containing SiO_2, CaO, P_2O_5 are suitable alternatives as implant materials [133]. However, public perception of industrial wastes makes it very difficult to market a waste-derived implant material even if it was proved to be non-toxic. A variety of ways to produce porous materials will be briefly discussed below. In the present research project, highly porous glass-ceramic foams were fabricated from a combination of wastes.

4.1 Use of Hollow Microspheres

Hollow glass microspheres were introduced to create uniformly spherical or near-spherical pores in sintered material [134, 135]. Boccaccini [135] successfully fabricated porous glass specimens containing borosilicate glass powder and microspheres by hot-pressing. The processing method was optimised to produce spherical pore shape in the DURAN® glass samples with the lowest possible pressure (1.5MPa) at 740°C for 60 minutes. The hot-pressing, however, is a cost-intensive processing method.

Work has also been done on direct sintering of glass microspheres for the production of lightweight ceramics [136-138]. Another drawback of this method is the limited range of microspheres available, meaning there is a limited number of porous materials that can be produced or matrix materials that are compatible to the incorporated hollow microspheres. Note, however, efforts are being made concurrently on the production of hollow microspheres using current or developing

technologies. For example, iron microspheres have been produced using plasma technology [139]. In addition to hollow microspheres of pure constituents, hollow coal fly ash particles (cenospheres) have been used to produce insulation panels by heat-treatment of coal cenospheres packed with an inorganic binder [138, 140].

4.2 Use of Foaming Agents

Foaming agents generate porosity within the sample by reaction or thermal decomposition during sintering. There are two types of foaming agents: solid and liquid. It is difficult to create fine pores with solid foaming agents as the degree of open porosity, pore shape and pore size of porous materials made by this method depend on the volume, particle shape and size of the pore forming agent [141]. Fine solid foaming agents for making fine pores tend to agglomerate strongly and are not dispersed homogeneously in the powder compact. Hence, this method is more suitable for cost-effective preparation of porous materials with relatively large pores and high open porosity. In contrast, liquid foaming agents such as liquid paraffin do not have such problems, and thus they have been used to create very fine, submicron pores in ultrafine powder compacts [142, 143]. Water may be considered as a liquid foaming agent as demonstrated by the preparation of porous glass-ceramics using hydrothermal hot pressed glass compacts [144]. This is a very interesting technique in which the foaming caused by the evaporation of molecular water during a conventional heat-treatment of the powder compact when the softening of the matrix material occurred. The water molecules were incorporated in a new phase that was formed during the hydrothermal hot pressing of the raw material at conditions developed by the researchers. Relatively fine pores (40-75 microns) were incorporated in the glass-ceramic matrix using 10wt% water.

In terms of solid foaming agents, carbonaceous solids and carbonates have been used as foaming agents in various studies [145-151]. Abe et al [146] added coal powder to fly ash to porous cordierite ceramics. The size and the shape of pores were approximately the same as those of the original coal powder particles, and thus pore size could be controlled in the range from 50 to 1000μm. In another study, Sarkar and Das [147] used marble dust as the pore forming agent by powder sintering route. The formation of pores relied on the decomposition of carbonates in marble dust.

One of the most common solid foaming agents for inorganic materials is calcium carbonate ($CaCO_3$). Cathode ray tubes were recycled and mixed with 5wt% of $CaCO_3$ to produce glass foams [148]. By direct insertion of the powder compacts into a furnace at 725°C and holding for 30 minutes, this allowed $CaCO_3$ to decompose at 700-950°C, generating CO_2 gas in the compact, and caused foaming in the glass. A similar approach was used by Gorokhovsky et al [149], who produced foamed glass-ceramics by sintering mixtures of wastes with addition of limestone. A material composition of 80wt% oil shale ash, 16wt% soda ash, and 4wt% sand provided the optimal properties in terms of softening temperature and crystallisation behaviour while using minimal amount of additives. 5wt% of limestone was also used as quantities above 5wt% were found to be detrimental to the mechanical properties of the foamed glass-ceramics. The foamed pyroxene glass-ceramic had a density of 0.35g/cm^3 and a porosity of 86±8% with open pores (50-120μm in diameter) and closed pores (5-20μm). It had a low thermal conductivity of 0.10-0.13 W/(m.K) and a flexural strength of 3MPa, which is equally thermally insulating but much stronger when compared with a commercial foamed glass compliant with Russian Standard GOST 24748-81 (thermal conductivity of 0.07-0.10W/(m.K) and flexural strength of 0.3-0.8MPa) [149]. It has also been demonstrated that silicon carbide (SiC) is a very effective foaming agent [150, 151]. This reducing agent can react with different oxides, especially transition metal oxides, in the matrix system to form CO_2/CO gas, thus generating porosity within the softened sample. The reaction takes place beyond 800°C [150, 151] and therefore the matrix material has to have a similar range of softening temperature to match this reaction. The match between the glass softening temperature and the decomposition/reaction temperature of the foaming agent is the key to obtaining the best foaming result by maintaining the gas bubbles, thus pores, during sintering. If the temperature is too low, it results in either lack of decomposition/reaction of foaming agent, or the glass matrix is too rigid for the gas bubble to form. On the other hand, with increasing temperatures, the glass is less viscous but can lead to collapse of wall struts. Hence, the pore morphology can be more difficult to control and more irregular at the extreme ends of heat-treatment temperature.

4.3 Inclusion of Secondary Organic Solids

The inclusion of organic phase is slightly different from the use of foaming agents because the organic phase is normally removed well before the matrix material reaches sintering temperature. Therefore, no volume expansion is observed. Polyvinyl butyral (PVB) and polyvinyl chloride (PVC) polymers have been used by Liu [152] and Vaz et al [153], respectively, for the study into the effect of the pore geometry and distribution on the mechanical properties of HA bioceramics. Another example is where Hayashi et al [154] successfully produced porous PZT ceramics with controlled porosity by the decomposition of spherical polymethylmethacrylate (PMMA) particles mixed with the starting PZT powder. Natural organic materials, such as different types of starch (potato, wheat, corn and rice starch), have also been effectively used as pore-forming agents in porous ceramics [155-158] by mixing either dry or in a suspension (starch consolidation casting, SCC). The amount of starch added (1-20wt%) helped to control the level of porosity which varied from 10-50% [156, 157]. In principle, the organic phase creates voids after pyrolysis and thus hinders the full sintering of the matrix material.

4.4 Burn-out of Polymeric Preforms

Porous polymeric performs have been utilised as pore creator in a number of studies on the fabrication of highly porous glass-ceramic materials using pure [159-161] or waste raw materials [162, 163]. The difference from the method in section 4.3 is that a preform is a continuous organic phase. Therefore, the porosity is definitely open (interconnected). Also known as the polymeric sponge method, commercial polyurethane sponges are often used as the decomposing template. Each template was immersed in a slurry, i.e. a suspension of the raw material with composition of the desired final product, and then subjected to drying before the burnt-out stage. Once the coated sponge was dried at <150°C, the polyurethane was burnt out before sintering/crystallisation took place at a higher temperature depending on the optimum heat-treatment temperature of the raw material. In general, a large pore size in the range of 200-800μm was obtained. One of the disadvantages of using polymeric pore forming agents is the evolution of large volume of gas during the decomposition, therefore, a proper ventilation exhaust is required at decomposition.

4.5 Introduction of Gas during Processing

The principle behind this method is to saturate a powder compact of desired composition with gas or liquid under pressure. Micro-sized cells can then be nucleated in the compact when the pressure is dropped, and the pores are retained in the compact for heat-treatment. A preceramic polymer, polysiloxane, has been used as the starting material [164]. The polymer was milled into powder and then uniaxially pressed into disks after addition of a binder. Using a pressure chamber, the green compacts were saturated for 24hr with carbon dioxide under 5.5MPa of pressure (gaseous CO_2) or 41.4MPa (liquid CO_2) at ambient temperature. By dropping the pressure rapidly, a thermodynamic instability is induced, driving nucleation and growth of microcells in the compacts, resulting in a porous material. The resulting cell sizes, as shown in Figure 4-1, for the 5.5MPa-saturated and 41.4MPa-saturated were ~50μm and ~2μm, respectively [164].

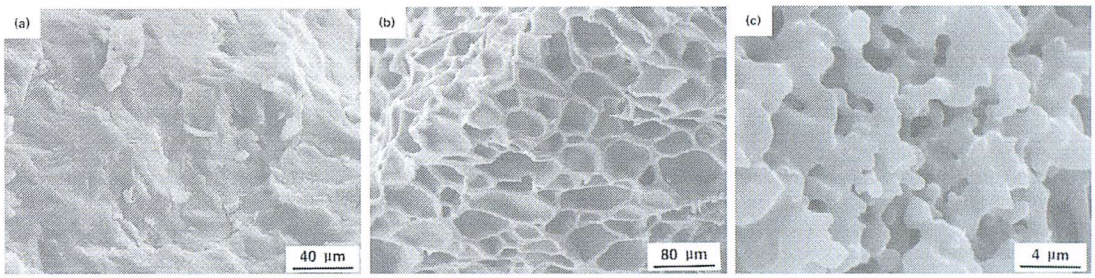


Figure 4-1: From left to right, as-pressed compact, 5.5MPa, and 41.4MPa-saturated samples [164]

4.6 Loose-Packed Powder Sintering

Porous materials can be produced by sintering a loosely packed powder [165, 166]. The porosity or voids are generated from the limited sintering achieved by the sparsely packed powder. Figure 4-2 illustrates sintering or the forming of necks between particles while the voids between particles are retained as pores. It is possibly the most economical method for producing a porous material via sintering. However, there is a limited control over the level of porosity and the morphology of pores after sintering. There may also be a size effect on the homogeneity of pores because the weight of powder may cause the consolidation to be denser near the bottom (i.e. less voids).

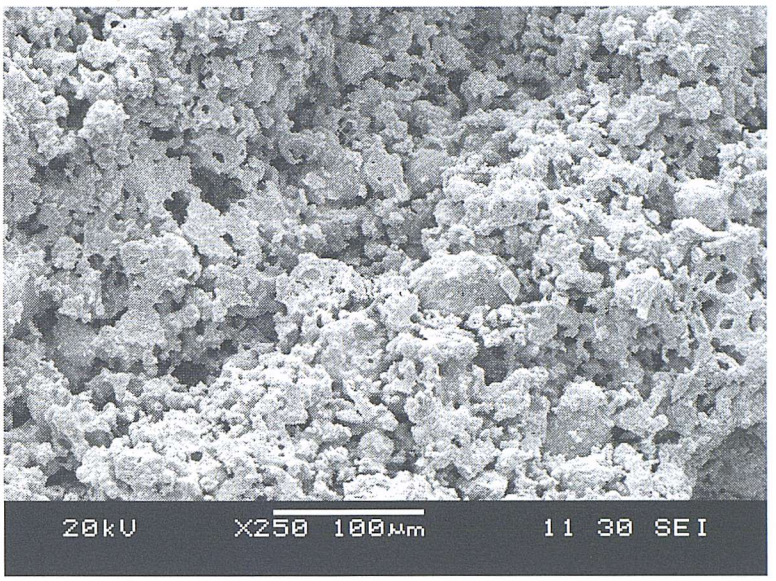


Figure 4-2: SEM illustrating surface of a sintered sample from loose-packed coal ash

4.7 Sol-Gel Technique

As explained in Section 2.6, sol-gel technique is not applicable to the production of glasses and glass-ceramics from wastes. However, this technique has been used for producing porous inorganic materials [167, 168] and it is briefly discussed here for the completion of this literature review. An example of ceramic foam by a thermostimulated sol-gel technique is given in reference [168]. In this technique, the aqueous solutions of the desired composition (in this work, zirconium containing solution) were processed into a suspension, i.e. sol. Gas bubbles were introduced into the sol by evaporation of CCl_3F or Freon11. Using surfactants, the dispersion of the bubbles were controlled and thus retained in the sol, which solidified in a gel form after thermal treatment. Similar to using liquid foaming agents, the sol-gel technique allows fine pores (macro: ~65-100µm, micro: 0.3-0.9µm) to be produced. The disadvantage of this method is clearly the ageing of the wet gel foam takes more than 100 hours and drying takes a further 50 hours to avoid cracking of the gel.

4.8 Chemical Leaching

Chemical leaching is commonly used in glass and glass-ceramic systems [169, 170], where the separation of phases after heat-treatment allows users to remove the

undesired phase(s) using a chemical solution in which the phase dissolves. The possible disadvantage of this process is the disposal or treatment of the by-product of this process, i.e. the leachate. The pore morphology of the porous material is dependent on a number of factors. First of all, the result of phase separation will determine the proportion of porosity and the pore morphology. This is also dependent on the strength of the leaching solution and the leaching time. In a way, this provides an adequate control over the level of porosity.

4.9 Plasma-Spraying

Plasma spraying is well-known for making ceramic coatings [171], and voids are common defects in a plasma-sprayed coating. This technique was applied to introducing porosity into a metallic material. An aluminium foam was produced by plasma spraying a combination of Al and CaO powder [172]. The ceramic phase is then dissolved in water or glycerol. In a way, this is a hybrid technique in that plasma-spraying was used as the consolidation technique and the principle of chemical leaching was used to form the porous skeleton. However, it is an energy-intensive process.

4.10 Microwave Processing

The main use of microwave processing has been in serving as an alternative to conventional furnace sintering. It is a relatively recent technique used in the making of porous materials, and has been used to form closed pores in a glass matrix composite material [173, 174]. The concept behind this method is to localise the heating, creating a differential temperature profile from the centre of the sample to the surface of it. The high concentrated energy is capable of melting the inside of the sample, while the sample retains its shape due to the heat loss and thus lower temperature near the surface. The heat induced from the microwave leads to gas formation in the central molten glass region, thus creating well-defined spherical pores distributed across the entire sample upon cooling. This gives the possibility of fabricating a density-graded material where the denser and harder shell helps the material to be easily handled while retaining its light weight. However, given that

only small samples were used in the studies (10mm diameter and 2mm thickness), there may be limitations to the size of the specimens suitable for this technique.

4.11 Summary

Table 4-1 shows a list of the processes described in this chapter, including advantages and disadvantages of each method.

Table 4-1: Advantages and disadvantages of different processing methods for porous materials

Method	Ref	Advantages	Disadvantages
Use of hollow glass microspheres	[134-138, 140]	Perfectly spherical pores; control over the level of porosity and pore size	Limited compositions of hollow microspheres
Use of foaming agent	[141-151]	Relatively low cost; large volume expansion possible; adequate control over level of porosity and pore morphology	Problems with scaling up;
Inclusion of secondary organise phase	[152-157]	Limited control over the pore size and shape;	Gas evolution; carbon residues
Burn-out of polymeric performs	[159-163]	Easy to obtain open porous structure; near-net shape;	Gas evolution; carbon residues; hollow struts and thus mechanically weak
Introduction of gas during processing	[164]	Fine pore size; control over pore size; good dispersion of pores	Time-consuming
Loose-packed powder sintering		Low cost; applicable for many materials; limited control over level of porosity	No control over pore morphology; very difficult to obtain closed porosity
Sol-Gel Technique	[167, 168]	Very fine pores and well dispersed pores;	Time-consuming; chemistry may not work for some systems
Chemical Leaching	[169, 170]	Open porous structure;	Possible problem with disposal of liquid effluents;
Plasma-Spraying	[171, 172]	Can be used in conjunction with chemical leaching	Energy-intensive; difficult to control pore morphology; limited porosity if only rely on randomly occurring voids
Microwave processing	[173, 174]	Closed porosity; density-graded functions	Very limited level of porosity; possible limitation to sample size

Chapter 5 Experimental

5.1 Materials

Five waste materials from three different sources were investigated. First supplier was a thermal power plant in Huntly, New Zealand. The two waste by-products from the power plant were coal fly ash and coal pond ash. Combustion of coal resulted in the production of ash, 75-80vol% of which was fly ash collected in electrostatic precipitators and 20-25vol% was bottom ash removed from the bottom of the furnace. A proportion of fly ash from this plant (an estimated 52% in the calendar year 2002) was sold to a cement company for recycle use. The remaining fly ash and the furnace bottom ash were hydraulically transported to ash storage ponds to the north of the power station. The fly ash used in this work was collected from the outlet of an electrostatic precipitator, and the pond ash was collected from one of the storage ponds.

The second supplier works with a local steel mill in northern New Zealand, dealing with slags from the mill, where iron-making melter slag and steel-making KOBM (Kontinous Oxygen Blast Maxite) slag are the two main waste streams. The melter slag is unusual in terms of its chemical composition; it contains a very high (~30wt%) concentration of TiO_2. This is due to the fact that for more than 30 years, black ironsand (titanomagnetite) of the West Coast of New Zealand's North Island has been used in steel making. KOBM slag has a typical composition of steel-making slag, that is, with high content of calcium oxide (lime).

Finally, the last type of waste material was mixed soda-lime glass cullet supplied by a glass recycling plant in Christchurch, New Zealand. This plant specifically collects waste soda-lime glass and refines it into different grades of glass cullet products. The glass cullet was used in this work as additive to change the material composition to favour glass formation or sintering as explained later in Chapter 6.

5.1.1 Milling

As-received waste materials were dry milled for 5 minutes inside a "Gyro" (ring-and-puck) mill to prepare powders. The apparatus consisted of hardened steel milling components (ring, puck, and bowl) as shown in Figure 5-1. After 5 minutes milling,

an average particle size of <50 μm can be achieved. Details of the particle size analysis are given in Section 5.2.2.

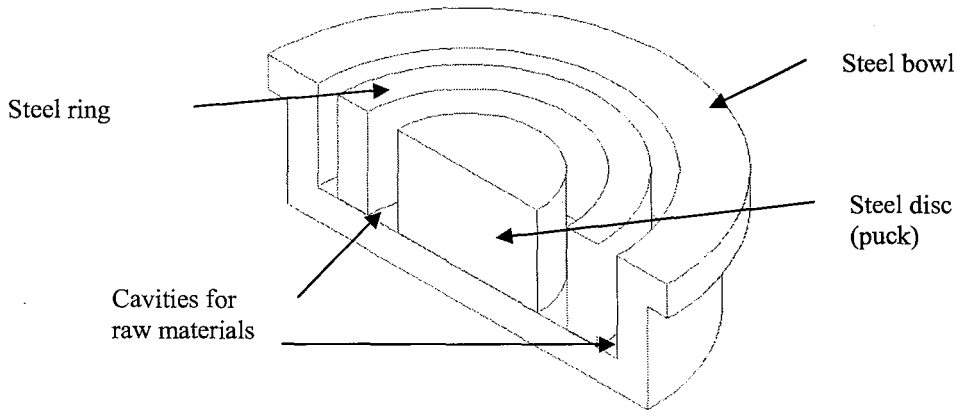


Figure 5-1: Graphical representation of the milling components (sectioned view)

5.1.2 Powder Compaction

A uniaxial press was used at room temperature to consolidate milled waste material in fine powder form. For preliminary studies, a 10mm diameter hardened steel die was used to consolidate the powder at 100 ± 5 MPa. Each green pellet weighs between 0.2 to 0.6g depending on the desired height. For mechanical testing, which require larger and more specific specimen dimensions, green compacts of various shapes and sizes were uniaxially pressed using different compaction dies under a pressure of 45 ± 5 MPa according to Table 5-1. The thickness of compacts was determined by the amount of powder used, thus the thickness values in the table were typically used.

Table 5-1: Uniaxial pressure (MPa) used for various compaction moulds

Shape	**Cross-sectional dimensions of mould cavity**	**Typical thickness of compacts made**	**Pressure used (MPa)**
Cylindrical	10mm diameter	4mm	45, 100
Rectangular	45×4mm^2	4mm	45
Rectangular	65×7mm^2	7mm	45
Square	50×50mm^2	5mm	45

5.1.3 Melting / Glass Frit Making

Selected composition / combination of waste materials were dry mixed and melted in crucibles made of alumina or platinum at 1450°C in an electric furnace with a holding time of 2 hours. For making frits, the molten glass was poured in a bucket of water with a steel sieve in the bottom to catch the frits. For bulk glass, the melt was poured on a steel plate and cooled with another plate on the top to assist cooling, or the molten glass was poured into a pre-heated steel or graphite mould for shaped glass products. The as-cast glass was then annealed at 100°C below the glass transition temperature (T_g) for 5 hours or longer, depending on the thickness of the glass product, and then furnace cooled to room temperature.

5.1.4 Heat-treatments

Electric chamber furnaces were used for heat-treatments (including sintering of green compacts and crystallisation of as-cast glass). Each sintering schedule was a single step heat-treatment, performed under normal atmosphere. The heating / cooling rates used were 2 and 10°C/min. The standard condition used was a heating rate of 10°C/min and 1 hour holding period at the chosen temperature which varied from 850°C to 1200°C. The sintered specimen was then cooled inside the furnace at 10°C/min. The justification for choosing these heat-treatment conditions will be discussed in Chapter 6.

5.1.5 Sample Preparation

5.1.5.1 Cutting / Grinding / Polishing

All glass and glass-ceramic samples were cut with diamond bonded cutting blades using either a high-speed (Struers Accutom-5 precision cut-off machine) or a low-speed (Buehler ISOMET Low Speed Saw) cutting machine. Using a Struers Labopol-21 Rotopol, samples for microscopy were ground with silicon carbide paper (from grit size P#500, 800, 1200, 2400 to 4000) and then polished with Struers diamond paste sprays (3μm and 1μm) on soft cloths.

5.1.5.2 Cold Mounting

Small or irregular shaped specimens were cold embedded in epoxy resins for the ease of handling. Struers Epofix resin and hardener were used in a weight ratio of 25:3, respectively. The resin had negligible curing heat (43°C) and shrinkage. Therefore, it is suitable for brittle materials such as glasses, ceramics, and glass-ceramics. The moulding was normally left for at least 8 hours to cure before grinding and polishing.

5.1.5.3 Specimen Etching

For microstructural analysis of crystallised glasses, a 2vol% HF solution was used as the etching solution. The acid solution was prepared by diluting 48vol% HF with tap water. The standard etching time of 20 seconds was used for the samples. However, the etching condition varied with the solubility of the residual glass in etching solution. Be aware that distilled water is preferred as the carbonates in tap water can react with the acid and thus reduce the strength of the etching solution.

5.2 Characterisation of Materials

5.2.1 Chemical Analysis

Chemical composition of each raw material was determined using X-Ray Fluorescence (XRF) by the suppliers or external laboratories. Samples of fly ash and pond ash were prepared as powder briquette and borate fusion, respectively, and then analysed using XRF spectroscopy (SpectraChem Analytical limited, Lower Hutt, New Zealand). The compositional information of iron-making melter slag and steel-making KOBM slag was given by the supplier: SteelServ Ltd., New Zealand. Mixed glass cullet from a recycling plant in Christchurch, New Zealand, was analysed by CERAM, Stoke-on-Trent, UK. All of the results were based on oven dried material (110°C).

5.2.2 Laser Particle Size Analyser

A Malvern Mastersizer, which was adjustable with three different types of lens, provided a combined detection range for average particle size from 0.1 to 600μm

(Table 5-2). An ultrasonic bath was used to assist the dispersion of particles when agglomeration of fine particles occurred.

Table 5-2: Lens Specification of Malvern Mastersizer

Lens Type / Focal Length (mm)	Detectable Particle Size Range (μm)
300	1.2-600
100	0.5-180
45	0.1-80

The results were given in single values, which represent the maximum particle size of 90% of the sample representing the whole population. For example, D[v,0.9] = 30μm means that 90vol% of the sample has a particle size less than or equal to 30μm.

5.2.3 Microscopy

5.2.3.1 Optical (Light) Microscopy

Optical microscopes have been used in conjunction with an image analysis package, Motic Image Plus 2.0, for preliminary microstructural examination and for determining the proportion of phases by image processing.

5.2.3.2 Scanning Electron Microscopy (SEM)

Gold (K550) and carbon (K450) sputter coating units from EMITECH were used for coating non-conductive specimens. A JEOL JSM 5610 LV SEM was used for high quality secondary images with a standard voltage at 15-20kV. The microscope was equipped with backscattered electron detector. A JEOL JSM 840 SEM was used to acquire, in particular, the chemical composition of the specimen using energy dispersive analysis of X-rays (EDAX).

5.2.4 X-Ray Diffraction Analysis (XRD)

5.2.4.1 Standard

Philips X-ray diffractometers (PW2273/20) with X-ray generators (PW1719 and PW1729) were used to identify phases in both bulk and powder samples. CuKα radiation was used in the 2θ range from 15° to 75° with a step size of 0.04° and 2 second scan time per step.

In order to semi-quantify the analysis for the ease of comparison between samples, an equal amount of each powdered sample of the same particle size was used. The scan parameters were kept at a constant to standardise the procedure.

5.2.4.2 High-Temperature

High-temperature XRD (HT-XRD; Philips X'Pert, equipped with a conduction/radiation furnace capable of temperatures up to 1000°C) was used to investigate the crystallisation behaviour of the as-cast glass powder and the evolution of the crystalline phases with increasing temperature. Measurement was carried out in the 2θ range from 15° to 45° on a thin layer of powdered sample on a heated platinum substrate. A step size of 0.04° with 5-second hold per step was used. An initial measurement was taken at room temperature, after which the first high-temperature scan was taken at 600°C (set temperature), and then a scan was taken with every 25°C increase up to 900°C (set temperature).

5.2.5 Thermal Analysis

A STA-780 series Staton Redcroft Thermal Analyser with thermogravimetric analysis (TGA) and differential thermal analysis (DTA) capabilities (i.e. measuring sample mass as a function of time/temperature and the temperature difference between the sample and the reference alumina powder during a controlled temperature programme, respectively) was used for the investigation of phase transformation, melting point, and glass transitions of different systems under normal atmosphere. The standard heating rate applied was 10°C/min.

5.2.6 Dilatometry

5.2.6.1 Sintering Studies

A Netzsch dilatometer 402 E with an alumina holder was used to measure the variation of length of the specimen with respect to temperature. Sintering studies were conducted on green compacts of the as-received coal pond ash composition to investigate the sintering behaviour of the material. The specimens were 10mm length and 2-6mm diameter and the standard heating rate employed was 10°C min^{-1}.

5.2.6.2 Coefficient of Linear Thermal Expansion (CTE)

The dilatometer was also used for measuring the CTE of materials. The specimens were solid bars or rods of dimension 25mm in length and 2-6mm in diameter or width. The standard heating rate was 10°C min^{-1}.

5.2.7 X-ray Microtomography (XMT)

X-ray microtomography (XMT) or micro-computed tomography (μ-CT) is based on the principle of the 2D method: computerised axial tomography (CAT-scan or CT-scan), which is well-established in the medical field. The technique is becoming more readily available for acquisition of 3D structural information of an object for different purposes: from studying the sintering process (i.e. the mechanisms) of glass powder compacts [175], pore morphology and interconnectivity of bioactive glass foams [176] as well as natural materials such as porous sandstone [177], to quantification of phases and simulation of mechanical strength of a metal matrix composite [178]. Bernard et al [175] were able to use XMT to identify different sintering stages at a microscopic level, looking at individual grains where the solids were the dominant phase and the voids were defects. On the other hand, Atwood et al [176] examined in a highly porous glass foam the size and level of open porosity, which is essential for tissue growth in a tissue engineering scaffold. This work demonstrated an effective use of the technique to not only accurately quantify pore morphology by image analysis but to correlate the results with processing parameters to find the optimum sintering temperature. In the study by Nakashima et al [177], the results obtained from XMT showed an extremely good agreement with measurements from conventional laboratory techniques. With a high accuracy in the XMT data, the possibility of generating a microstructurally accurate and robust mesh for finite element modelling was shown by Watson et al [178].

The main advantage of this technique over conventional methods such as microscopy is that a complete 3-dimensional volume can be scanned and the data can be processed efficiently to acquire accurate information regarding the phase difference (porosity, defects, and secondary reinforcements). This can be achieved in relatively lower time as well as being non-destructive to the specimen. In addition, this digital information can be further used in finite element analysis for prediction of properties.

The principle behind the image acquisition using XMT can be explained as follows: an X-ray image is generated by the different absorption (X-ray mass attenuation coefficient) properties of different object features. The intensity (I) of the X-ray beam after penetrating a material of known density (ρ) and thickness (t) is given by the exponential attenuation law [179]:

$$I / I_o = \exp[-(\mu/\rho)x]$$

Equation 5-1

where I_o is the incident intensity of the beam, $x = \rho t$, and μ/ρ is the mass attenuation coefficient. The effect of μ and t on I are illustrated schematically in Figure 5-2; x-ray attenuation is higher in the denser object A than in the less dense B, while the thicker B absorbs more radiation than thinner object C of the same density. In summary, only features or defects which have good contrast between their X-ray mass attenuation coefficients can be distinguished in XMT.

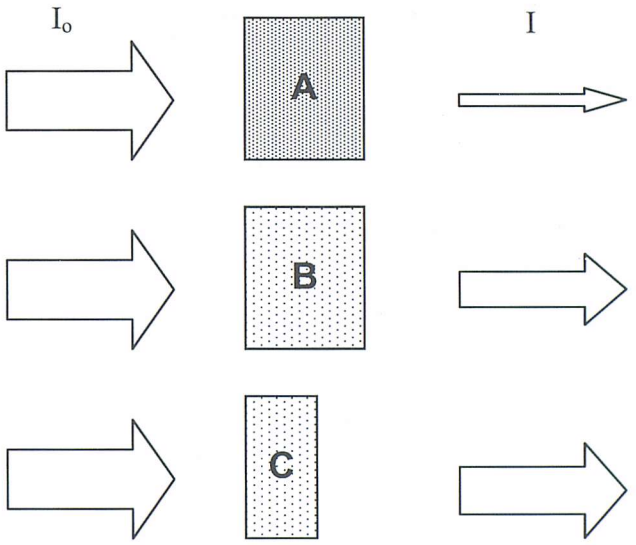


Figure 5-2: Irradiated by the same X-ray intensity, the higher density object A absorbs more radiation than the object B which is of lower attenuation coefficient. Object B absorbs more radiation than the thinner object C.

With regards to the resolution and thus the quality of each X-ray image, the size of the focal spot is extremely important. The focal spot is the actual area on the target where

the electrons transfer their energy to the target atoms and where the X-rays are generated. As the focal spot decreases in size, resolution and the ability to detect detail are improved, enabling geometric or projection magnification without causing geometric unsharpness (see the grey areas in Figure 5-3).

Ideally, the focal spot would have a diameter close to zero (i.e. a point rather than an area), so that there is little geometric unsharpness and thus a sharper image is obtained. The commercial unit used (Phoenix X-ray Systems and Services GmbH) in this study can run with a 1μm spot size, allowing practical resolutions of about 2μm voxels. In 2D imaging, the basic unit of the composition of an image on a television screen, computer monitor or similar display is a 'pixel'. Similarly, for 3D digital imaging the basic unit is a 'voxel', derived from a combination of the words 'volume' and 'pixel'.

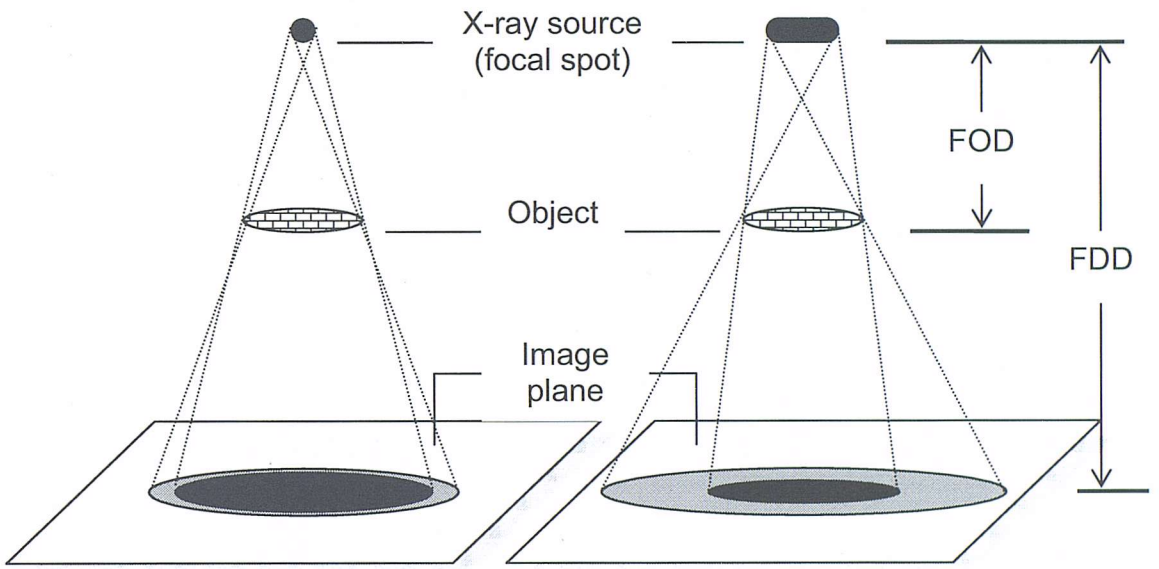


Figure 5-3: Comparison between X-ray sources with different focal spot sizes, illustrating the relationship between spot size and geometric unsharpness (grey areas).

Geometric magnification (M_{geo}) is a feature which helps to improve the observation of smaller features. It may be defined as:

$$M_{geo} = \frac{FDD}{FOD}$$

Equation 5-2

Where FOD is the Focus to Object Distance and FDD is the Focus to Detector Distance as shown in Figure 5-3. For example, if a system has the lowest possible FOD of 0.4mm and FDD of 1m as the upper limit, then a maximum geometrical magnification of 2500 times can be achieved. M_{geo} can be increased by moving the sample closer to the focal spot (i.e. decrease FOD) or moving the detector farther away from the focal spot (i.e. increase FDD). Note that the system used in this study has a fixed FDD. Nevertheless, in principle, the latter reduces the amount of X-ray intensity that reaches the detector and, thus, deteriorates the quality of the X-ray image (the image gets noisier and darker because of the weaker X-rays picked up by the detector). The X-ray intensity arriving at the image plane decreases by square of FDD as the FDD increases (inverse square law), and hence doubling the FDD reduces the X-ray intensity reaching the image plane by one fourth. Reducing the FOD by half achieves the same increase in geometric magnification as doubling the FDD, but without any loss in X-ray intensity.

There are ways to improve the resolution of the images. One of which requires the use of a stronger source of radiation, such as synchrotron radiation [175, 177]. The synchrotron radiation is highly collimated and hundreds of thousands of times more intense than conventional X-ray tubes, and the residual X-ray radiation detected is much stronger and resolutions of 0.1 microns can be achieved. Note that maximum theoretical resolution can often hindered by size of sample, detector, and other scanning parameters that limits the resolution achieved. The synchrotron radiation will not be discussed any further as it was not used in the study.

This completes a brief introduction to the concept behind XMT. Part of the work in this thesis comprised the use of XMT for the characterisation of highly porous waste-derived glass-ceramic materials. It demonstrates the value of using XMT to quantify the level of porosity and to measure the pore morphology as well as to enable correlations between structural information, material properties measured experimentally and simulated by finite element analysis. The experimental parameters used are described below and results are presented and discussed later Chapter 9.

Scans using XMT (Phoenix-X-ray Systems and Services GmbH, Munich, Germany) were carried out on foamed, porous glass-ceramics produced by the powder sintering route with foaming agents. The XMT unit used in this study was a "v|tome|x s" type

by Phoenix-X-ray. It is a high resolution (1-2μm) XMT system designed for 3D inspection of small mechanical and electronic devices and packages in industries.
A small (~1.5mm^3, approximately 5mm wide each side) sample of foam from each processing condition was mounted on a rotating steel sample holder and imaged under the following X-ray power: accelerating voltage = 80kV and tube current = 125μA.
Image analysis packages, "ImageTool 3.0" and "VGStudio MAX 1.2", were used for quantifying the amount of pores in 2D and 3D, respectively. "Amira 3.1" is a 3D visualization and modelling software that was used for generation of mesh, and "ABAQUS CAE 6.3" is a finite element analysis software package that was used to simulate thermal properties of the meshed specimen.

5.2.8 Density Measurement

The density of powder material was determined using the density bottle method [180], where the mass of water displaced by a known mass of the sample material was measured.

$$\frac{W_3 - W_1}{W_2 + W_3 - W_1 - W_4} \times \text{Density of water}$$

Equation 5-3

Where W_1 = Mass of empty dry bottle

W_2 = Mass of bottle filled with distilled water

W_3 = Mass of dry bottle with sample powder

W_4 = Mass of bottle with powder and filled with distilled water

The density of bulk specimens was measured using Archimedes principle.

$$\frac{\text{Dry Weight}}{\text{Wet Weight - Suspended Weight}} \times \text{Density of Water}$$

Equation 5-4

The physical measurement was accompanied by porosity estimation using image analysis and characterisation software (Motic Images Plus, version 2.0).

5.2.9 Water Uptake

Water uptake or water absorption of sintered products was carried out according to the British Standards, BS3921:1985 [181]. The procedure consisted of drying the product to constant mass, weighing dry, boiling in water for 5 hours and allowing to cool in the water for a further 19 hours before re-weighing wet. The water uptake results were expressed as a percentage. This is a useful test when products are used externally as facing materials. According to the standard [181], a material with compressive strength greater than 70 MPa and water absorption less than 4.5% can be classed as an engineering A class material, and an engineering B class requires a compressive strength greater than 50 MPa and water absorption less than 7.0%. These criteria can be used later as application guidelines for the products developed from this project.

5.3 Determination of Mechanical and Thermal Properties

5.3.1 Modulus of Elasticity

The modulus of elasticity was determined using the impulse excitation technique (Mk5 Grindosonic, J.W. Lemmens Ltd, Belgium). The technique involved the use of a small impulse tool to tap an elastic solid (the subject material, assumed to be isotropic), causing the solid to vibrate at its natural frequencies. Although an elastic solid can vibrate in several modes simultaneously (e.g. flexural, torsional, and longitudinal), the sample was supported and struck in ways that only one mode was prevalent. Hence, this technique was applicable to specimens of different shapes and sizes. The elastic constants were then calculated from the dimensions and mass of the sample and from the known mode of vibration and the frequency of the vibration using established equations [182].

5.3.2 Microhardness and Indentation Fracture Toughness

An Indentec model 6030LKV Vickers Hardness Testing Machine (1, 3, and 5kg loads, 10s) was employed for preliminary hardness testing. A microhardness tester (Zwick/Roell Indentec ZHV, at 500g load, 10s) integrated with computer software was used for determination of microhardness as well as for indentation fracture toughness. Based on the work by Ponton and Rawlings [183] on a range of equations for calculating the fracture toughness directly from indentation crack length, an equation derived by Anstis et al [184] was chosen to calculate indentation fracture toughness (K_C, MPa $m^{-1/2}$):

$$K_C = 0.0154 \times \left(\frac{E}{H}\right)^{1/2} \left(\frac{P}{c^{3/2}}\right)$$

Equation 5-5

where E is Young's modulus (GPa), H is Vickers hardness value (GPa), P is the indenter load (N) and c is the mean surface radial crack length measured optically (μm). Each reported value is the average of ten indentations made on each specimen.

5.3.3 K_{IC}, Chevron Notched Beams and Elevated Temperature Tests

For fracture toughness (K_{IC}) determination, the Chevron notch technique was used in conjunction with 3-point bending test. Measurements at room and elevated temperature were carried out. The reliability of this technique on glass specimens has been demonstrated by Boccaccini et al [185]. The cross-sectional dimensions of the bars were 3mm by 4mm. Chevron notches were cut on each sample by a thin diamond wheel saw (thickness = 0.2mm). For high temperature testing, a Zwick Z50 testing machine equipped with high temperature furnace (up to 1200°C) was used. The heating rate was 8-10°C min^{-1}, the holding time at the test temperature before starting the test was 15 minutes. The temperature was measured by two independent systems: the furnace control system, which measures and controls the temperature in the three zones, and by another thermocouple located directly on the specimen surface.

Special high-temperature fixtures allowing deflection measurements on the test piece were used. The crosshead speed was 0.01 mm min^{-1} and the load cell capacity was 1kN. After testing, the sample fragments were removed by means of tweezers and put on a ceramic pad for normal cooling. Graphs of load versus deflection were recorded and the fracture toughness was calculated from the maximum load (F_{max}) and the corresponding minimum value of geometrical compliance function (Y^*_{min}) using the following equation [185]:

$$K_{IC} = \frac{F_{\max}}{BW^{1/2}} Y^*_{\min}$$

Equation 5-6

where B and W are the width and height of the specimens, respectively. The determination of the function Y^*_{min} for chevron notched bars was based on the Bluhm's slice model as reported in an earlier publication [186]. The initial notch depths necessary for fracture toughness determination were measured from optical macrographs by "Vtip" image analysis software. The software (supplied by TESCAN company) enabled optimisation of optical macrographs capturing and direct quantitative measurements on digital pictures of fracture surfaces.

5.3.4 Bending Strength

The bending strength was measured using the 3-point bend test on a Hounsfield H5KS tensile/compression testing machine, loading at 0.5mm min^{-1}. A span of 20mm was used. Based on the maximum load, the span of the supports where the specimen was placed upon, and the cross-sectional dimensions of the specimen, the bending strength can be evaluated using the following equation:

$$\sigma = \frac{3F_{\max}L}{2BW^2}$$

Equation 5-7

Where F_{max} is the maximum load (N), L is the span (20mm in this case), B is the width (mm) and W is the height of the sample (mm). The average size of the

specimen was about 35mm long and a cross-section of 3mm (B) by 4mm (W) after the surfaces of the specimen were polished with 1μm diamond paste.

5.3.5 Compressive Strength Test

The compression strength (plate to plate) was determined using a Zwick Benchtop tensile/compression tester with a 10 kN load cell at a crosshead speed of 0.5 mm per minute. Five rectangular samples were used for each determination, and the dimensions of each sample were approximately $6\times3\times3$ mm^3.

5.3.6 Thermal Conductivity

The thermal conductivity of a solid depends upon the composition, the combination of phases present and the porosity. The thermal conductivity of a gas is usually much lower than that of a solid. Therefore, the heat transfer across a porous solid is generally lower than through a dense material. The apparatus used here was a modified Lee's Disc method [187] for measuring the thermal conductivity of a solid material.

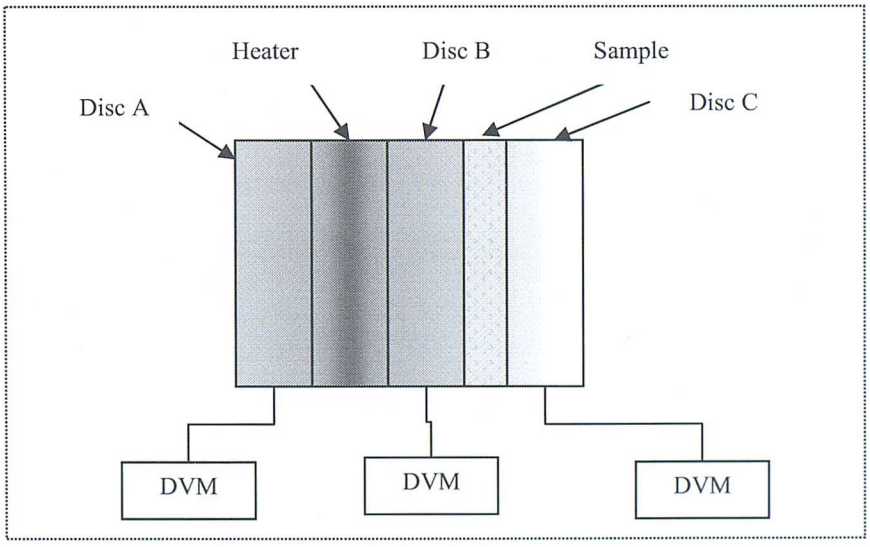


Figure 5-4: Schematic diagram of the Lee's Disc setup for determination of thermal conductivity (3 digital voltmeters for temperature measurement, one heater, and 3 steel discs)

Figure 5-4 is a schematic diagram of the apparatus, showing steel discs A, B, C, which were fitted with thermocouples and connected to digital voltmeter (DVM) or

multimeter for temperature readings. A heater was embedded in another steel disc between discs A and B, and the sample under investigation was placed between discs B and C as shown in Figure 5-4. A current was passed through the heater until the temperatures of the steel discs reach equilibrium. T_A, T_B, and T_C are the temperatures of the discs above the ambient temperature, that is, room temperature should be subtracted from the measured temperatures of the discs. The heat generated from the heater transfers through the discs, and some heat was emitted from the exposed surfaces of each disc. The temperature of the sample is taken to be the mean of B and C. Similarly, the temperature of the heater is taken as the average of Disc A and B. Hence, the total heat emitted per second (J s^{-1} or W) is given by [187]:

$$A = h(a_A T_A + a_H T_H + a_B T_B + a_S T_S + a_C T_C)$$

Equation 5-8

In this equation, 'h' is the heat transfer coefficient (W m^{-2} K^{-1}) of the whole assembly and 'a' is the exposed surface area (m^2) of each disc. The exposed areas for Discs A and C include the flat end surfaces. The quantity of heat (in joules) is completely supplied by the heating element. Therefore, the total heat (J) emitted per second (heat transfer rate in W) can be represented as:

$$A = Vi$$

Equation 5-9

'V' is the potential difference across the element and 'i' is the current. By rearranging Equation 5-8 and Equation 5-9, 'h', the heat transfer coefficient can be calculated based on the parameters of the power supply and the heat emitted (as a rate) from the assembly:

$$h = \frac{Vi}{a_A T_A + a_H T_H + a_B T_B + a_S T_S + a_C T_C}$$

Equation 5-10

The heat flow through the specimen is given by:

$$q_S = k\pi r^2 \frac{T_B - T_C}{d}$$

Equation 5-11

Where 'k' is the thermal conductivity, 'r' is the radius, and 'd' is the thickness of the sample. Note that not all the heat entering the sample from disc B goes into C since some is emitted from the curved surface of the sample. The heat flowing through the sample is taken as the mean of the heat entering the sample from disc B and leaving the sample for disc C. The heat entering the sample from B is that which is emitted by the sample and disc C. That is:

$$q_{B->S} = ha_S T_S + ha_C T_C$$

Equation 5-12

The heat leaving the sample for disc C is that which is emitted by disc C alone, that is:

$$q_{S->C} = ha_C T_C$$

Equation 5-13

Taking the mean of Equation 5-12 and Equation 5-13 gives:

$$q_S = \frac{1}{2} h(a_S T_S + 2a_C T_C)$$

Equation 5-14

By rearranging Equation 5-11 and Equation 5-14,

$$k = h \frac{d}{2\pi r^2 (T_B - T_C)} [a_S T_S + 2a_C T_C]$$

Equation 5-15

Hence, the thermal conductivity can be calculated from Equation 5-10 and Equation 5-15. Figure 5-5 is an illustration of the apparatus, where the discs are 50mm in diameter each.

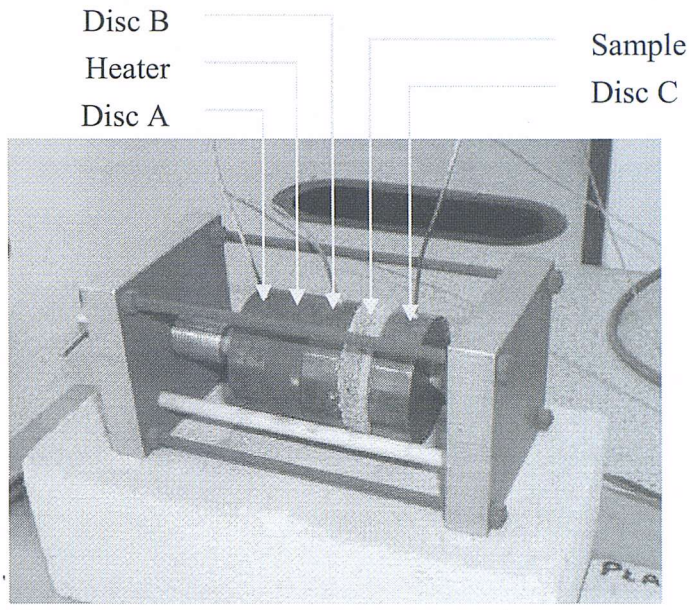


Figure 5-5: Illustration of the setup of the apparatus used for measuring thermal conductivity

5.3.7 Thermal Shock Resistance

The method of determining the thermal shock resistance was to quench bend test bars into water from a range of temperatures, namely 100°C to 700°C. The thermal shock resistance was quantified by the critical quenching temperature at which the material's mechanical property (in this case, the residual flexural strength) reduced dramatically due to thermal damage.

The specimens were heated in a muffle furnace to the furnace temperature, allowed to equilibrate for 30 minutes and dropped from a set height of 100mm measured from the surface of a water bath and quenched within a set time of 5 seconds (i.e. the heated specimens were left exposed to the cooler atmosphere for no more than 5 seconds before quenching) into the bath at room temperature. The quenched bars were dried overnight and then subjected to 3 point bending test for determination of retained flexural strength. One thermal shocked specimen from each composition and condition was left intact and was used for microstructural analysis. Five bars were tested at each of the selected temperatures.

5.3.8 Chemical Resistance Test

To ensure the public's acceptance of a waste-derived material, it is important to be able to specify the endurance of the product under relevant environments. In this particular project, it was chosen to examine the level of chemical resistance of the materials in extreme conditions, and thus, if it passed the test, there would be no risk when using the material under typical, milder, service environments. A leaching test was conducted on the dense glass-ceramics made during the project according to the same experimental procedure as reported by Laurent Gruner [188] when the slag-based glass-ceramic 'Silceram' was investigated. Three different solutions were used in the test:1N HCl, 1N NaOH, and distilled water as the control. The test involved the immersion of the specimens in different solutions for 15 hours at 50°C. Each specimen had dimensions of ~45×6×8mm^3, and the surfaces were polished to 3μm finish for subsequent SEM analysis.

Chapter 6 Characterisation of Raw Materials

Table 6-1 summarises the chosen industrial waste materials which were introduced in Section 5.1, and each has been given a code name as shown below:

Table 6-1: Starting raw waste materials with their code names

Material	Code	Supplier
Coal fly ash	FA	Huntly Power Station, New Zealand
Coal pond ash	PA	Huntly Power Station, New Zealand
Iron-making melter slag	MS	BHP NZ Steel, Glenbrook, New Zealand
Steel-making KOBM slag	KS	BHP NZ Steel, Glenbrook, New Zealand
Mixed waste bottle glass (soda-lime composition)	G	RMF, Christchurch, New Zealand

6.1 Chemical Composition

Table 6-2 gives a summary of the chemical compositions of the waste materials provided by the suppliers from New Zealand. Of particular note are the high SiO_2 and Al_2O_3 contents of the coal ashes (FA and PA), the high TiO_2 content of MS and the high CaO content of KS. Note that the glass cullet was mixed, not colour-sorted.

Table 6-2: Typical compositions of the waste materials (wt%)

	FA as-received	PA after drying	MS	KS	G
SiO_2	51.13	59.20	12.1	8.0	72.7
Al_2O_3	20.97	18.97	17.6	2.6	1.6
Fe_2O_3	7.34	7.50	4.1	13.6	0.3
CaO	14.38	8.72	14.5	56.2	11.0
MgO	2.04	1.55	13.6	8.5	0.5
K_2O	0.64	0.47	-	-	0.3
Na_2O	0.54	0.25	-	-	13.0
MnO	0.04	0.06	1.1	2.4	0.01
TiO_2	1.19	1.49	34.3	2.5	0.04
P_2O_5	0.32	0.33	-	1.4	0.02
V_2O_3	-	-	0.2	4.3	-
Cr_2O_3	-	-	-	0.3	-

The unusually high TiO_2 content in the iron-making melter slag (MS) can be explained by the use of the black ironsands, which are an abundant mineral in the North Island of New Zealand.

6.2 Particle Size Distribution

It is important to note that it is possible that phase transformation during heat-treatment leads to change in density of sintered materials. Therefore, the measured powder density of each waste material does not give an accurate representation of the theoretical density of the sintered samples. However, the powder densities are still useful for ranking the specimens in terms of their relative densities.

Apart from the coal fly ash, all of the as-received waste materials were too coarse to be processed using the powder route. Hence, milling was part of the pre-treatment before sintering experiments. The powder density and the average particle size of the milled materials are as shown in Table 6-3.

Table 6-3: Density and particle size distribution of the waste materials

Raw Material	Condition	Powder Density (g/cm^3)	Particle Size - 90vol.% (μm)
FA	As-received	2.24	<45
FA	Milled 5mins	2.26	<50
PA	Milled 5mins	2.64	<45
MS	Milled 5mins	3.59	<36
KS	Milled 5mins	3.48	<48
G	Milled 5mins	2.46	<31

The densities of the slags were significantly higher than the coal ashes and glass. This is explained by the higher contents of heavier elements, for instance, iron and titanium containing compounds in the slags. The particle size distribution for all the milled wastes was bimodal as exemplified by the distribution given in Figure 6-1. As illustrated in Figure 6-2, the bimodal size distribution was a result of the short milling time which resulted in particle sizes of the two extremes.

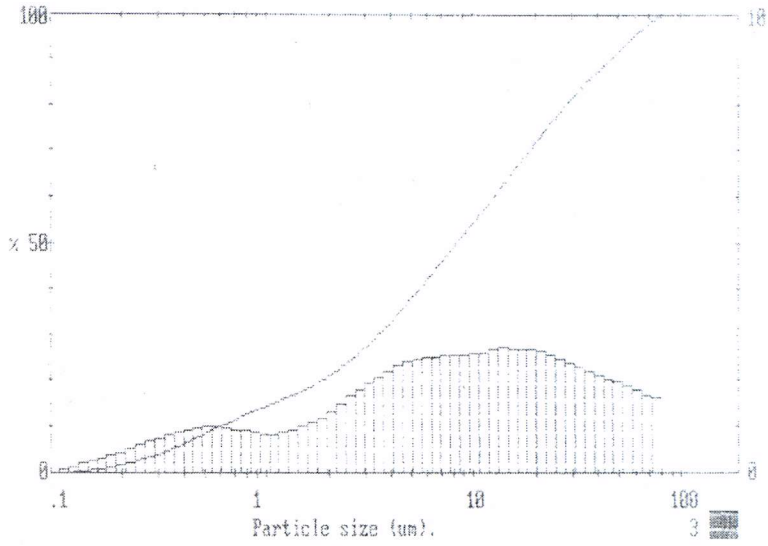


Figure 6-1: Illustration of the particle size distribution of milled PA

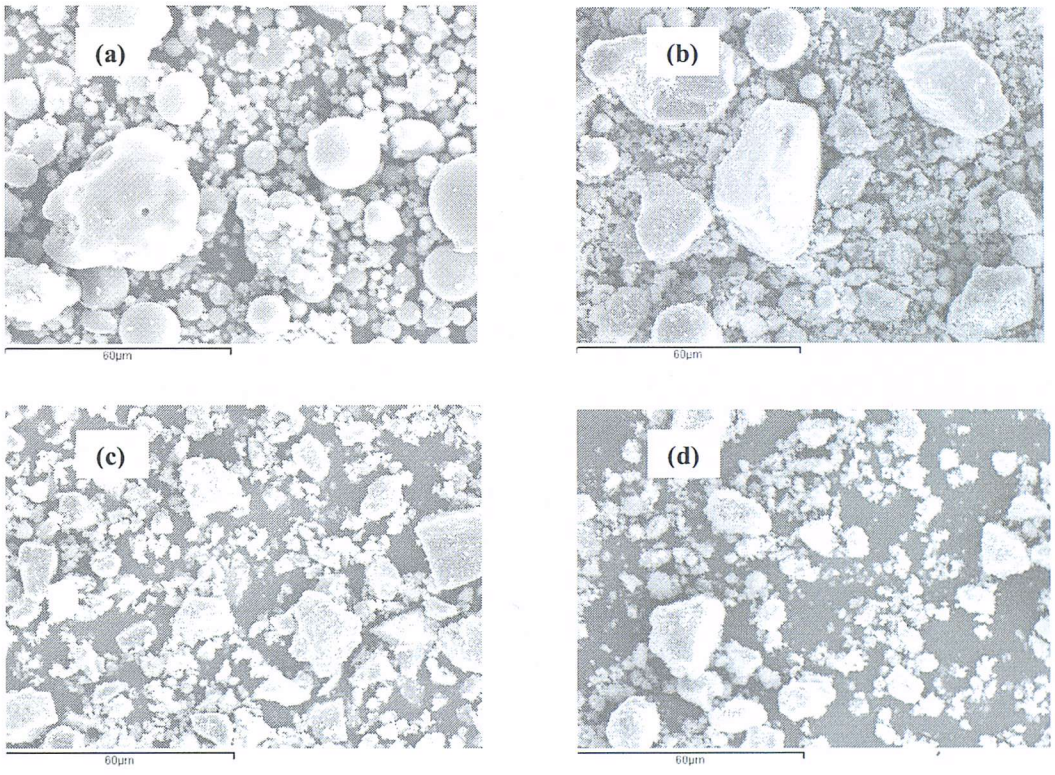


Figure 6-2: Morphology of a) as-received FA; b) milled PA; c) milled MS; and d) milled KS

6.3 Phase Identification

The combination of peaks and an amorphous halo in Figure 6-3 demonstrates that the coal ashes are partially crystalline. The main crystalline phase for both the fly ash (FA) and pond ash (PA) is quartz, with a minor trace of mullite.

The XRD scan of the waste glass surprisingly revealed the presence of a small amount of X-ray detectable quartz. The most likely explanation for the presence of quartz is contamination during the recycling process. Note that the recycling plant operates with large quantities of waste bottle glass, and despite the refinement process having screens and dust traps for unwanted materials, e.g. paper, contamination is unavoidable.

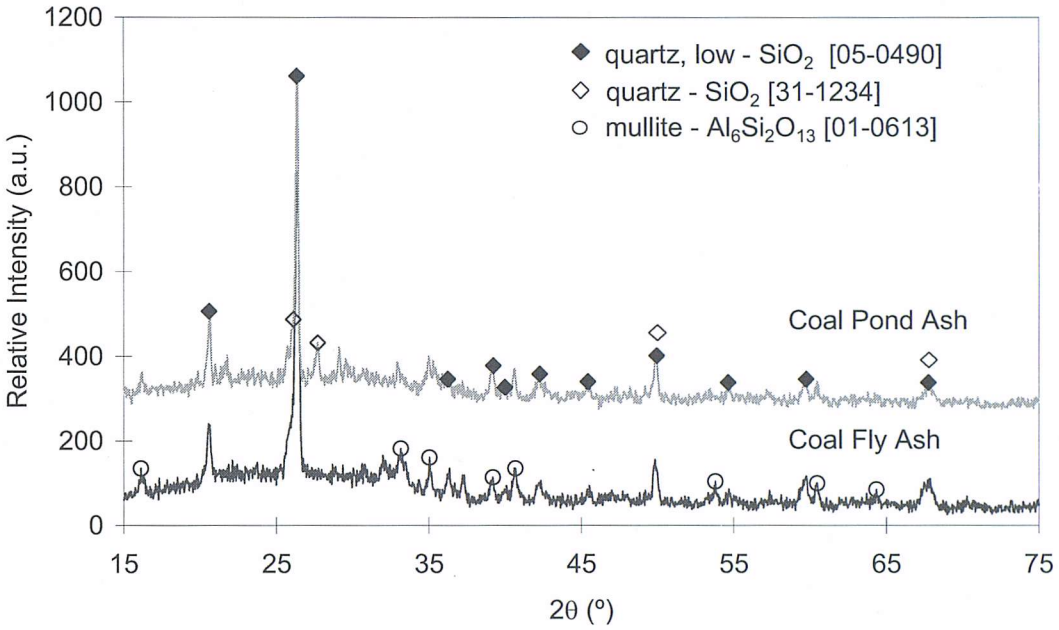


Figure 6-3: XRD patterns on as-received coal ash samples (FA and PA)

The XRD pattern (Figure 6-4) of melter slag (MS) showed multiple crystalline phases, including a spinel phase (titanomagnetite), perovskite, augite and several other components.

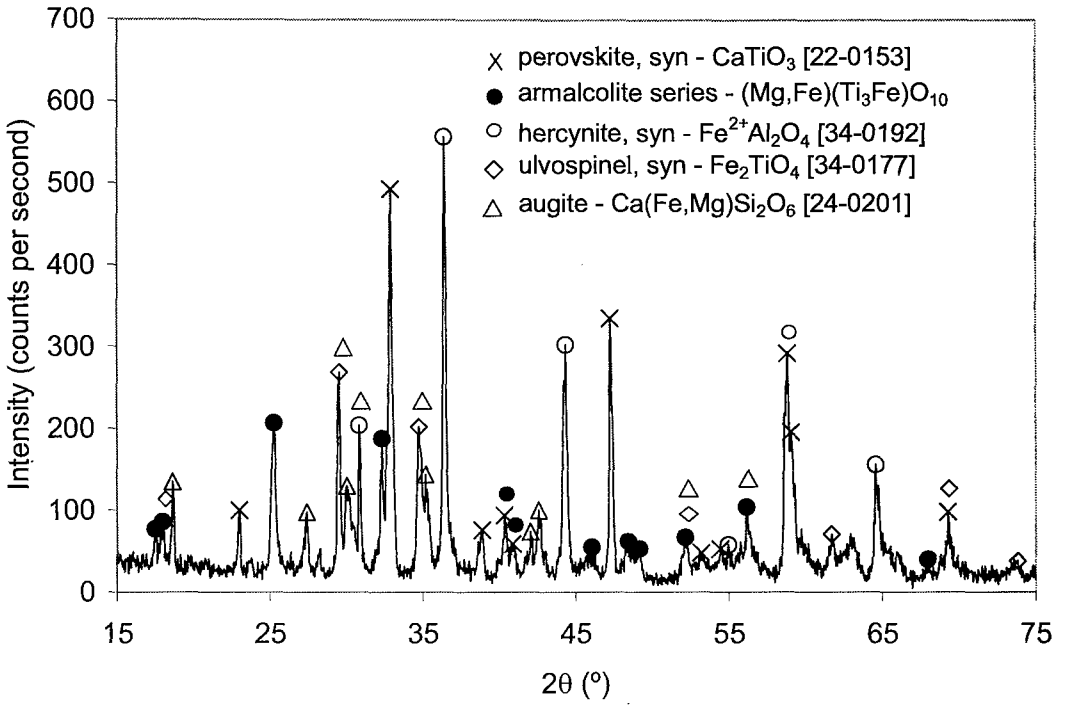


Figure 6-4: XRD pattern of MS – iron-making melter slag

Figure 6-5 illustrates the mineral composition of typical steel-making KOBM slag. Because a large quantity of lime (CaO) was introduced as a purifying agent at the start of the iron-making process, after the conversion from iron to steel, the remaining calcium is in the form of steel-making KOBM slag. XRD analysis showed that after weathering, KOBM slag contained mainly calcium hydroxide, which turned into lime after calcination. The calcined KOBM slag also contained calcium based silicate and iron oxide. The composition of the KOBM slag suggests that it will be difficult to process thermally because of the high calcium content (and low silica, and thus low Si:Ca ratio).

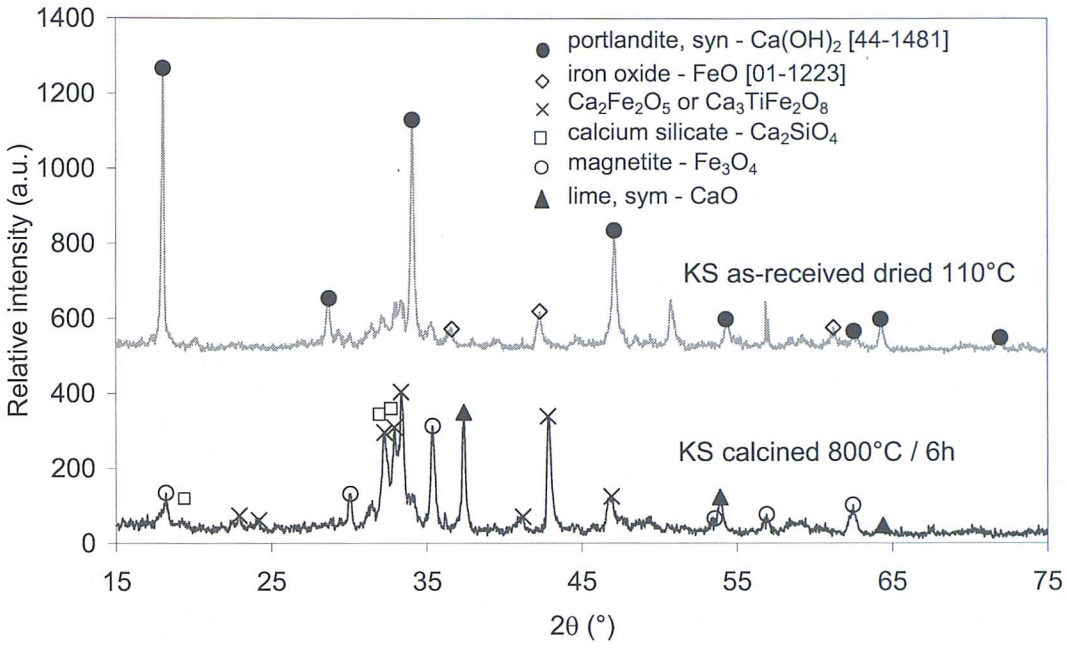


Figure 6-5: XRD pattern of KS – steel-making KOBM slag

6.4 Thermal Analysis

TGA (Figure 6-6) for the as-received pond ash, which showed a 5% reduction in weight, indicates that the material contained more hydrates and/or volatile material than the fly ash (1.3% reduction, see Figure 6-7). The weight loss of pond ash from about 250°C to 650°C suggests that the material may need calcination at about 600~700°C.

On the other hand, melter slag (Figure 6-8) appears to be inert at temperatures below 1000°C. Figure 6-9 shows the DTA/TGA result of the high-CaO-containing steel-making KOBM slag. The two endothermic peaks at ~430°C and ~660°C are believed to correspond to the decomposition of calcium compounds. The three major peaks in the XRD pattern (Figure 6-5, top) of KS correspond to the presence of $Ca(OH)_2$, portlandite, which appears to have decomposed into other phases after heating (Figure 6-5, bottom) as suggested by the weight loss and endothermic troughs in the DTA/TGA plot. Therefore, for preliminary sintering experiments, samples of coal pond ash (PA) were calcined at 700°C for 6 hours and samples of KOBM slag (KS) were calcined at 800°C for 6 hours. For consistency and the ease of comparison, samples of coal fly ash (FA) and melter slag (MS) were calcined 6 hours at 700°C and 800°C, respectively.

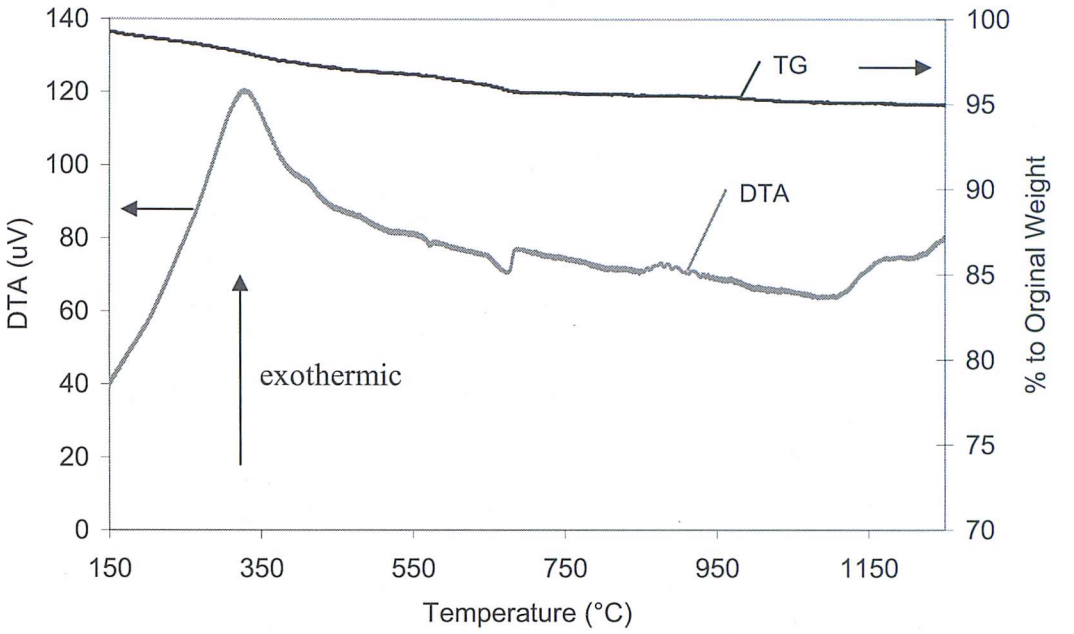


Figure 6-6: DTA/TGA curve for PA (heating rate = 10°C/min)

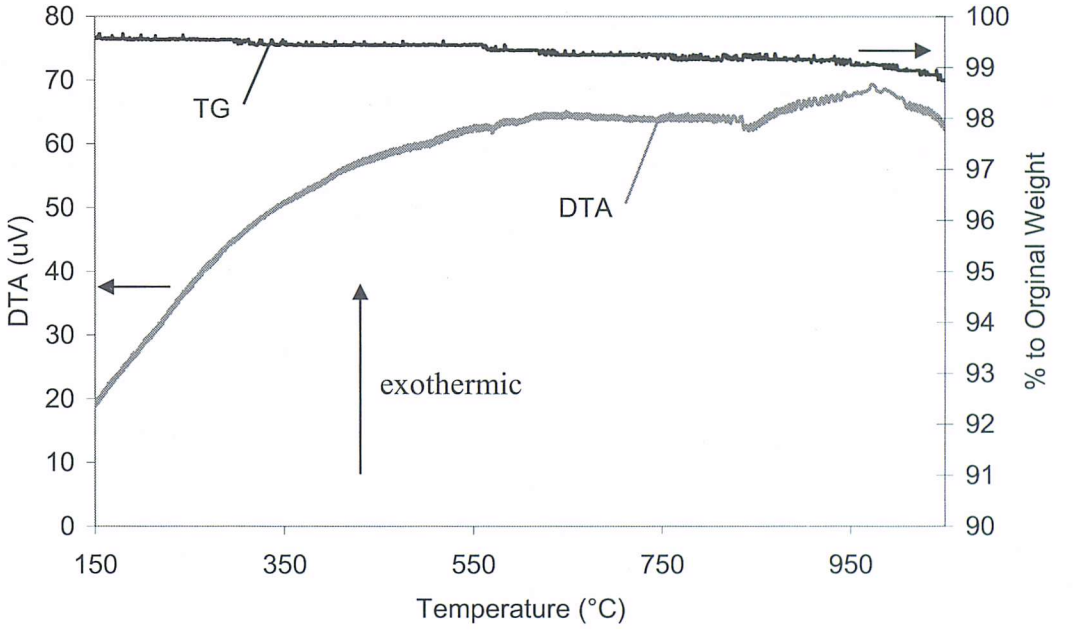


Figure 6-7: DTA/TGA curve for as-received FA (heating rate = 10°C/min)

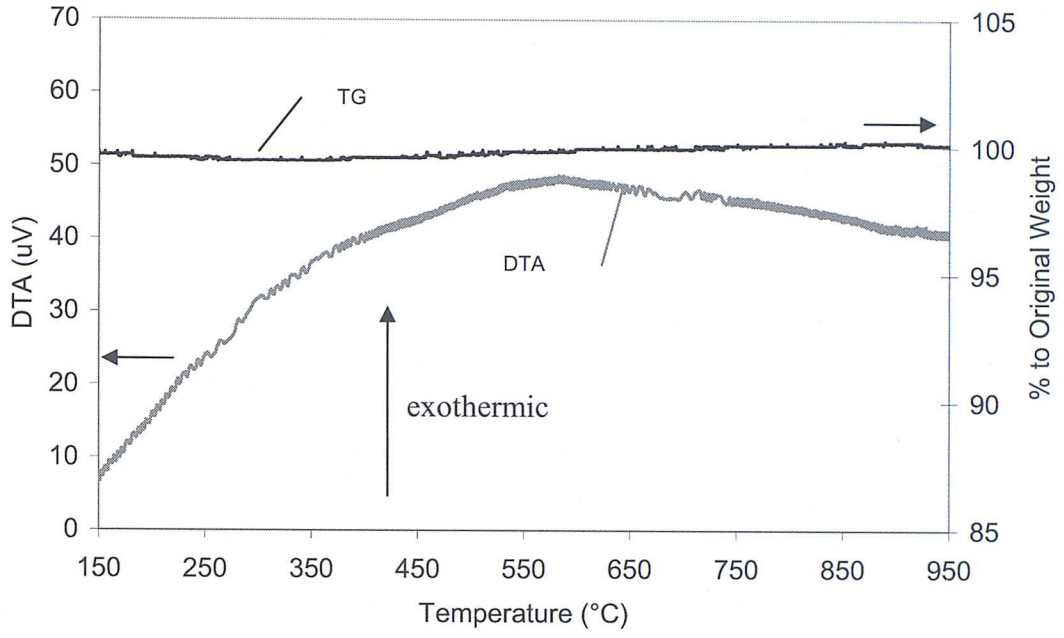


Figure 6-8: DTA/TGA curve for MS (heating rate = 10°C/min)

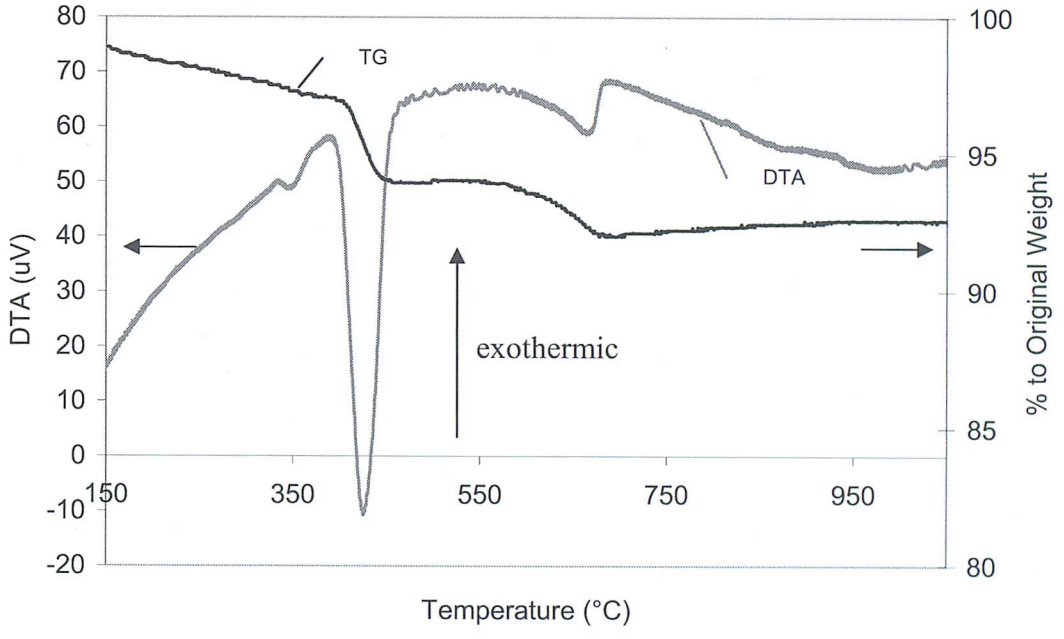


Figure 6-9: DTA/TGA curves of KS (as-received, heating rate = 10°C/min)

6.5 Preliminary Sintering Experiment

Sintering of powder materials is a well-established practice in metal and ceramic production. It is a cost-effective method for turning powdered substances into a dense solid without the need for melting and casting. It is equally applicable to the fabrication of glass and glass-ceramic materials. Figure 6-10 illustrates the versatility of powder sintering in producing specimens in simple shapes and sizes from a range of waste materials.

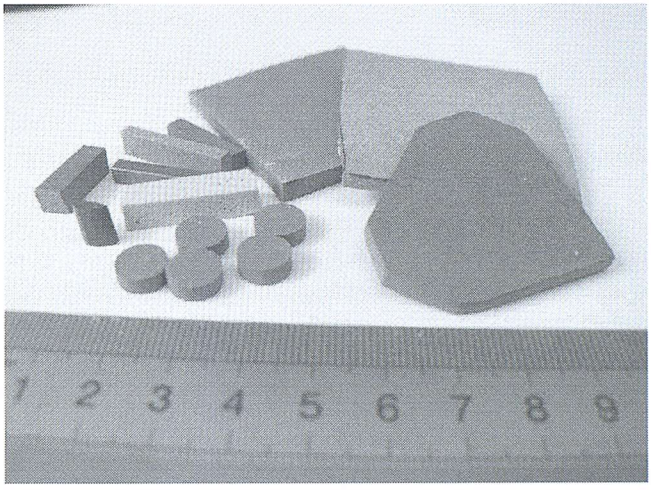


Figure 6-10: Illustrations of the various sintered specimen in different sizes and shapes produced in the course of the study

This section is divided into sub-sections in each of which the preliminary sintering experiments, together with appropriate experimental details, or a different waste material is discussed.

6.5.1 Coal Fly Ash

The relative densities of fly ashes mixed with up to 50wt% glass cullet and sintered at different temperatures are presented in Table 6-4. XRD patterns from the sintered FA50G mixture are given in Figure 6-11.

Table 6-4: Relative densities of sintered samples containing calcined coal fly ash

Composition (wt%)	Sintering Temperature for 1 hour (°C)	Relative Density*
100% coal fly ash (FA)	1050	80 (83)**
	1075	81 (86)
	1100	83 (84)
	1150	Molten
90% fly ash + 10% glass cullet (FA10G)	1050	78
	1075	82
	1100	89
	1150	Molten
60% fly ash + 40% glass cullet (FA40G)	900	83
	1000	86
	1050	89
	1100	Molten
50% fly ash + 50% glass cullet (FA50G)	800	63
	900	66
	1000	89
	1050	84

* Relative density = bulk density / theoretical density, bulk density (see section 5.2.8)

** Values in brackets: relative density for as-received (not calcined) coal fly ash

As results show, there is no benefit of calcining coal fly ash. In fact, the sintered specimens using as-received fly ash seem to have slightly better densities than the ones which were calcined first. This is consistent with the DTA data, which showed the fly ash was inert to temperatures up to the calcination temperature of 700°C.

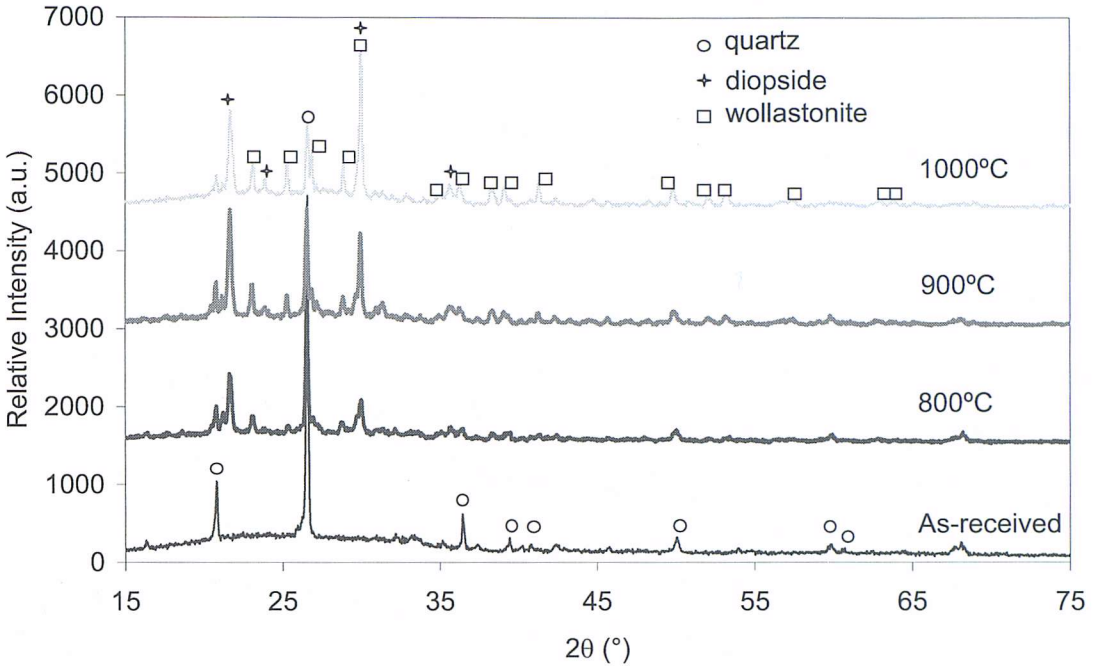


Figure 6-11: XRD patterns of FA50G samples sintered at different temperatures

All samples could be sintered to a relative density of greater than 80%. The best relative density achieved was 89% which was achieved with all specimens but for 100% fly ash. The optimum sintering temperature decreased with increasing glass content as expected (1100°C with 10wt% glass, 1050°C with 40wt% and 1000°C with 50wt%). The main crystalline phases in these specimens were diopside, wollastonite, and quartz as exemplified by the data for FA50G in Figure 6-11. The amount of wollastonite increased with increasing glass cullet content.

6.5.2 Coal Pond Ash

Preliminary experiments of this material showed promise in producing dense glass-ceramics via powder route as exemplified by PA and PA10G samples with relative densities in excess of 90%. Coal pond ash was easier to compact than the fly ash, and relative density measurement results indicate there was no improvement after calcination of the pond ash as found for FA, even though PA showed a greater weight loss after calcining. It was postulated that the higher proportion of hard crystalline material to amorphous phase in the calcined ash (see Figure 7-2 in section 7.1) may have acted as obstacles during the viscous phase sintering [54]. Therefore, PA was sintered as-received to minimise the processing cost with or without additives.

Table 6-5: Relative densities of sintered samples containing coal pond ash

Composition (wt%)	Sintering Temperature for 1 hour (°C)	Relative Density
100% coal pond ash (PA)	1050	76 (79)*
	1075	88 (92)
	1100	91 (89)
	1150	Molten
90% pond ash + 10% glass cullet (PA10G)	1050	78
	1075	91
	1100	86
	1150	Molten
60% pond ash + 40% glass cullet (PA40G)	900	77
	1000	80
	1050	81
50% pond ash + 50% glass cullet (PA50G)	800	82
	900	80
	1000	83
	1050	70

*Values in brackets: relative density for as-received coal pond ash

6.5.3 Melter Slag

Temperatures of 1200°C or above were required to sinter the melter slag without glass addition. The main crystalline phases in the sintered samples were found to be spinel ($MgAl_2O_4$), perovskite ($CaTiO_3$) and pseudobrookite (Fe_2TiO_5), with augite and quartz as minor constituents. Soda-lime glass was added to lower the sintering temperature. However, visual observations have found that there was a tendency for these glass-containing mixtures to bloat at high sintering temperature, causing a drop in relative density (see data at 1050°C for MS50G in Table 6-6). This could be due to the decomposition or reaction of the low melting point glass inclusion with the high melting point slag. In general, the relative densities obtained from the slag were at least 10% lower than those derived from the coal ashes.

Table 6-6: Relative densities of sintered samples containing melter slag

Composition (wt%)	Sintering Temperature for 1 hour (°C)	Relative Density
100% melter slag (MS)	1100	73 (73)*
	1200	77 (83)
90% melter slag + 10% glass cullet (MS10G)	1050	72
	1100	74
	1150	77
60% melter slag + 40% glass cullet (MS40G)	1000	76
	1050	75
	1075	74
	1100	74
50% melter slag + 50% glass cullet (MS50G)	800	86
	900	84
	1000	78
	1050	63

*Values in brackets: relative density for as-received melter slag

A slower heating rate than 10°C min^{-1} may be used during sintering and sometimes this leads to an improvement in the densification. The waste material has to be vitrified into a glass, crushed to a powder in order to be sintered at lower temperatures as well as to obtain denser materials via the powder route. This is clearly an expensive processing route and not as attractive as sintering the raw material. However, as Figure 6-12 shows, the residual porosity is very high and the microstructure of the sintered compact of melter slag (MS) is highly heterogeneous even with addition of glass.

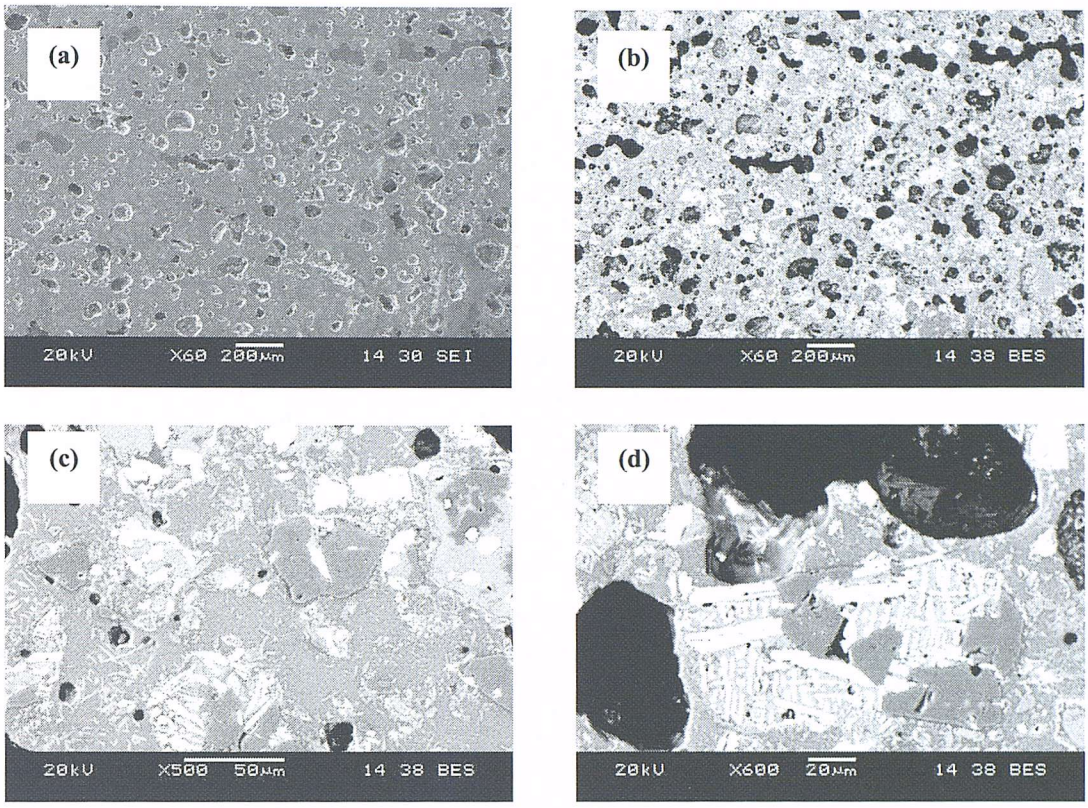


Figure 6-12: MS50G sintered at 10°C min^{-1} up to 1000°C for 1h: (a) secondary image; (b) backscattered image; (c) and (d) higher magnification images showing the complex heterogeneous microstructure and residual porosity

Given the heterogeneous nature of the raw material and the high porosity content of the sintered product, particularly with high MS contents, the melting route may be the only option to overcome the rigid crystalline material to produce a dense glass-ceramic. Consequently, the melter slag will be subjected to a study on the vitrification and devitrification behaviour of bulk samples. Because of its high TiO_2 content, and thus high content of nucleating agent, it has the potential to give a glass-ceramic with novel mechanical and physical properties.

6.5.4 KOBM Slag

The KOBM slag has over 50wt% of calcium oxide, which makes it very difficult to be sintered at temperatures lower than 1200°C. Waste glass added to the slag helped the sintering, but the porosity of the sintered material was still extremely high (20-30%) according to Table 6-7. Nonetheless, the sintered slag has one interesting property: namely a very weak interaction with magnets was found with sintered specimens containing over 50wt% of the slag. The main crystalline phases of the sintered

materials were pyroxene and melilite groups: wollastonite and gehlenite. The magnetite crystals were the minor phase that was responsible for the magnetic property (Figure 6-13). As briefly mentioned in the literature survey, high-iron content wastes have potential in the production of magnetic glass-ceramics [189, 190].

Table 6-7: Relative densities of sintered samples containing KOBM slag

Composition (wt%)	Sintering Temperature for 1 hour (°C)	Relative Density
100% KOBM slag (KS)	1100	66 (60)*
	1200	70 (67)*
90% KOBM slag + 10% glass cullet (KS10G)	1050	62
	1100	63
	1150	61
60% KOBM slag + 40% glass cullet (KS40G)	1000	65
	1050	67
	1075	65
	1100	Deformed
50% KOBM slag + 50% glass cullet (KS50G)	800	77
	900	74
	1000	71
	1050	71

* Values in brackets: relative density for as-received KOBM slag

In conclusion, the inclusion of glass cullet has reduced the sintering temperature and improved the densification of all materials to a certain extent. The promoted formation of acicular wollastonite crystals may also give the potential of better mechanical properties.

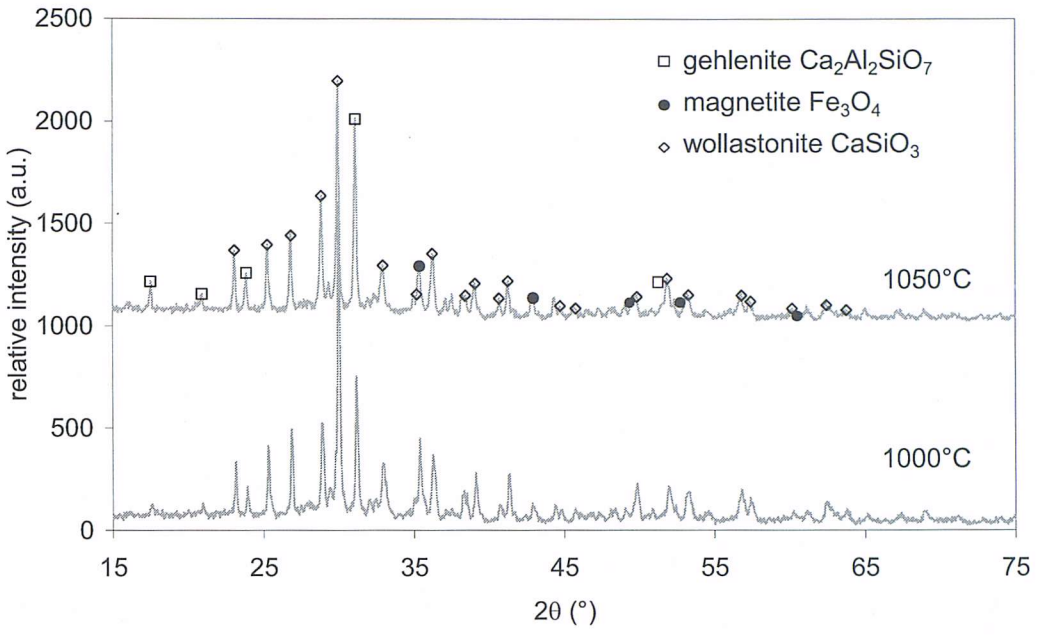


Figure 6-13: High-lime steel-making (KOBM) slag-based glass-ceramics produced by powder sintering, 50/50 KOBM slag and glass cullet.

6.6 Chapter Conclusions

Pond ash (PA) has been chosen as the material for further sintering studies as it has the best potential to be used as a raw material in producing dense glass-ceramic material using the powder sintering route. In addition, coal fly ash (FA) is known to have been well-utilised in the cement industry as a raw constituent. It is the disposal of PA that seems to be the more of a problem at the moment. Therefore, only PA will be investigated more thoroughly using the powder route.

As for the slag materials, the high content of CaO in KOBM slag (KS) means that a significant amount of additives is required to adjust the chemical composition to enable low temperature sintering or production of a glass precursor for heat-treatment. On the other hand, the melter slag (MS) has more SiO_2 (glass forming oxide) than KS in weight % and an abundant amount of TiO_2 as a nucleating agent, and therefore MS is more appealing as a main constituent to produce the precursor glass. Therefore, only MS will be investigated further but using the melt heat-treatment route given the poor sintered densities from preliminary experiments.

Chapter 7 Coal Ash-based Glass-Ceramics by the Sintering Route

It has been shown that coal ashes are one of the main problematic industrial wastes around the world [54, 58]. Comprehensive studies have been done, in particular, using the melt heat-treatment method to produce glass-ceramic material from coal fly ash with promising results (see section 3.2.1). However, this energy-intensive process adds a tremendous amount of cost to the making of any product out of this waste. Developing low temperature processing routes will lower the production costs and thus favour the material as an alternative to commercial products. One of the more technically-sound and economical route is the powder sintering method. The waste under investigation is called coal pond ash, where the name is directly related to the environment the waste is stored in. In common practice, residual coal fly ash (unutilised by cement industries) and bottom ash are weathered and stored in water ponds located near the power station that generates these solid wastes. Preliminary study has already shown that the pond ash is easier to process than fly ash in terms of handling and sintering. Calcination of pond ash (700°C for 6 hours) was found to be unnecessary, indeed proved to be unhelpful, as the calcined material had a higher fraction of hard crystalline phases which acted as obstacles during the viscous phase sintering, resulting in a reduction in densification.

The processing method used in this research was not only relatively simple and economical, but the composition used was also advantageous in terms of the high weight fraction of waste (80-100wt%) incorporated in the starting mixture. Further optimisation of the process and composition should help to reduce the porosity and thus to improve the mechanical properties.

In summary, for this study, coal pond ash (PA) was chosen for developing dense glass-ceramic materials without the need to calcine or vitrify the wastes. The microstructures and properties of the glass-ceramics produced were characterized. The aim of the current work was to produce a glass-ceramic material suitable for the building industry by a very simple and economical process, using a cheap raw material.

7.1 Sintering studies – Linear Shrinkage

After a series of optimisation experiments, the sintering temperature range for subsequent investigation was reduced from 850-1200°C to 1050-1075°C. The optimised sintering temperature and time at the optimum temperature of the as-received pond ash were determined by dynamic and isothermal dilatometry.

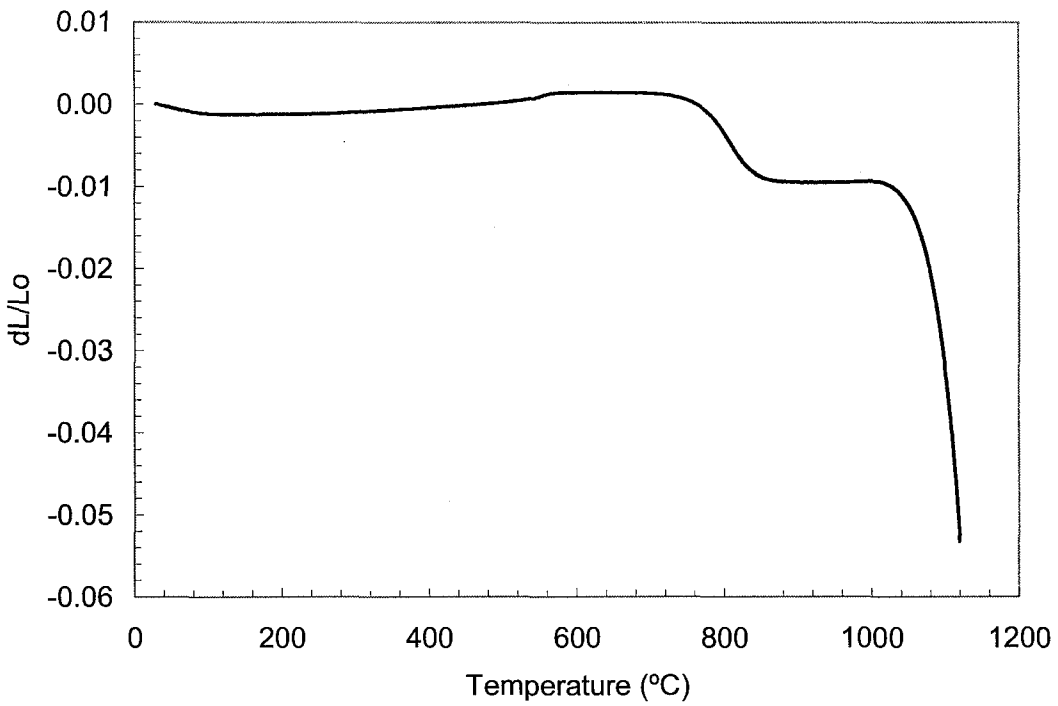


Figure 7-1: Linear shrinkage of as-received coal pond ash as a green compact

As the typical dilatometry curve in Figure 7-1 shows sintering had not finished by 1120°C. Furthermore, it is obvious that there were two stages of shrinkage of the material, the first occurred at about 750°C and was followed by the second at 1000°C. The shrinkage, at the end of the experiment, was relatively low: ~5%. XRD analysis (Figure 7-2) revealed XRD-detectable phases (anorthite and quartz) in pond ash after heat-treatment at different temperatures. The noticeable difference between the material sintered at 810°C and 1031°C was the increase in the relative crystal peak heights to the amorphous halo with the increase in temperature. The crystallization may have hindered the sintering at the lower temperature of ~800°C, which perhaps explains why there was a plateau in the dilatometry plot and the second stage of

shrinkage occurred only after the temperature was raised to above 1000°C when material was softened enough to reinitiate sintering.

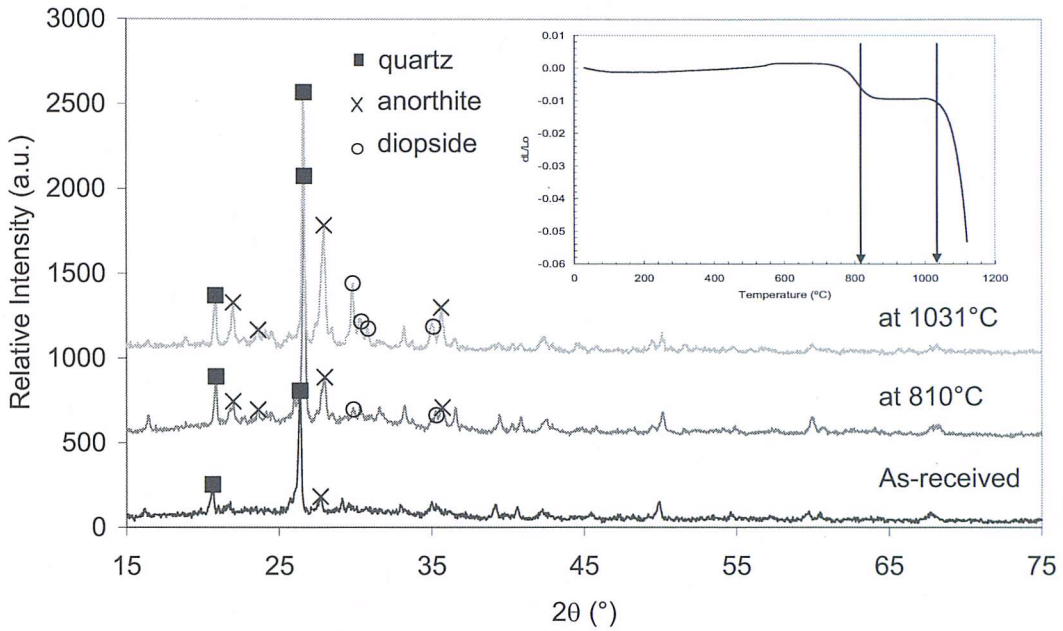


Figure 7-2: XRD patterns showing the phase formation and crystallization during different stages of the sintering study: as-received (bottom), at 810°C (middle), and at 1031°C (top).

Therefore, after a number of sintering studies and experiments, the optimum sintering temperature to achieve good sintered density was determined to be around 1075°C. Despite observation that the material still shrinks after 1100°C, it was shown that the suitable sintering temperature range is relatively narrow as localised melting occurred after independent sintering experiments were carried out at 1100°C and above. Regarding the optimum sintering time, the result from an isothermal sintering experiment (Figure 7-3) indicates that one hour at the sintering temperature is acceptable as the rate of sintering slowed down past that time frame, suggesting little benefits to be gained with longer times while the energy cost increased with time.

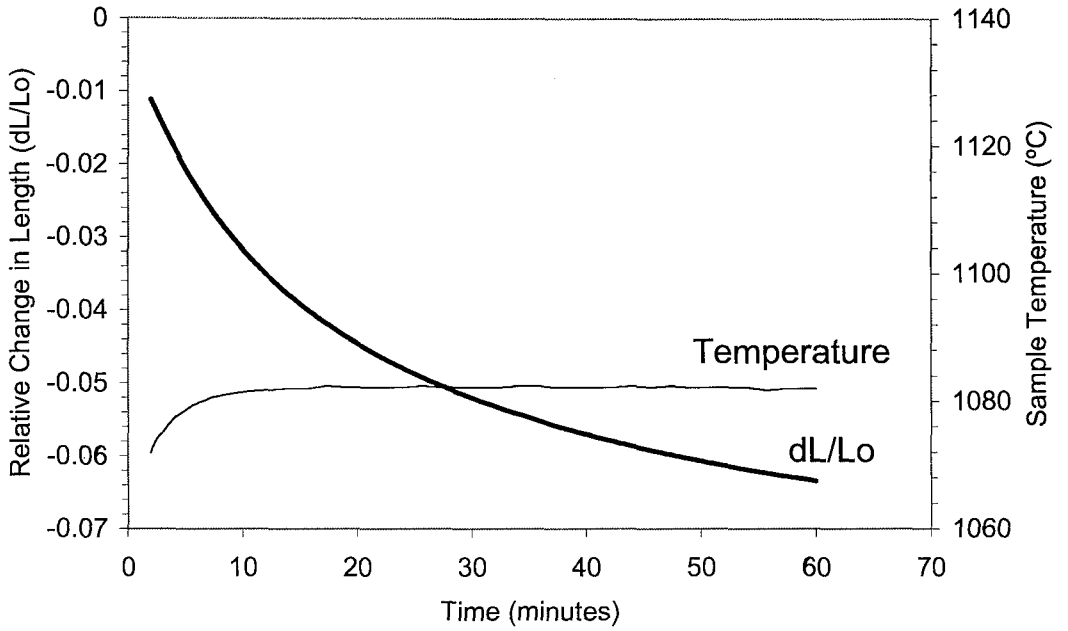


Figure 7-3: Isothermal shrinkage of the PA as-received specimen at set temperature of 1105°C for 1 hour

Additional experiments (see Table 7-1) have also shown that a slower heating rate (~2°C/min) was beneficial to densification (up to ~95% of the theoretical density achieved) than with the standard heating rate of 10°C/min (data extracted from Table 6-5). It was found that slower heating rate assisted the sintering of pond ash significantly, as the viscous phase was allowed to flow through the hard, crystalline structure that already existed in the compact. That is, more time was allowed for sintering in the lower temperature range before the onset of further crystallisation.

Table 7-1: Effect of heating rate on percentage of theoretical density of various sintered PA specimens

Materials/Sintering Temperature (°C)		**Heating Rate**	
		10°C min^{-1}	2°C min^{-1}
PA as-received			
	1075	92	96
	1100	89	92
PA calcined			
	1075	88	93
PA10G			
	1075	91	94
PA50G			
	1050	80	87

As an aside, investigation into the effect of cold isostatic pressing (CIP) on the final density of specimen was carried out and showed a very slight improvement to the

sintered density compared with that obtained with uniaxial cold pressing. Hence, it is unjustifiable to include CIP in the process, with a concomitant increase in cost, when the improvement is negligible.

7.2 Phase Identification

Micrographs in Figure 7-4 illustrate the residual porosity (<10%) and the crystalline phases present in the sintered PA10G compact (optimised condition). Quartz, feldspar, and diopside were the main crystalline phases detected under SEM using EDX. A minor trace of hematite was also present.

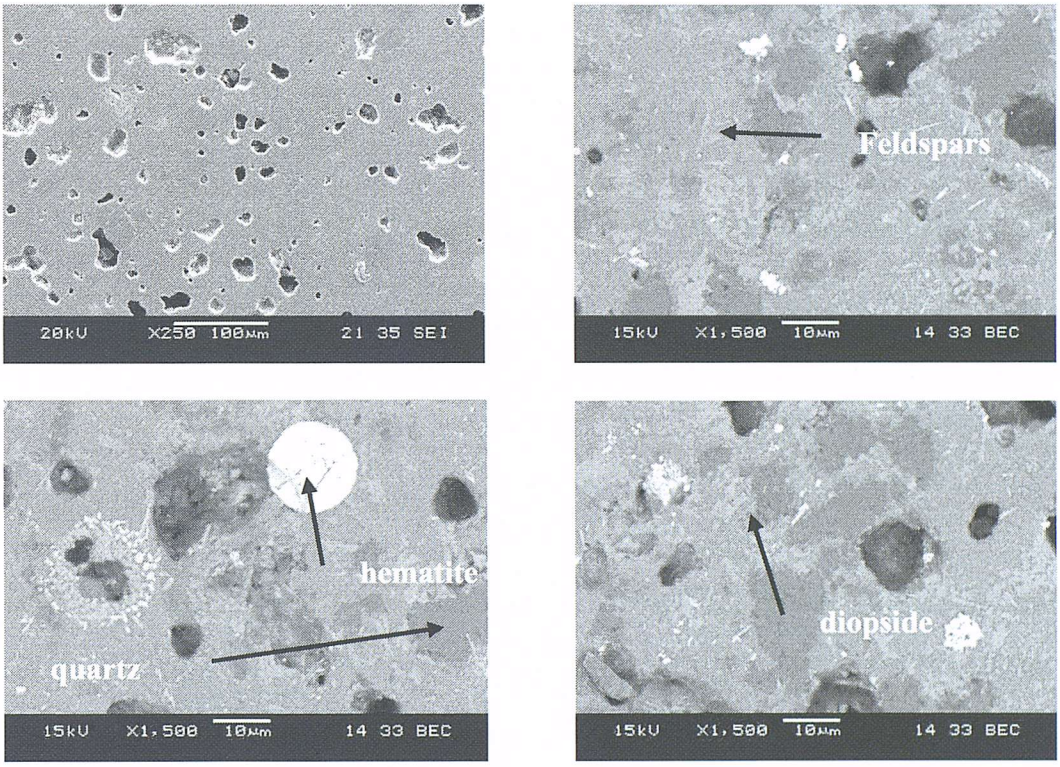


Figure 7-4: Secondary electron micrograph and backscattered electron micrographs of coal pond ash with 10wt% waste glass heated at 2°C/min and sintered at 1075°C for 1h

In conjunction with SEM, XRD was used for phase identification. As shown in Figure 7-5, supporting the microscopic observation, the sintered coal ash (PA as-received) was rich in quartz, anorthite ($CaAl_2Si_2O_8$, feldspar group), and diopside ($CaMgSi_2O_6$, pyroxene group). By increasing glass content (of soda-lime composition), thus increasing the relative amount of network modifiers such as Na_2O and CaO, the overall phase composition moved towards a sodium and calcium rich

silicate region, where the favourable phases became albite ($NaAlSi_3O_8$, feldspar) and wollastonite ($CaSiO_3$, pyroxene).

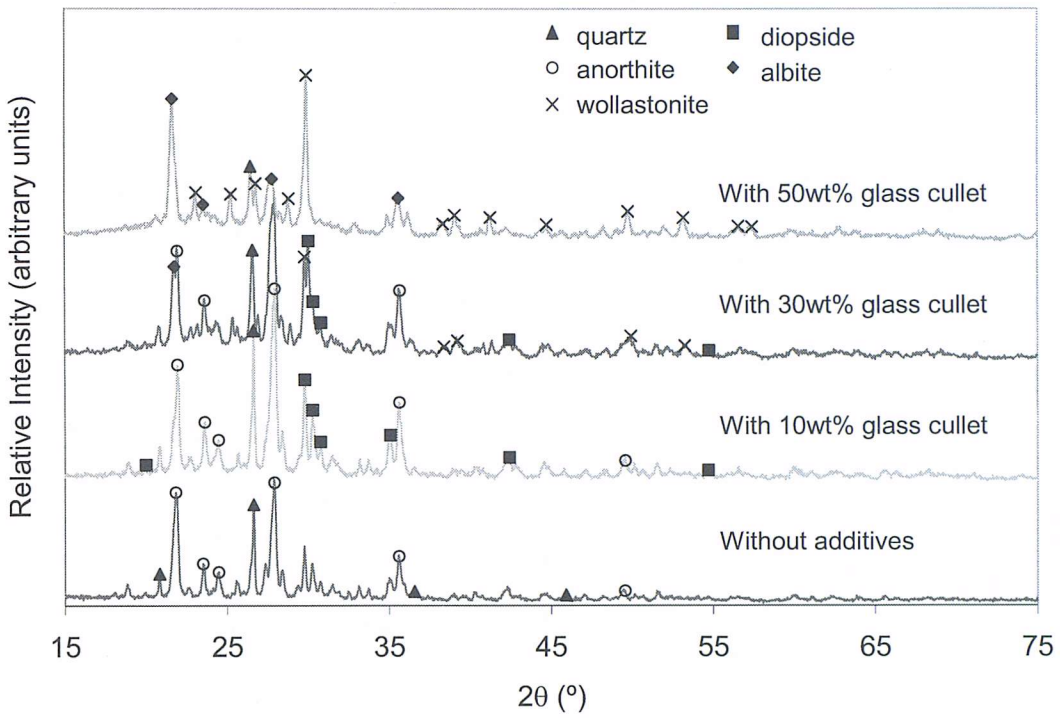


Figure 7-5: XRD plot: Illustration of crystalline phase present with changes with glass content

In order to show the added, or lack of, benefits from vitrification before sintering, samples (designated "PA glass") of sintered coal pond ash that had been vitrified and powdered were examined by XRD analysis (Figure 7-6) and their physical and mechanical properties measured. First of all, it shows that the vitrification of the material before sintering has no effect on the mineralogy, i.e. the crystalline phases remained the same with or without vitrification. The only benefit of vitrification is that the vitrified waste, which was amorphous, sintered much easier and at lower temperature (900°C) than the as-received waste. However, there is already an added cost to the beginning of the process, which is the energy-intensive melting stage plus milling the vitrified waste. It is concluded that the minimal benefits do not warrant the extra cost.

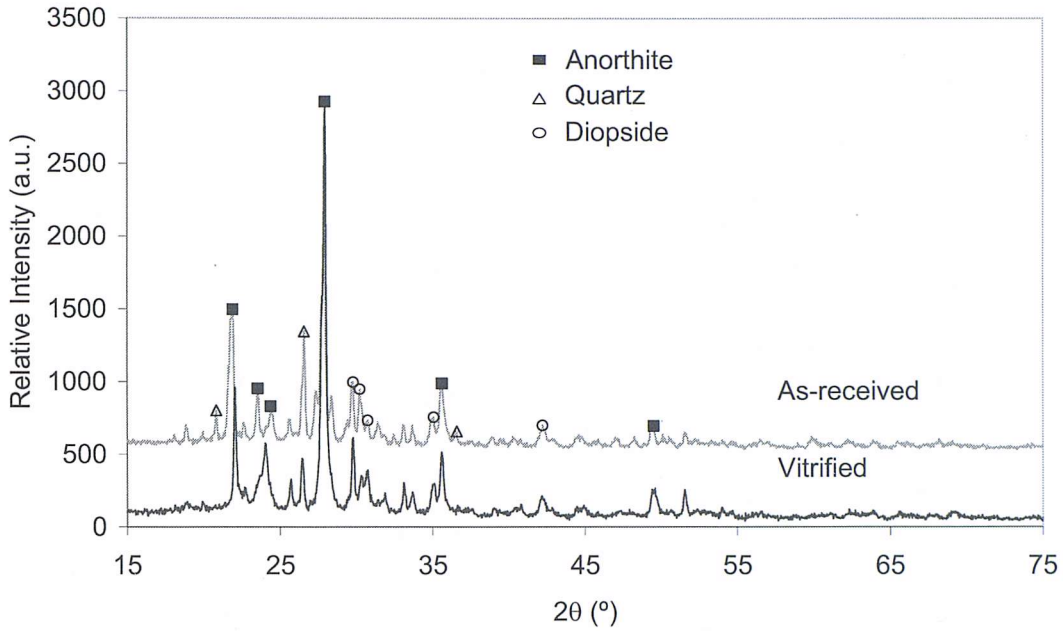


Figure 7-6: XRD plots of the sintered vitrified pond ash and sintered as-received pond ash

7.3 Coefficient of Linear Thermal Expansion

Dilatometry was also used for determining the coefficient of linear thermal expansion (CTE). This was part of the characterisation study of these pond ash based glass-ceramics and the results are presented in Figure 7-7. Both "PA as-rec" and "PA glass" have the same phases present even though the latter was sintered with vitrified waste, consequently their CTEs were very similar. For mixtures with additional glass cullet, the trend as shown by the data was the same irrespective of the temperature range over which CTE was measured, i.e. the CTE increases with increasing amount of glass additive (Figure 7-8).

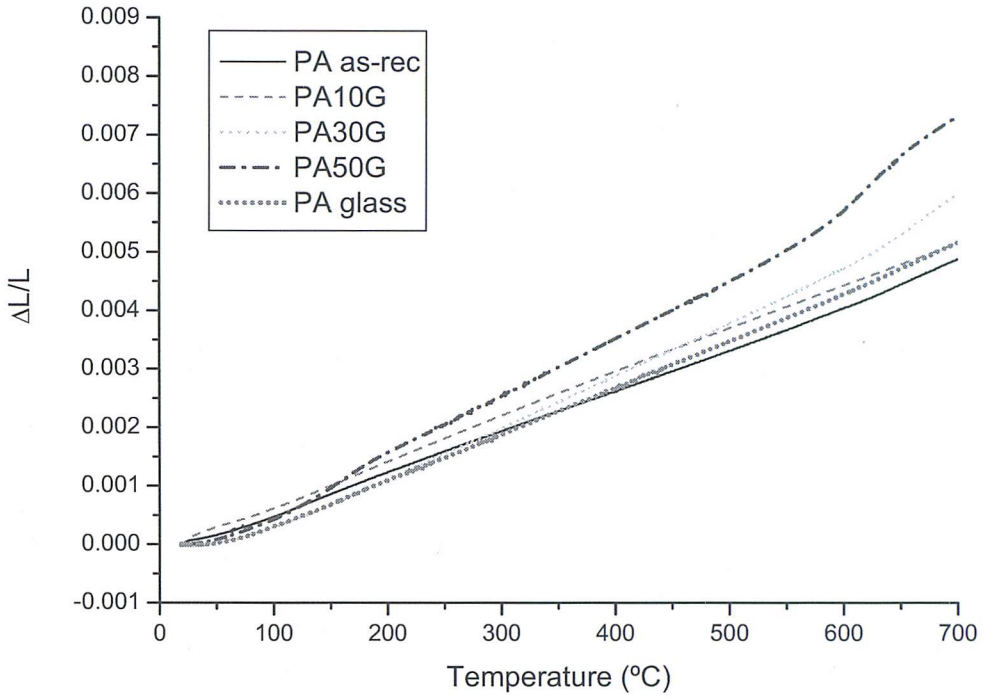


Figure 7-7: Change in length with temperature, where the gradient of each slope is the CTE of that particular material

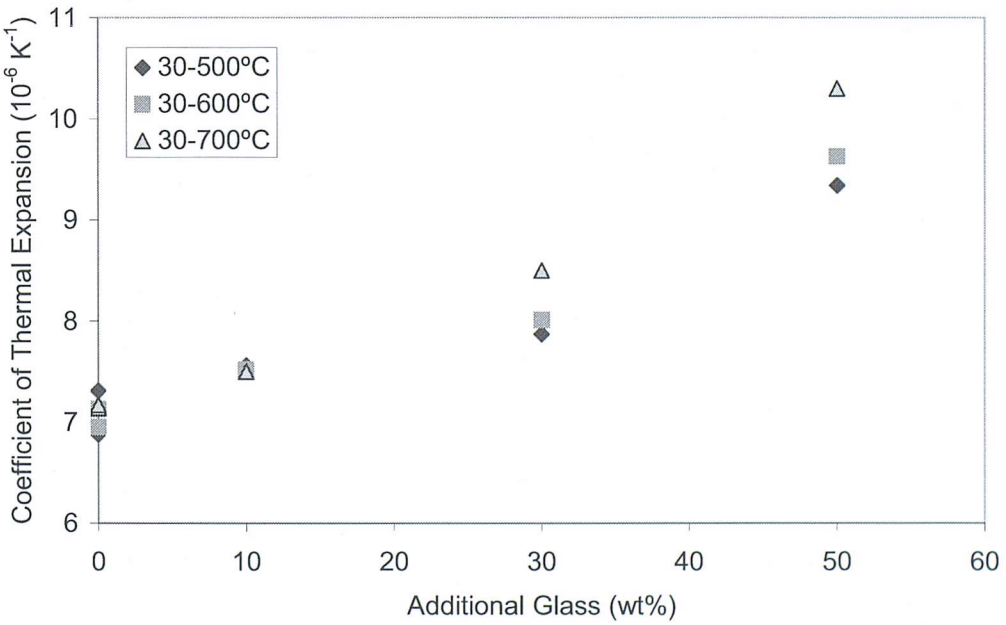


Figure 7-8: Increasing CTE with increasing additional glass content in the pond ash mixture

This increase in linear CTE with increasing amount of glass addition can be explained by one of the following scenarios. The CTE of the residual glass phase in each of the sintered glass-ceramics was unknown. Therefore, assumptions were made with information gathered from reference materials as shown in Table 7-2.

Table 7-2: Typical linear CTE values of individual crystalline phases present in the investigated materials

Crystalline Phase	**Crystal System**	**Linear CTE ($\times 10^{-6}$ °C^{-1})**
Diopside [191]	Monoclinic	10.4
Anorthite [1]	Triclinic	4.5
Albite [192]	Triclinic	0.9
Wollastonite [193]	Triclinic	7.0

If CTE of the residual glass is lower than that of diopside (Table 7-2), then in order for the CTE of the sintered glass-ceramic to increase with increasing amount of glass additive, then there must be more crystallisation with increasing amount of glass additive. That is, there is more diopside regardless of an increasing amount of albite/wollastonite formation. The other possibility is that the CTE of residual glass is higher than that of diopside. Hence, if the residual glass content increases (i.e. lower percentage of crystallisation with higher contents of glass additive), then the CTE of sintered glass-ceramic material is expected to increase as a higher percentage of residual glass is present. The first scenario was proved incorrect as shown by Table 7-3. Using a semi-quantitative XRD technique, which involved calculations of the ratios between the area under amorphous halo and the areas under the crystalline peaks, it appears that the degree of crystallinity decreased with additional glass content.

Table 7-3: Relative percentage of crystallisation of each sintered material

Sintered Materials	**Additional glass content (%)**	**Relative % crystallisation**
PA glass	0	73.4
PA as-received	0	69.7
PA10G	10	64.7
PA30G	30	63.0
PA50G	50	47.6

Further information obtained from a semi-quantitative XRD analysis also helped to explain the increasing CTE with increasing additional glass content. 10wt% of MgO (99.9% pure synthetic periclase) was added to each of the PA series powder samples. The mixtures were ground and blended using a mortar and a pestle. The known amount of MgO was used as a reference pattern with independent peaks, which was used to calculate relative ratios of the various crystalline phases present in each sample. The analysis also involved 'de-convoluting' overlapping peaks by refitting XRD patterns using the Philips XRD software package. An example is shown in Figure 7-9. The treatment helped to remove the effect of overlapping peak areas and thus give the 'real' peak intensity of each peak.

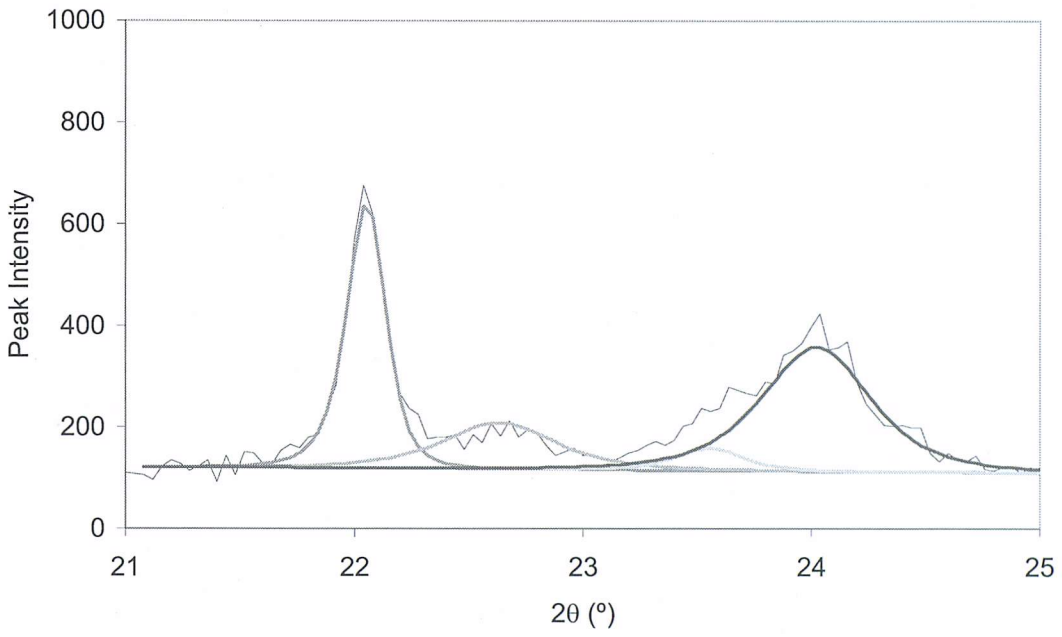


Figure 7-9: An example of XRD pattern treatment – where 4 individual patterns from the PA glass sample were highlighted.

Using the peak intensities measured after the pattern treatment, a summary of relative amounts of crystalline phases in each sintered material was plotted in Figure 7-10. First of all, note the difference in phase composition between the two materials: PA glass and PA as-rec; both without any additional glass. PA glass, as discussed earlier, was sintered from the powder of vitrified pond ash, whereas PA as-rec was sintered directly using as-received pond ash. Hence, the lower quartz content in PA glass may be explained by the melting, i.e. homogenisation of the starting powder, which led to

a different chemical composition of the parent glass powder and thus the higher content of anorthite crystals. As for the PA materials with increasing additional glass content, the amounts of quartz, anorthite and diopside have all reduced while the relative amounts wollastonite and albite have increased slightly over the range of 0 to 50wt% additional glass content. In addition, the relative degree of crystallinity of each sample follows the same trend as the result in Table 7-3, i.e. lower degree of crystallinity with higher additional glass content. In summary, the increasing amount of glass cullet added to the starting PA powder have caused the sintered material to have lower degree of crystallinity, thus higher residual glass content, and hence higher overall CTE.

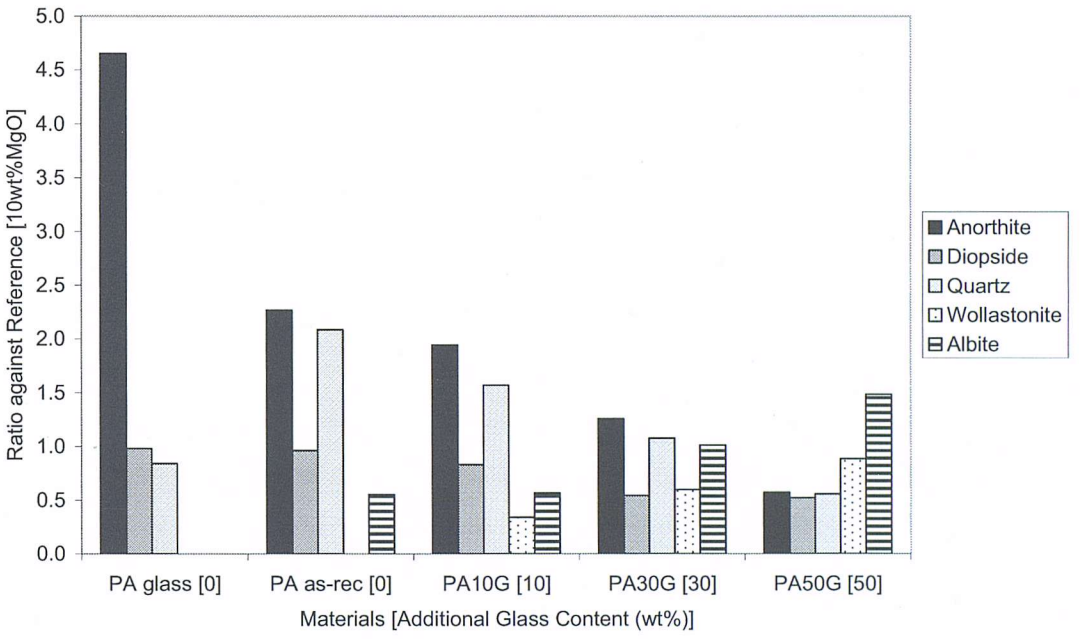


Figure 7-10: Summary of amount of various crystalline phases (relative to 10wt% MgO) present in sintered PA-based samples, showing the relationship with additional glass content.

7.4 Mechanical Properties

Table 7-4 summarises physical and mechanical properties of a series of sintered coal pond ash-based glass-ceramics. The optimised composition, i.e. sintered best, composition contained 30wt% waste glass (PA30G). Because of the high sintered density of ~95% of theoretical density, this material also had the best overall

mechanical properties (Young's modulus, flexural and compressive strengths) out of the four compositions (0, 10, 30, and 50wt% glass addition).

Looking at the individual properties in more detail, it is obvious that Vickers hardness (Hv) values for sintered pond ash based glass-ceramics varied significantly between samples because of the inhomogeneous nature of the material, i.e. porosity and complex crystalline structure. The presence of pores has made the attainment of consistent hardness data difficult as demonstrated by the large standard deviations associated with many of the hardness values quoted in Table 7-4. This is supported by the Hv value for the sintered glass-ceramic from vitrified ash, which had a lower porosity content and was tested for comparison purposes; the hardness value was higher and had a lower standard deviation than for the other sintered materials. Compared to the sintered as-received pond ash (Table 7-4), sintered PA10G and PA30G had the most significant increase in mechanical performance in particular in the flexural and compressive strengths, and these properties started to fall back to similar level as the sintered PA as-received when the additional glass content reached 50wt%. The poorer mechanical property of the glass cullet may also be responsible for the low resulting properties of PA50G. In terms of the best densification, the optimised composition was that with 30wt% waste glass, which also had the best overall mechanical properties out of the four sintered materials without vitrification treatment. Apart from the sintered porosity, which appears to be the key factor in decreasing mechanical strengths, a lower degree of crystallinity also explains the reduction in mechanical performance as typically parent glass is general weaker than its crystallised counterpart mechanically. This is supported by the earlier XRD analysis for the CTE study showing a higher residual glass content in PA50G than the one with lower additional glass. Hence, the mechanical properties were not only affected by the porosity but also by the degree of crystallinity.

Table 7-4: Physical and mechanical properties of coal pond ash based sintered glass-ceramics, compared with relevant values of other materials from the literature

Material Property	Granite [194]	Marble [194]	PA as-rec	PA10G *	PA30G	PA50G	PA glass
Apparent Density (g/cm^3) [1]	2.6-2.9	2.6-2.8	2.55 ±0.07	2.48 ±0.04	2.43 ±0.04	2.24 ±0.02	2.65
Water Uptake (%)	0.2-1.0	0.2-1.0	0.9	0.3	0.1	0.4	0.1
Porosity (%) [1]	0.5-1.5	0.5-2	10±3	6±2	4±2	13±2	1±1
Thermal Expansion Coefficient (10^{-6} /K) [30-600°C] [2]	4.7-9.0	11.0	6.9	7.5	8.0	9.6	7.1
Vickers' Hardness (GPa) [3]	8	4-5	2.7±0.2	6.2±1.7	5.4±0.9	3.3±1.0	6.7±0.1
Young's Modulus (GPa) [4]	43-61	28-84	55±5	62±6	64±2	52±1	82±1
Flexural Strength (MPa) [4]	12-20	10-18	50±3	77±5	85±3	50±2	62±4
Compressive Strength (MPa) [4]	100-250	100-250	240±60	340±90	500±70	290±30	260±40

[1] Average of 3 samples

[2] Single specimens, ~25mm long

[3] Average of 10 indentations

[4] Average of 5 samples

* PAxxG where xx is the glass content in wt%

The last column (PA glass) shows properties of a material sintered from milled amorphous glass derived from the pond ash (i.e. vitrified pond ash); in general, this material possessed no significant superiority over the sintered non-vitrified one (PA as-rec). This further illustrates that it is unnecessary to vitrify this particular waste before sintering.

There are many positives as the study has shown that the coal pond ash does not need to be calcined before sintering. Furthermore, the pond ash based glass-ceramic materials possessed promising mechanical properties that can be utilised in building applications. Compared to natural rocks, such as granite and marble, the sintered pond ash based glass-ceramics have very similar mineralogical compositions as well as competitive, if not superior, mechanical strengths (Table 7-4). Considering the material was fabricated using the powder route, which normally produces inferior products than the conventional melt route, the properties were actually comparable to many other waste-derived glass-ceramics as shown in Chapter 3. Hence, the sintered glass-ceramic material has a realistic potential to be used as a synthetic alternative to these natural materials in the building industry. It was also found that sintering powdered vitrified raw waste (i.e. PA glass in Table 7-4) has no justifiable benefits

since we can obtain the similar, if not superior, properties by sintering the as-received (untreated) waste with a small addition (10-30wt%) of glass cullet. Avoiding vitrification and the need to calcine the material prevents a significant amount of energy being used during the manufacturing process, thus making the development of waste-derived building material more attractive.

7.5 Thermal Shock Resistance

In addition to the determination of the basic mechanical properties, two of the best sintered materials (PA10G and PA30G) were chosen for thermal shock resistance measurement, typically quantified by a critical temperature (ΔT_c), which is determined by measuring the residual bending strength after quenching in water from different temperatures. This property becomes useful if the material is to withstand thermal loading under the chosen working environment. The quenching was achieved at a relatively rapid rate, and since thermal conductivities of materials (glasses and ceramics) investigated are relatively low, the Biot Modulus (β) is high and therefore can be neglected from the derivation of the 'R' parameter. The general expression for R as a measure of thermal shock resistance is as derived originally by Hasselman [195, 196]:

$$R = \Delta T_c = \frac{\sigma_f (1-\nu)}{E\alpha}$$

Equation 7-1

Where; σ_f = fracture stress following thermal shock,
E = Young's modulus,
α = coefficient of linear thermal expansion,
ΔT_c = critical differential temperature,
ν = Poisson's ratio

Note that there is more than one way to determine the thermal shock resistance of a material depending on the material as well as the test condition, please refer to the work by Hasselman. In principle, in order for an engineering material to possess adequate resistance to thermal crack initiation, a high strength, high thermal

conductivity and a low modulus is required. This also means, however, the material will fail dramatically if crack does initiate. On the other hand, in order for a material to be resistant to subsequent thermal cycling, then a high modulus, high fracture toughness and low strength is preferred. Typical SEM images of the transverse cross-sections of quenched bar specimens (of PA30G composition), with the cracks initiated from quenching highlighted in white using a computer drawing package (e.g. Microsoft Paint) are given in Figure 7-11.

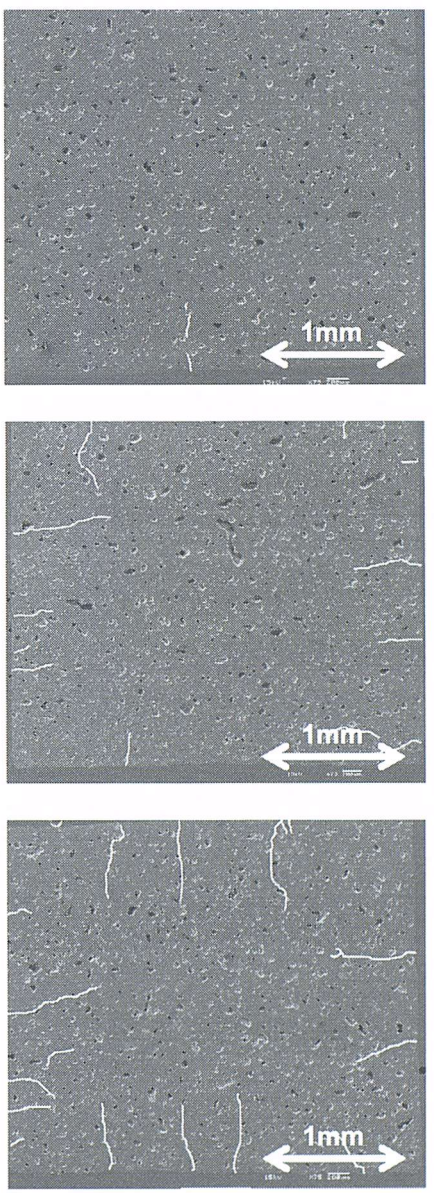


Figure 7-11: PA30G quenched from (top) 200°C; (middle) 340°C; and (bottom) 600°C. Cracks initiated from quenching were highlighted in white using a computer drawing package.

In addition to measuring the residual flexural strength of the quenched bars, theoretical strength values were also calculated based on the average crack length observed from the SEM examination and the following assumptions.

First of all, crack density and average crack length of samples at each quenching temperature were measured and plotted as shown in Figure 7-12 and Figure 7-13, respectively. Note that a large statistical error is expected from the sampling method; however, the general trends are still exemplified by the figures namely that crack density and length increase with increasing temperature.

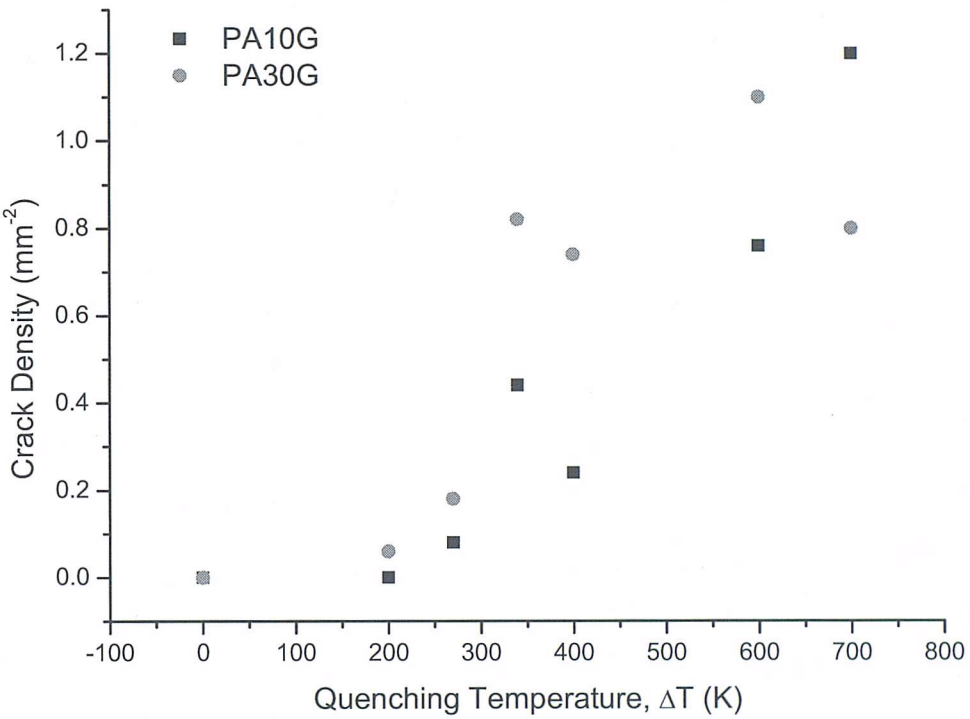


Figure 7-12: Crack density, number of cracks per unit area, versus the quenching temperature

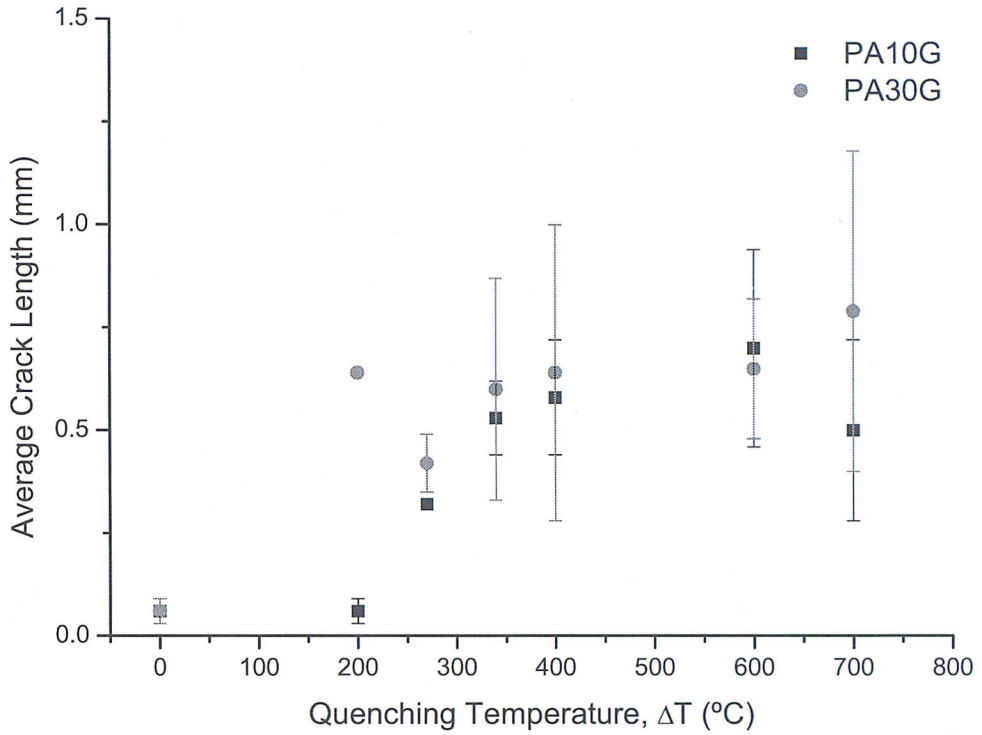


Figure 7-13: Average crack length measured from the cross-section of each quenched bar

Figure 7-14 and Figure 7-15 illustrate the critical temperatures, ΔT_C, for PA10G and PA30G, respectively, at which each material's strength falls dramatically because of the thermal stresses induced by quenching. Experimental ΔT_C (read from the line plot) for PA10G was about 250-300K and for PA30G was about 50K lower. Given that the both materials have very similar mechanical strength and modulus, this small difference in the critical temperature can be supported by the slightly higher thermal expansion coefficient of PA30G, which is one of the factors that influence ΔT_C (equivalent to the R parameter, see Equation 7-1).

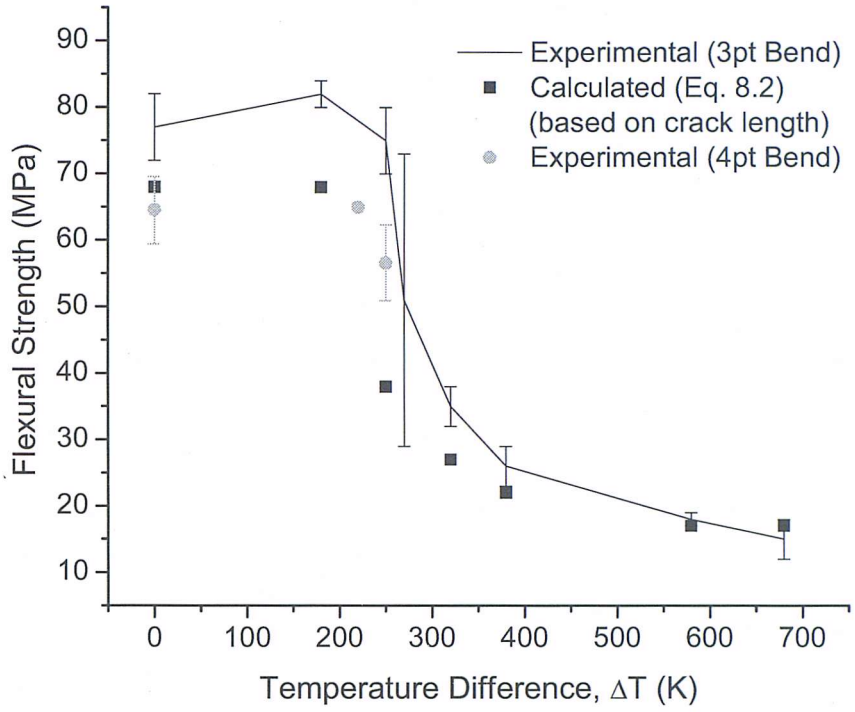


Figure 7-14: Critical thermal shock resistance temperature for glass-ceramic PA10G

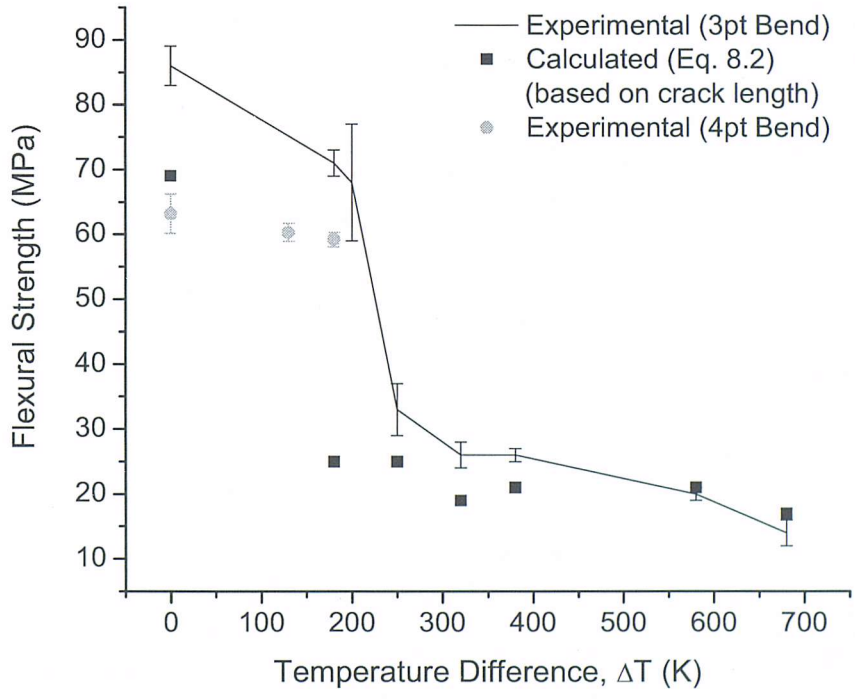


Figure 7-15: Critical thermal shock resistance temperature for glass-ceramic PA30G

Assuming that the average crack length is the critical failure factor, it is substituted into the following equation along with the measured K_{IC} for calculating flexural strengths:

$$\sigma = \frac{K_{IC}}{\sqrt{2\pi r}}$$

Equation 7-2

Where 'r' is the measured crack length, 'σ' is the calculated critical flexural strength, and K_{IC} is the fracture toughness of the material. Note that the calculated residual flexural strengths, as shown in Figure 7-14 and Figure 7-15, indicate that the onset of strength reduction (i.e. the critical temperature) is sooner (i.e. at lower temperature) than the experimental. This may be explained by the argument that the calculated results are only based on crack length, whereas crack density contributes to the failure of the material as well.

When the data of calculated residual strengths (black solid squares) was compared with the experimental data obtained from 3-point bend test, both Figure 7-14 and Figure 7-15 showed the mathematical based result indicate the critical temperature is about 25-50K lower than the experimental value. This is believed to have been caused by the type of testing used, i.e. 3-point bending, in which the effect of critical crack length will be particularly apparent. The geometry for a typical 3-point bending test, the force is more concentrated like a point load, whereas in a 4-point bend test the load is distributed across the volume of the sample more. Therefore, the crack length can be taken into account as well as its density across the test specimen will be taken into account. It was expected that a 4-point bend test result will match the trend of the calculated values.

Unfortunately, Figure 7-14 and Figure 7-15 have both shown that the 4-point bending test result did not follow the mathematical data. The slight reduction in the strength values were within range of the typical ratio between 3-point and 4-point bend test values. Nevertheless, these materials have shown their ability to withstand at least one thermal fluctuation within 200°C without significant reduction in strength.

7.6 Chemical Resistance

To ensure the public's acceptance of a waste-derived material, it is important to be able to specify the endurance of the product under certain environments. In this particular project, it was chosen to examine the level of chemical resistance of the material in extreme environments, and thus, if it passed the test, there would be no risk when using the material under typical, milder, service environments. A leaching test was conducted on the sintered pond ash with 30wt% glass addition (PA30G) material according to the same experimental procedure as reported by Laurent Gruner when the slag-based glass-ceramic 'Silceram' was investigated [188]. Three different solutions were used in the test: 1N HCl, 1N NaOH, and distilled water. The test involved the immersion of these specimens in different solutions for 15 hours at 50°C. Each specimen had dimensions of ~45×6×8mm^3. The weight loss per unit exposed area for each leaching condition was as follows: 0.31 mg/cm^2 in 1N HCl, 0.04 mg/cm^2 in 1N NaOH, and < 0.01 mg/cm^2 in distilled water. It was concluded that PA30G is more prone to attack in acid than neutral or alkali solutions. In other work [40, 197], chemical resistance tests on waste-derived glass-ceramics also indicated more corrosion in HCl solutions than in NaOH. Note the test conditions in the work by Cheng et al [197] were much more severe than the work done here. However, relative comparisons do show that the material was more prone to corrosion in acidic solutions.

Table 7-5: Percentage weight loss of gehlenite based glass-ceramics after exposing to acid and alkali solutions

Leaching Solution	**Powder** [197]	**Melt** [197]
	850°C	850°C
20wt% HCl (12N)	19.0	16.9
20wt% NaOH (12N)	<0.1	0.2

In the present work, wollastonite crystals, which are soluble in HCl, were responsible for the poorer chemical resistance whereas the feldspar and the residual glass matrix (i.e. <10% residual glass) were less prone to the acid attack.

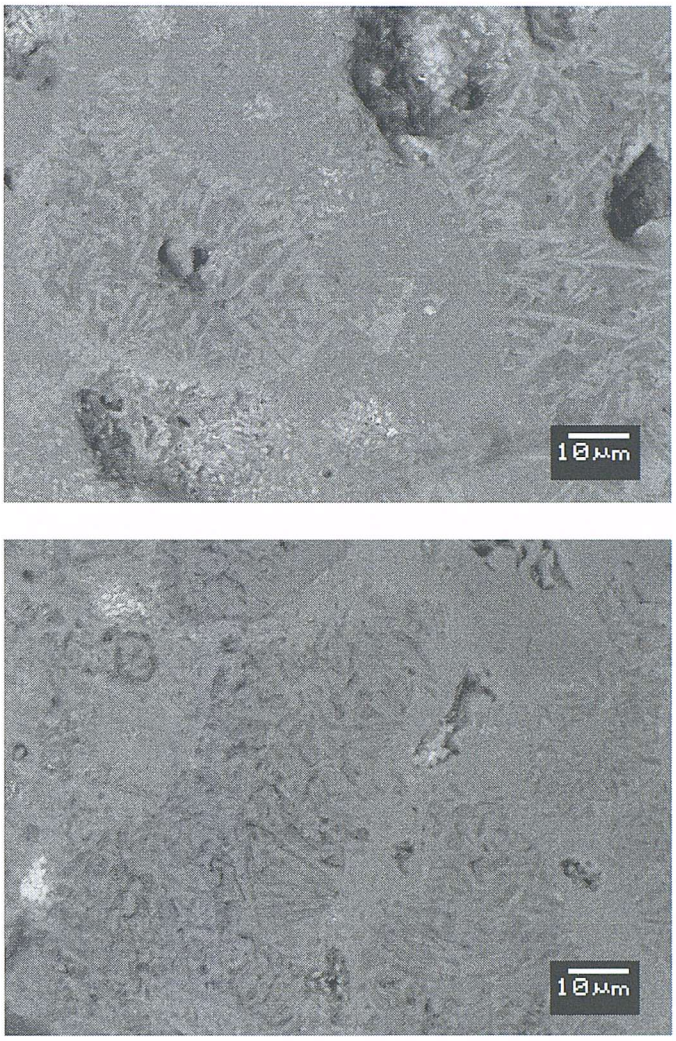


Figure 7-16: Secondary electron micrographs illustrating the corrosion of wollastonite crystals present in the sintered PA30G material; (top) before leaching, (bottom) after leaching.

7.7 Conclusion

It has been demonstrated that as-received coal pond ash with or without additional glass cullet can be economically processed into mechanically sound products by the commonly used powder sintering technique, providing an alternative solution to the disposal of coal ash. By controlling the composition of the starting waste mixture, it is possible to produce sintered glass-ceramic material with relatively high density, competitive mechanical strengths and good chemical resistance for building applications where pure and natural materials are currently being used.

Chapter 8 Dense Slag-based Glass-Ceramics via Melting Route

Finding uses for metallurgical slag is an important issue for the steel industry from both an economic and environmental point of view. Millions of tonnes of slag are produced around the world, so its disposal in special dumpsites is costly and it is not a sustainable solution for the environment. SteelServ Limited (New Zealand), who supplied the slag material for this research work, co-operates with the steel mill in Glenbrook, New Zealand, on management of solid wastes from the mill. One of the by-products of New Zealand's steel manufacturing industry, iron-making melter slag, is unique with regards to its composition (>30wt% TiO_2 by chemical analysis) when compared with blast furnace slags from the rest of the world. Instead of iron ore, black ironsands from the west coast of New Zealand's North Island is used as the starting material for the local iron and steel industry. The iron slag is formed by fusion of limestone, ash and other fluxes added to the original ironsand that contains mainly titanomagnetite. Even though slag is not a waste of serious concern in New Zealand at present, a significant amount of effort is being made to establish alternative solutions to utilise such a waste instead of relying on conventional landfill disposals. This study is driven by the need to highlight practical use of slag in glass-ceramic production and, from the scientific point of view, to study a slag of such a unique composition.

Conventionally, a nucleating agent is added to the glass composition for nucleation of crystals within the bulk material to occur efficiently, resulting in a large number of micro or nano-sized crystals. However, through the rich, natural presence of TiO_2 in the slag investigated here, it is hoped that a fine-grained microstructure can be obtained, and a high-strength glass-ceramic can be consequently produced without additional nucleating agents. This chapter delves into the microstructural analysis of the waste-derived glass-ceramic material (60wt% slag and 40wt% glass cullet) as well as a detailed investigation of its physical and mechanical properties.

8.1 Preparation of Precursor Glass

An initial melting experiment, conducted at 1480°C in a platinum crucible, showed the need for additives to reduce the melting temperature of melter slag (MS) and thus improve glass formation at this temperature level. Figure 8-1 illustrates the partial crystallinity (presence of a spinel and a pseudobrookite phase) of the quenched MS material. To make the process more commercially viable, the melting point has to be lowered so the process is more economical and suitable for the refractory materials used in the glass-making industry.

Based on the results in Section 6.5.3, 40wt% waste glass was added as a source of SiO_2 and fluxing agent such as Na_2O. MS40G (Melter Slag with 40wt% Glass) was used to produce a dark-amber coloured glass by melting at 1450°C. Visual observations have indicated severe corrosion of the zirconia crucibles by the molten glass and XRD analysis (Figure 8-2) has also indicated zirconia contamination after melting. In contrast with mullite and alumina crucibles, there was only minor corrosion but the as-cast material was of the same amber colour. Therefore, for subsequent melting experiments, large high-purity alumina crucibles were used. The glass was fully x-ray amorphous as Figure 8-2(b) demonstrates. Note that in large scale production, the less expensive ceramic crucible, such as alumina and mullite crucibles, could still be used as the contamination will be even less significant because the relative area of crucible exposed to the corrosive molten slag glass will be less comparing to the amount of molten material, i.e. area/volume ratio is reduced with increasing crucible size.

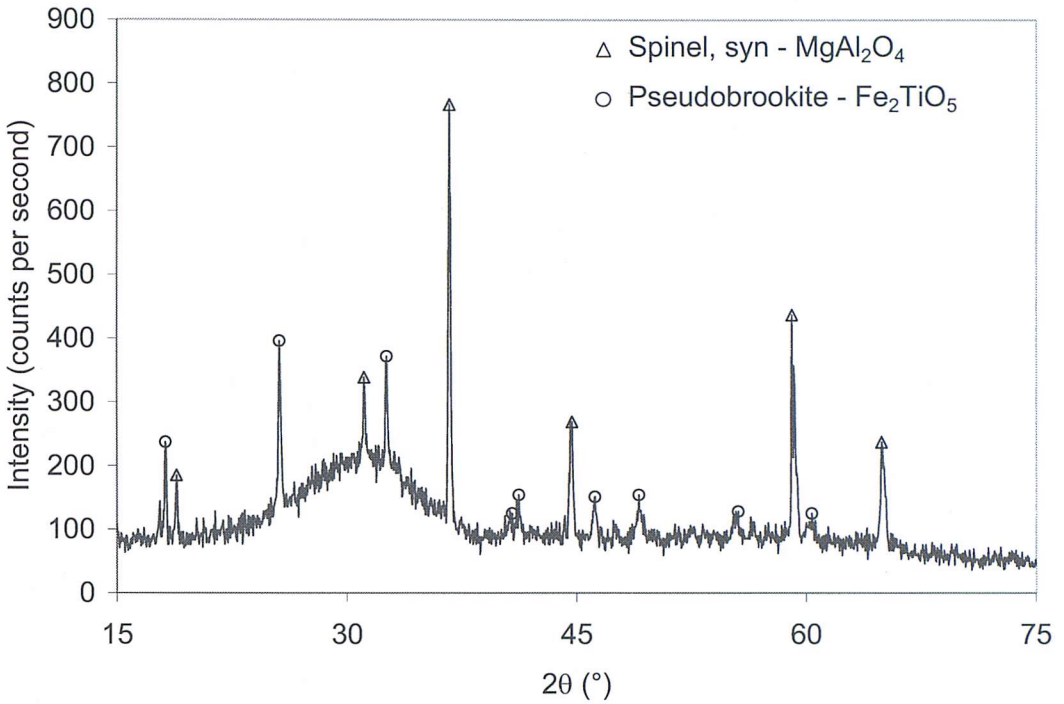


Figure 8-1: XRD patterns of the as-quenched melter slag after melting at 1480°C.

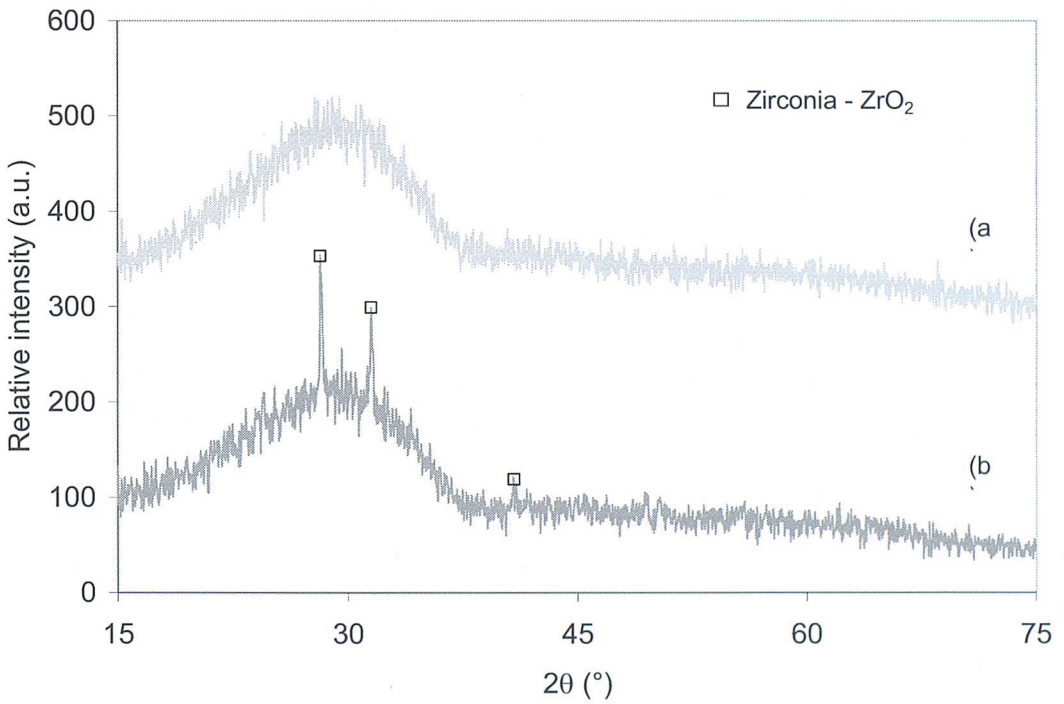


Figure 8-2: XRD patterns of MS40G as-quenched glass after melting at 1450°C in (a) alumina and (b) zirconia crucibles

Table 8-1 illustrates a compositional comparison between a typical blast furnace slag (from Brazil) against the unusual TiO_2-rich melter slag from New Zealand. The last three columns show the compositions between Silceram [41] and the slag-based glass-ceramic produced in this study. This was calculated using the rule of mixture principle, i.e. the theoretical chemical composition is the product MS40G (60wt%MS-40wt%G) was calculated by adding 60 parts of the oxides in melter slag (MS) to 40 parts of the oxides in glass cullet (G) [for SiO_2, $12.1\times0.6+72.7\times0.4 = 36.3$]. The theoretical composition was confirmed by comparing against energy dispersive X-ray analysis (EDAX).

Table 8-1: Chemical composition of waste materials and slag-based glass-ceramics

Raw Materials	**Blast furnace slag [198]**	**Iron-making melter slag (MS)**	**Waste bottle glass cullet (G)**	**Typical Silceram [41]**	**Slag with 40wt% glass cullet (MS40G)**	
					Theoretical	EDAX
SiO_2	35.8	12.1	72.7	48.3	36.3	32.3
Al_2O_3	11.8	17.6	1.6	13.3	11.2	11.2
Fe_2O_3	0.3	4.1	0.3	4.0	2.6	3.4
CaO	43.5	14.5	11.0	24.7	13.1	15.8
MgO	6.2	13.6	0.5	5.7	8.4	9.2
MnO	0.7	1.1	0.01	0.4	0.7	-
TiO_2	0.8	34.3	0.04	0.6	20.6	21.0
Cr_2O_3	-	-	-	0.8	-	-
K_2O	-	-	0.36	1.1	-	-
V_2O_3	-	0.2	-	-	0.1	-
Na_2O	0.1	-	13.0	1.2	6.0	7.2

Crushed waste bottle glass, of soda-lime silica composition, was used as additive to lower the melting temperature of the iron-making slag. The uniqueness of the glass-ceramic material in this study (now referred as MS40G) was the high percentage of TiO_2 as shown in Table 8-1. Energy dispersive X-ray analysis (EDAX) confirmed the chemical composition of MS40G as similar to the calculated composition from the proportion of the raw components. Some of the minor elements that were undetectable by EDAX are missing in the table. Preliminary experimental results showed that 40wt% of glass cullet was an appropriate amount to be added to the as-received slag for producing a stable amorphous material. The as-received slag was mixed with the glass and milled for 5 minutes to reduce the overall particle size for ease of melting. Part of the as-cast glass was crushed into coarse (> 2 mm) particles and some of these were then milled into fine powder (< 50 μm). Both coarse and fine particles were examined by thermal analysis.

8.2 Thermal Analysis

Powder samples of different specific area (different particle size) were studied by DTA to determine the nature of crystallisation mechanism. Figure 8-3 shows the DTA curves for finely (< 50 μm) powdered and coarse (> 2 mm) particles (termed 'bulk' in Figure 8-3).

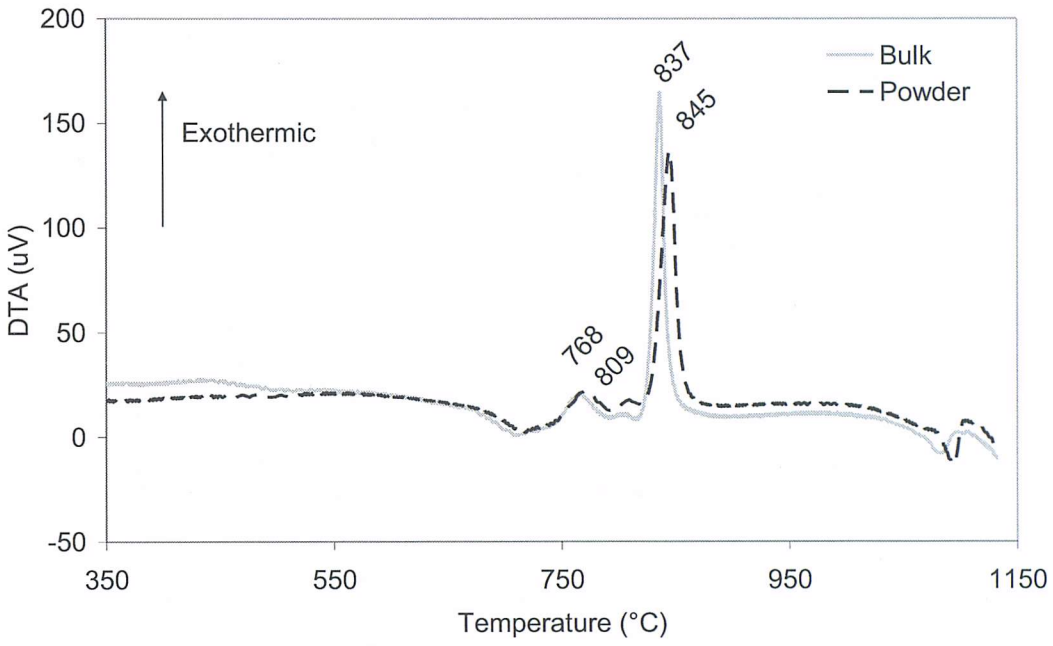


Figure 8-3: Combined DTA plot of MS40G glass in bulk and powder form, each sample weighed about 35mg.

The curves for both samples were similar indicating that the specific area of the sample was not significantly affecting any of the reactions. The first transition was an endothermic trough approaching 700°C, which is associated with the glass transition temperature. The next visible transition was two minor exothermic peaks (at around 770°C and 810°C) followed by a major peak at about 840°C corresponding to the main crystallisation process. No further exothermic transitions were visible at higher temperatures, suggesting that the glass can be converted into a glass-ceramic at a relatively low temperature. Finally, an endothermic reaction at ~1070°C, which was originally presumed to be the melting of the glass, but in fact may have been the dissolution of a particular crystalline phase since the resulting sample did not melt.

XRD was subsequently used to confirm the findings (see section 9.3). It was observed that all crystallisation peaks have shifted slightly towards lower temperature with decreasing specific surface area, i.e. larger particles. This suggests that the preferred crystallisation mechanism is volume crystallization. Figure 8-4 shows three DTA curves terminated at the end of each exothermic peak and illustrates the good reproducibility of the thermal analysis data, and Figure 8-5 shows the corresponding XRD plots of samples heat-treated at the temperature of each peak, indicating the crystalline phase(s) present at each stage.

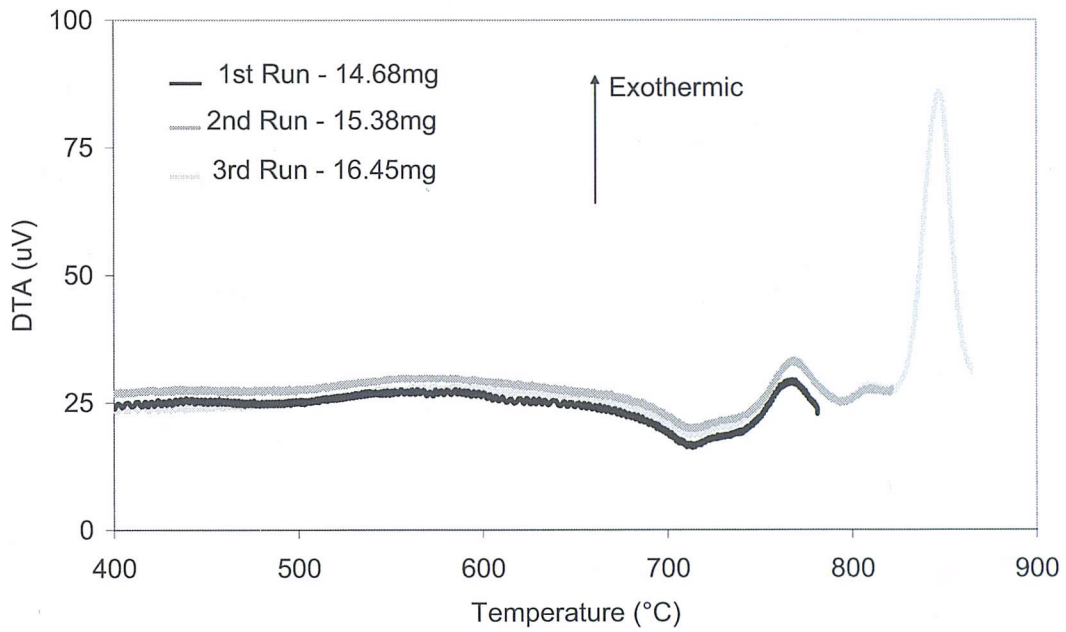


Figure 8-4: DTA plots showing consistency over 3 individual runs of powder samples each weighed about 15mg

Examining Figure 8-5, it is clear that there was negligible amount of crystallisation occurring at the temperatures where the first two exothermic peaks were observed, and it is difficult to identify which phases were present. However, at the end of the last exothermic reaction (~865°C), the XRD plot clearly indicates the presence of nepheline ($NaAlSiO_4$) and diopside ($Ca(Mg,Al)(Si,Al)_2O_8$) from the pyroxene group. Extensive XRD analysis, in particular, high-temperature XRD was carried out to determine how each crystalline phase evolves with temperature and during prolonged heat-treatments, as shown next.

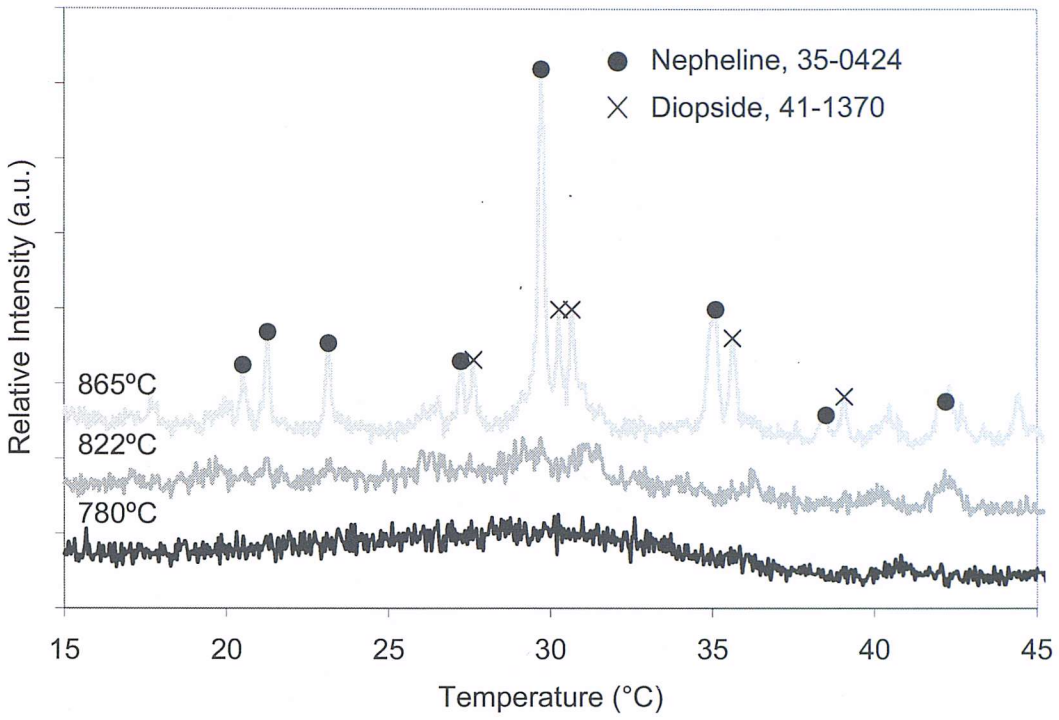


Figure 8-5: Corresponding XRD patterns (bottom to top) to the DTA peaks of results from previous figure (left to right)

Based on the DTA results, the rest of the as-cast glass was heat-treated at temperatures of 900°C and 1100°C for 2h before being cut into test bars, for mechanical testing, of 30x4x3mm^3 with a Struers Accutom apparatus equipped with a high-speed diamond wheel.

8.3 X-Ray Diffraction and Microstructural Analysis

XRD analysis (Figure 8-6) suggests that the first crystalline phases to precipitate were of the pyroxene series. Both nepheline and diopside were among the detectable phases at the lower heat-treatment temperatures, which is in agreement with X-ray results from the thermal analysis samples. At 900°C, calcium titanate (perovskite, $CaTiO_3$) began to precipitate in increasing amount with increasing heat-treatment temperature. The most dramatic change occurred at 1100°C, where the relative amount of pyroxene crystals dropped dramatically. This may account for the endothermic reaction at 1070°C shown in the DTA plot (Figure 8-3), i.e. the final endothermic transition was caused by the dissolution of pyroxene crystals rather than melting of the material. Meanwhile, another titanium-rich phase, armalcolite

($FeMgTi_4O_{10}$), formed and became the main crystalline phase in the material at temperatures over 1000°C although there was no evidence of this reaction in the DTA data. It has to be noted that there will always be discrepancies between the crystallisation temperature found using DTA and temperatures reported from furnace treatment work as a normal muffle furnace have a greater volume and therefore larger temperature gradient across the chamber.

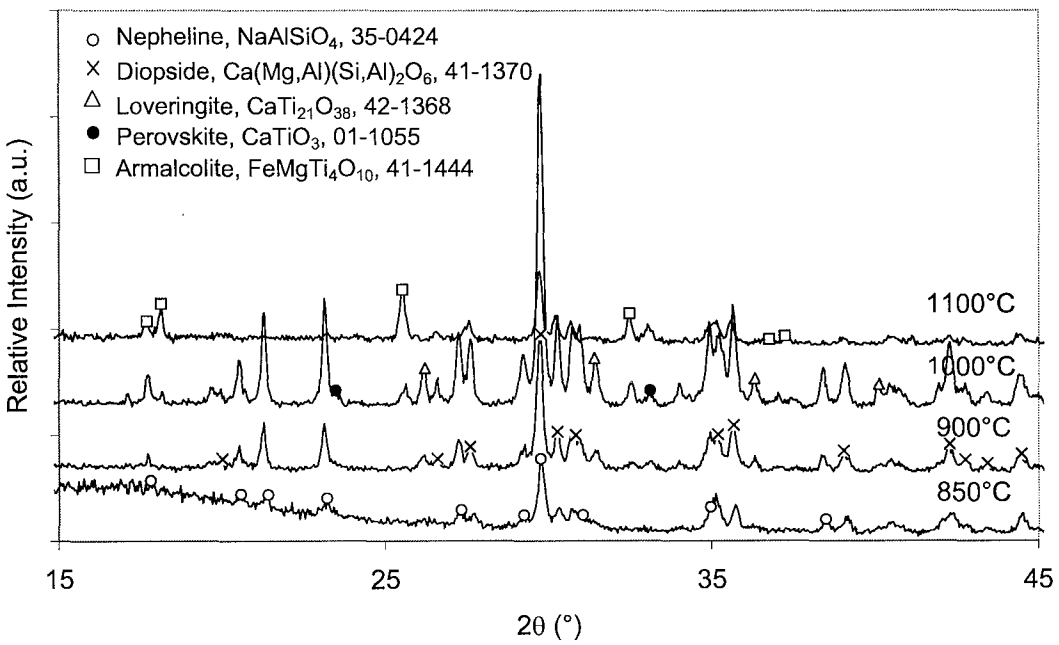


Figure 8-6: XRD pattern of powdered samples from bulk specimens heat-treated at 850, 900, 1000, 1100°C for 2h. ▲perovskite ■ armalcolite ○ nepheline × diopside ◊ loveringite

The sequence of crystalline phase evolution with increasing temperature originally derived from the standard XRD analysis is well supported by HT-XRD analysis, as shown in Figure 8-7. It should be noted that the set temperature of the HT-XRD furnace, which are the temperatures quoted in Figure 8-7, can be 100-150°C lower than the actual temperature of the specimen. This is a direct result of the temperature gradient in the furnace. The thermocouple for the furnace (for set temperature) is underneath the heater whereas the thermocouple for the sample (for actual temperature) is hung on top of the sample, a small thermal gradient is expected. Taking this into account, it was seen that the precipitation of Ti-rich phases, such as armalcolite and perovskite, do not occur until temperatures of around 900-950°C

(actual temperature), which agrees with the results from standard XRD analysis (Figure 8-6).

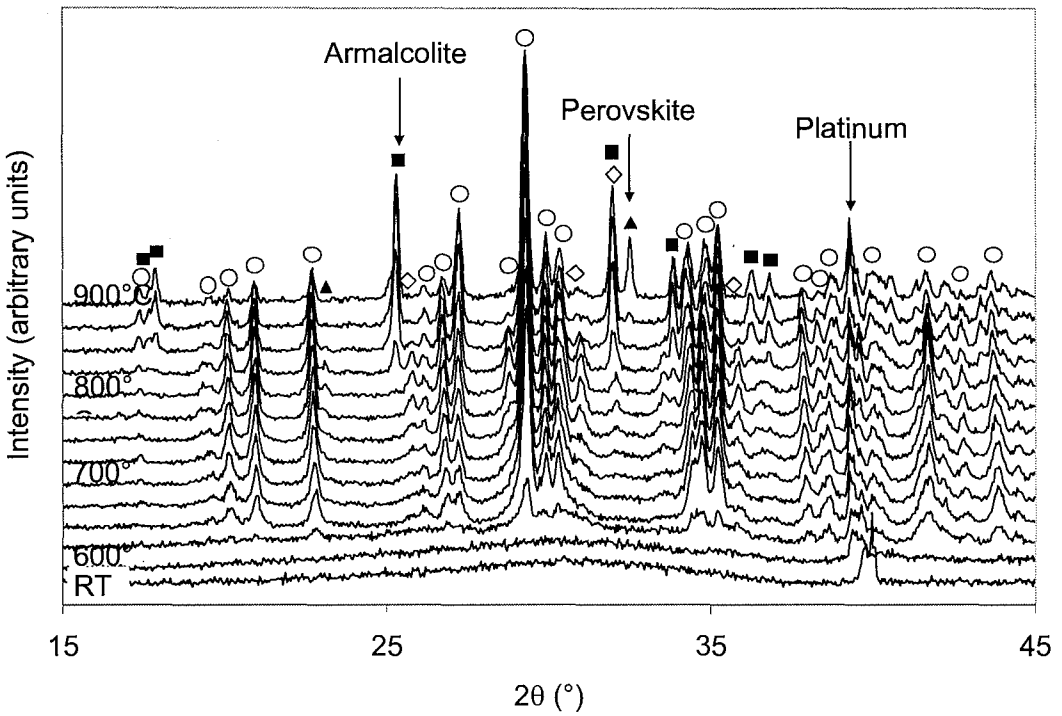


Figure 8-7: HT-XRD of MS40G showing the precipitation and dissolution of ▲perovskite ■ armalcolite ○ pyroxene (nepheline and diopside) and ◊ loveringite

SEM micrographs of relevant glass-ceramic microstructures are shown in Figure 8-8. Figure 8-8(a) shows an etched surface of the annealed MS40G at 900°C. The dark voids are the residual glass phase that was removed during etching. However, the two crystalline phases (nepheline and diopside), which were detected by XRD, cannot be differentiated under SEM. A significant amount of titanium-rich phases (perovskite and armalcolite) were visible as brighter phases when the glass-ceramic material was annealed at temperatures above 1000°C. The image in Figure 8-8(b) corresponds to the material that was annealed at 1100°C; the microstructure consists of clusters of irregular shaped calcium titanate (perovskite) crystals distributed throughout the multiphase matrix (pyroxene, titanium-rich armalcolite and residual glass). The multiphase matrix is shown in detail in Figure 8-8(c) and (d), where the most noticeable feature is the light-coloured acicular armalcolite crystals embedded in the original pyroxene-and-glass matrix.

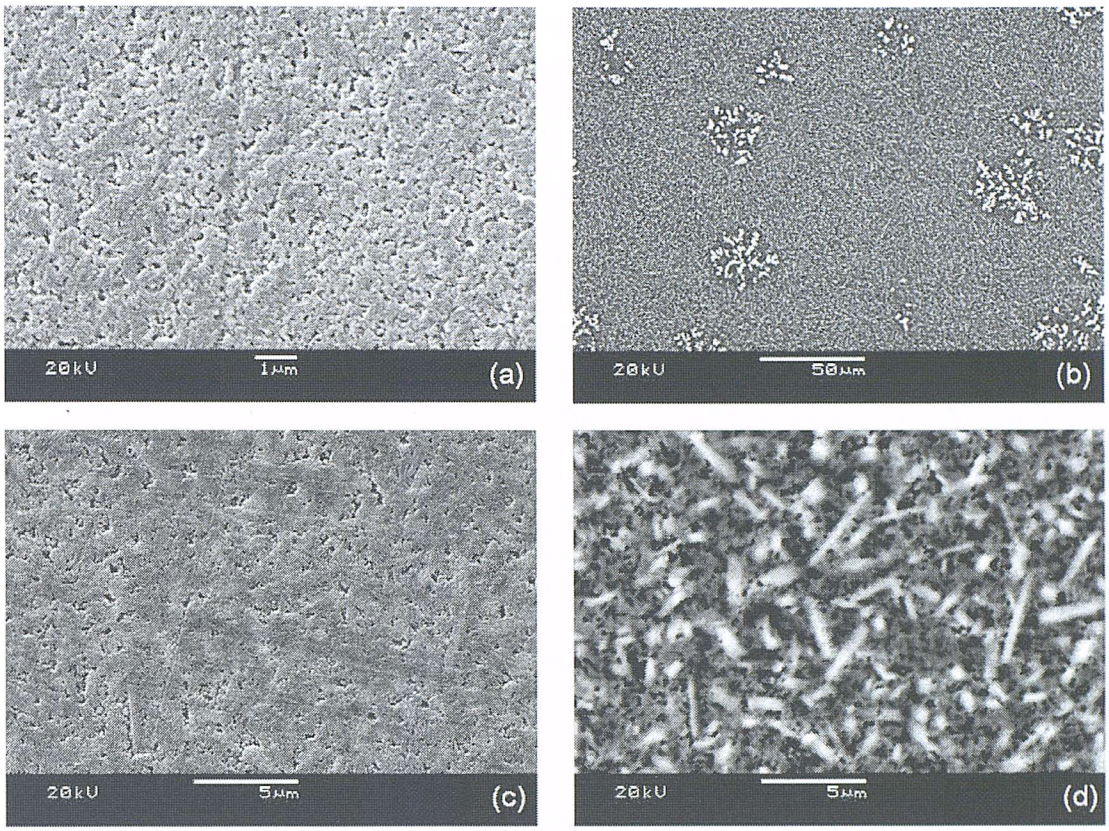


Figure 8-8: SEM images of (a) MS40G heat-treated at 900°C for 2h; (b) MS40G annealed at 1100°C for 2h; (c) and (d) magnified area of the matrix under secondary electron and back-scattered electron modes, respectively

8.4 Coefficient of Linear Thermal Expansion

The polycrystalline form resulting from the heat treatment of a parent glass usually has a lower coefficient of thermal expansion (CTE) than the amorphous parent glass. However, this is not always the case in this work as discussed below.

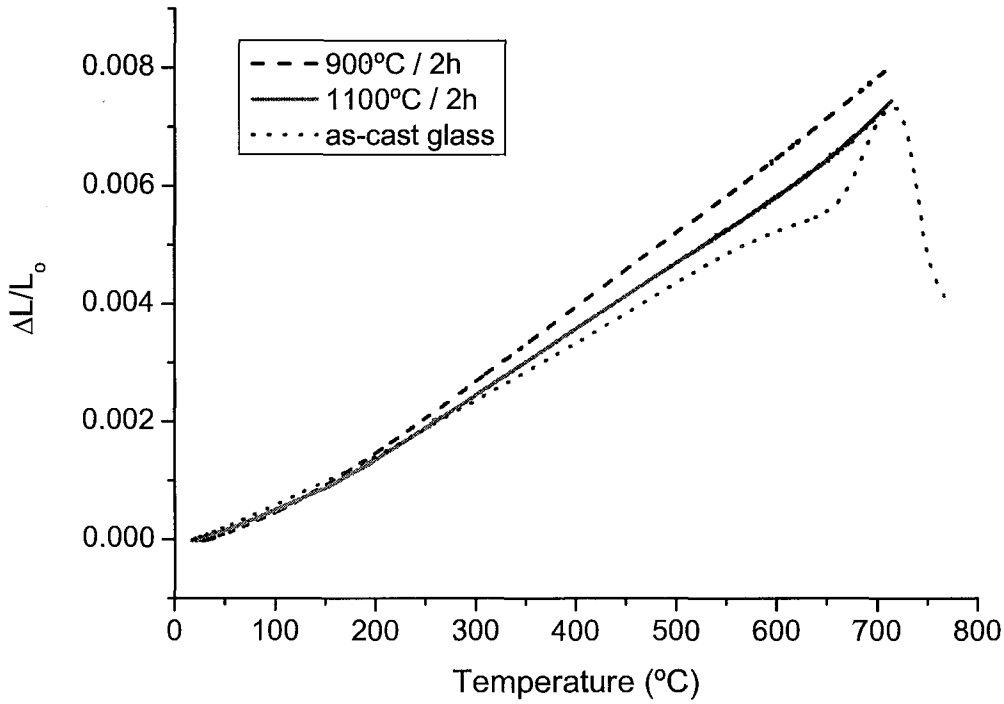


Figure 8-9: Linear thermal expansion (change in length versus temperature) of MS40G samples in the form of as-cast glass, glass-ceramics heat-treated at 900°C and 1100°C (L_o = ~25mm).

Figure 8-9 illustrates the CTE of each material represented by the slope of each plot. It was concluded that the as-cast glass has a lower CTE than both of its polycrystalline glass-ceramics. It was shown that the glass material began to soften and thus resulting in a negative change in length beyond its glass transition temperature around 700°C (Figure 8-9). This is a classic behaviour of the amorphous material, as-cast glass, at its T_g glass transition temperature (which is supported by the DTA results).

The variation in CTEs between different samples can be explained by their phase compositions. Results from both phase identification using XRD and microstructural analysis using SEM have confirmed that after a heat-treatment at 900°C, the only crystalline phases present in the MS40G sample were diopside and nepheline, both of which have high linear CTEs, 10.4×10^{-6} °C^{-1} and 16.9×10^{-6} °C^{-1}, respectively [199]. Hence, it explains the significant increase in CTE when the parent glass (CTE = 9.11×10^{-6} °C^{-1}, 30-500°C) was heat-treated at 900°C. In the case of MS40G glass heat-treated at 1100°C, the slight reduction in CTE was due to the high heat-treatment

temperature, at which the pyroxene crystals dissolved to negligible amounts and therefore no longer detectable by XRD. There were two new phases formed at the same temperature, armalcolite and perovskite, with residual glass as the matrix. However, both Ti-rich phases have lower linear CTEs than nepheline. The combination of lower CTEs of residual glass and Ti-rich phases contributes to the lower overall CTE of MS40G glass-ceramics heat-treated at 1100°C than the 900°C.

Table 8-2: Typical linear CTE values of individual crystalline phases present in the investigated materials

Crystalline Phase [30-500°C]	**Linear CTE ($\times 10^{-6}$ °C^{-1})**
Constituent Phases	
Diopside [191]	10.4
Nepheline [199]	16.9
Perovskite [200]	12.6
Armalcolite [201]	9.0
Glass-Ceramics	
Silceram, [30-400°C] [15, 41]	7.5
MS40G as-cast	9.1
MS40G 900°C/2h	10.8
MS40G 1100°C/2h	9.7

8.5 Mechanical Properties

A range of experiments, including 3-point bending test, Vickers' hardness indentation, and compression strength test were conducted to determine mechanical properties of the resulting glass-ceramics. The results for the as-cast glass and glass-ceramics heat-treated at 900°C and 1100°C, each for 2 hours, are given in Table 8-3. In general, this glass-ceramic material possessed a high hardness compared to many other waste-derived glass-ceramics fabricated using the melting routes [37, 60, 87, 198] (see Table 3-2) including those derived from slag, coal ash and incinerator ash.

Crystallisation yielded a material with better mechanical properties than the parent glass. The increase in heat-treatment temperature, which resulted in the precipitation of titanium-rich phases, also had a positive effect on the room-temperature mechanical properties of the glass-ceramic material, except for the hardness. As mentioned above, XRD analysis showed the reduction in the relative ratio between pyroxene and titanium-rich phases (Figure 8-6) as well as a reduction in the relative amount of amorphous halo against crystalline phases, indicating a lower degree of

crystallinity in the material heat-treated at 1100°C than the one heat-treated at 900°C. Therefore the higher presence of residual glass phase, which has a lower density and lower hardness value, explains the reduction in the apparent density and hardness of the sample heat-treated at 1100°C than the one heat-treated at 900°C.

The slight improvement in the indentation fracture toughness of the glass-ceramic material is thought to be caused by presence of one of the titanium-rich crystals, armalcolite, which has a high aspect ratio (see Figure 8-8(d)). A polycrystalline multiphase material is generally toughened by crack bridging and crack deflection, and both of these mechanisms are enhanced as the aspect ratio of the secondary crystals in the matrix increases (in this case, the acicular iron titanate [202]. A crack will therefore either deflect away from these crystals in order to propagate further or the crystals are helping to restrict the crack propagation by bridging in the crack path, both of which act as toughening mechanisms. Fracture toughness determined using chevron notched beams are discussed in detail in the following section.

Table 8-3: Effect of heat-treatment on the properties of MS40G glass and glass-ceramics (properties of 'Silceram' are given for comparison purposes

Material Property	**Unit**	**Heat-treatment**			**Silceram [15, 41]**
		As-cast	900/2h	1100/2h	
Density [3]	g/cm^3	2.93	3.20	3.05	2.9
Thermal Expansion Coefficient [30-500°C] [1]	$10^{-6}/K$	9.11	10.82	9.67	7.5 [30-400°C]
Vickers' Hardness [10]	GPa	6.5±0.1	9.1±0.2	7.8±0.2	6.8
Indentation Toughness [10]	$MPa.m^{-1/2}$	0.9±0.1	1.0±0.1	1.6±0.2	-
Fracture Toughness (CNB)	$MPa.m^{-1/2}$	-	-	1.4±0.1	2.1
Young's Modulus [5]	GPa	104±7	125±4	121±3	130
Flexural Strength [5]	MPa	100±10	130±40	180±30	180
Compressive Strength [3]	MPa	-	500±100	700±100	850

[1] Average of 10 samples; [2] Average of 5 samples; [3] Average of 3 samples

Overall, the present samples exhibited competitive mechanical properties in comparison with other glass-ceramics produced from silicate waste, as summarised in Table 3-2 and Table 8-3. For technical applications, however, other technological properties need to be assessed, which include thermal shock resistance, high

temperature performance, wear resistance, impact resistance and chemical resistance. Most of the properties were assessed and will be discussed in the following sections.

8.5.1 Fracture Toughness at Elevated Temperatures

Figure 8-10(a) shows the room temperature fracture surface of a sample of MS40G heat-treated at 1100°C. Unlike fracture surfaces of a brittle glass material, the fracture surface of the MS40G glass-ceramic was much more rugged. Further microscopic examination on a polished surface of cracks initiated from Vickers' hardness indentation (Figure 8-10 (b)) confirms significant crack deflection which is consistent with the rugged fracture surface.

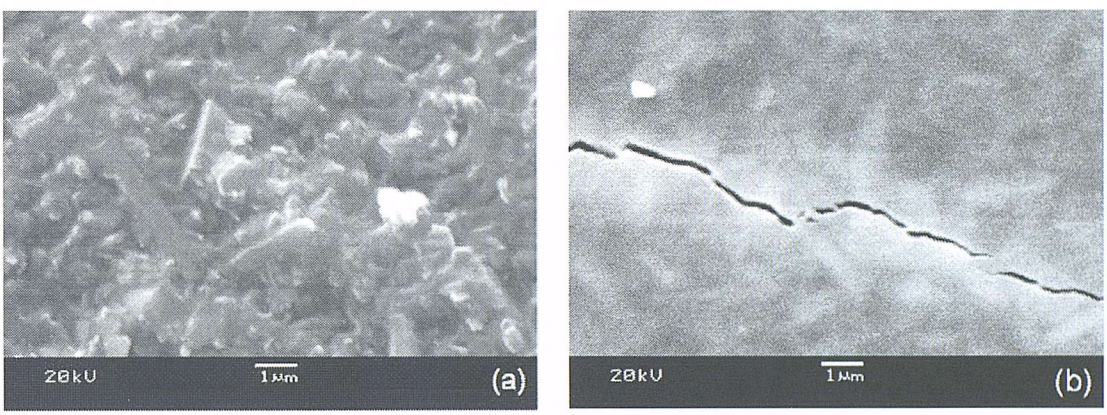


Figure 8-10: Micrographs showing (a) fracture surface of MS40G glass-ceramic annealed 1100°C for 2h; (b) microscopic crack deflection across the material.

The fracture toughness behaviour of the glass-ceramic material (annealed at 1100°C) was further examined at elevated temperatures by determining K_{IC} using Chevron-notched specimen technique [185]. Tests were firstly carried out at room temperature and at 500°C. K_{IC} slightly decreased with increasing temperature up to 500°C (Figure 8-11). There was an acceptable scatter of data from all measurement and the mean values were 1.35±0.12 $MPam^{1/2}$ at room temperature falling to 1.13±0.20 $MPam^{1/2}$ at 500°C.

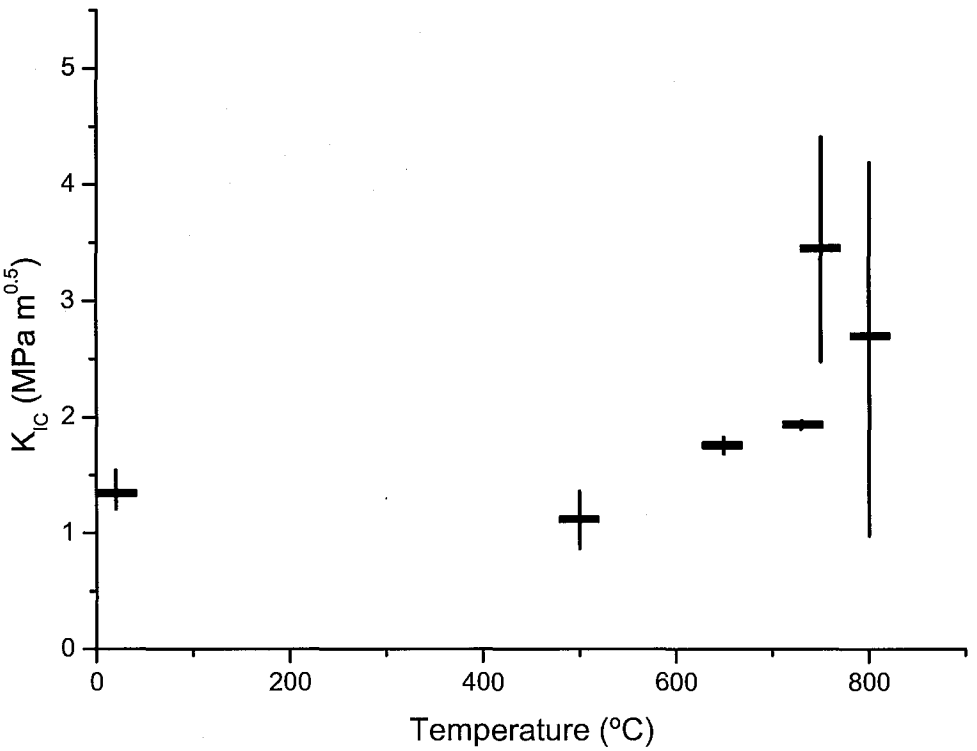


Figure 8-11: Summary plot of fracture toughness values of MS40G glass-ceramics heat-treated at 1100°C for 2 hours with testing temperature, showing the range from the minimum to the maximum of each dataset as vertical lines, and the mean K_{IC} values as the solid horizontal lines

A standard Student's t-test was carried out on the two datasets with the hypothesis that the data ranges overlap by chance. The result, however, showed that the probability of the difference in the fracture toughness values between room temperature and 500°C was due to chance was low (0.056), therefore the hypothesis was rejected. The decrease in fracture toughness was surprising as it is unlikely that the elastic modulus decreases significantly over that temperature range. An earlier study on a monolithic lithium aluminosilicate (LAS) glass-ceramic by Brennan and Prewo [203] has shown that the elastic modulus has minimal reduction and the fracture toughness of the material remained constant from room temperature to 800°C. Figure 8-12 shows a typical load-displacement trace of a Chevron notched specimen tested by 3-point bending. In the case of high temperature tests, a very sharp trace can be seen. This is associated with poorer function of the Chevron notch tip (higher accommodation of elastic energy in the system of specimen and machine). However, there is still some small departure from the linearity showing that crack initiation

occurred before reaching the maximum load and data obtained from these records have been taken as valid. In comparison against the room temperature (RT) test results, the slope for RT specimens was steeper and thus indicating higher stiffness as expected.

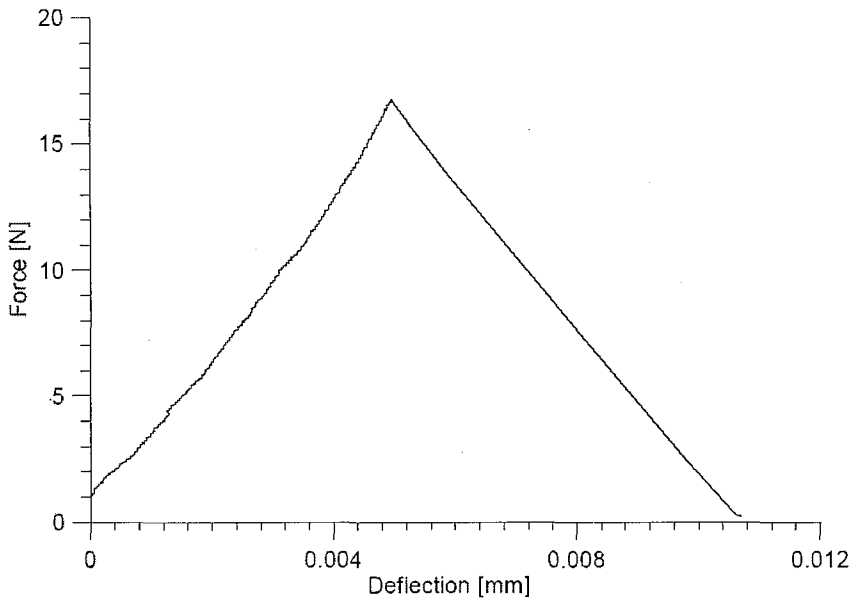


Figure 8-12: A typical force-displacement plot of high temperature (500°C) 3-point bending test with Chevron notched MS40G glass-ceramic bars.

Samples were also tested at temperatures close to the glass transition temperature (650°C and 730°C). There was an increase of fracture toughness when the test temperature was higher than 500°C. This phenomenon was observed for the fracture strength measurements of Brennan and Prewo [203], however, the fracture toughness of their LAS monolithic glass-ceramic material did not follow the same trend but remained constant up to 1000°C.

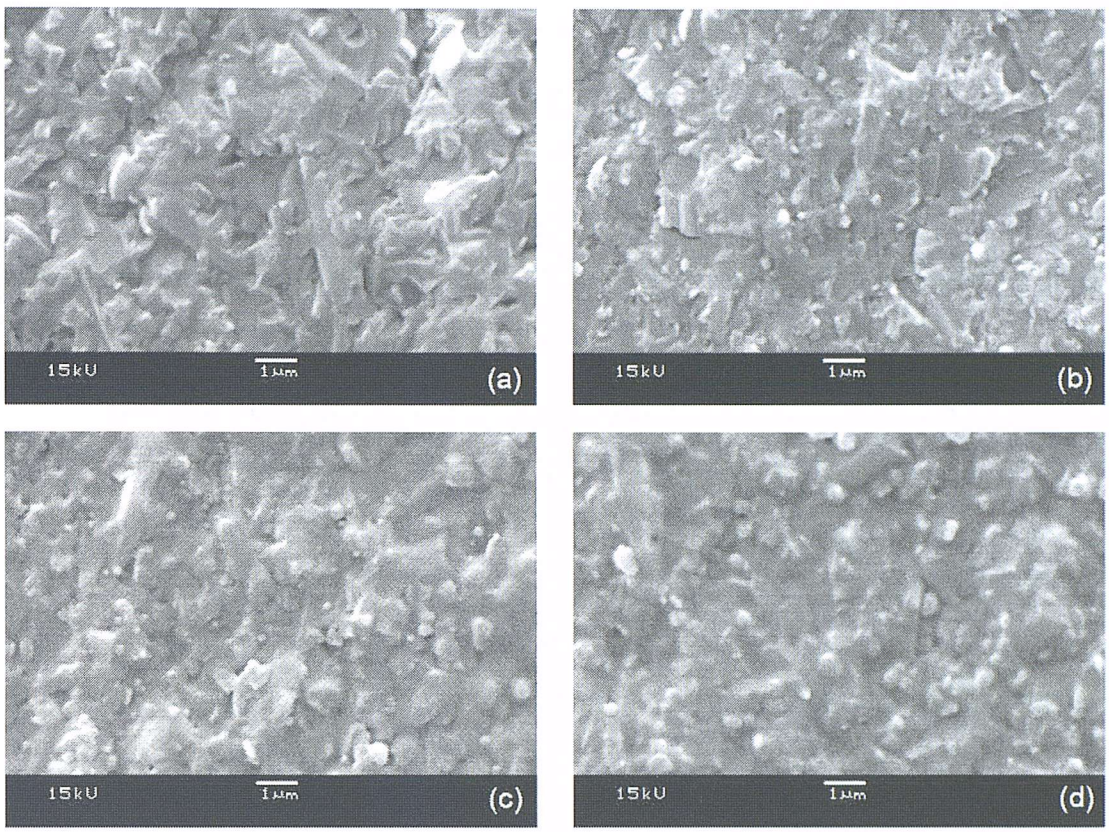


Figure 8-13: SEM images of fracture surfaces of MS40G glass-ceramic specimens at point of failure at (a) ambient temperature, (b) 500°C, (c) 650°C, and (d) 730°C.

In general, the possible toughening mechanisms based on crack blunting, induced by the softening of the residual glass phase at T > 500°C, in addition to some extent of crack deflection, can be supported by the series of SEM images shown in Figure 8-13, where the fracture surfaces appeared much more rounded in samples tested at elevated temperatures in comparison to those of samples tested at room temperature.

At temperatures well beyond the glass transition temperature, the residual glassy phase within the matrix usually has a low viscosity and hence, the viscous flow occurs readily leading to a drop off in strength and toughness. Additional tests were carried out at a temperature of 800°C, and the mean value obtained was lower than that for 750°C. However, the results (also shown in Figure 8-11) exhibit a very large scatter but an overlap, which is supported by the Student's *t*-test indicating no significant difference between the fracture toughness values at these two temperatures. The mechanical properties at these high temperatures are expected to be very temperature dependent and the scatter could be attributed to variations in test temperature. However, this may be disregarded as they are only indicative of a complex material

behaviour at that temperature range. The possibility of microstructural changes at elevated temperature, which led to the marked fluctuation of measured fracture toughness values, has been ruled out by additional thermal analysis on the heat-treated glass-ceramic. Results showed that there was no apparent phase transformation up to a temperature of ~870°C. Because of the inhomogeneous nature of the starting waste material, perhaps small variations in the overall composition of the parent glass and/or slight changes in the degree of crystallisation results in sufficient variation in the proportion and/or composition of the residual glass to account for the scatter at this temperature. Further work needs to be carried out in order to understand the true behaviour of the material at temperatures above the glass transition temperature.

8.5.2 Thermal Shock Resistance

As shown in Figure 8-14, the critical thermal shock resistance temperature of MS40G glass-ceramics is ~100-120°C which is lower than that reported for the sintered materials (~200-250°C) discussed in Chapter 7. According to Equation 7-1, two of the material properties affecting the thermal shock resistance are Young's modulus and CTE. Compared to the sintered materials in the previous chapter, MS40G glass-ceramic has a higher Young's modulus (121 GPa) as well as a higher CTE (9.67×10^{-6} $°C^{-1}$). Equation 7-1 indicates that both of these properties would tend to decrease the thermal shock resistance of the MS40G material with respect to the sintered glass-ceramics. Results from the elevated temperature experiments suggest that the material can be used at temperatures up to 500°C without significant reduction in mechanical strength. However, thermal shock has to be avoided as the material cannot sustain thermal fluctuation of more than 100°C without damage.

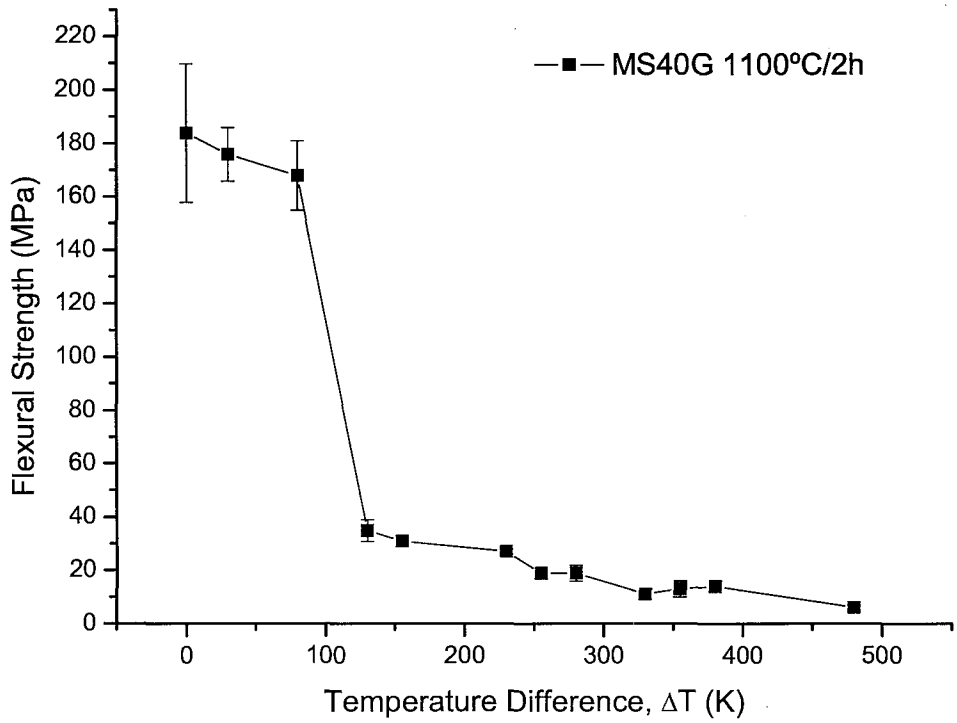


Figure 8-14: Residual flexural strength versus quenching temperature difference for slag-based glass-ceramic materials heat-treated at 1100°C.

8.6 Chemical Resistance

Chemical resistance tests were carried out on MS40G glass-ceramics and as-cast samples. 1N HCl solution was chosen as previous work (Chapter 7) has already shown the negligible weight loss in alkaline and neutral solutions. Results showed the following weight losses: 10.26 mg/cm^2 for as-cast MS40G glass, 5.18 mg/cm^2 for MS40G heat-treated at 900°C, and 1.26 mg/cm^2 heat-treated at 1100°C (comparing to 0.31 mg/cm^2 for sintered glass-ceramic PA30G, see section 7.6). Visual information of polished surfaces of corroded samples that supports the measurements is given in Figure 8-15. Figure 8-15(a) illustrates a typical corroded glass surface, whereas in Figure 8-15(b) and (c) both show confined corrosion of the residual glass, thus defining the crystals, with less severe corrosion on the surfaces. Figure 8-15(c), which represents a surface of MS40G glass-ceramic heat-treated at 1100°C, appears to have the least amount of corrosion.

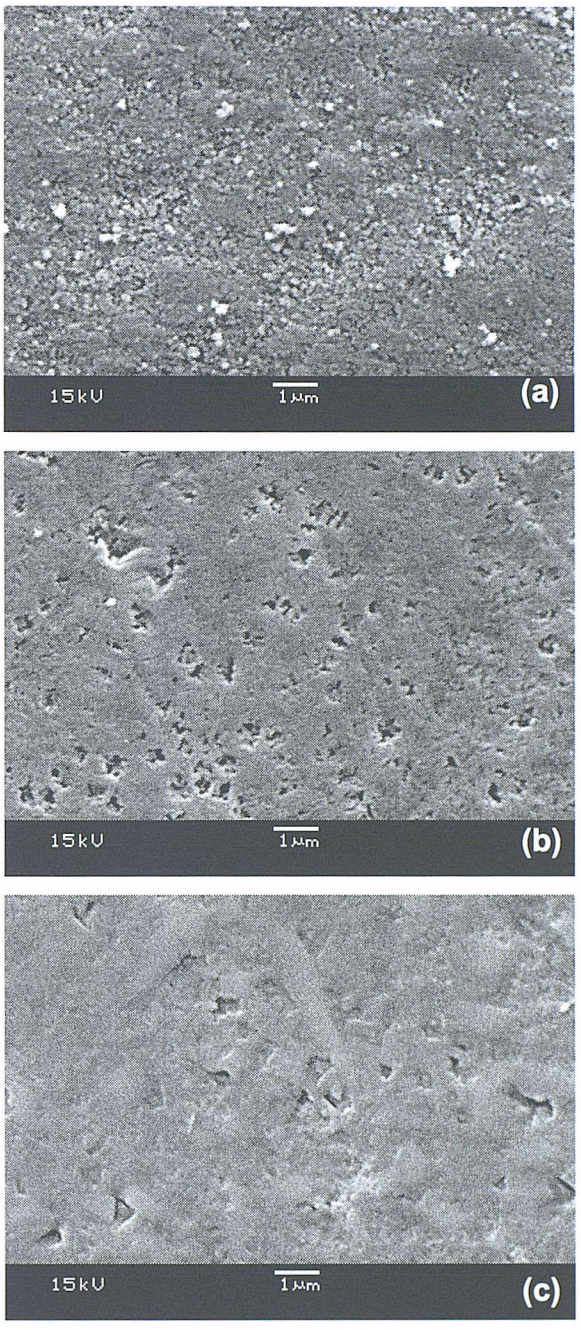


Figure 8-15: Corroded surface of MS40G samples as (a) as-cast glass, (b) heat-treated at 900°C, and (c) heat-treated at 1100°C, after immersing in 1N HCl for 15 hours at 50°C.

It seems that higher degree of crystallinity is beneficial to the chemical resistance of these glass-ceramic materials. Hence, the chemical resistance of these slag-based glass-ceramics may be improved by increasing heat-treatment time, thus yielding a higher degree of crystallinity, but this is associated with a higher energy and thus production cost.

8.7 Conclusion

A glass-ceramic material was successfully obtained from a parent glass made from an unusual TiO_2-containing slag material with additional waste glass cullet. The resulting polycrystalline material possesses high hardness, Young's modulus, flexural and compressive strengths and relatively high fracture toughness. The overall performance of the material is optimized when heat-treated at higher temperatures (~1100°C) at which the precipitation of titanium-rich phases occurs, prompting the possibility of tailoring material properties by heat-treatment. K_{IC} measurement at elevated temperature has been carried out on these waste-derived silicate glass-ceramics, which will be relevant if these materials find applications in specialised high-temperature (<500°C) areas. The end product has the potential to be used as load-bearing structural components, e.g. high-temperature resistant machine elements, as well as chemical/wear resistant components in the architectural and building industry. Therefore, wear and impact resistance should be assessed in the future.

Chapter 9 Waste-derived Glass-ceramic Foams

9.1 Introduction

As mentioned previously, much work has been carried out to produce dense glass-ceramics with improved mechanical, thermal, chemical, and physical properties from waste materials. The intention has been to obtain glass-ceramics with competitive properties to replace or act as an alternative to existing commercial glass-ceramics and/or building and structural materials in general, e.g. floor and wall tiles, architectural panels, and other specialised products. Sometimes, because of the complexity of these wastes, pre-production refinements, which may complicate and increase the cost of a recycling process, are needed in order to yield a refined waste material or a combination of wastes that is worth recycling into a dense material. On the other hand, if pores in a material can be exploited to achieve a certain function or property, e.g. sound or thermal insulation, then porous materials become a viable option for reusing waste without a (usually costly) refining process. Current research should demonstrate not only that it is feasible to reuse silicate waste in the production of foamed glass-ceramics but also it should confirm the versatility of the chosen processing method, which should be applicable to many different types of industrial wastes with minor adjustments to parameters such as chemical composition, type and amount of foaming agent, and variables in the heat-treatment process.

As described in Chapter 4, there is a wide range of methods for producing porous materials. Apart from loose-packed powder sintering, the incorporation of foaming agent is by far the simplest and probably the cheapest technique to produce porous ceramics on powder sintering [204]. In order to maintain the simplicity and thus favourable economics of recycling waste materials, it was intended from the beginning of this project that solid foaming agents are to be incorporated into the powder sintering method to create macro-porosity in the heat-treated products. The high level of porosity is targeted to provide a good insulation in thermal applications while mechanical properties of a glass-ceramic material should be sufficient to provide the required structural stability.

Different types of foaming agents, $CaCO_3$, PMMA, SiC, TiN_2, and starch, have been used in the preliminary work. The key to an optimised foaming process relies on matching the softening temperature of the matrix and the reaction/decomposition

temperature of the foaming agent and thus maintaining distinct gas bubbles, and hence final porosity, during heat-treatment. Subsequent analysis was carried out using only the best foaming agent. This includes phase characterisation, the level of porosity, pore morphology analysis, degree of open/closed porosity, mechanical properties (Young's modulus, flexural and compressive strength), and thermal properties (thermal expansion coefficient and thermal conductivity). It has been demonstrated in this study that x-ray microtomography (XMT) is a powerful, non-destructive tool for investigating the pore morphology of highly porous silicate based materials. Although there has been work done using XMT on a silicate bioactive glass [176] and glass-ceramic foams [160], this is the first time that XMT has been used in waste-derived technical porous glass-ceramics and the emphasis was placed on developing quantitative analysis of the XMT scans for such materials and the results are discussed later in the chapter. Apart from the overall aim to reuse silicate wastes in glass-ceramic production, correlations between processing conditions, structure and properties of glass-ceramic foams are an important aspect of this work.

9.2 Process Optimisation

9.2.1 $CaCO_3$ as a Foaming Agent

Preliminary sintering experiments showed that the cullet glass itself can be sintered at 675-750°C. At 800°C, the material starts to significantly soften. The key to foaming (volume expansion) is to let the evolution of gas from the reaction/decomposition of foaming agent occur while the viscosity of the matrix material is low enough for gas bubbles to form but high enough to retain the trapped gas and thus maintain the porous structure. $CaCO_3$ was chosen as the candidate foaming agent for preliminary experiment with waste glass. As Figure 9-1 shows, foaming and a volume expansion of 400-500% was achieved with porosity (~75-80%) that was primarily open.

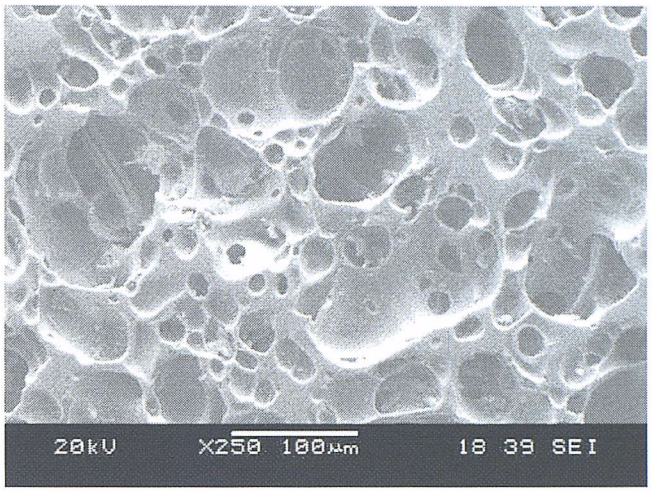


Figure 9-1: Soda-lime glass + 5wt%$CaCO_3$ sintered at 700°C for 15min.

Preliminary foaming experiments showed that the heat-treatment temperature as well as the chemical composition of the matrix material is very important to the effectiveness of the foaming. This can be explained in two ways, either (i) the heat-treatment temperature was below the softening temperature of the mixture so that the mixture was still too rigid or viscous to be foamed or (ii) the temperature was too high so the carbonate had decomposed and escaped already at lower temperatures. The latter explains the lack of foaming in an mixture of carbonate and PA. Note that if the waste material had been vitrified first (i.e. molten in a glass), then the softening temperature would be lower and foaming agents with low decomposition/reaction temperatures such as $CaCO_3$ could have been used. However, this is not an option as we are trying to minimise the cost of production and thus avoid the higher energy consumption in vitrification. The feasible solutions to effective foaming are changing the composition by adding more waste glass (i.e. lower loading of the ash or slag, <50wt%) in an attempt to decrease the softening temperature (<1000°C), and/or using alternative and probably more expensive foaming agents which react/decompose at higher temperatures.

9.2.2 SiC as a Foaming Agent

Because of the higher reaction temperature of silicon carbide (SiC) [151, 205, 206], it was chosen for further investigation of foaming of PA80G. The foaming produced by SiC has been more effective when compared with $CaCO_3$ at temperatures around 1000-1100°C. Coalescence of pores was also observed in specimens produced in

prolonged heat treatment time and at higher sintering temperature. Figure 9-2 illustrates the volume increase with respect to quantity of foaming agent. Note the slight greater volume expansion when 5wt% of SiC was incorporated.

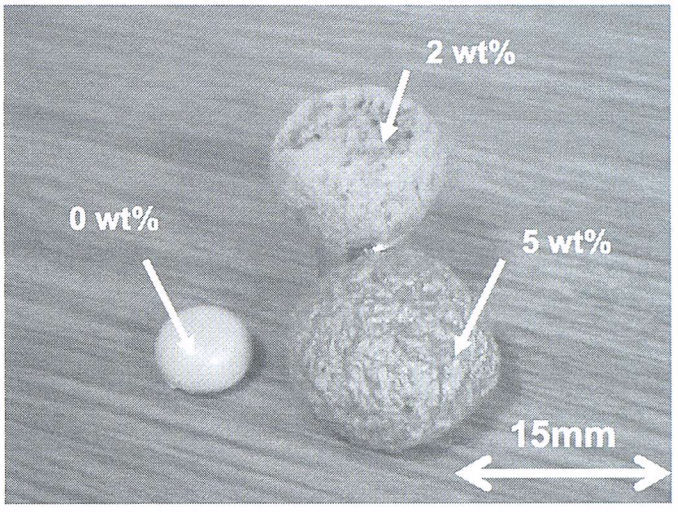


Figure 9-2: PA80G glass-ceramics with 0, 2, and 5wt%SiC, heat-treated at 1050°C for 5min

A comparison between X-ray diffractograms (Figure 9-3) of foamed samples with 2 and 5 wt% SiC showed a detectable amount of residual SiC present in the heat-treated material incorporated with 5wt% SiC. That is, under the same processing condition, some of the foaming agent has not completely reacted. Therefore, it is possible to use less than 2wt% SiC as foaming agent. It also means that the foamed material can be tailored with the amount of foaming agent used. The crystalline phases present in the foams will be discussed in the section 9.3.

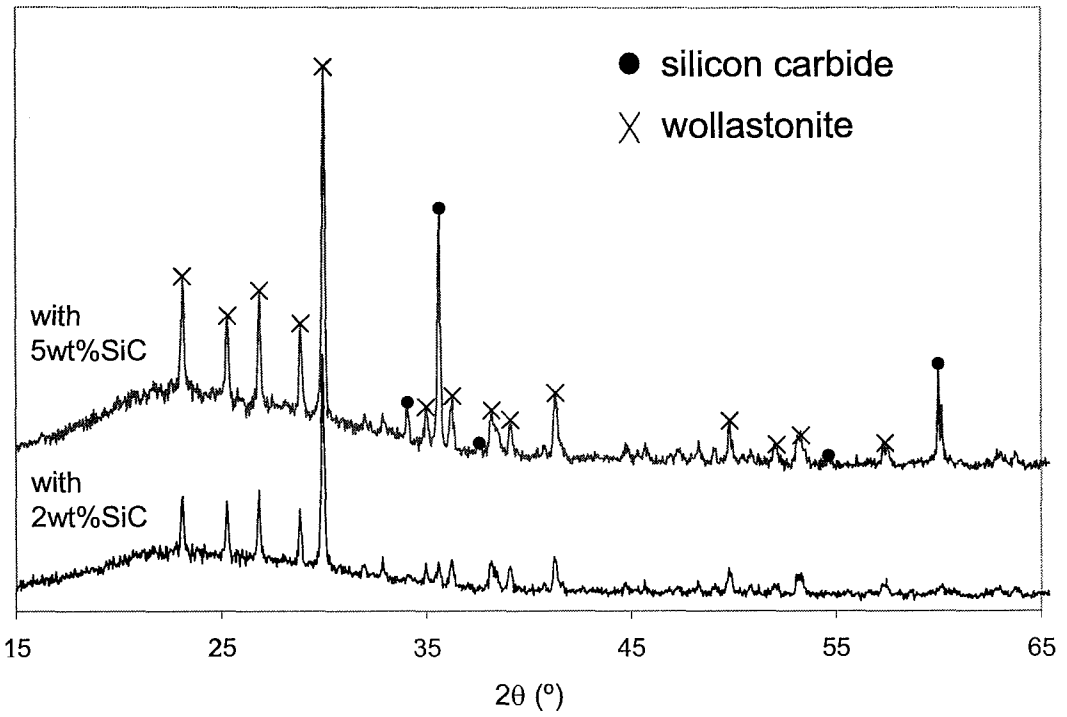


Figure 9-3: XRD plots illustrating the crystalline phases present in samples containing different amounts of SiC after heat-treatment at 1025°C for 5 minutes

As shown in Figure 9-4, a solid foaming agent tends to give large pores as fine pores usually agglomerate during foaming. Despite the effectiveness of SiC at foaming the starting mixture, it is a concern that SiC is more expensive when compared to $CaCO_3$. Fortunately, waste SiC is available in the abrasive and ceramic industries where used SiC abrasives have been recycled [207, 208]. Abrasive Grit Corporation [209] (formed in 1997) serves the abrasive, motor, foundry and blasting industries. The company is situated in Spartan, Kempton Park, South Africa. It specialises in recycling brown aluminium oxide, black silicon carbide, green silicon carbide, and vitrified abrasives for reuse. There are other evidences of waste SiC (or spent carborundum) available from different abrasive industries around the world [210, 211]. Note however pure SiC powder was used for the experiments in the present work.

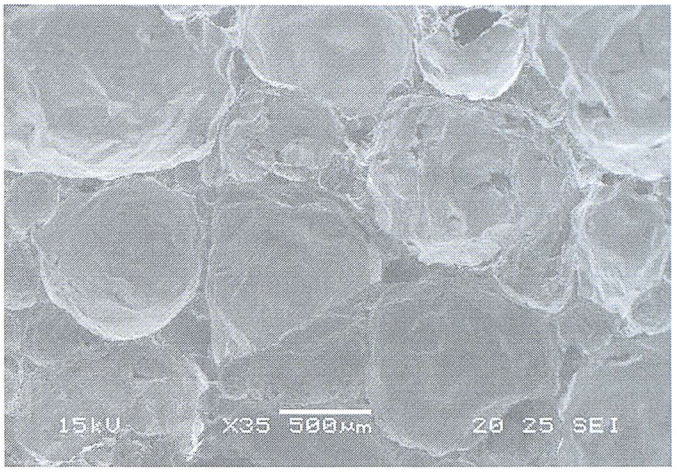


Figure 9-4: SEM micrograph showing the cross section of the glass-ceramic foam made by mixing 2wt% SiC powder with PA80G glass powder

It was found that the silicon carbide undergoes a far more complicated reaction process than the decomposition process with oxygen in the case of carbonates. There was no exothermic or endothermic reaction observed by DTA when SiC was heated up to 1070°C in air (as shown in Figure 9-5). The DTA plots are typical background signals from the heating of reference material (alumina); therefore, indicating that SiC alone does not react under oxygen rich atmosphere, and it seems that the presence of oxides is essential to foaming as claimed by earlier study [205, 206].

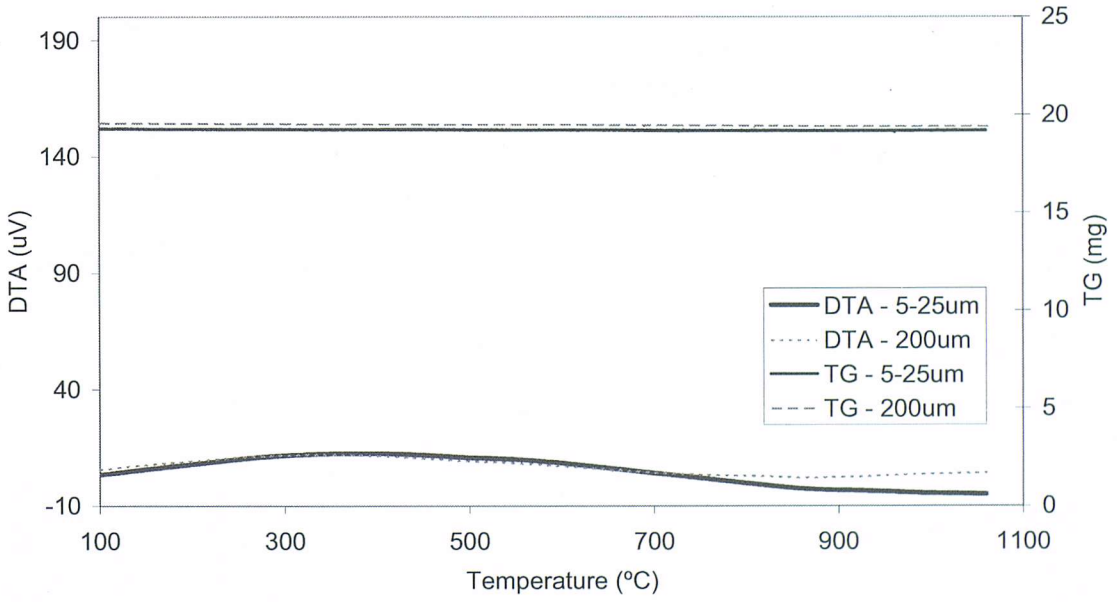


Figure 9-5: DTA/TG plots of silicon carbide powder of different particle size (5-25µm and 200µm)

SiC is a very effective reducing agent, meaning the carbide can be readily oxidised into CO_2 gas bubbles (or CO with a lack of oxygen atmosphere). There are a number of possible reactions occurring but the formation of CO_2 gas is the key to foaming:

$SiC + 2O_2 \xrightarrow{MO} SiO_2 + CO_2$ (reaction of carbide with oxygen)

$SiC + 2MO \xrightarrow{O_2} Si + 2M + CO_2$ (reduction of metal oxide)

$M + O_2 \rightarrow MO_2/MO$ (not a balanced equation as it depends on M)

In is possible for SiC to react with the different oxides present in a glass matrix. This was proved experimentally as foaming occurred when 5wt% of SiC was mixed with waste glass cullet and heat-treated at 1000°C. Bayer et al [206] claimed that the foaming reaction is enhanced by the presence of additional transition metal oxides (e.g. Fe_2O_3, CuO, MnO_2). This synergetic effect was also proved experimentally when a small amount of the coal pond ash was mixed with the glass cullet and SiC. This mixture appeared to have foamed more readily with more homogeneous pore morphology than SiC with just glass cullet. The presence of pond ash (i.e. transition metal oxides) has enhanced the reaction (i.e. consumption) of SiC as demonstrated by the relatively lower amount of residual SiC that was shown in XRD of the PA containing glass-ceramic foam (Figure 9-6). The figure also shows that the foamed glass without pond ash did not crystallise as much as the one with pond ash.

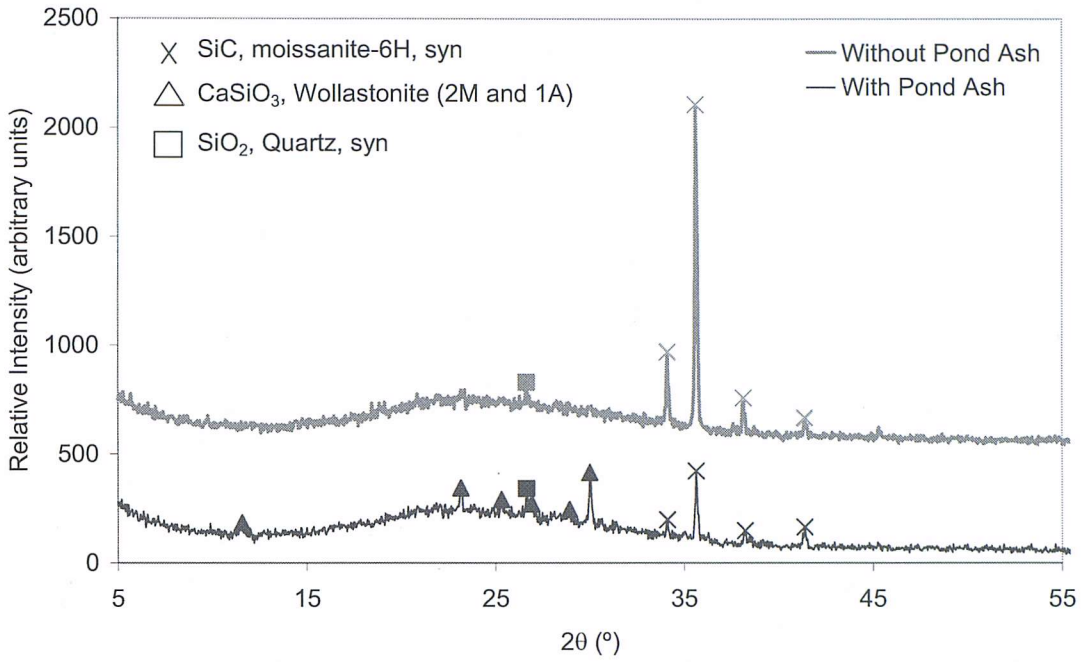


Figure 9-6: XRD spectra showing the synergetic effect of pond ash on reaction of SiC and glass oxides

The results from the foaming experiments have helped to determine the optimised composition of the initial mixture (PA80G, containing 20wt% coal pond ash and 80wt% waste glass cullet), heat-treatment temperature range (925-1100°C) and process time (5 minutes), and the type and quantity of foaming agent (SiC, <2wt%). By adjusting a combination of these parameters, it is possible to produce glass-ceramic foams with different level of porosity, pore size, morphology, and thus thermal and mechanical behaviour.

9.3 Phase Identification

Extensive XRD analysis (Figure 9-7) has indicated that the main crystalline phase in the foamed PA80G (pond ash with 80wt% soda-lime glass) is wollastonite (calcium silicate, triclinic, $CaSiO_3$). It was observed that at lower heat-treatment temperatures, there was a minor presence of SiO_2 (cristobalite and quartz) in the glass matrix. The precipitation of cristobalite is a common occurrence when glass powder of borosilicate composition is heat-treated at temperatures around 1000°C with or without foaming agents [206]. This phenomenon is less marked in the case of soda-lime silica glass [205]. Literature has shown that the crystallisation of cristobalite can be, and has been, inhibited by addition of alumina-containing compound [206], and in

this case, coal pond ash (essentially alumino-silicate) has helped to inhibit the precipitation, particularly at high temperature. The presence of quartz came as a contamination from the glass cullet used.

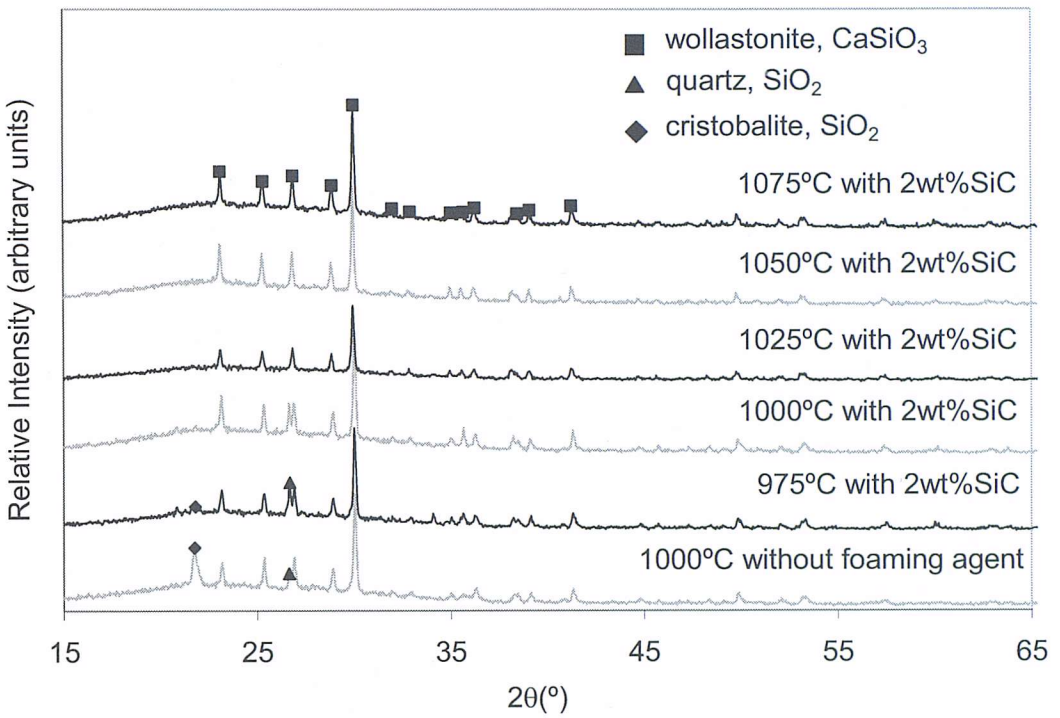


Figure 9-7: XRD analysis illustrates the crystalline phases present in PA80G glass-ceramic with and without foaming agent at different sintering temperatures

Furthermore, the relative degree of crystallinity (refer to Section 5.2.4) was determined using XRD plots from Figure 9-7. The results (Figure 9-8) showed a gradual increase in crystallinity from the lowest temperature (975°C) before reaching a maximum at around 1025°C, confirming that crystallisation of wollastonite takes place in this range of temperatures. Beyond 1025°C, there appears to be dissolution of wollastonite crystals as the relative degree of crystallinity reduces. In addition, when the degree of crystallinity of the 100% dense solid was compared against that of the porous material foamed at the same sintering temperature (1000°C), the dense solid was less crystalline because the surface area of the foamed material is much greater than the dense solid and the crystallisation of wollastonite is dominated by surface crystallisation.

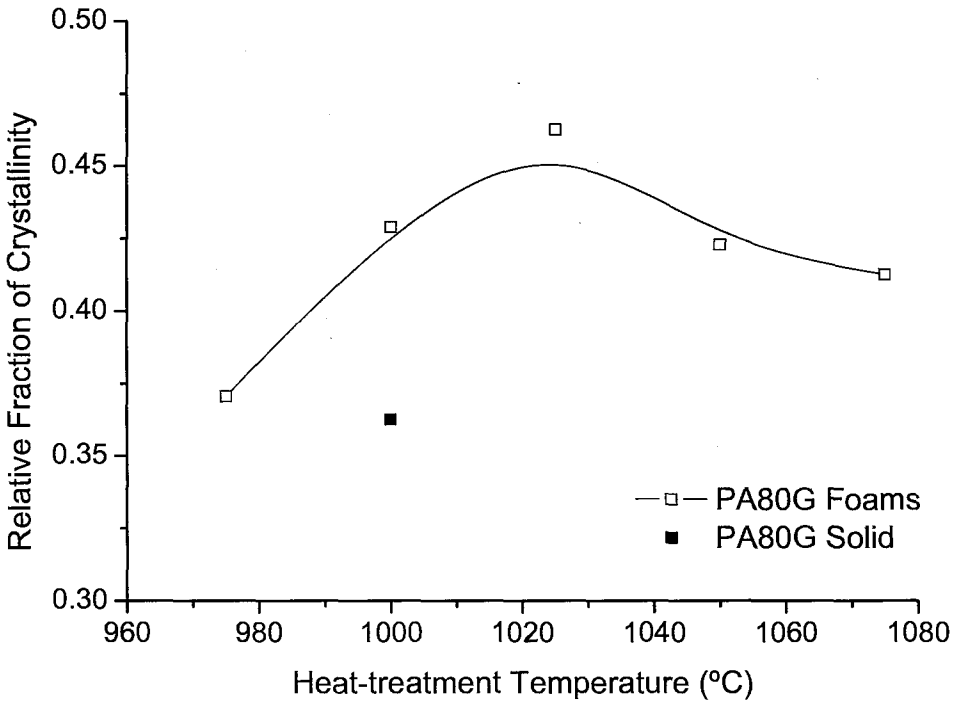
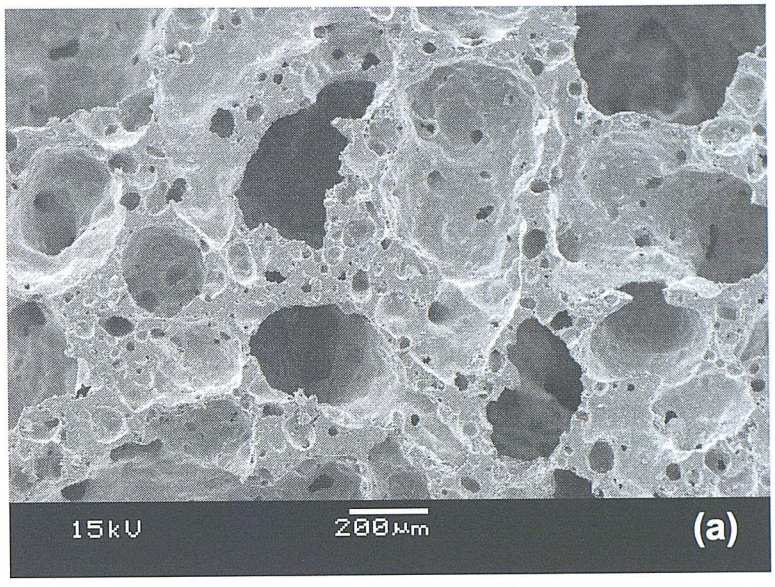


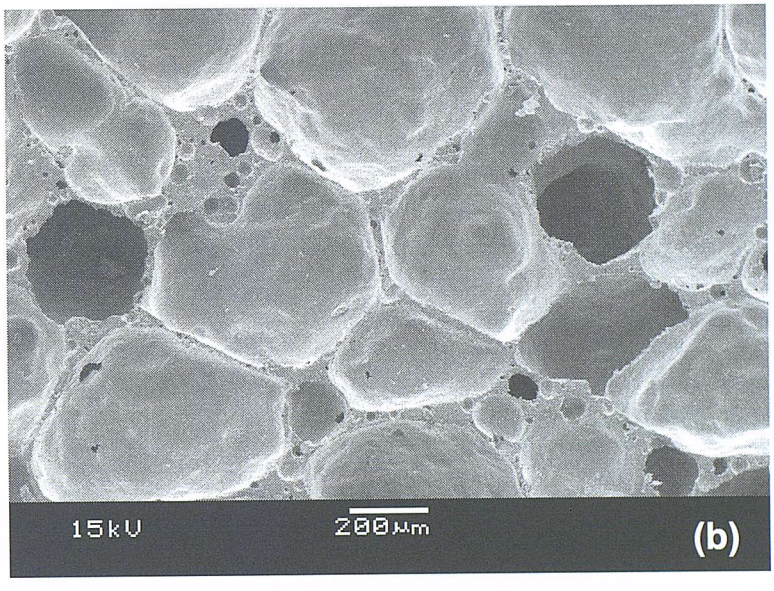
Figure 9-8: Relative degree of crystallinity of PA80G foams with 2%SiC and dense PA80G solid at various heat-treatment temperatures.

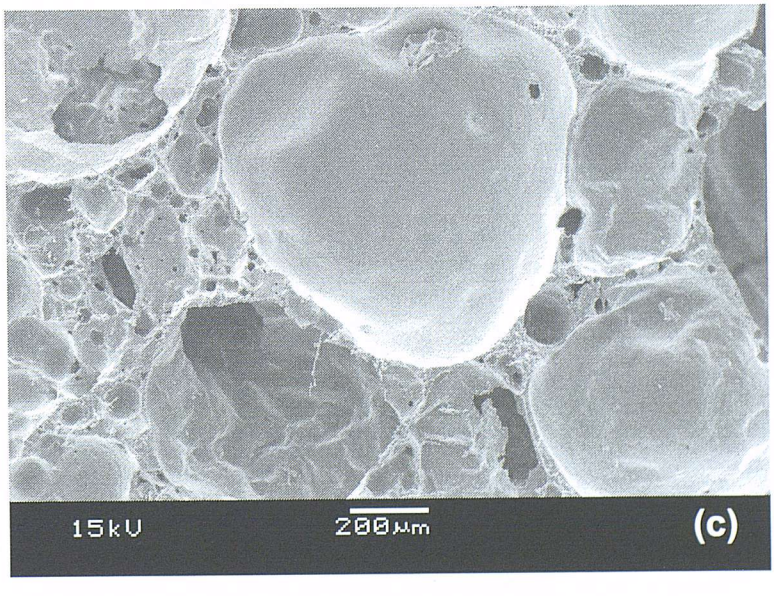
9.4 Microstructural analysis

9.4.1 Conventional Microscopy

Microstructural analysis was first carried out using conventional techniques such as scanning electron microscopy (SEM). Figure 9-9(a-d) gives indications of the effect of temperature on the level, size, and morphology of the porosity of PA80G foams. The irregularity of pore size and shape in Figure 9-9(a) indicates that the heat-treatment temperature was slightly too low for the gas bubbles to form and expand. The roundness of pores begins to improve as the temperature increases (Figure 9-9(b)). In the meantime, an increasing heat-treatment temperature has resulted in a greater tendency for smaller pores to coalesce which led to larger, isolated pores (as shown in Figure 9-9(c) and (d)). The coalescence of pores also resulted in thicker average pore walls (cell struts). Note that the interconnectivity of pores is more apparent in foams from low heat-treatment temperatures, mainly due to the partial sintering of particles where the voids from incomplete sintering act as interconnections.


15kV
200µm
(a)


15kV
200µm
(b)


15kV
200µm
(c)

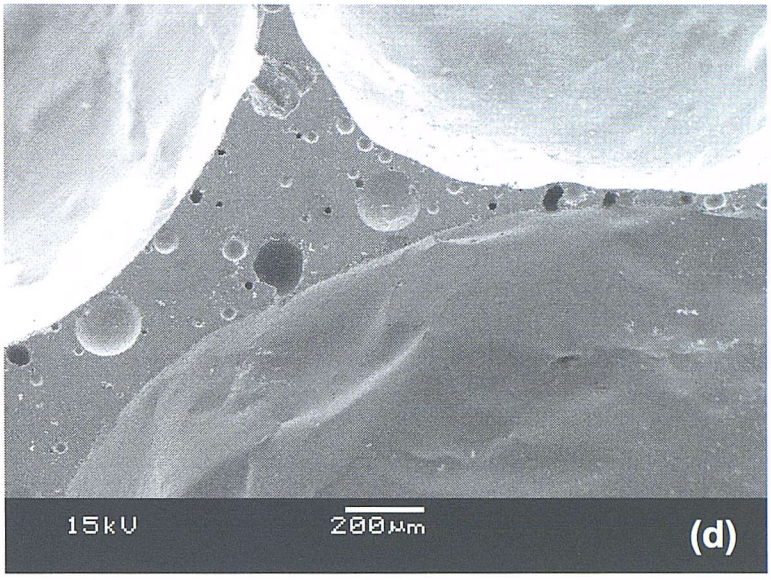


Figure 9-9: Scanning electron micrographs showing the pore morphology of glass-ceramic foams of composition PA80G +2wt%SiC heat-treated at (a) 975°C, (b) 1000°C, (c) 1050°C, (d) 1100°C.

One of the drawbacks of microscopy is the time required to prepare specimens. The process can be tediously long, especially when each microscopy session only allows the examination of one face. Therefore, many examinations are required of different sections of each sample in order to obtain representative figures for the 3-D pore morphology. X-ray microtomography (XMT) is demonstrated here as an alternative structural 3-D characterisation technique, and comparisons between the two techniques are made in the following section.

9.4.2 X-ray Microtomography

XMT is well-known as a non-destructive technique for structural examination in 3D. Since the foamed glass-ceramics has the matrix and the air, each of which has a contrasting X-ray attenuation coefficient from the other, it was appropriate to use XMT to acquire detailed visual information of these foams and to analyse the pore structure 3-dimensionally.

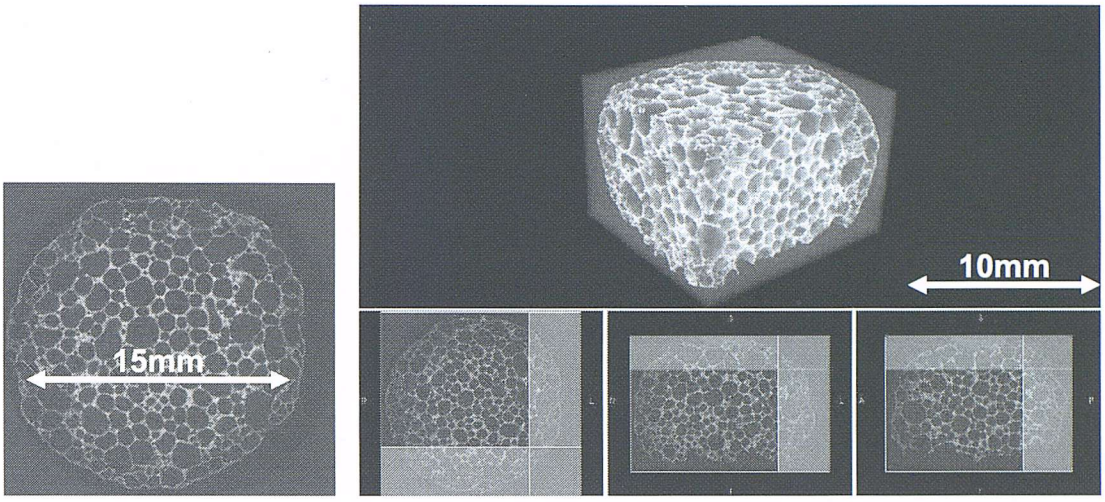


Figure 9-10: 2D and cropped 3D representations of PA80G + 2wt%SiC foamed at 1050°C for 6min

The 2D image and a composite of 2D cross-sections and 3D volume (Figure 9-10) illustrate the first stage of image processing after the reconstruction of an array of X-ray images from an XMT scan. Commercial visualisation software packages (e.g. VolView and VGStudio) allow users to examine different sections of a specimen by simple image cropping functions with precise control of the locations. The 3D volume (Figure 9-11) is a sample ready to be further refined before 'defect' analysis (in this case, porosity) is conducted.

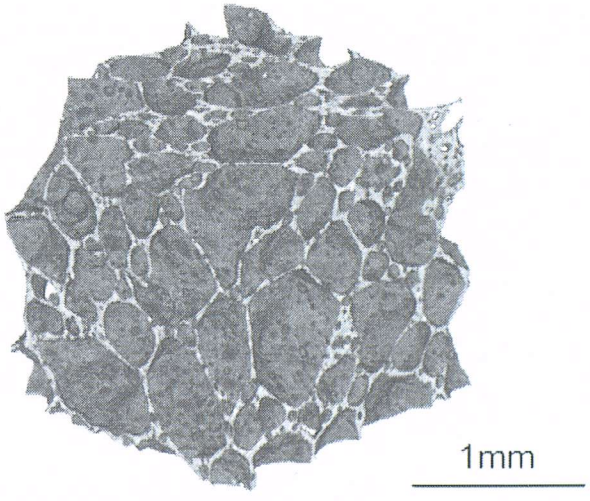


Figure 9-11: XMT reconstruction showing a cropped section (the inner core) of a waste-derived porous glass-ceramic material PA80G with 2wt%SiC sintered at 1050°C for 5min

Figure 9-12 illustrates the use convolution (a series of dilation/erosion operations for digital image processing) to remove interconnects for better pore size estimation

and/or to measure the relative fractions of different pore sizes especially when there is a bimodal distribution.

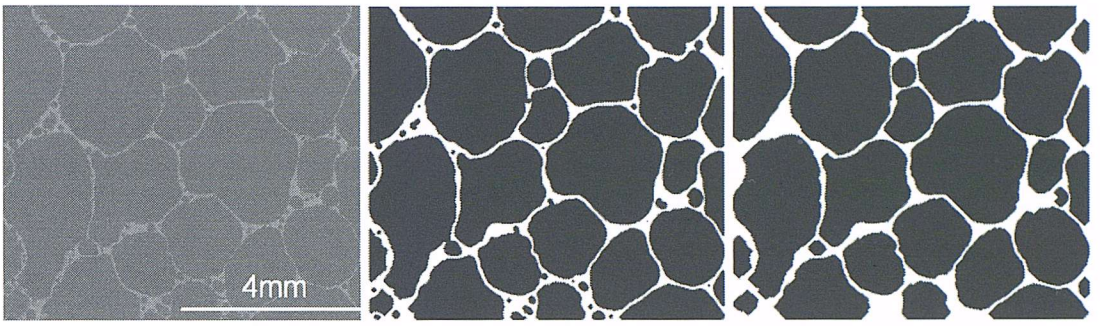


Figure 9-12: From left to right: Original axial (xy) slice of PA80G 2wt%SiC 1100°C; processed using less aggressive convolution operation (3 iterations); processed using more aggressive operation (9 iterations).

Using a much more aggressive filtering mechanism, the interconnections are removed and smaller pores trapped within the pore struts get filled with white pixels (material) to a stage where there are no more black pixels (pore/air) in the walls for erosion to occur. However, the bigger pores remain the same original size for measurements. A comparison between the images before and after filtering will give an indication as to the relative proportions of small pores and large pores.

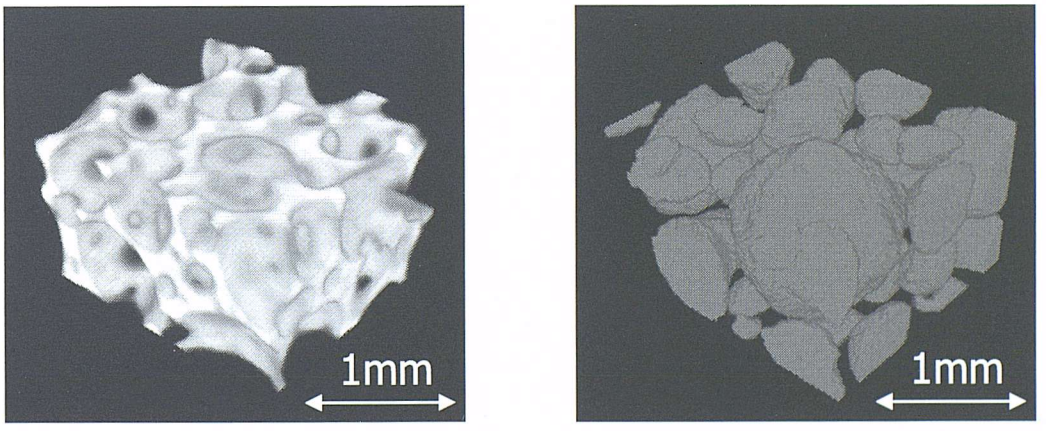


Figure 9-13: Example of a 3D defect analysis conducted on a small volume of PA80G foam using VGStudio; (left) porous sample; (right) volumes representing the defects/pores

Similar image processing functions were applied to each XMT data using VGStudio as shown in Figure 9-13; demonstrating that it allows defect analysis to be carried out and the pore morphology to be measured. To document the application of the method,

a set of XMT data has been completed on the following samples: PA80G + 2wt% SiC heat-treated at 975, 1000, 1050, and 1100°C for 5 minutes each. A summary of the analysis is presented in Table 9-1. Since the heat-treatment temperature range was optimised to match both the reaction temperature of SiC and the softening range of the matrix, the density decreased with increasing temperature as expected. Foaming was most effective at higher heat-treatment temperatures. Given that level of porosity is inversely proportional to the density of a sample, porosity increases with heat-treatment temperature.

Table 9-1: Effect of heat-treatment temperature on pore morphology of glass-ceramic foams as measured by XMT

Material Property	**Unit**	**Heat-treatment**			
		975°C	*1000°C*	*1050°C*	*1100°C*
Apparent density – experimental	g/cm^3	0.34±0.01	0.28±0.01	0.16±0.01	0.13±0.01
Porosity – XMT	%	81.5±4.2	83.5±2.7	80±2.7	88±1.7
Roundness (Sphericity) – XMT	Scale (0-1)	0.73±0.01	0.77±0.02	0.79±0.05	0.79±0.03
Average pore diameter – XMT	mm	0.27±0.02	0.39±0.03	0.80±0.05	1.37±0.18

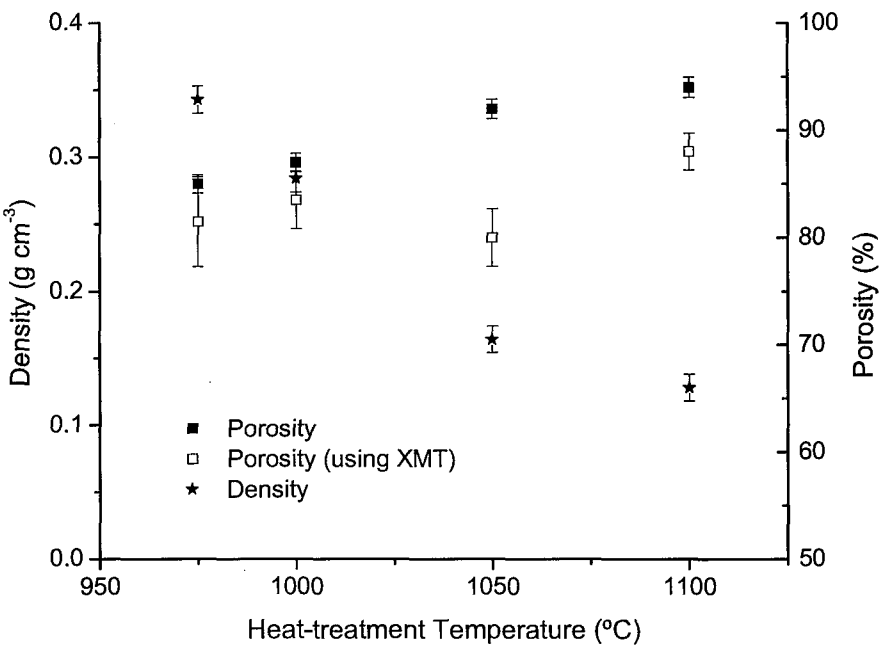


Figure 9-14: Effect of heat-treatment temperature on density and level of porosity of PA80G glass-ceramic foams

The discrepancy between XMT porosity and actual porosity (porosity evaluated from density measurements) is illustrated in Figure 9-14, and this is solely affected by limited resolution achievable by the XMT set-up. Because the resolution is limited to a particular length per voxel (pixel for 3D volumes), any feature that is smaller than the limit will be undetectable. This means that submicron pores, especially ones within cell walls, can be easily neglected from the XMT measurement, resulting in an underestimation of porosity level (by about 5% in general). This limitation is emphasised by the larger offset (~10%) for a XMT sample (with 2%SiC at 1050°C), which was 3-4 times the volume of any of the other samples. In order to cover the width of the sample during scan, the FOD (please refer to section 5.2.7 for the principle behind XMT) had to be increased, which led to a much inferior resolution (0.038mm per voxel) than for the rest of samples (0.008-0.015mm per voxel). Apart from minimising the sample size and thus FOD, a stronger X-ray source, e.g. synchrotron radiation, can enhance the intensity and therefore compensate for the sample size factor.

The heat-treatment temperature is a very significant parameter for the microstructure of foams as illustrated in Figure 9-14 and Figure 9-15. The roundness of pores has improved with increasing temperature; this is commonly observed because as the matrix material becomes less viscous, it allows the gas to expand and establish the most stable form, i.e. a sphere. In fact, the level of roundness reaches a plateau of 0.79 (a sphere gives a value of 1) at temperatures over 1050°C, and the deviation is slightly less at 1100°C than at 1050°C. Another aspect of pore structure that changes with the viscosity of the matrix is the pore size. As the gas bubbles are more mobile at higher temperatures, small pores have a greater tendency to coalesce, resulting in large pores. The changing pore size in a constant volume of material means that the original material in thinner walls will flow and combine into a thicker wall with increasing temperature (as illustrated by Figure 9-16). Hence, the wall thickness increases with increasing diameter of pores which is directly affected by the heat-treatment temperature (Figure 9-15).

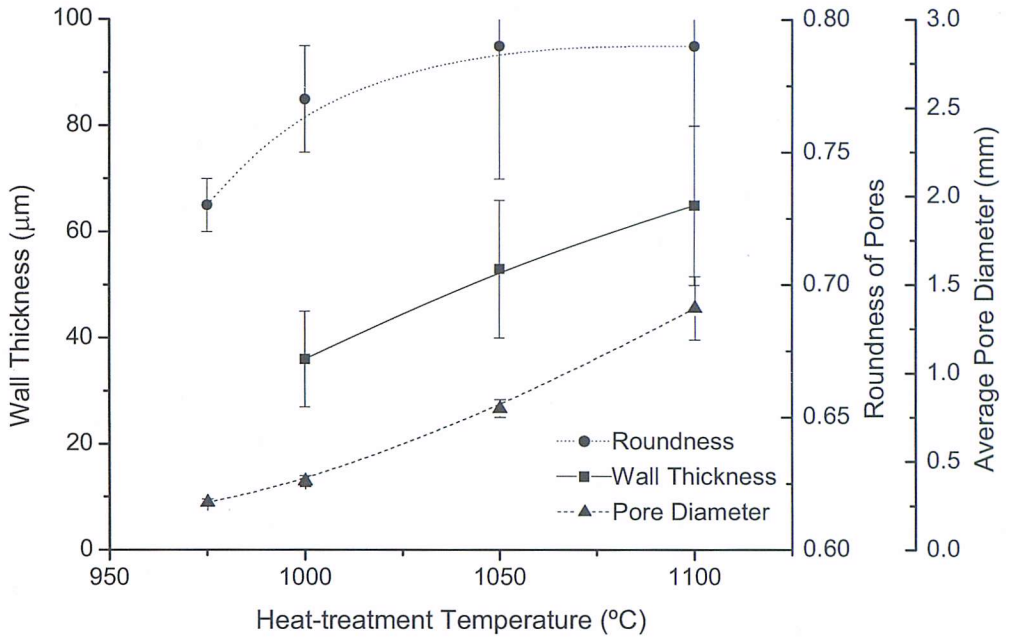


Figure 9-15: Effect of heat-treatment temperature on pore morphology (roundness, pore size, and wall thickness)

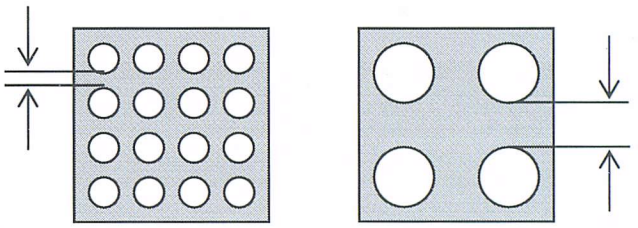


Figure 9-16: Schematic representation of the effect of increasing pore size on wall thickness at constant porosity

Finally, the size distribution of each foamed sample at different heat-treatment temperature is shown in Figure 9-17; these plots are obtained from the post-convolution data and are consistent with the average values of pore size as tabulated in Table 9-1. It has been demonstrated that XMT is an excellent non-destructive method for obtaining comprehensive structural information with accuracy and precision within technical limitations to replace conventional techniques.

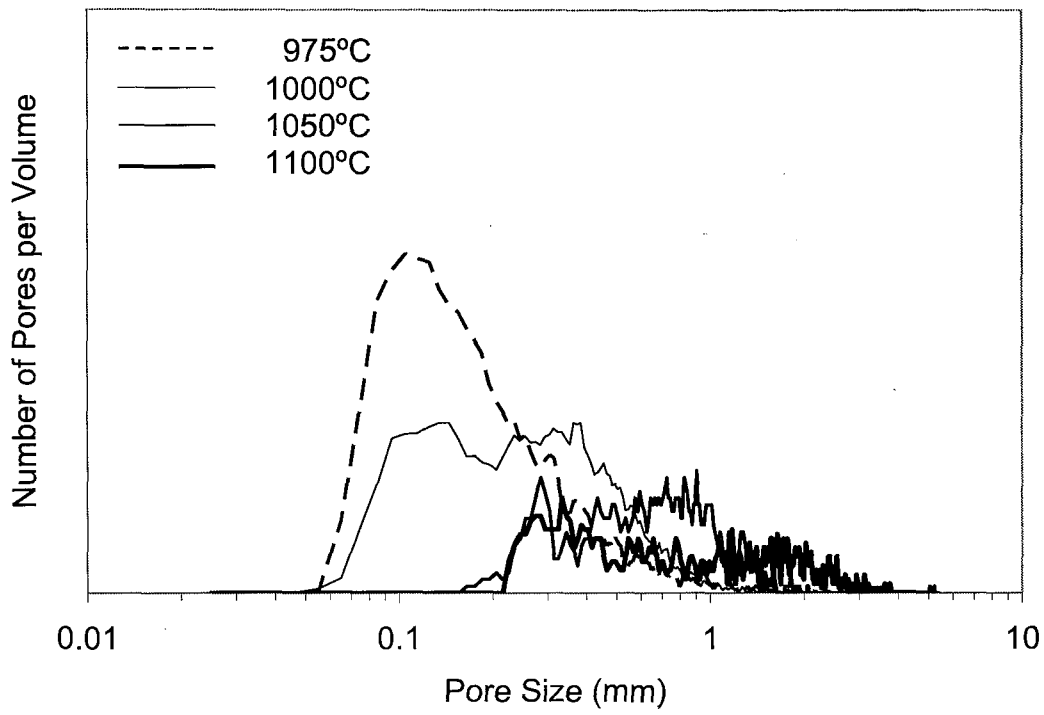


Figure 9-17: Pore size distribution (post-convolution) of PA80G foams heat-treated at 4 different temperatures

9.5 Coefficient of Linear Thermal Expansion

Values of CTE of a number of foams and the solid were measured using dilatometry. In theory, since foam is a framework of a solid material, the coefficient of linear thermal expansion (CTE) should be the same as that of the solid of which the framework is made regardless of the structural difference. This hypothesis was proved by comparing the CTE of bars of PA80G composition containing different levels of porosity and pore size. Values of CTE of a number of foams and the solid were measured using dilatometry.

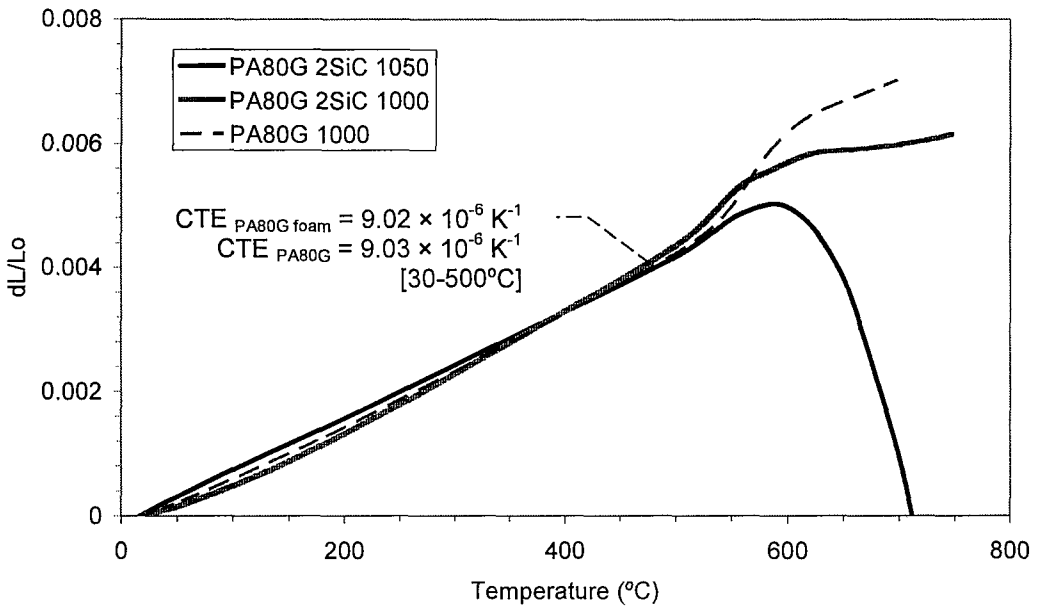


Figure 9-18: Change in length versus temperature plot, showing the linear CTEs of bulk solid and foams of the same composition (PA80G). (L_o = ~25mm)

Results showed a good agreement between the CTE values up to 500°C; up to this temperature both dense and foamed materials expanded at similar rates. The changes in the gradient of each slope occurred at around the same temperature, indicating the glass transition temperature (T_g) of the PA80G material is about 530°C. There are explanations for the different behaviours (change in rate of expansion and shrinkage) based on difference in initial degree of crystallinity and thus phase transformation (crystallisation) during dilatometry, and difference in initial level of porosity between samples and thus sintering (shrinkage) beyond T_g. First of all, the level of shrinkage is highest for the most porous material, and lowest (in fact, no shrinkage) for the dense material. High porosity, thus high surface area, provides a large driving force for coalescence of pores, i.e. there is a tendency to sinter (shrink). Therefore, at temperatures beyond T_g, the rate of shrinkage of the most porous material overshadowed the rate of linear expansion, resulting in a reduction in thermal expansion. There was no major structural change due to sintering as illustrated by the SEM images (Figure 9-19) taken before and after dilatometry. In addition, a degree of crystallinity analysis was carried out using XRD on samples before and after dilatometry, and the results showed that the porous foams underwent further crystallisation (increased degree of crystallinity by 5-10%, see Figure 9-20) whereas the dense PA80G solid has negligible change in crystallinity. Crystallisation is

usually associated with an increase in density which would be reflected in further shrinkage. This means that the subsequent phase transformation at elevated temperature caused the difference in the expansion behaviour of the porous foam from the solid.

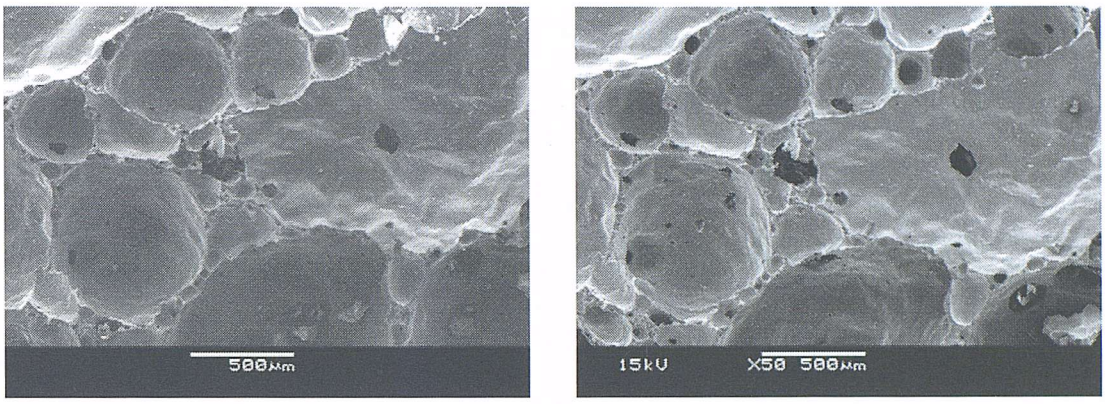


Figure 9-19: SEM images of a PA80G + 2wt% SiC bar foamed at 1050°C (left) before and (right) after subjected to a thermal treatment up to 700°C in a dilatometer

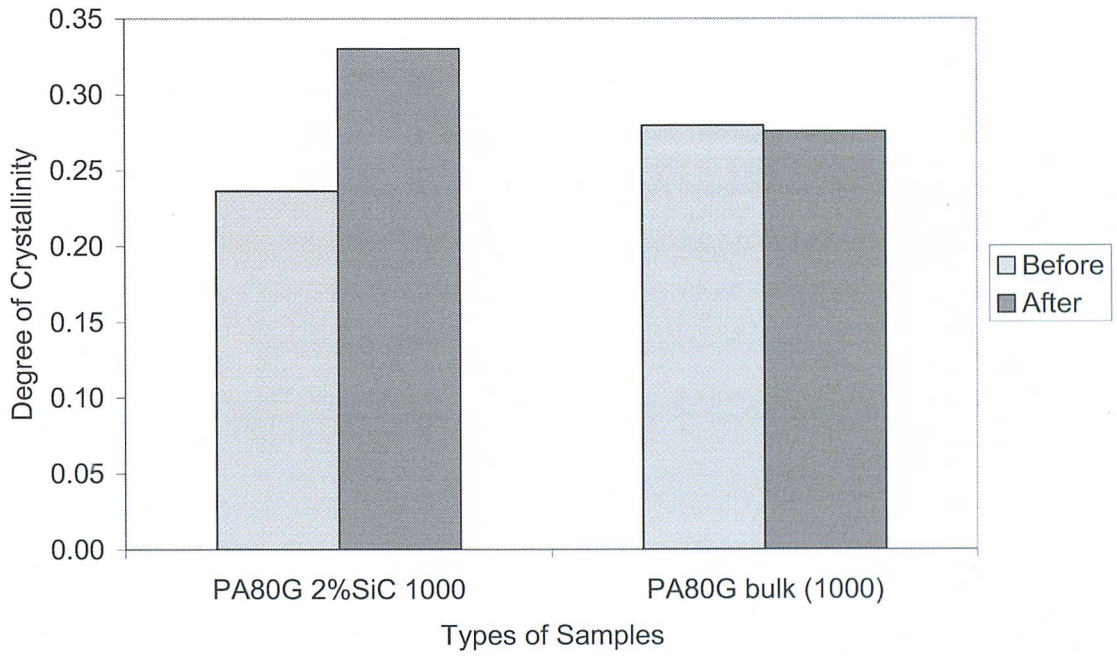


Figure 9-20: Change in degree of crystallinity after further heat-treatment of glass-ceramic foams and bulk sample at 750°C at 10°C/min

Supplementary experiments were also carried out to locate or to eliminate other factors leading to the difference in expansion behaviour. The hypothesis is that the compressive stress on the specimen (from the spring-loaded sample holder) may have

caused some viscous flow which would have been recorded as linear shrinkage at elevated temperature [212]. A piece of the same porous material (PA80G 2wt%SiC 1050°C) was heated up to 750°C at 10°C/min in an electric furnace (i.e. without the compressive loading). There was 0.9% linear shrinkage on a 25mm long specimen, similar dimensions to the one used for dilatometry. There was no significant difference in linear shrinkage when compared with the linear shrinkage of 0.5-0.6% that was recorded for the specimen (PA80G 2SiC 1050°C) as shown in Figure 9-18. Despite the obvious difference, the measurement error was much greater than the measurement taken from dilatometry. Therefore, it was concluded stress was not playing any role in the dilatometry experiments. In terms of the CTE values, it was demonstrated that the CTE values of foams up to 500°C are the same as the value of the cell strut.

9.6 Thermal conductivity

9.6.1 Experimental – Lee's Disc

The thermal conductivity of the foamed specimen (50mm in diameter and ~5-10mm thick, see Figure 9-21) was measured experimentally using Lee's Disc (refer to section 5.3.6). The objective of this experiment was to determine what is (are) the dominating factor(s) for the thermal conductivity of the porous glass-ceramics.

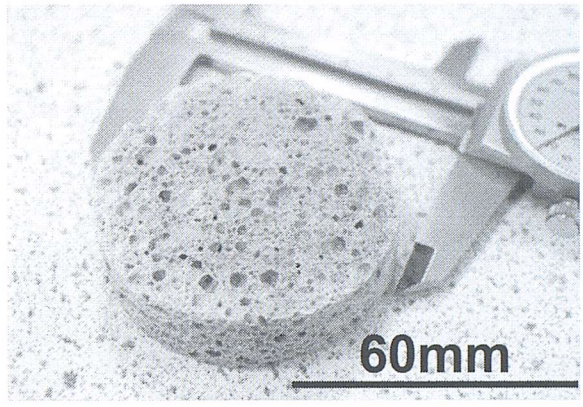


Figure 9-21: Photograph showing a specimen of glass-ceramic foam for Lee's disc measurement

The thermal conductivities measured experimentally were plotted against a) measured density (mass per volume); b) porosity derived from the measured density (1 – relative density); and c) pore size measured by image analysis software (Feret diameter = diameter of a circle of the same area of the object). Figure 9-22 illustrates a good linear trend (Regression analysis gave a coefficient value of 0.97, where 1 is for a perfectly fitted straight line) between the density and the thermal conductivity; as the density decreases the glass-ceramic foam becomes more insulating.

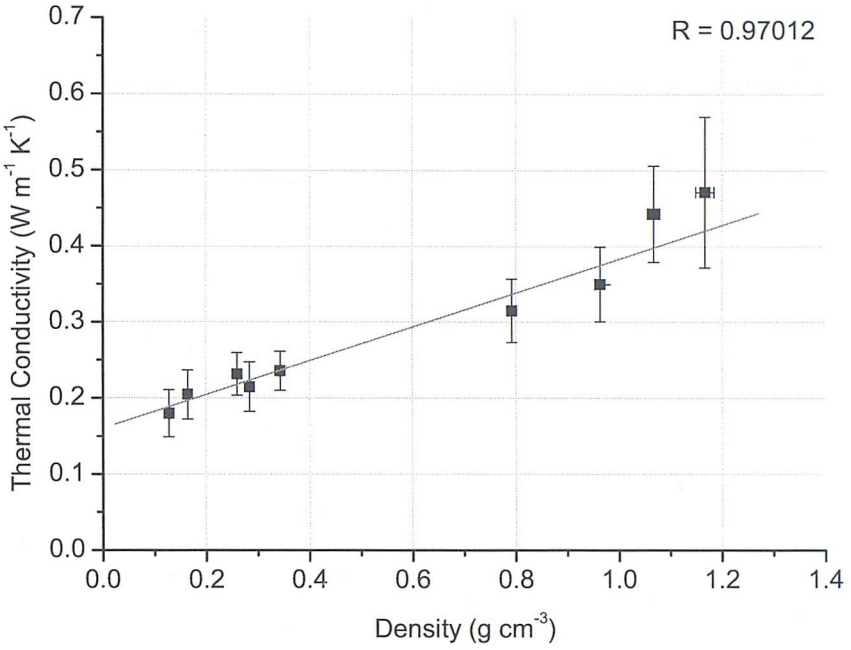


Figure 9-22: Thermal conductivity values versus actual density of PA80G foams

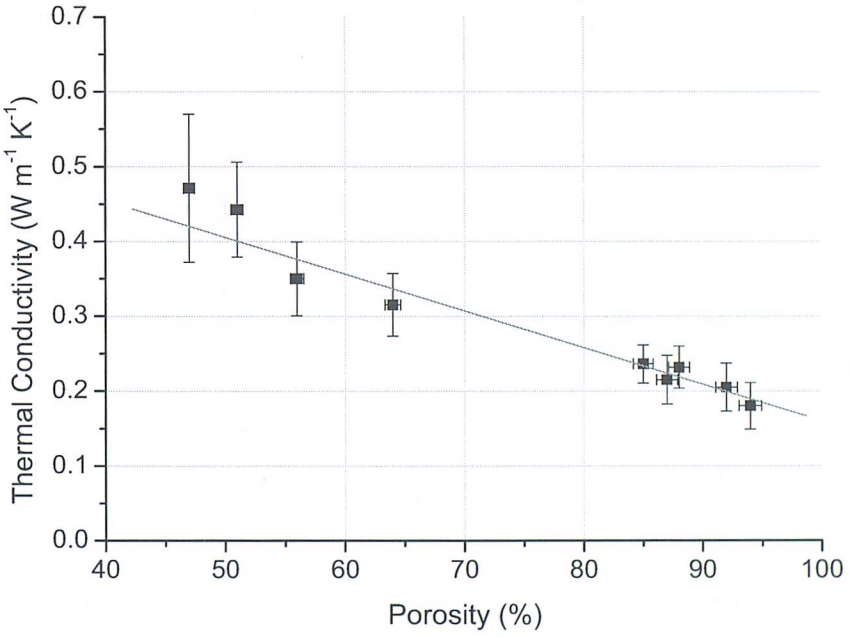


Figure 9-23: Thermal conductivity versus actual porosity of PA80G foams

Since the level of porosity is inversely proportional to the density, the same but inversed linear trend on thermal conductivity is also observed against porosity as

shown in Figure 9-23. Finally, the thermal conductivity is presented as a function of pore size in Figure 9-24. The thermal conductivities of five samples with similar porosity level (85-95%) but with very different pore sizes are highlighted in this figure and demonstrate that there is no clear dependence of thermal conductivity on pore size. It follows that thermal conductivity is largely determined by the level of porosity as illustrated in Figure 9-23.

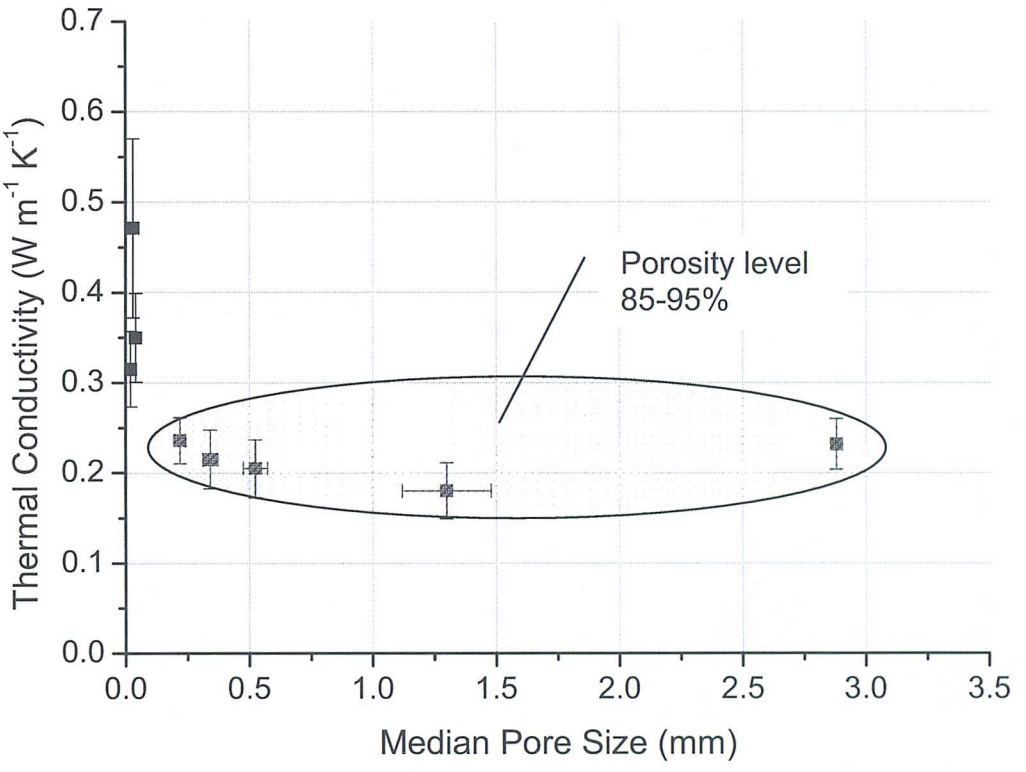


Figure 9-24: Thermal conductivity versus Median Pore Size of PA80G glass-ceramic foams

9.6.2 Models for Heat Conduction

In foams of small pore size, heat transfer by convection is negligible, and radiation at low temperature (room temperature) has minimal effect. Therefore, only conduction was taken into account when analysing the thermal conductivity of the glass-ceramic foams. Leach [213] formulated an equation which predicts the thermal conductivity of a porous solid as a function of the proportion of solid material (i.e. relative density):

$$k = \frac{2}{3} k_s \upsilon_s + k_a$$

Equation 9-1

where 'k_s' is the thermal conductivity of the 100% solid, 'k_a' is the value for air, and 'v_s' is the volume fraction of solid (also known as relative density). The experimental data was plotted against the values extracted from the Leach model, using a k_s value of 1.1 W m^{-1} K^{-1}, as shown in Figure 9-25. The straight line overlaps the first four experimental data points at lower level of porosity but underestimated the thermal conductivities of the foams of higher porosity level.

In order to confirm the misfit of the prediction against experimental data, a sensitivity analysis was carried out by plotting two more Leach curves with a lower (0.8) and a higher (1.4) value of k_s (which are also shown in Figure 9-25); these demonstrate that even with the change in gradient of the curves, the Leach model was not suitable for predicting thermal conductivity of the glass-ceramic foams. It was concluded that the Leach model can only be used for a limited range of porosity levels (<65%), and even then the k value selected for a 100% solid has to be higher than the measured k_s. The Leach curve is best-fitted when k_s = 1.25-1.3 W m^{-1} K^{-1}, which is higher than the experimental value of 1.1 W m^{-1} K^{-1}. The next approach, with the readily available XMT data, is to attempt to predict thermal conductivity of these glass-ceramic foams more accurately by simulation using finite element analysis. The non-destructive nature of this technique is a major advantage, and it enables the possibility of predicting the thermal properties of these foams in different sizes, and acting as a quality assurance step.

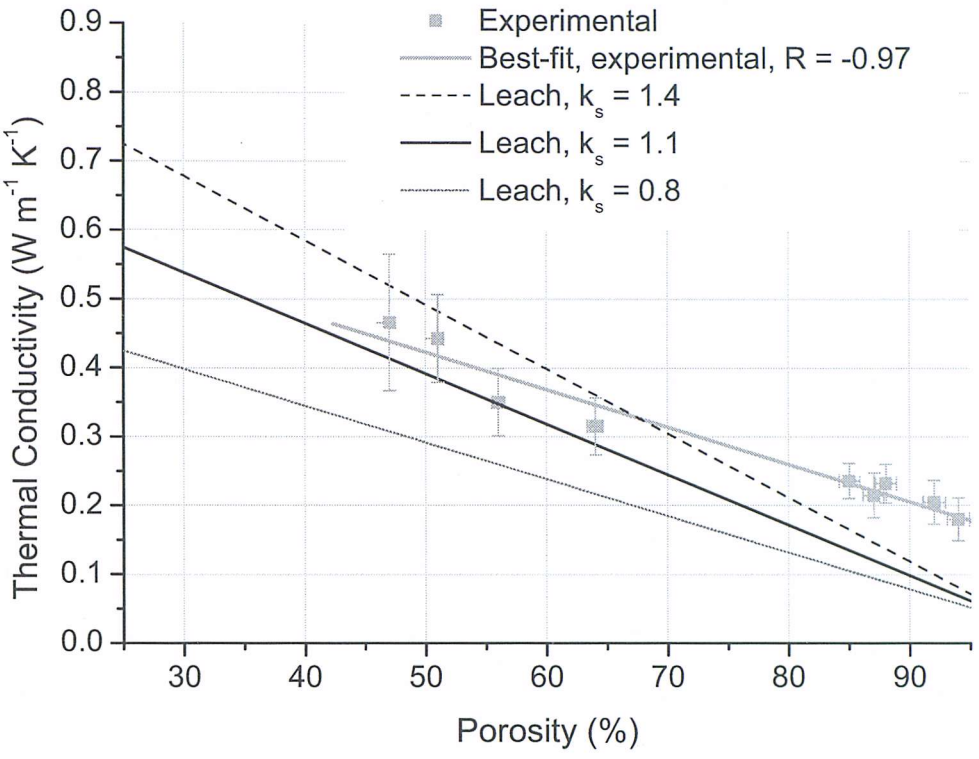


Figure 9-25: Comparison between the experimental data and Leach model

9.6.3 Simulation – Finite Element Analysis

Finite element analysis (FEA) is a computer simulation technique commonly used in engineering analysis. In its application, the object is represented by a geometrically similar model consisting of multiple, linked, simplified representations of discrete regions, i.e. finite elements. Equations of equilibrium, for thermal conduction in this case, are applied to each element, and a system of simultaneous equations is constructed. The system of equations is commonly solved for unknown values using the techniques of linear algebra or nonlinear numerical schemes. While being an approximate method, the accuracy of the FEA method can be improved by refining the mesh in the model using more elements and nodes. In the following section, it is demonstrated that FEA can be used to predict thermal conductivity of a porous material with excellent accuracy. In this study, a mesh was applied (Amira v3.0) to the XMT data of each of the glass-ceramic foam specimens produced under different conditions. Each mesh consists of tetrahedral elements, DC3D4, which are classified for thermal analysis.

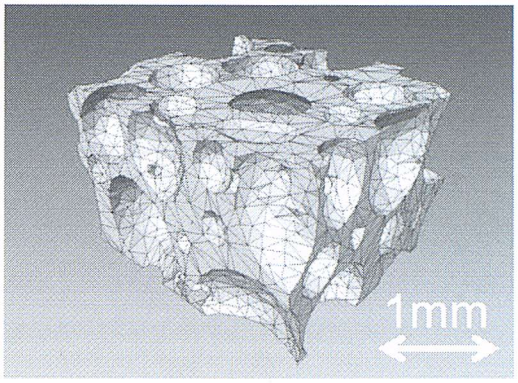


Figure 9-26: A mesh of tetrahedral elements of a sample of PA80G + 2wt%SiC heat-treated at 1050°C

Our initial approach, for simplicity, was only to apply a mesh on the solid struts. This enables a much faster processing time because the number of elements and thus the input file for each model is smaller than if the pores were also modelled. Figure 9-26 is an example of the meshed foam. The thermal conductivity of each sample was simulated using ABAQUS/CAE. Boundary conditions were set to create a temperature gradient across the sample of known cross-section area and thickness. Figure 9-27 gives an illustration of thermal simulation where a piece of foam is subjected to a heat source of 40°C when the initial condition was at 0°C. The input in the analysis is the thermal conductivity of the 100% dense solid, k_s, which was measured at 1.1 ± 0.1 W $m^{-1} K^{-1}$. The output of each simulation, generated after the system reached steady state, was presented in the form of heat flux (W per unit area). The average heat flux per element was then used to back-calculate the thermal conductivity (k) base on the formula for thermal conduction (Equation 9-2):

$$q'' = k\frac{\Delta T}{L}$$

Equation 9-2

Where q'' is the heat flux, ΔT is the temperature difference, and L is the thickness.

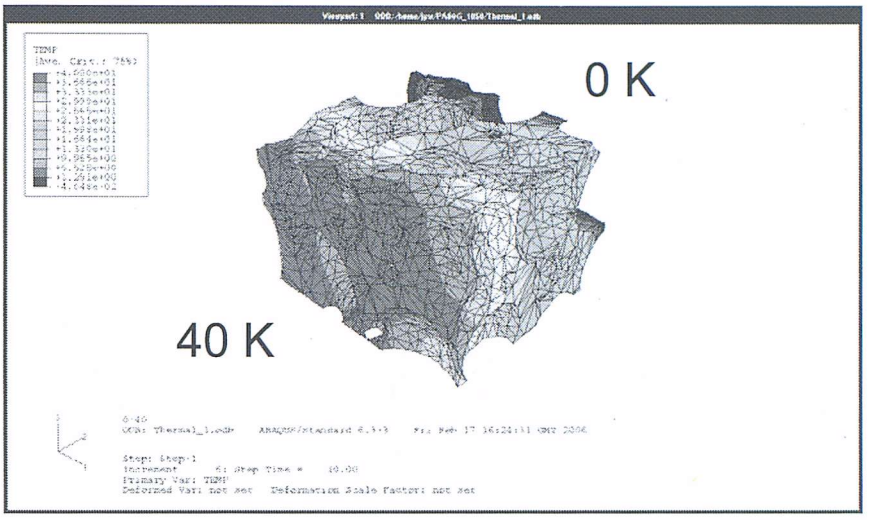


Figure 9-27: Temperature profile of a sample of foam at steady state

The same principle was applied to various temperature differences (70°C and 100°C), and results have showed similar outputs at these temperature differences.

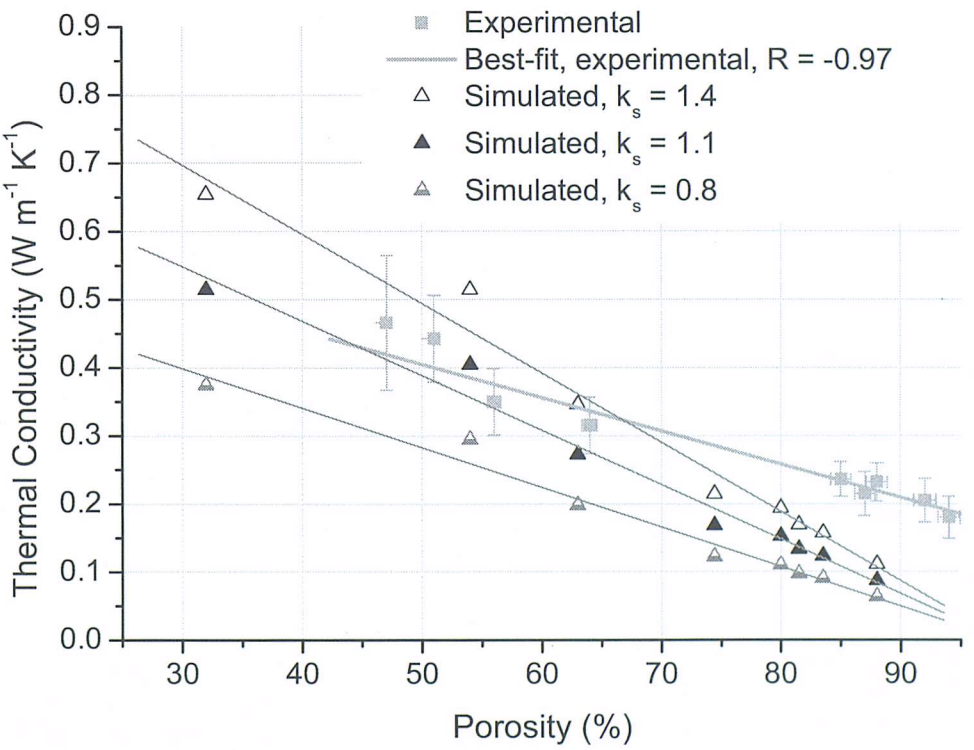


Figure 9-28: Comparisons between the simulated thermal conductivity values and experimental values

Figure 9-28 illustrates the poor fit between the simulated thermal conductivity values by FEA against the experimental data, in particular for highly porous specimens (>60% porous). A sensitivity analysis was also carried out, and straight lines were drawn through each of the simulated data sets as a guide for eyes. In this case, the value of k_s has a very similar effect on the overall slope of the predicted data set as for the Leach model shown in Figure 9-25. The poor prediction by FEA simulation prompted further consideration of a number of factors, which were likely to be direct results of over-simplification of our simulation. It is believed that this discrepancy was caused by one or a combination of the following factors: 1) the accuracy of the XMT model, 2) the accuracy of the mesh (e.g. size of element, level of porosity, pore morphology after meshing), and/or 3) the effect of heat transfer of air (gas) inside pores. A comprehensive analysis was therefore carried out to identify the parameter(s) which had the most influence on the simulation work.

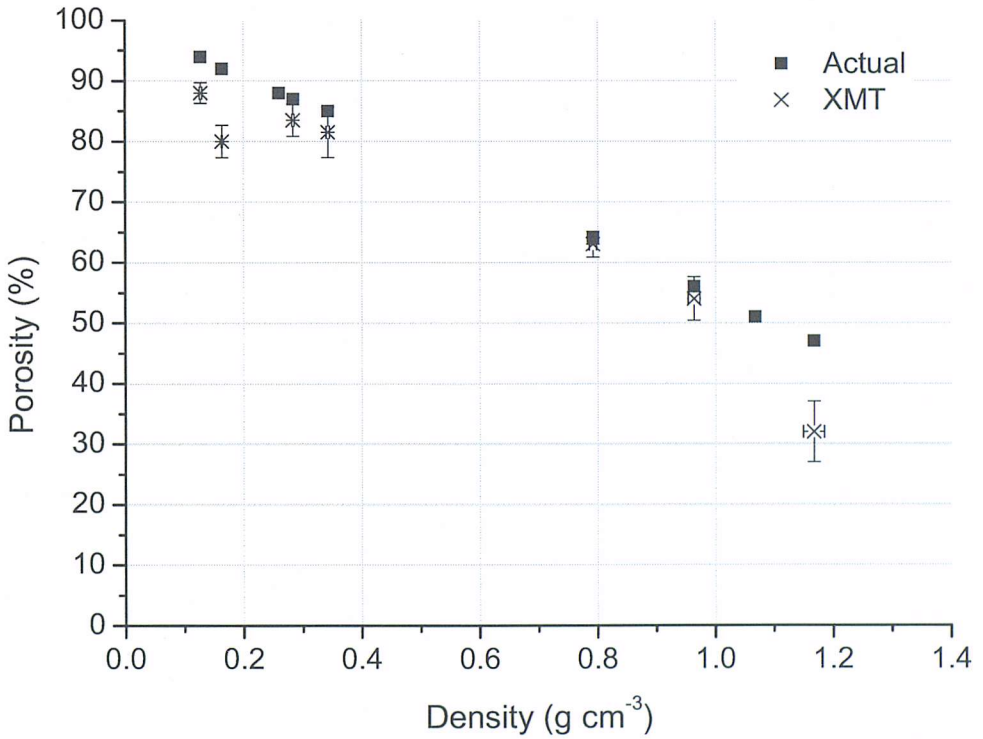


Figure 9-29: Plots of actual density versus actual porosity and XMT porosity

First of all, Figure 9-29 is a plot of the level of porosity versus the actual density measured experimentally. The solid data points represent the level of porosity

directly calculated from the actual density against the density of a fully dense PA80G solid. The crosses represent the porosity values measured from XMT. As the figure showed, there is a ~5% error for most cases, which is mainly due to the limited resolution achievable by the XMT unit used in this study, as mentioned (section 5.2.7). There is always micro-porosity within wall struts that are under the detection limit and thus regarded as solid when scanned. This is especially noticeable for denser foams where the porosity was low and the pores were very small (less than 15μm). Another limitation to the resolution comes from the size of the specimen. In order for the beam of X-ray to scan the entire sample, the distances between the focal point, object, and detector (FOD and FDD, see section 5.2.7) have to be adjusted and thus limiting the maximum achievable resolution. This is demonstrated by the second most porous sample (XMT porosity = 80%) in Figure 9-29, where the error is just over 10%. This particular sample was about 2-3 times the volume of other specimens. Therefore, the resolution of this particular scan was only 35μm per voxel, whereas other scans were done at 10μm per voxel. This means that more micropores (under 35μm) were not detected but considered as solid material. This offset in level of porosity, unfortunately, does not account for the discrepancy from in simulation because the simulated value varies with the level of porosity of the input data (i.e. the meshed model) and thus follows the same linear trend regardless of the improvement in accuracy in the level of porosity. In another attempt, the accuracy of the meshes was enhanced by increasing the number of elements and nodes, which improves the representation of the volume and level of porosity of the output mesh. This, once again, did not provide any marked improvement in the predicted thermal conductivity. The last potential cause is the exclusion of pores in the earlier attempt of our FE analysis. This over-simplification may work only in stress analysis where the gas (air) component does not affect mechanical loading unlike other fluids. It was believed that the thermal conduction of air ($k = 0.025$ W m^{-1} K^{-1}) does have an impact on the overall conductivity of a porous solid, especially when the level of porosity is high. Therefore, instead of excluding the pores during meshing or assuming the pores are 100% thermally insulating, the XMT volumes were re-meshed to include the porosity with a generalized thermal conductivity of 0.025 W m^{-1} K^{-1} (Figure 9-30).

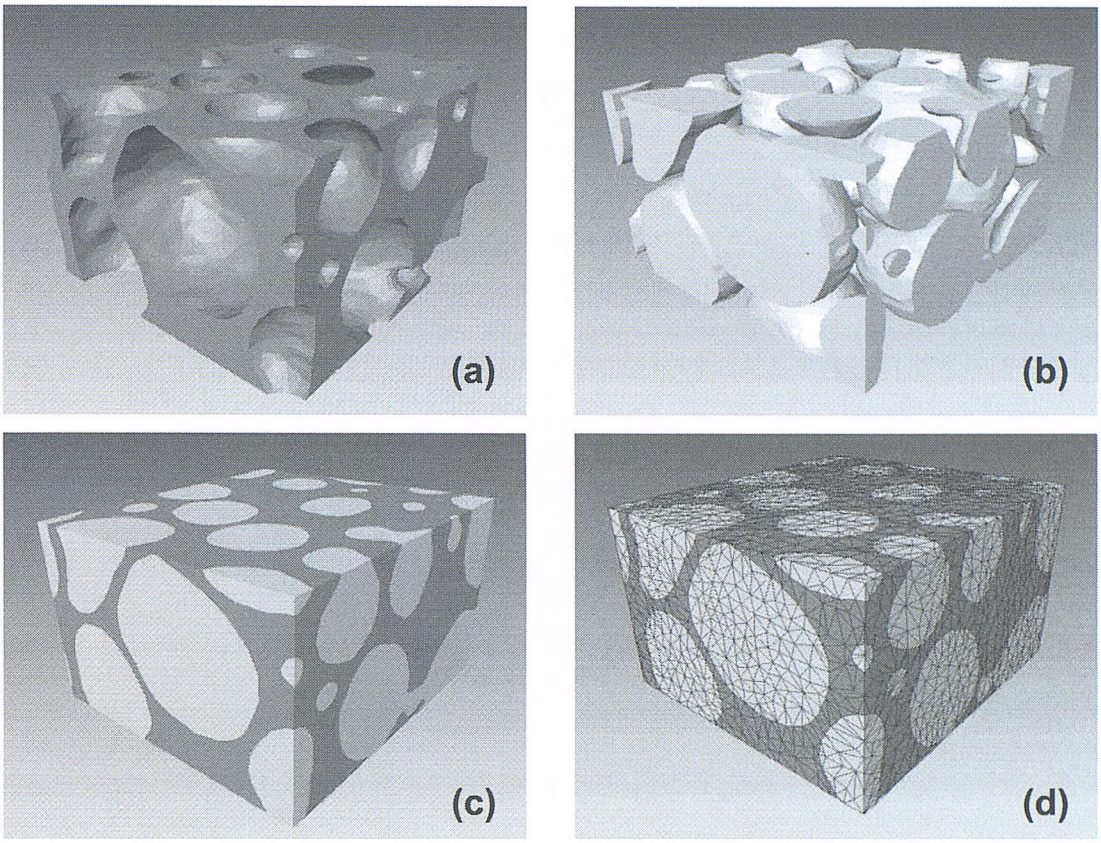


Figure 9-30: Computer generated volume of PA80G glass-ceramic with 2wt%SiC (1050°C), (a) matrix, (b) pores, (c) combination of the two phases, and (d) meshed volume

As Figure 9-30(d) illustrates, there are now two phases (air and glass-ceramic matrix) included in the improved mesh, when the conductivity of air is taken into account. The end result showed a significant improvement in the agreement between the simulated data and the experimental results, as shown in Figure 9-31. A sensitivity analysis using different values of k_s (0.8 and 1.4) indicated it is highly unlikely that the simulated data fitted the experimental data by chance. That is, the prediction was only made possible by inputting the correct k_s (1.1 in this case). In conclusion, the effect of thermal conduction by air on the overall thermal conductivity of each sample is of importance especially at high level of porosity. This is a very satisfactory result as we are able to demonstrate that an accurate prediction can be made on thermal property of porous solids by using FEA in conjunction with the technique XMT. Note that, sufficient computing power and software capabilities are required for efficient analysis. Otherwise, it can be a time-consuming process.

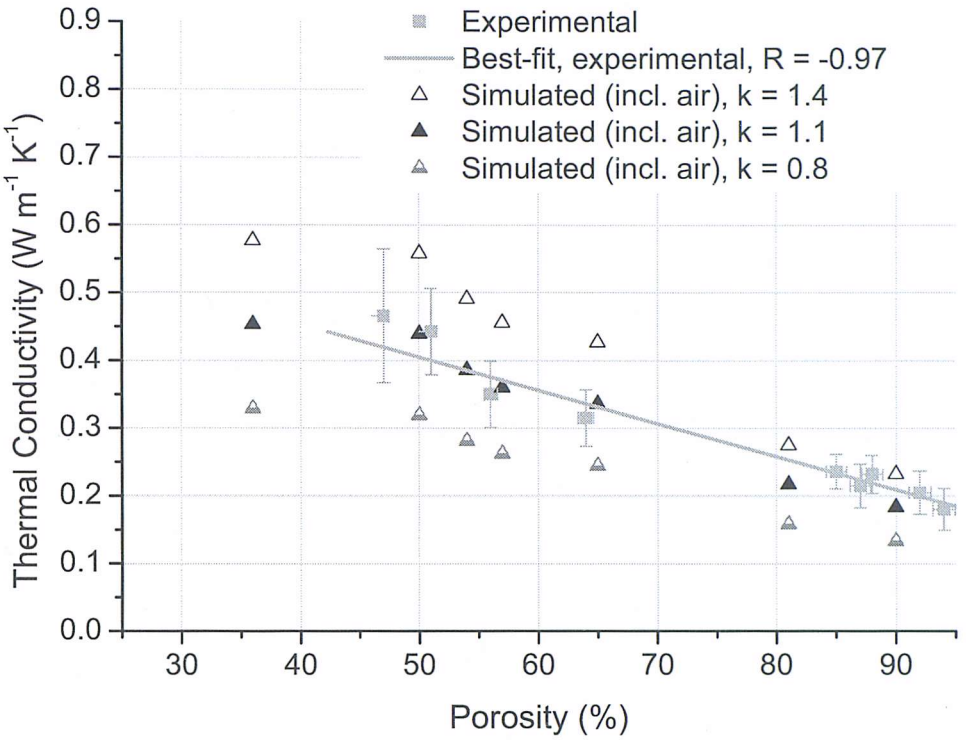


Figure 9-31: Simulated thermal conductivity values showing good agreement with the experimental values obtained from Lee's Disc.

9.7 Mechanical Properties

The mechanical properties of a highly porous material are significantly different to its dense parent material due to the presence of porosity (flaws). Table 9-2 shows a comparison between the foam produced in the preliminary study and commercial products such as Foamglas® which is a well-established insulation material manufactured by Corning and NORFOAM^{TM} A from Saint-Gobain Ceramics. The mechanical properties (except for the elastic modulus) of the PA80G are fairly competitive, if not better, when compared with the commercial products. In terms of insulation property, Foamglas® has porosity that is fully closed (without interconnection), which optimises the insulating ability, i.e. low thermal conductivity, of the porous material. Since the PA80G glass-ceramic foam is denser than the Foamglas, this may explain the higher mechanical strength and the poorer insulation. Similar comparison can be made between NORFOAM^{TM} A and the PA80G glass-ceramic foam.

Table 9-2: Comparison of the properties of PA80G foams, Corning Foamglas®, and Saint-Gobain NORFOAM™A

Material Property	Unit	PA80G 2wt% SiC (1050°C)	NORFOAM™ A	Foamglas ®
Density, average	g/cm^3	0.23	0.5	0.12
Coefficient of thermal expansion (25°C to 300°C)	$10^{-6}\ K^{-1}$	8.3	-	9.0
Thermal Conductivity	$W\ m^{-1}\ K^{-1}$	0.26	0.45	0.04
Young's Modulus	MPa	670	-	900
Flexural Strength	MPa	0.66±0.17	1	0.48
Compressive Strength	MPa	1.41±0.29	1	0.62

Overall, the PA80G glass-ceramic foam has the potential to be used as a thermal insulation material provided that it is completely characterized. The following section delves into detailed investigations on the determination of Vickers hardness, modulus of elasticity, flexural strength and compressive strength. Some of these properties are correlated against relative density, providing a better understanding of the behaviour of these foams so these materials can be designed with different properties by controlling the relative density (level of porosity).

9.7.1 Vickers Hardness

Vickers indentations were made on the wall struts of PA80G with 2wt%SiC heat-treated at 1000°C. Student's t-test has confirmed that the Vickers hardness (25g, 10s) on wall struts (5.2 ± 0.2 GPa) has no significant difference from the hardness values of the 100% dense parent material (5.3 ± 0.1 GPa).

9.7.2 Modulus of Elasticity

The modulus of elasticity (E) was measured on bar specimens of bulk and foamed glass-ceramics using the impulse excitation technique (See section 5.3.1). For the fully dense PA80G glass-ceramic, E = 63 ± 4 GPa, and a range of E-values were also obtained from foams of various relative densities (Figure 9-32). The level of porosity was obtained by adjusting the amount of SiC used as well as the heat-treatment temperature. The error on the individual relative density is approximately 0.1-0.3% contributed from measurement errors.

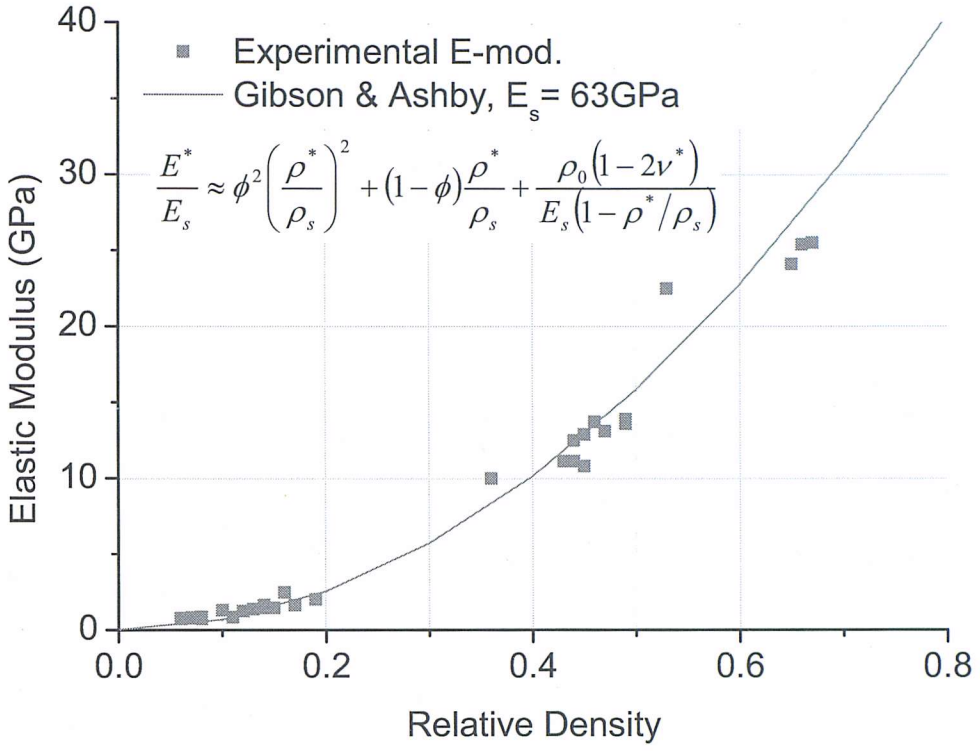


Figure 9-32: Comparison between the modulus of elasticity values obtained experimentally and mathematically.

Note that a model (Gibson & Ashby) [214] was applied to investigate the agreement between the model and the experimental results. Gibson & Ashby's model consists of three components or contributions which sum up to give a prediction of the Young's modulus. The formula derived by Gibson and Ashby is expressed as:

$$\frac{E^*}{E_s} \approx \phi^2\left(\frac{\rho^*}{\rho_s}\right)^2 + (1-\phi)\frac{\rho^*}{\rho_s} + \frac{p_0(1-2\nu^*)}{E_s(1-\rho^*/\rho_s)}$$

Equation 9-3

E^* is the Young's modulus of the material of a certain relative density, E_s is the Young's modulus of the solid (100% dense), Φ is the volume fraction of solid in the cell edge ($\Phi = 1$ for an open cell foam), ρ^*/ρ_s is the relative density, p_o is the gas pressure (it is assumed to be atmospheric pressure for simplicity in this case), and υ^* is Poisson's ratio.

The first component that contributes to the stiffness of the material is cell-edge bending; the second contribution is that caused by the compression of the cell fluid, in this case, air; and the third one comes from the cell faces, which stretch when the cell edges are bent. When the cell fluid is air (at atmospheric pressure in this case), the contribution is very small. Nevertheless, it was included for the completeness of the model [214].

Figure 9-33 shows the effect of gas pressure was indeed negligible (an example was shown at $\Phi = 1$). Therefore, the main mechanisms for the stiffness of the foam are cell-edge bending and cell-face stretching. Furthermore, Figure 9-33 gives indication to the effect of open/closed nature of the porosity on its mechanical behaviour. As the figure illustrates, the Gibson & Ashby model gives a different fit with different values of Φ, and a best-fit curve was found at approximately $\Phi = 0.9$.

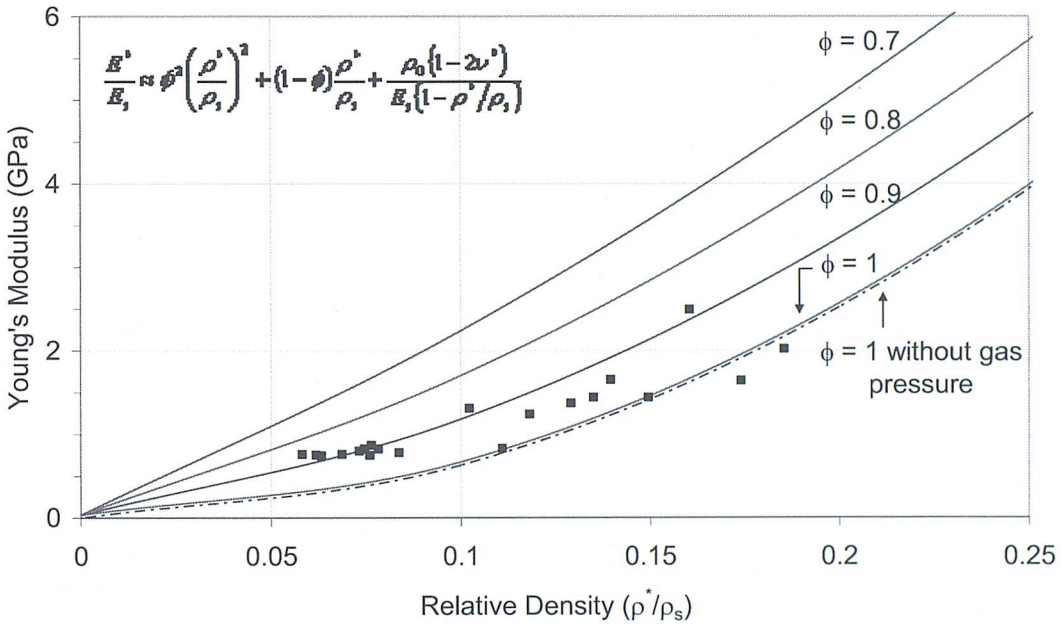


Figure 9-33: Young's modulus values of low-density glass-ceramic foams and its corresponding fit curves derived from a Gibson & Ashby model using different Φ values.

To prove that the value of Φ (for the best-fit curve) is realistic, a cubic model (Figure 9-34) shows the simulated configuration of a closed cell pore, with 'T_e' as the thickness of each cell edge, 'T_f' as the thickness of the face, and 'd' as the cell diameter (length).

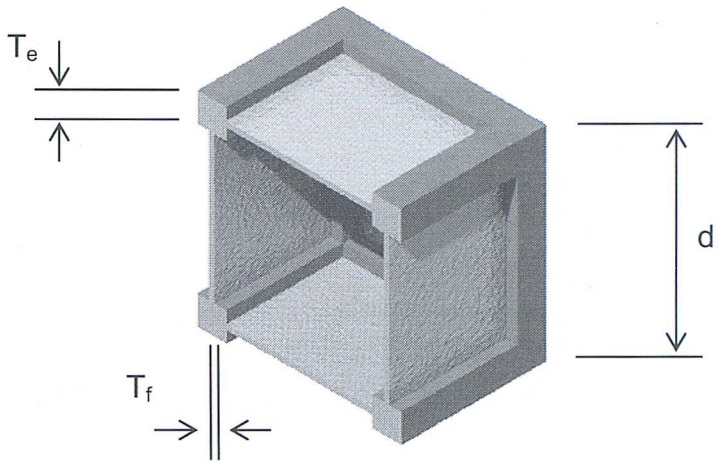


Figure 9-34: Illustration of a closed unit cell with cell edges and cell walls

This model was used to approximate the volume fractions of solid in the cell edges (Φ):

$$\text{Total Volume} = 4T_e^2 d + 8T_e^2(d - 2T_e) + 6(d - 2T_e)^2 T_f$$

$$\text{Volume of Cell Edge} = 4T_e^2 d + 8T_e^2(d - 2T_e)$$

$$\phi = \frac{\text{Volume of Cell Edges}}{\text{Total Volume}}$$

Equation 9-4

The pore size and face thickness (wall thickness) values correspond to the results obtained from XMT (refer to Figure 9-15), and the results are tabulated as follows:

Table 9-3: Volume fraction of solids in cell edges of different PA80G glass-ceramic foams, calculated using Gibson & Ashby model

Material	**Average Pore size, d (μm)**	**Edge Thickness, T_e (μm)**	**Face Thickness, T_f (μm)**	**φ**
1000°C/2wt%SiC	390	108	36	0.84
1050°C/2wt%SiC	802	230	53	0.89
1100°C/2wt%SiC	1370	355	65	0.89

The Φ -values were in between 0.8~0.9, which is in reasonable agreement with the approximated cell morphology (Φ = 0.9) from the Gibson & Ashby model and hence confirms the validity of the prediction model (Figure 9-33).

9.7.3 Flexural and Compressive Strengths

Three-point bending test was conducted to determine the flexural strength of PA80G glass-ceramic foams. As Figure 9-35 shows, the flexural strength follows a similar trend as the elastic modulus. The flexural strength increases with relative density (i.e. decreasing number of flaws). However, since the failure mechanism under bending is relatively more complicated due to tension below the neutral plane and compression above the plane, only the experimental compressive strength values were compared against the theoretical model obtained by Gibson & Ashby [214].

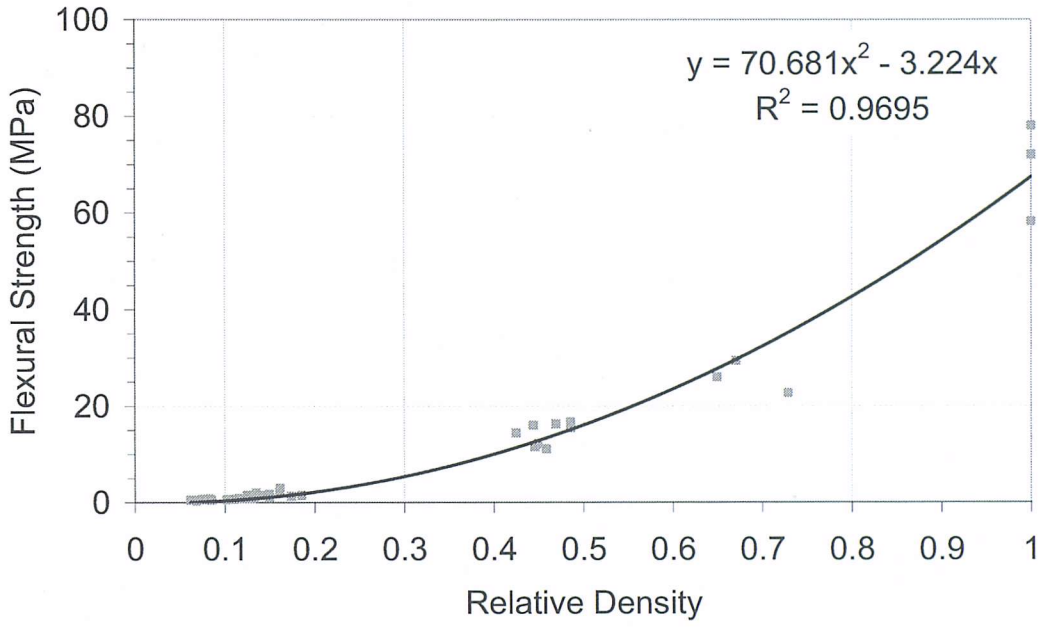


Figure 9-35: Flexural strength versus relative density shows a trend following a polynomial equation to the degree of 2

The best-fit curve was a polynomial (to the degree of 2) function which follows a similar profile as the data points (Figure 9-35). The regression analysis factor of 0.9695 corresponds to the best-fit curve expressed in the following equation:

$$y = 70.681x^2 - 3.224x$$

Equation 9-5

where 'y' is the flexural strength and 'x' is the relative density. Under closer examination, there is a resemblance of this formula to the Gibson & Ashby model

(Equation 9-3) used for the prediction of Young's modulus without the gas pressure component. In this case, the polynomial equation may be expressed in terms of the relative density, provided $\phi = 0.9$:

$$\frac{\sigma_{fs}^*}{\sigma_{fs}} = 1.26\phi^2\left(\frac{\rho^*}{\rho_s}\right)^2 - 0.46(1-\phi)\left(\frac{\rho^*}{\rho_s}\right)$$

Equation 9-6

where σ^*_{fs} (or y in Equation 9-5) is the flexural strength of the foam, σ_{fs} is the flexural strength of the fully dense solid, and ρ^*/ρ_s is the relative density. A more detailed plot of the flexural strength data for the low density foams (0.05-0.20 relative density) shows (i) considerable scatter in the experimental values and (ii) that the best-fit curve to all the data falls slightly below the low density results (Figure 9-36). This raises the issue of predicting the complex material behaviour in bending.

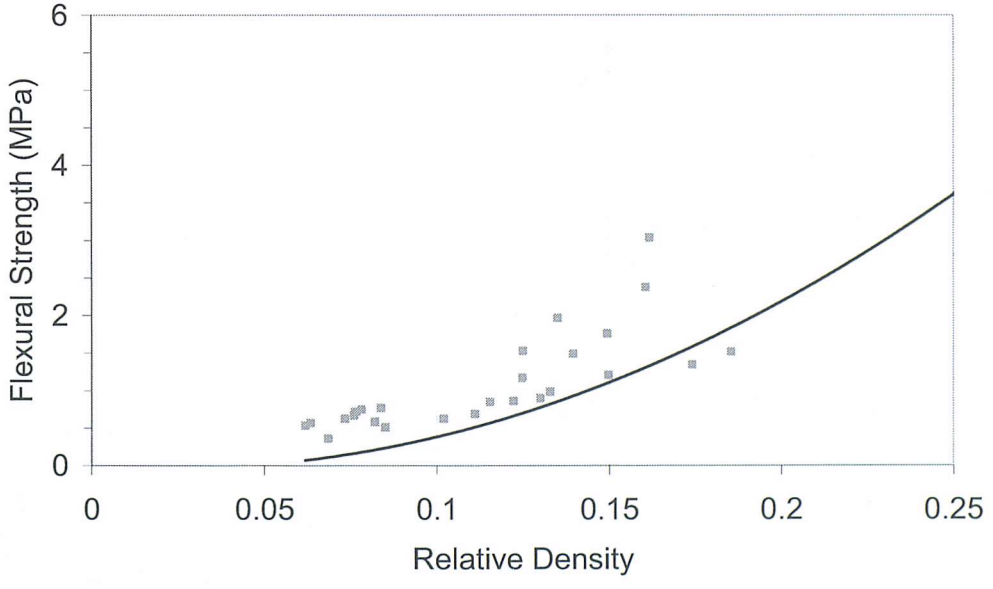


Figure 9-36: Flexural strength values of PA80G glass-ceramic foams with relative densities of 0.05 to 0.20

In terms of compressive strength, cubic foam samples were subjected to compression according to the procedure outlined in Chapter 5. As far as compressive strength is concerned, when the load is compressive the plateau in the typical stress versus strain curve is associated with collapse of the cells near the contact ends by brittle crushing

in a brittle foam (e.g. ceramic, glass, and glass-ceramic) [214]. When the cells have almost completely collapsed opposing cell walls touch and further strain compresses the solid itself, giving the final region of rapidly increasing stress. This phenomenon is demonstrated by examples of stress versus strain plot of PA80G glass-ceramic foams under compressive loading (Figure 9-37). The figure shows an elastic region for each sample, followed by a plateau where the brittle crushing took place, and then finally the densification stage where the collapsed cells compressed together furthermore. Note that increasing the relative density of the foam increases Young's modulus (as found earlier), and thus raises the plateau stress and reduces the strain at which densification starts (Figure 9-37). Similar behaviours such as the progressive crushing of cells have been reported in brittle cordierite foams [215].

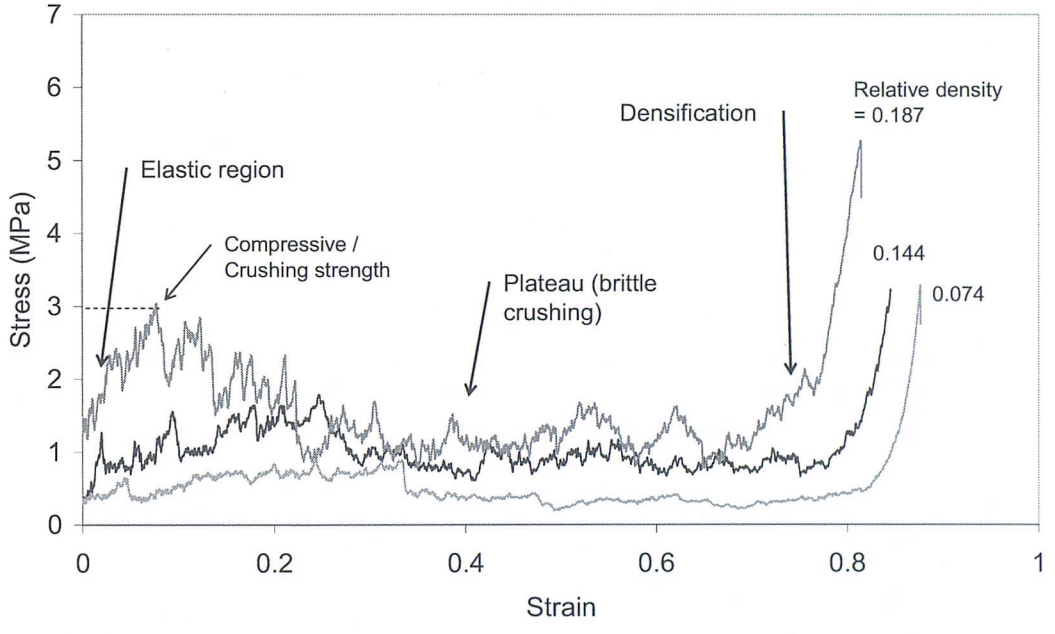


Figure 9-37: Stress versus strain curves of PA80G glass-ceramic foams of different relative density showing typical behaviour of a brittle foam under compression

Figure 9-38 illustrates the surfaces of two glass-ceramic foams that had undergone brittle crushing (at 20-30% strain). These images were taken at the top and bottom surfaces of the foams which were in contact with the compression platens. Note that the fractures appeared very brittle and any cracking was only visible near the contacting surfaces, indicating that the foams did fail gradually as suggested by the brittle crushing mechanism

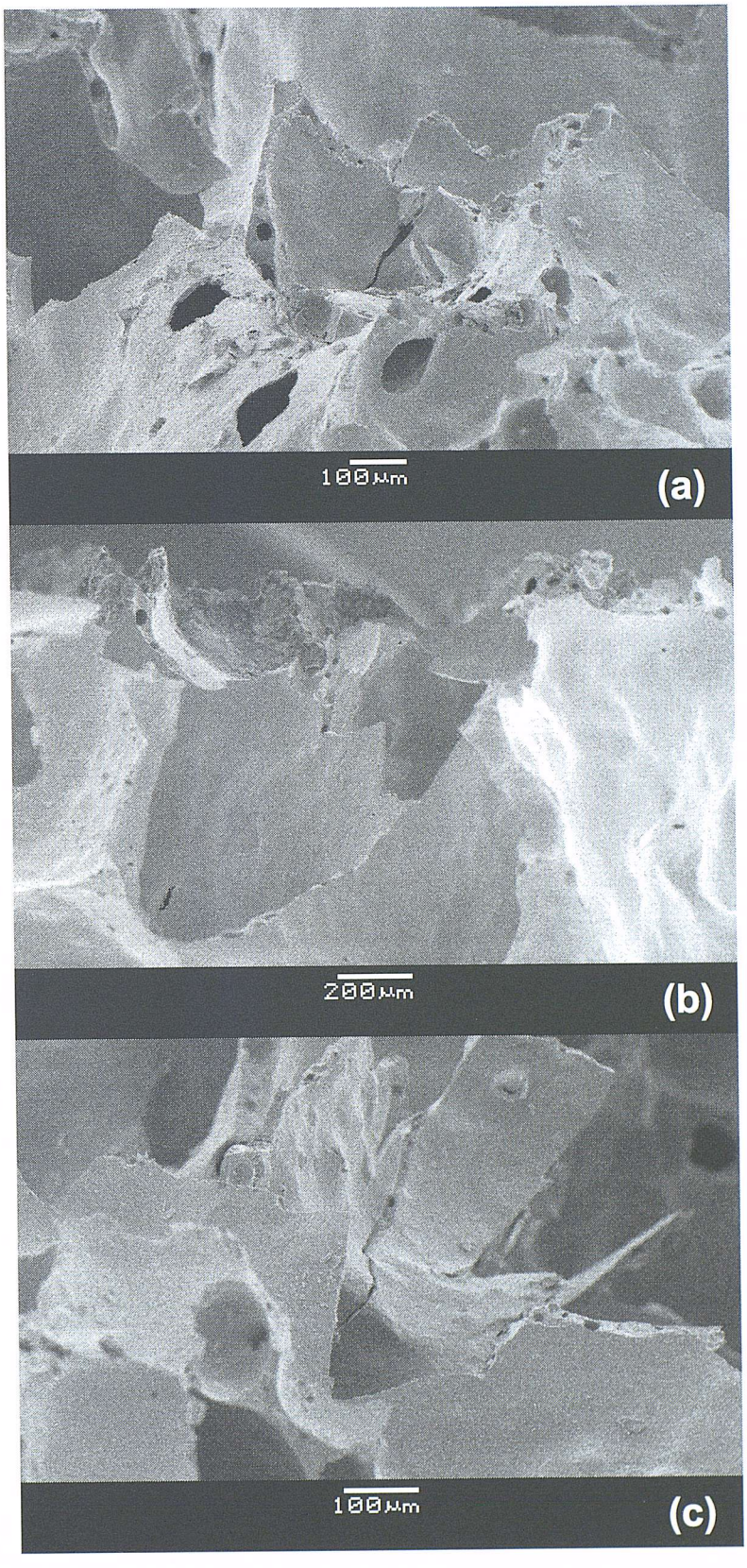


Figure 9-38: Fracture surfaces of PA80G glass-ceramic foams heated treated at (a) 1000°C, (b) and (c) 1050°C.

In Figure 9-39, the compressive strength (or crushing strength for a brittle foam) values were plotted against the relative density of foams and compared against the theoretical compressive strengths derived using a Gibson & Ashby model (Equation 9-7).

$$\frac{\sigma^*_{cr}}{\sigma_{fs}} = 0.2\left(\phi\frac{\rho^*}{\rho_s}\right)^{3/2} + (1-\phi)\left(\frac{\rho^*}{\rho_s}\right)$$

Equation 9-7

'σ^*_{cr}' is the crushing strength, 'σ_{fs}' is the flexural strength, 'ρ^*/ρ_s' is the relative density, and ϕ is the same parameter as in Equation 9-3 (and it equals 1 when the foam is 100% open-celled).

The comparison was encouraging as the data points fitted best when ϕ (the same parameter representing the volume fraction of solids in cell edge) equals 0.90 ± 0.05, which agrees with the previous approximation for Young's modulus. Note that each data point represents a single measurement of a sample of particular relative density. Despite no error bars were included in the figure, the error from calculation of the relative density is low (0.1-0.3%), and the systematic error from the compressive strength values is minimal (contributed mainly from measurement of cross-sectional area).

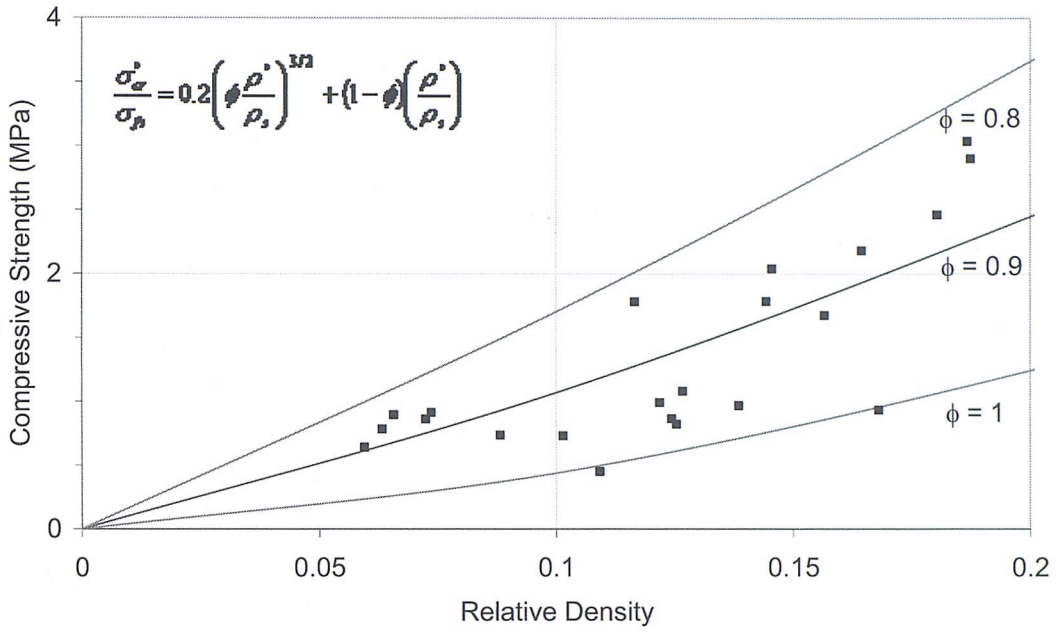


Figure 9-39: Comparison between experimental compressive strength and values determined theoretically

The failure mode for the highly porous foams, as mentioned before, is the layer-by-layer brittle crushing. However, it was sometimes observed in the load versus extension curves that a specimen can fail dramatically caused by cracks running parallel to the loading direction. One possibility is barrelling, which can occur if there is friction between the contact surfaces [216]. Barrelling can cause tension perpendicular to the compressive loading direction, initiating cracks across the sample. Another possible cause is contributed by an accumulation of debris from the brittle crushing of layers of porous material on the top and bottom surfaces (an illustration is given in Figure 9-40). When the fragments start to fill up the outer pores, this can cause tension in the pore walls, and thus initiate cracking from the cell walls. This is a hypothesis which needs further work to be proven.

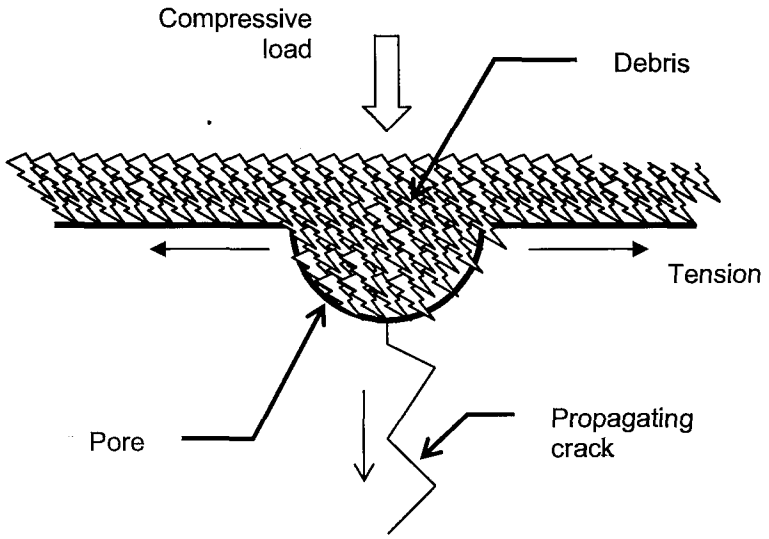


Figure 9-40: Illustration of foam fragments building up in pores on the contact surface, and generating tension and thus cracks parallel to the compressive loading.

One of the major advantages of porous materials is their light weight and therefore specific strength. Figure 9-41 is a summary of generic materials in relation to their specific strength and specific stiffness (specific modulus). Also included in the chart are data points representing the samples of waste-derived materials tested during this study and relevant reference materials, indicating where these materials belong in terms of specific modulus and strength. It is very encouraging, first of all, that the dense materials from Chapter 7 and Chapter 8 have specific properties similar to most glass, ceramic, and composite materials. The PA80G glass-ceramic foams, on the other hand, have a very good stiffness to weight ratio (i.e. high specific modulus) but relatively low strength to weight ratio, which is common for most foams (as illustrated in Figure 9-41).

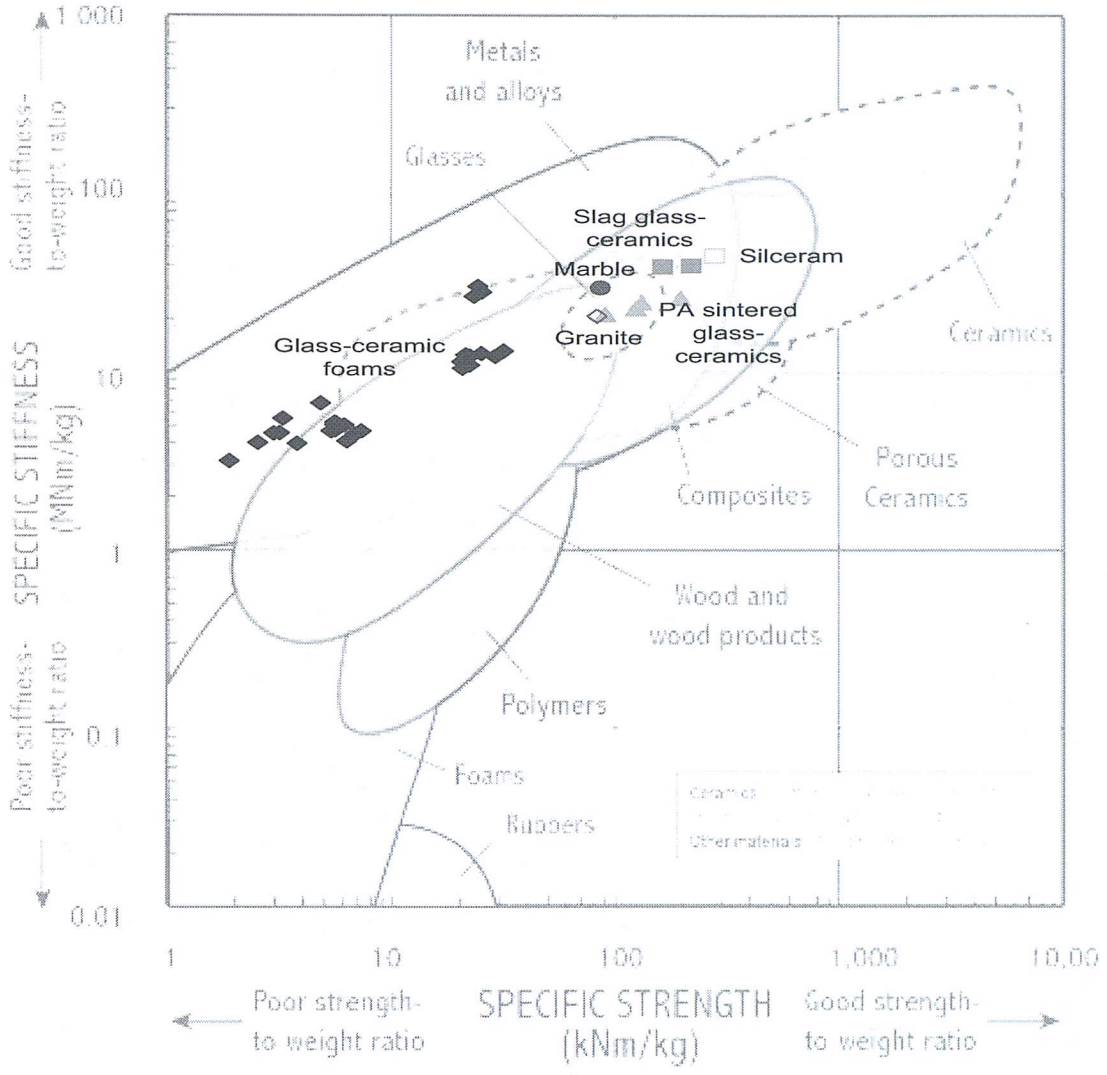


Figure 9-41: Specific stiffness versus specific strength chart [217] for generic materials, materials investigated during the study, and reference materials from literature.

9.7.4 Effect of Thermal Shock on Compressive Strength

Thermal shock resistance of the foamed glass-ceramic was also measured. For materials that contain large flaws (such as the pores in the foams), their resistance to thermal shock should be good although their initial strengths would be low as expected [218]. The subject was PA80G with 2%SiC heat-treated at 1000°C for 5 minutes. Each specimen was machined to cubes about 10mm wide each side (Figure 9-42). Relative thermal shock resistance was determined by their compression strengths.

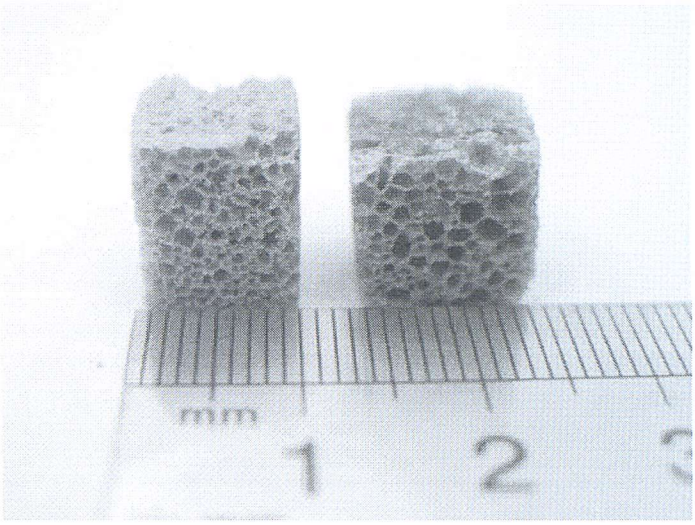


Figure 9-42: Specimens of PA80G with 2wt% SiC used for compressive strength test

Figure 9-43 summarises the results obtained from 3 different batches of tests, and shows a gradual reduction in compressive strength with increasing ΔT. It was expected that the thermal shock resistance is better for a foam when compared to its parent fully dense solid. The resistance also improves as the density of the foam decreases [214]. The thermal shock resistance is improved because the porous network can withstand thermal strain by bending.

There is no clear critical temperature as the material slowly deteriorated in strength with quenching temperature. The deterioration was contributed by the additional defects as the material could no longer withstand the strain under elevated temperatures. In the case of dense materials, as shown in the previous two chapters (Chapter 7 and Chapter 8), there was a thermal resistance limit (critical temperature) above which the mechanical properties of the thermally shocked materials are significantly inferior to the as-received one. For example, a 300K quench from ambient temperature has led to a 33% reduction in strength (from about 1.5MPa to 1.0MPa) for the foam, whereas for dense materials it was greater (Chapter 7: 56% for PA10G, 67% for PA30G, and Chapter 8: 89% for MS40G). This indicates that the highly porous (flawed) materials do have better thermal shock resistance than dense materials in general.

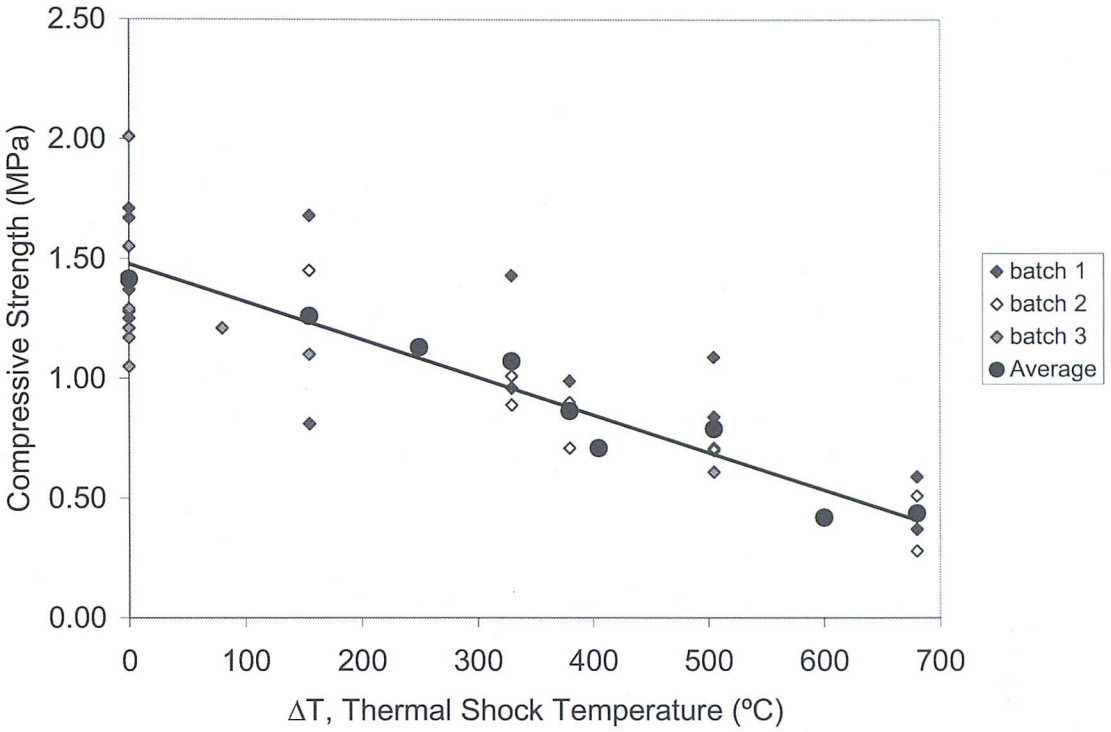


Figure 9-43: Compressive strength of PA80G + 2 wt% SiC 1000°C foams as-sintered, and quenched from various temperatures

9.8 Density-Graded Glass-Ceramic Foam

In an attempt to produce near-net shaped foams at relatively low temperature (900-975°C), a foam with noticeable density gradient was produced (Figure 9-44). The material was characterised using XRD and its compressive strength was measured.

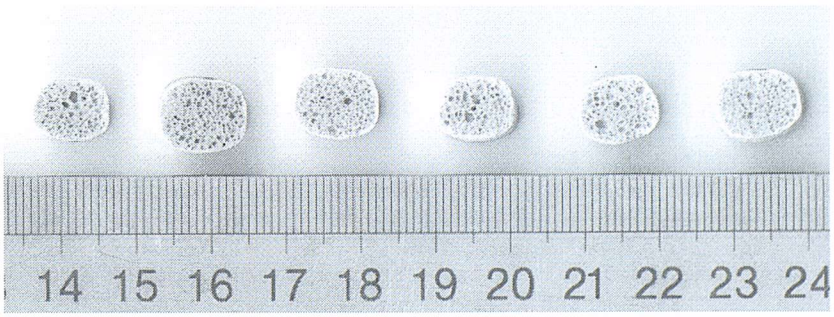


Figure 9-44: Cross-sections of the density-graded foams (PA80G 2wt%SiC) produced at 950°C

XRD (Figure 9-45) showed that there is no significant difference in the crystalline phases present in the porous core and the denser outer shell. The degree of

crystallinity was very similar at 22±2%. The main crystalline phase of this density-graded foam is wollastonite, which is the same as the more porous glass-ceramic foams discussed earlier in this chapter. Similarly, there is a minor trace of silica which was also present when the foams were produced at temperatures around 950°C.

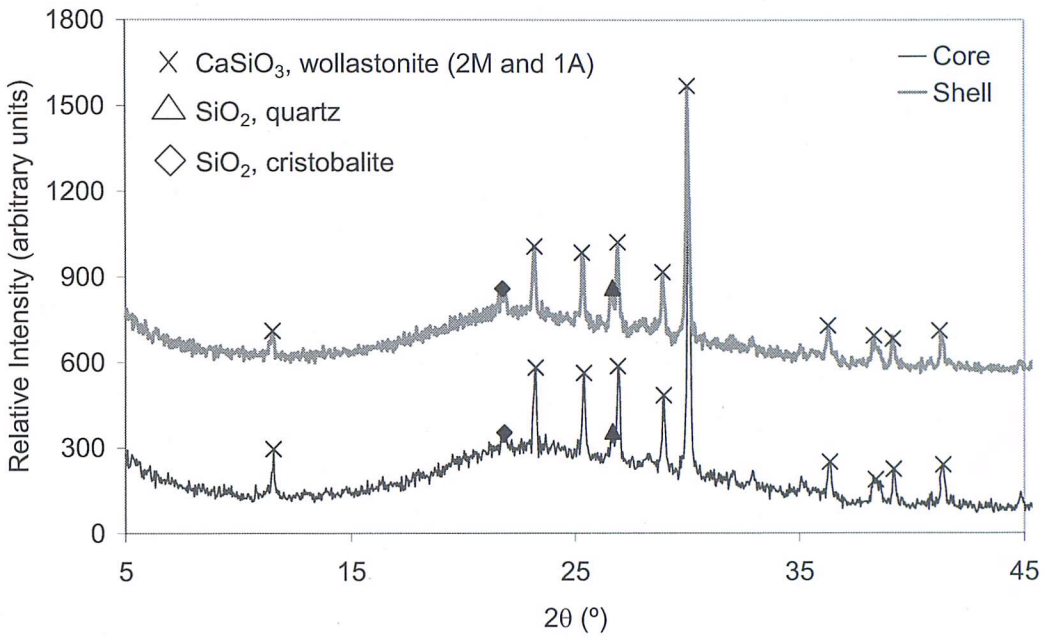


Figure 9-45: XRD spectrums showing the crystalline phases present in the core and shell of the density graded glass-ceramic foam

The compressive strength of the density-graded foam was measured at 3.91 ± 1.36 MPa, which is almost 3 times higher than the same porous material but without the dense shell. A mathematical model was applied to simulate this configuration, so this information could be used to adjust the structure (density) in order to obtain desired mechanical properties. First of all, there are two principle models to predict the mechanical strength of a composite material according to its configuration; Voigt and Reuss, which are illustrated in Figure 9-46.

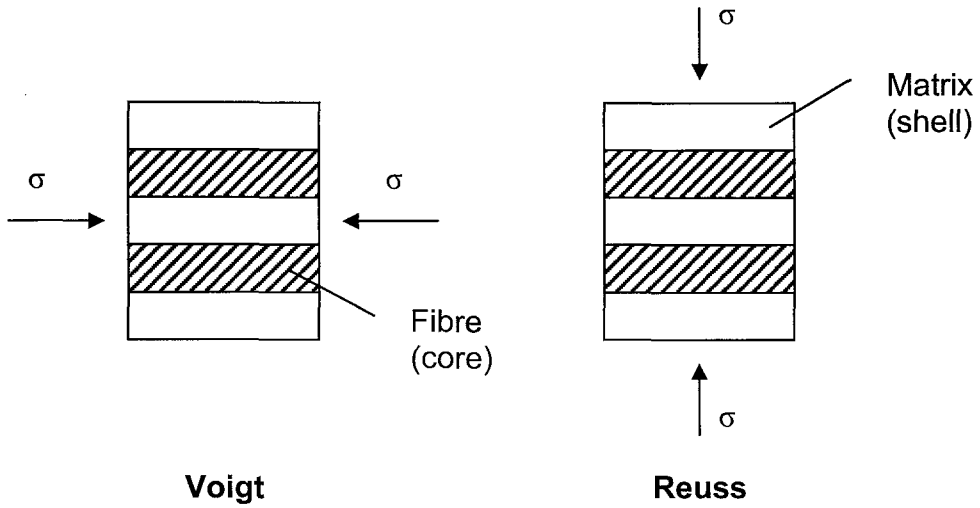


Figure 9-46: Voigt and Reuss models for predicting the mechanical strength of fibre-reinforced composites

The Voigt model [219] can be applied when the stress applied is parallel to the layers of fibre and matrix:

$$\sigma_{comp} = v_f \sigma_f + v_m \sigma_m$$

Equation 9-8

On the other hand, the Reuss model [219] is when the stress applied is perpendicular to the layers:

$$\frac{1}{\sigma_{comp}} = \frac{v_f}{\sigma_f} + \frac{v_m}{\sigma_m}$$

Equation 9-9

The subscripts '*f*' and '*m*' are for fibre and matrix, respectively. 'υ' is the volume fraction of a phase [in the case of the investigated foams, $\upsilon_{shell} = 0.18$, $\upsilon_{core} = 0.82$], and 'σ' is the compressive strength [$\sigma_{shell} = 63$MPa, $\sigma_{core} = 1.4$MPa]. Based on the two simple models, the Voigt model predicted an overall strength value of $0.18 \times 63 + 0.82 \times 1.4 = 12.49$MPa and the Reuss model gave a value of 1.70MPa. Although the experimental values lie between the bounds given by Voigt (upper bound) and Reuss

(lower bound), neither model gave a reasonable value because neither model has a good approximation to the actual configuration of the porous structure (air/matrix composite). Therefore, a more complex model was introduced. In the study of bone mechanics, a composite model was derived from a combination of Voigt and Reuss modes for the mechanics of bones [219]. Since the foam with density gradient has a structure similar to bone where the porous core is like the porous trabecular bone, and the dense shell is like the dense cortical bone, the following equation was applied to the glass-ceramic foam [220]:

$$\frac{1}{\sigma_{composite}} = x\left(\frac{1}{\upsilon_{shell}\sigma_{shell} + \upsilon_{core}\sigma_{core}}\right) + (1-x)\left(\frac{\upsilon_{shell}}{\sigma_{shell}} + \frac{\upsilon_{core}}{\sigma_{core}}\right)$$

Equation 9-10

where 'χ' is the relative proportion of the material that is arranged in the parallel strain condition (Voigt) [In this case, 0.575, assuming that the core has 50% in the Voigt configuration]. Using Equation 9-10, the results are summarised in Table 9-4.

Table 9-4: Comparison between the experimental compressive strength and predicted value

	Experimental compressive strength (MPa)	**Predicted compressive strength (MPa) -**
PA80G density-graded foams	3.91 ± 1.36	3.4 ± 0.9

This prediction was very successful. Therefore, as an aside, Equation 9-10 was used to predict the compressive strength of the density-graded foam with an array of volume fractions of shell and core, as well as looking at different configurations (mechanical behaviour under different loading conditions). The results are summarised as Figure 9-47 and Figure 9-48. In Figure 9-47, three different orientations were investigated: (a) dense shell parallel to the compressive load, (b) shell perpendicular to the load, and (c) where the porous core completely covered by the shell.

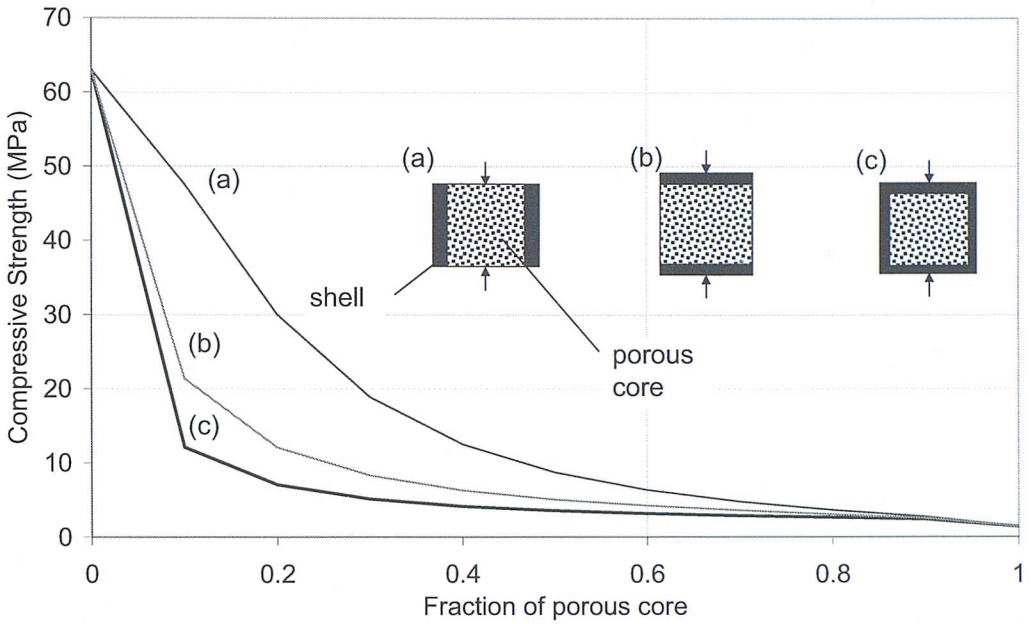


Figure 9-47: Prediction of the compressive strength with respect to the loading configuration and fraction of porous core

All three configurations gave different predicted strength values at different volume fraction of porous core, this is particularly noticeable at low density (i.e. with high quantity of dense shell), where the mechanical strength of dense material had most impact. However, note that the materials (foams) that were readily produced in this study are highly porous, so the most applicable data would come from ones with core volume fractions over 0.5. The experimental data comes from configuration (a) and had 0.82 as the volume fraction of porous core.

Under a closer examination, Figure 9-48 illustrates that the effect of core volume fraction is much less on the different orientations when over 0.9. Nevertheless, the presence of a dense outer shell has provided an improved level of mechanical performance (from 1.4MPa without a dense shell to ~2.8MPa with 10% of the material as dense shell) and enhanced handling ability.

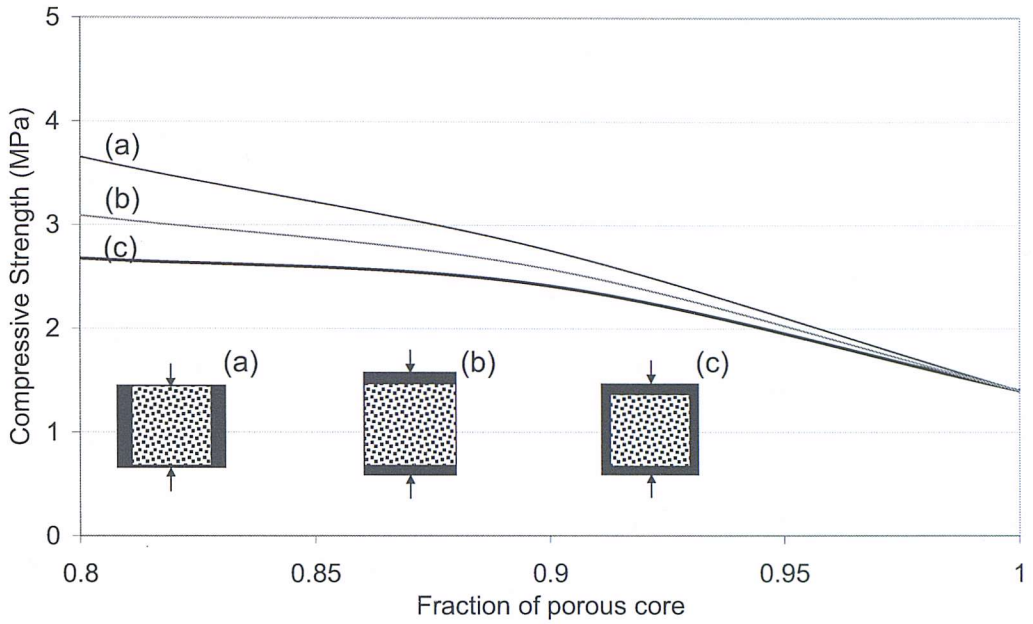


Figure 9-48: Indications of an improvement in compressive strength with the presence of dense shell; however, negligible difference in mechanical performance between different configurations

9.9 Applications

Thermal insulation appears to be the obvious choice of application for these glass-ceramic foams, where glass foams have been used when fire hazard is a major consideration (as in some buildings) or when a very long life is envisaged (as in pipes and roofs). There are other possible applications where the waste-derived foams can be used, for example, in low load-bearing structural components, sound insulating panels, or light-weight aggregate / filler for building and buoyancy applications. Filter application is a possibility but the openness of the cells needs to be improved for the filtration process to work, so there is still work to be done before such an application can be realised. It has been demonstrated that the presence of a dense outer shell improves the mechanical properties and thus ease for handling of the porous material. Therefore, a sandwich structure incorporating the glass-ceramic foam as the insulating core could be the ideal configuration for above-mentioned applications.

Chapter 10 Conclusions

1. The preliminary chemical analysis had shown that out of the four main silicate wastes investigated in this project (namely coal fly ash, coal pond ash, iron slag and steel slag), only the coal ashes contained adequate amounts of glass network forming oxides (network formers) as well as network modifiers. The fifth waste, soda-lime glass cullet, was abundant in silica, calcia, and sodium oxide. Therefore, it was used as an additive to adjust the overall chemical composition to help sintering as well as glass making. The XRD analysis of the wastes showed that only glass cullet was completely amorphous with trace amount of quartz crystals present as a contaminant. The coal ashes were the next pair of materials with less complicated mineralogy. Slags were very complex systems with various amounts of silicates and iron oxides. This suggested that the slag would be most difficult to process (sinter) without pre-treatment (i.e. melting) and led to the decision to melt the slag material before further heat-treatment.

2. Powder sintering was used as a simple way to investigate the behaviour of a raw material or a combination of wastes under thermal treatment. As supported by thermal analysis, it was concluded that coal pond ash is the most suitable material for powder sintering of the investigated wastes. Iron-making slag had an unusual chemical composition (high in TiO_2) compared to the conventional blast furnace slag. It was also a more favourable material to be used for glass making as the Si:Ca ratio was too low for the KOBM steel-making slag to be used without a strong dependency on additives. Therefore, the aim was to produce a high-strength, fully dense, glass-ceramic material with high content of Ti-rich crystals by melting, whereas the coal pond ash should be used as-received to produce a relatively dense material via cheap and simple powder sintering process.

3. The sintering behaviour of coal pond ash was studied using dilatometry where linear shrinkage of a green compact under elevated temperature was used to indicate the onset as well as the end of sintering. Two-step shrinkage was observed, and it was concluded that the first stage of sintering (750°C) was

hindered by crystallisation which occurred at the same temperature as at the end of the first shrinkage (800°C). The second, and the main sintering stage, took place only after the temperature was raised to above 1000°C. The sintered glass-ceramics exhibited a pyroxene-feldspar based (diopside and anorthite) crystalline structure with limited residual glass matrix. The addition of waste glass cullet was optimised to about 10-30wt% in order to lower sintering temperature as well as to aid the final densification. As the content of additional glass cullet increased, there was a change in the dominant phase to the more Na- and Ca-rich feldspar (albite) and pyroxene (wollastonite) crystals. A slower heating rate (of 2°C/min) also improved the densification by allowing time for viscous flow sintering.

4. The coefficient of thermal expansion (CTE) of sintered glass-ceramics was found to be affected by the amount of additional glass cullet incorporated into the original raw material (pond ash). The increase in this incorporation has resulted in a reduction in the degree of crystallinity and a consequent increase in residual glass content, and hence increase in CTE values.

5. The best mechanical properties were measured from samples sintered using the optimum condition and composition: PA30G, pond ash with 30wt% glass cullet sintered at 1050°C. The sintered glass-ceramics had a Vickers hardness value of 5.4 GPa, Young's modulus of 64 GPa, flexural strength of 85 MPa, and a compressive strength of 500 MPa. These mechanical properties are promising for the use of the materials in building applications when compared against commercial granite and marble products. The mechanical properties appeared to follow a decreasing trend with increasing glass cullet content and increase in porosity level. Hence, this optimised material performance was not only a direct result of highest sintered density (low residual porosity) but a higher degree of crystallisation, as supported by the CTE studies.

6. The thermal shock resistance of sintered pond ash (PA) based glass-ceramics was determined by measuring the residual flexural strength of test specimens after quenching in water from different furnace temperatures. The critical temperature difference was 275K for PA10G and 225K for PA30G. Since the

mechanical properties were very similar for both materials, the only major difference was their value of CTE. This was the main factor for lowering the thermal shock resistance of PA30G because of its higher CTE compared to the one for PA10G material. The sintered glass-ceramics, PA30G, also had a good chemical resistance, especially against alkaline solutions.

7. Iron making slag was chosen as the main silicate waste for single-stage heat-treatment experiments. Its unusually high content of TiO_2 was the key for crystallisation and thus fine-grained microstructure. The mixture of 60wt% iron slag and 40wt% glass cullet was melted into a dark-amber coloured glass at temperatures over 1400°C. The parent glass was subjected to thermal analysis, and based on the temperatures at which crystallisation took place, the parent glass was heat-treated in a single-step heating regime with a top temperature up to 1100°C and held for 2 hours. The XRD and SEM confirmed the presence of Ti-rich compounds (armalcolite and perovskite) and a well-defined microstructure for the MS40G glass-ceramic material. The HT-XRD enabled a detailed record of the phase evolution over the heat-treatment temperature range, and clearly agreed with the standard XRD scans as well as SEM observations in terms of the order in which each crystalline phase appeared.

8. The coefficient of thermal expansion of a polycrystalline material is normally lower than that of its parent glass. However, in the case of MS40G glass, its glass-ceramic had a higher CTE than its parent as-cast glass. This was due to the high CTE value of the individual crystalline phase precipitated. The phases present after a heat-treatment at 900°C: diopside and nepheline, both had higher CTE values than the parent glass. Therefore, the overall CTE of the glass-ceramic was higher than the parent glass. As the heat-treatment temperature increased, the dissolution of those pyroxene phases allowed the Ti-rich phases, which had relatively lower values of CTE, to precipitate and thus led to a slightly lower overall CTE for the glass-ceramic (heat-treated at 1100°C) than the one heat-treated at 900°C. Nevertheless, it was still higher than the parent glass.

9. Crystallisation of MS40G glass has yielded polycrystalline materials with better mechanical properties in comparison to the parent glass. The increase in heat-treatment temperature, which resulted in the precipitation of Ti-rich phases, had a positive effect on the room-temperature properties of the glass-ceramic material, except for the hardness. One of the Ti-rich phases had an elongated morphology, and its crystals were well-distributed across the glass matrix. Due to this high aspect ratio of the crystals, two toughening mechanisms: crack bridging and crack deflection, were thought to have helped to restrict crack propagation and thus enhance fracture toughness of the material. The fracture toughness at elevated temperature was also assessed. It was found that the fracture toughness of the glass-ceramic improved as temperature approached the softening range of the glass matrix, where crack blunting took place to inhibit crack propagation. This is a typical behaviour for materials with a glass transition temperature. However, the glass-ceramic material has a poor thermal shock resistance because of its high CTE. Nevertheless, the MS40G glass-ceramics exhibited superior overall mechanical properties in comparison with many other glass-ceramics produced from silicate wastes as reported in the literature.

10. Powder sintering with the incorporation of foaming agent was chosen as the method to produce highly porous glass-ceramics due to the simplicity of the technique. A number of foaming agents ($CaCO_3$, PMMA, SiC, TiN_2 and starch) were tested, but the key to an optimised foaming process relies on matching the softening temperature of the matrix and the reaction/decomposition temperature of the foaming agent. This match in temperature helps to retain distinct gas bubbles and thus final porosity.

11. The main crystalline phase in the foamed PA80G glass-ceramic was wollastonite (calcium silicate). At temperatures below 1000°C, there was a trace amount of quartz (contaminant from waste glass cullet) and cristobalite as well. Precipitation of cristobalite is a common occurrence for glass powder of borosilicate and soda-lime compositions. This can be inhibited by the addition of alumina-containing compound, and in this case, the presence of

these oxides in coal pond ash has helped to inhibit the precipitation particularly at high temperatures.

12. 2-D microstructural analysis of the porous materials was conducted using SEM. It was observed that the roundness of pores improved with temperature, and simultaneously there was a greater tendency for smaller pores to coalesce into larger pores. The disadvantage of conventional 2-D techniques is the need to prepare cross-sections for better image quality as well as to sample more than one cross-section to get sufficient amount of data from a statistical point of view. XMT has enabled a non-destructive acquisition and characterisation of pore morphology at the 3-D level. In conjunction with computer algorithms, parameters such as porosity level, pore size and its distribution, roundness, and wall thickness, were measured from the 3-D representation of each XMT specimen. The combination of heat-treatment temperature and the reaction temperature of SiC has resulted in an increase in most of these parameters as observed over the temperature from 975°C to 1100°C.

13. The limited interconnectivity had restricted the full thermal insulating property of these waste-derived glass-ceramic foams. The lowest thermal conductivity appeared to be around 0.15-0.20 W m^{-1} K^{-1} even at a level of porosity about 90%. The use of XMT and subsequent FEA allowed an accurate prediction of the thermal conductivity of the glass-ceramic foam with various porosity levels. This demonstrated an opportunity for XMT to be used as a non-destructive technique that could be integrated into production lines as a mean of assuring the quality of products.

14. In terms of the mechanical properties of the glass-ceramic foams, a detailed record of values was obtained over a range of densities. The foams have a relatively high stiffness (elastic modulus) to weight ratio (i.e. high specific modulus) but a low specific strength like most common foams. The Gibson and Ashby models proved to be a simple but accurate way to approximate the Young's modulus and compressive strength of the glass-ceramic foams. The

overall properties of the waste-derived foams were adequate to compete against some of the commercially available insulating materials.

It has been demonstrated that dense as well as highly porous glass-ceramics can be produced via economical methods, and the products possess physical, mechanical, thermal and chemical properties that are of a quality sufficient to compete against commercially available materials. The use of XMT has also been a highlight of this project, where this relatively novel characterization method has been integrated with conventional techniques from materials science. The combination of XMT and FEA has successfully assisted the prediction of thermal conductivity of glass-ceramic foams. It is believed that the results from this research will provide information for the production of various types of glass-ceramics with a wide range of properties. It also provides an excellent stepping stone towards the ultimate goal, which is the scaling-up of the glass-ceramic process from laboratory environment to industrial relevant dimensions and shapes.

Chapter 11 Further work

The following list contains suggestions for further work to be conducted either as additional work and short term tasks for the current research or as new areas to investigate in the long term:

1. The coal ash derived dense glass-ceramics (Chapter 7) as well as the slag based glass-ceramics (Chapter 8) would be interesting subjects for wear and erosion tests to assess their resistance under those environments, and such information can be used to relate the materials' ability to compete in the commercial market against current products. An example of readily available standard tests to measure abrasion wear resistance of ceramic materials would be ASTM G65, the dry sand / rubber wheel abrasion wear test, which is commonly used to measure wear by weight loss. It was adapted by Carter et al [46] when testing the abrasion resistance of Silceram glass-ceramics in the early 1990s. The only difference is that a slurry (sand and water) was used instead of dry sand, and the distribution funnel was replaced by a bath of the slurry in which the rubber wheel is partially immersed in. The disadvantage of using this bath system is that the sand granules are recycled and the abrasive nature of the sand is expected to be poorer than its initial state. Therefore, the abrasion wear on the sample is not constant if the bath is not replenished regularly.

2. Other application-based properties, such as thermal shock resistance, have already been determined and such information gives valuable information to the working environment (in this case, level of thermal fluctuation) that the material can cope with. In addition to the determination of thermal shock resistance, however, thermal cycling experiments for dense materials would be an interesting property to measure. Given that the critical temperature difference for thermal shock resistance is known for each of the dense glass-ceramics, the next step would be determining how many cycles, if any, of thermal fluctuation (at the critical temperature difference) can the material withstand without a dramatic strength reduction.

3. Short term studies have shown that the dense glass-ceramics are chemically resistant, especially to alkaline solutions. It also has shown that although glass-ceramics were prone to acid attack, the corrosion was within acceptable range. A long term study would be the next step to investigate the chemical durability of these dense materials, and a residual strength test could be conducted to assess the retained mechanical performance of the corroded specimens.

4. From an economics point of view, it would be an interesting investigation to use waste silicon carbide from industry as the foaming agent to assess if the foamed products are still reproducible. This would involve the collection of recycled SiC powder, processing of the powder, and incorporation of the foaming agent into matrix powder. This should reduce the material cost and thus the overall cost of the foamed product.

5. The pore interconnectivity of the foams could be another aspect of the current research to be investigated further. In order to apply these foams as filtration mediums, an open-celled structure is desired. This requires further study of the foaming agent used and processing parameters. In addition, the density-graded foams are another subject for further development.

6. Successful prediction of thermal conductivity values of glass-ceramic foams using a combination of XMT and FEA has demonstrated the usefulness of computed tomography in this particular area of materials research. Therefore, stress analysis using FEA for the porous glass-ceramics to predict the mechanical properties could be another piece of work that would add to the current simulation work. The type of element will need to be changed to suit stress analysis rather than thermal analysis.

7. It has also been demonstrated that XMT has the capability to acquire valuable 3D structural information. It is still an area under constant development in materials science and worth improving both in hardware (new generation of X-ray source) and software (more versatile but also user-friendly image

analysis and finite element analysis packages) in order to improve the practical resolution, robustness, and efficiency.

8. Ultimately, the goal is to bring the waste-derived materials into the commercial markets. The next step, from our laboratory based experiments, would be a large scale pilot plant and subsequent characterisation of the properties of large-scale products. Examples from the past, Slagceram, Silceram, and the Italian work on zinc hydrometallurgical wastes, have all been successful in terms of scaling-up the glass-ceramic process, from melting the waste mixture to heat-treating the parent glass to produce glass-ceramic tiles. There were, and will always be, problems arising when the production process is scaled up. For instance, the increase in the size of the cast glass can lead to increasing annealing time in the glass making stage, increase in heat of reaction and thus heat-treatment temperature at the crystallisation stage, and there is always the possibility of inhomogeneous microstructure across a larger volume. The solution to the increase in heat of reaction is to decrease the heat-treatment temperature to compensate for the increase and to allow the heat of reaction to assist the crystallisation process. A prerequisite to succeeding in scaling up a process is capital investment. Without a party interested in investing in the development of a novel material, it would be very difficult for any project to progress any further. Perhaps, the most important factor for a successful product is social acceptability. Because of the product is derived from wastes, public perception on the safety and reliability of these glass-ceramics will have to be overcome by results from long-term testing proving its durability in various service conditions.

References

1. P.W. McMillan, *Glass-Ceramics*. 2nd ed. Non-Metallic Solids, ed. J.P. Roberts. Vol. 1. 1979, London: Academic Press Inc. (London) Ltd.,.
2. W. Holand and G.H. Beall, *Glass-Ceramic Technology*. 2002, Westerville, OH: American Ceramic Society.
3. Z. Strnad, *Glass-ceramic materials : liquid phase separation, nucleation and crystallization in glasses*. Glass science and technology. Vol. 8. 1986, Amsterdam: Elsevier.
4. W. Pannhorst: *Journal of Non-Crystalline Solids*, 1997, **219,** 198-204.
5. T. Manfredini, G.C. Pellacani, and J.M. Rincon, eds. *Glass-ceramic materials. Fundamentals and applications*. 1997, Mucchi Editore: Modena, Italy.
6. G.H. Beall: *Annual Review of Materials Science*, 1992, **22,** 91-119.
7. G. Partridge: *Advanced Materials*, 1990, **2,** 553-556.
8. V.N. Sigaev, E.V. Lopatina, P.D. Sarkisov, S.Y. Stefanovich, and V.I. Molev: *Mater. Sci. Eng. B-Solid State Mater. Adv. Technol.*, 1997, **48,** 254-260.
9. *Macor*, in *Machinable Glass Ceramic Code 9658*, Machinable Glass Ceramic Department, Corning Glass Works, Corning: New York.
10. C. Moisescu, C. Jana, S. Habelitz, G. Carl, and C. Russel: *Journal of Non-Crystalline Solids*, 1999, **248,** 176-182.
11. D.I. Atkinson and P.W. McMillan: *Journal of Materials Science*, 1975, **10,** 2012.
12. D.I. Atkinson and P.W. McMillan: *Journal of Materials Science*, 1976, **11,** 989-1002.
13. D.I. Atkinson and P.W. McMillan: *Journal of Materials Science*, 1977, **12,** 443-450.
14. Y. Yue, R. Keding, and C. Russel: *Journal of Materials Research*, 1999, **14,** 3983-3987.
15. R.D. Rawlings, *Production and properties of Silceram glass ceramics*, in *Glass-ceramic materials. Fundamentals and applications*, T. Manfredini, G.C. Pellacani, and J.M. Rincon, Editors. 1997, Mucchi Editore: Modena, Italy. p. 115-133.
16. M. Romero and J.M. Rincon: *Journal of the American Ceramic Society*, 1999, **82,** 1313-1317.
17. A.A. Francis, A.R. Boccaccini, and R.D. Rawlings: *Journal of Materials Science Letters*, 2002, **21,** 975-980.
18. P. Hing, V. Sinha, and P.B. Ling: *Journal of Materials Processing Technology*, 1997, **63,** 604-609.
19. K. Lambrinou, O. Van der Biest, A.R. Boccaccini, and D.M.R. Taplin: *Journal of the European Ceramic Society*, 1996, **16,** 1237-1244.
20. R.R. Tummala: *Journal of the American Ceramic Society*, 1991, **74,** 895-908.
21. E.M. Rabinovich, *Cordierite glass-ceramics produced by sintering*, in *Advances in ceramics*, J.H. Simmons, D.R. Uhlmann, and G.H. Beall, Editors. 1982, The American Ceramic Society: Columbus. p. 327-333.
22. W. Liu, S. Li, and Z. Zhang: *Glass Technology*, 1991, **32,** 24-27.
23. G.W. Scherer: *Journal of the American Ceramic Society*, 1977, **60,** 239-243.
24. A.R. Boccaccini, W. Stumpfe, D.M.R. Taplin, and C.B. Ponton: *Materials Science and Engineering A*, 1996, **219,** 26-31.

25. E.D. Zanotto and M.O. Prado: *Physics and Chemistry of Glasses*, 2001, **42,** 191-198.
26. R. Muller: *Glastech. Ber.-Glass Sci. Technol.*, 1994, **67C,** 93-98.
27. I. Gutzow, R. Pascova, A. Karamanov, and J. Schmelzer: *Journal of Materials Science*, 1998, **33,** 5265-5273.
28. T.J. Clark and J.S. Reed: *Journal of the American Ceramic Society*, 1986, **69,** 837-846.
29. A.R. Boccaccini and R.D. Rawlings: *Glass Technology*, 2002, **43C,** 191-201.
30. A.R. Boccaccini: *Journal of the Ceramic Society of Japan*, 2001, **109,** S99-S109.
31. C.J. Brinker and G.W. Scherer, *Sol-gel science*. 1989, New York: Academic Press.
32. M.W. Davies, B. Kerrison, W.E. Gross, W.J. Robson, and D.F. Wichell: *Journal of Iron Steel Institute*, 1970, **208,** 348-370.
33. M.W. Davies, G.S.F. Hazeldean, and W.J. Robson, *Science of Ceramics*, ed. C. Brosset and E. Knopp. 1970, Gothenburg: Swedish Institute of Silicate Research.
34. K.T. Bondarev. *Slag-Sitall - a material of the future*. in *9th International Congress on Glass*. 1971. Versailles, France.
35. M.L. Ovecoglu: *Journal of the European Ceramic Society*, 1998, **18,** 161-168.
36. V. Gomes, C.D.G. de Borba, and H.G. Riella: *Journal of Materials Science*, 2002, **37,** 2581-2585.
37. E.B. Ferreira, E.D. Zanotto, and L.A.M. Schdeller: *Glass Science and Technology*, 2002, **75,** 75-86.
38. N.A. El-Alaily: *Glass Technology*, 2003, **44,** 30-35.
39. A.R. West, *Solid state chemistry and its applications*. 1984, Chichester: Wiley.
40. A.A. Francis: *Journal of the European Ceramic Society*, 2004, **24,** 2819-2824.
41. P.S. Rogers, J. Williamson, J.F. Bell, and M. Campbell, *Ceramic Materials from Molten Blast-furnace Slag by Direct Controlled Cooling*. 1986, Commission of the European Communities, Energy R&D Programme - Energy Conservation, Final Report, EUR 10389 EN.
42. P.S. Rogers, J. Williamson, J.F. Bell, and M. Campbell, *Proceedings of International Seminar on Energy Conservation Industry*, A. Strub and H. Ehringer, Editors. 1984, Commission of the European Communities/VDI: Dusseldorf. p. 280.
43. S. Carter, R.D. Rawlings, and P.S. Rogers. *British Ceramic Proceedings 43 "Advance ceramics in chemical process engineering"*. 1989.
44. S. Carter, C.B. Ponton, R.D. Rawlings, and P.S. Rogers: *Journal of Materials Science*, 1988, **23,** 2622-2630.
45. P.S. Rogers, J. Williamson, J.F. Bell, and M. Campbell, *Proceedings of Contractor' Meetings*, H. Ehringer, G. Hoyaux, and P.A. Pilavachi, Editors. 1982: Brussels. p. 156 (Reidel, Dordrecht, 1983).
46. S. Carter, R.D. Rawlings, and P.S. Rogers: *British Ceramic Transactions*, 1993, **92,** 31-34.
47. F.C. McQuillan, R.D. Rawlings, and P.S. Rogers. *The ballistic resistance of Silceram glass-ceramics*. in *European Ceramic Society Conference*. 1991. Ausburg, Germany.
48. H.S. Kim, R.D. Rawlings, and P.S. Rogers: *Journal of Materials Science*, 1989, **24,** 1025-1037.

49. H.S. Kim, R.D. Rawlings, and P.S. Rogers, *British Ceramic Proceedings 42 "Complex Microstructures"*, ed. R. Stevens and D. Taylor. 1989, Durham: Institute of Ceramics. 59-68.
50. R. Cimdins, I. Rozenstrauha, L. Berzina, J. Bossert, and M. Bucker: *Resources, Conservation and Recycling*, 2000, **29,** 285-290.
51. K. Dana and S.K. Das: *Journal of Materials Science Letters*, 2003, **22,** 387-389.
52. R.D. Rawlings, J.P. Wu, and A.R. Boccaccini: *Journal of Materials Science*, 2006, **41,** 733-761.
53. E. Benavidez, C. Grasselli, and N. Quaranta: *Ceramics International*, 2003, **29,** 61-68.
54. A.R. Boccaccini, M. Bucker, and J. Bossert: *Tile & Brick International*, 1996, **12,** 515-518.
55. K. Hopkins, *Internal Communication*. 2003, Genesis Power: Huntly, New Zealand.
56. C.L. Carlsson and D.C. Adriano: *Journal of Environmental Quality*, 1988, **22,** 227-247.
57. G.L. Jablonski and S.S. Tyron. *Overview of Coal Cobustion By-Product Utilisation*. in *5th International Coal Conference*. 1988. University of Pittsburgh, Pittsburgh.
58. P.G. Zhao: *Fly Ash*, 1994, **4,** 39-42.
59. A.A. Francis, R.D. Rawlings, R. Sweeney, and A.R. Boccaccini: *Glass Technology*, 2002, **43,** 58-62.
60. L. Barbieri, I. Lancellotti, T. Manfredini, I. Queralt, J.M. Rincon, and M. Romero: *Fuel*, 1999, **78,** 271-276.
61. E.J. DeGuire and S.H. Risbud: *Journal of Materials Science*, 1984, **19,** 1760-1766.
62. B. Cumpston, F. Shadman, and S.H. Risbud: *Journal of Materials Science*, 1992, **27,** 1781-1784.
63. M. Erol, U. Demirler, S. Kucukbayrak, A. Ersoy-Mericboyu, and M.L. Ovecoglu: *Journal of the European Ceramic Society*, 2003, **23,** 757-763.
64. M. Erol, A. Genc, M.L. Ovecoglu, E. Yucelen, S. Kucukbayrak, and Y. Taptik: *Journal of the European Ceramic Society*, 2000, **20,** 2209-2214.
65. C. Leroy, M.C. Ferro, R.C.C. Monteiro, and M.H.V. Fernandes: *Journal of the European Ceramic Society*, 2001, **21,** 195-202.
66. F. Peng, K. Liang, A. Hu, and H. Shao: *Fuel*, 2004, **83,** 1973-1977.
67. F. Peng, K.M. Liang, and A.M. Hu: *Fuel*, 2005, **84,** 341-346.
68. A.A. Francis, A.R. Boccaccini, and R.D. Rawlings. *Production of Glass-Ceramics from Coal Ash and Waste Glass Mixtures*. in *7th Conference & Exhibition of the European Ceramic Society*. 2001. Brugge, Belgium: Trans Tech Publications.
69. N.N. Sampathkumar, A.M. Umarji, and B.K. Chandrasekhar: *Materials Research Bulletin*, 1995, **30,** 1107-1114.
70. M.C. Ferro, C. Leroy, R.C.C. Monteiro, and M.H.V. Fernandes: *Key Engineering Materials*, 2002, **230-232,** 408-411.
71. L. Barbieri, A.M. Ferrari, I. Lancellotti, C. Leonelli, J.M. Rincon, and M. Romero: *Journal of the American Ceramic Society*, 2000, **83,** 2515-2520.
72. L. Barbieri, I. Lancellotti, T. Manfredini, G.C. Pellacani, J.M. Rincon, and M. Romero: *Journal of the American Ceramic Society*, 2001, **84,** 1851-1858.

73. A. Garcia Verduch. *Materiales Obtenidos a Partir da Rocas y Escorias Dundidas*. in *Proceedings of the Jornadas Cientificas Sobre Ceramic y Vidrio*. 1980. Seccion de Ciencia Basica de la Sociedad Espanola Ceramica, Vidr y universidad de Oviedo, Oviedo.
74. G.A. Raschin and S.D. Tschetveritkov: *Izv. Rev. Inv. Geol. Prospec.*, 1964, **9,** 71-79.
75. A.R. Boccaccini, M. Bucker, J. Bossert, and K. Marszalek: *Waste Management*, 1997, **17,** 39-45.
76. J.M. Kim and H.S. Kim: *Journal of the European Ceramic Society*, 2004, **24,** 2825-2833.
77. C.T. Kniess, C.D.G. de Borda, E. Neves, N.C. Kuhnen, and H.G. Riella: *Interceram*, 2002, **51,** 140-143.
78. R. Cioffi, P. Pernice, A. Aronne, M. Catauro, and G. Quattroni: *Journal of the European Ceramic Society*, 1994, **13,** 143-148.
79. A. Harnisch and D. Hulsenberg: *Glastech. Ber.-Glass Sci. Technol.*, 2000, **73,** 67-72.
80. W. Pannhorst, *Development of the Optical Glass-Ceramic ZERODUR*, in *Low Thermal Expansion Glass-Ceramic*, H. Bach, Editor. 1995, Springer: Berlin and Heidelberg, Germany. p. 107-130.
81. A.R. Boccaccini, J. Janczak, H. Kern, and G. Ondracek. *Development of composite materials under ecological aspects as recycling concept for the coal mining wastes*. in *4th International Symposium on the Recllamation, Treatment and Utilization of Coal Mining Wastes*. 1993.
82. A.A. Francis, R.D. Rawlings, R. Sweeney, and A.R. Boccaccini: *Journal of Non-Crystalline Solids*, 2004, **333,** 187-193.
83. K. Morita, V. Nguyen, R. Nakaoka, and K.J.D. MacKenzie: *Materials Research Symposium Proceedings*, 1992, **269,** 471-476.
84. DEFRA, *Municipal Waste Management Survey 2002/03*. 2004, Department for Environment, Food and Rural Affairs: London.
85. N.J. Weinstein and R.F. Toro, *Thermal processing of municipal solid waste for resource and energy recovery*. 1976, Ann Arbor, Michigan: Ann Arbor Science.
86. C. Ferreira, A. Ribeiro, and L. Ottosen: *Journal of Hazardous Materials*, 2003, **96,** 201-216.
87. M. Romero, R.D. Rawlings, and J.M. Rincon: *Journal of Non-Crystalline Solids*, 2000, **271,** 106-118.
88. T.W. Cheng, T.H. Ueng, Y.S. Chen, and J.P. Chiu: *Ceramics International*, 2002, **28,** 779-783.
89. O. Hjelmar: *Journal of Hazardous Materials*, 1996, **47,** 345-368.
90. R. Derie: *Waste Management*, 1996, **16,** 711-716.
91. P.T. Williams, *Waste Incineration and the Environment, Issues in Environmental Science and Technology*, R.E. Hester and R.M. Harrison, Editors. 1994, Royal Society of Chemistry. p. 27-52.
92. R. Gutmann: *Glass Science and Technology*, 1996, **69,** 285-299.
93. M. KrauB: *Glass Science and Technology*, 1997, **70,** 375-381.
94. Y.J. Park and J. Heo: *Journal of Hazardous Materials*, 2002, **91,** 83-93.
95. D. Deegan, C. Chapman, and C. Bowen: *High Temperature Materials and Processes*, 2003, **7,** 367-372.

96. J.K. Park, Y.P. Moon, B.C. Park, M.J. Song, K.S. Ko, and J.M. Cho: *Journal of Environmental Science and Health Part A: Toxic/Hazardous Substances and Environmental Engineering*, 2001, **36,** 861-871.
97. T.W. Cheng, J.P. Chiu, C.C. Tzeng, and Y.S. Chen: *Waste Management*, 2002, **22,** 485-490.
98. T.W. Cheng: *Chemosphere*, 2003, **50,** 47-51.
99. Y.J. Park and J. Heo: *Ceramics International*, 2002, **28,** 689-694.
100. M. Romero, J.M. Rincon, R.D. Rawlings, and A.R. Boccaccini: *Materials Research Bulletin*, 2001, **36,** 383-395.
101. T.W. Cheng and Y.S. Chen: *Ceramics International*, 2004, **30,** 343-349.
102. A. Karamanov, M. Pelino, and A. Hreglich: *Journal of the European Ceramic Society*, 2003, **23,** 827-832.
103. A. Karamanov, M. Pelino, M. Salvo, and I. Metekovits: *Journal of the European Ceramic Society*, 2003, **23,** 1609-1615.
104. A.R. Boccaccini, J. Schawohl, H. Kern, B. Schunck, J.M. Rincon, and M. Romero: *Glass Technology*, 2000, **41,** 99-105.
105. S. Bethanis, C.R. Cheeseman, and C.J. Sollars: *Ceramics International*, 2002, **28,** 881-886.
106. C.R. Cheeseman, S. Monteiro da Rocha, C. Sollars, S. Bethanis, and A.R. Boccaccini: *Waste Management*, 2003, **23,** 907-916.
107. L. Barbieri, A. Corradi, I. Lancellotti, G.C. Pellacani, and A.R. Boccaccini: *Glass Technology*, 2003, **44,** 184-190.
108. P. Appendino, M. Ferraris, I. Matekovits, and M. Salvo: *Journal of the European Ceramic Society*, 2004, **24,** 803-810.
109. A.R. Boccaccini, M. Kopf, and W. Stumpfe: *Ceramics International*, 1995, **21,** 231-235.
110. K. Nishida, Y. Nagayoshi, H. Ota, and H. Nagasawa: *Waste Management*, 2001, **21,** 443-449.
111. M. Nishigaki: *Waste Management*, 2000, **20,** 185-192.
112. F. Andreola, L. Barbieri, A. Corradi, I. Lancellotti, and T. Manfredini: *Journal of Materials Science*, 2001, **36,** 4869-4873.
113. L. Barbieri, A. Corradi, I. Lancellotti, and T. Manfredini: *Waste Management*, 2002, **22,** 859-863.
114. V.K. Marghussian and A. Maghsoodipoor: *Ceramics International*, 1999, **25,** 617-622.
115. A.A. Omar, M.A. El-Gamal, W. Kotb, and M.M. Mahmoud: *Glass Sci Technol.-Glastech. Ber.*, 2000, **73,** 51-58.
116. M. Murat, S. Martel, and C. Bouster: *Ceramics International*, 1990, **16,** 171-175.
117. Z. Gao and C.H. Drummon III: *Journal of the American Ceramic Society*, 1999, **82,** 561-565.
118. M. Pelino, A. Karamanov, P. Pisciella, S. Crisucci, and D. Zonetti: *Waste Management*, 2002, **22,** 945-949.
119. H. Endo, Y. Nagoyoshi, and K. Suzuki: *Water Science and Technology*, 1997, **36,** 235-241.
120. S. Suzuki, M. Tanaka, and T. Kaneko: *Journal of Materials Science*, 1997, **32,** 1775-1779.
121. Y.J. Park, S.O. Moon, and J. Heo: *Ceramics International*, 2003, **29,** 223-227.
122. M. Romero and J.M. Rincon: *Journal of the European Ceramic Society*, 1998, **18,** 153-160.

123. M. Pelino, C. Cantalini, and J.M. Rincon: *Journal of Materials Science*, 1997, **32,** 4655-4660.
124. A. Karamanov, G. Taglieri, and M. Pelino: *Journal of the American Ceramic Society*, 1999, **82,** 3012-3016.
125. A. Karamanov, M. Pelino, G. Taglieri, and C. Cantalini. *Sintered building glass-ceramics based on jarosite.* in *XVIII International Congress on Glass.* 1998. San Francisco: The American Ceramic Society, Ohio.
126. P. Pisciella, S. Crisucci, A. Karamanov, and M. Pelino: *Waste Management*, 2001, **21,** 1-9.
127. M. Pelino: *Waste Management*, 2000, **20,** 561-568.
128. A. Acosta, I. Iglesias, M. Aineto, M. Romero, and J.M. Rincon: *Journal of Thermal Analysis and Calorimetry*, 2002, **67,** 249-255.
129. C. Diaz, S. Salgado, R. Jordan, E. Cruz, and M.E. Zayas: *American Ceramic Society Bulletin*, 2003, **82,** 9601-9604.
130. A.V. Gorokhovsky, J.I. Escalante-Garcia, V.A. Gorokhovsky, and D.V. Mescheryakov: *Journal of the American Ceramic Society*, 2002, **85,** 285-287.
131. T. Toya, Y. Kameshima, A. Yasumori, and K. Okada: *Journal of the European Ceramic Society*, 2004, **24,** 2367-2372.
132. Y.H. Yun, C.H. Yoon, J.S. Oh, S.B. Kim, B.A. Kang, and K.S. Hwang: *Journal of Materials Science*, 2002, **37,** 3211-3215.
133. L.L. Hench and E.C. Ethridge, *Biomaterials - An Interfacial Approach.* 1982. 70,130.
134. M.A. Ali, W.J. Knapp, and P. Kurtz: *Ceramic Bulletin*, 1967, **46,** 275-277.
135. A.R. Boccaccini: *Journal of Porous Materials*, 1999, **6,** 369-379.
136. D.J. Green: *Journal of the American Ceramic Society*, 1985, **68,** 403-409.
137. H. Verweij, G. De With, and D. Veeneman: *Journal of Materials Science*, 1985, **20,** 1069-1078.
138. T.T. Meek and R.D. Blake: *American Ceramic Society Bulletin*, 1984, **63,** 1477-1477.
139. I. Bica: *Materials Science and Engineering A*, 2005, **393,** 191-195.
140. A. Briggs. *High quality thermal insulation materials from power station ash.* in *The 4th International Meeting on Modern Ceramics Technologies.* 1979. Saint-Vincent, Italy: Elsevier Scientific Publishing Company.
141. K. Ishizaki, S. Komarneni, and M. Nanko, *Porous Materials: Process technology and applications.* Materials Technology Series, ed. R.G. Ford. 1998, Dordrecht: Kluwer Academic Publishers.
142. Y. Seki, S. Kose, T. Kodama, M. Kadota, T. Ogura, K. Tanimoto, and I. Matsubara: *Nippon Seramikkusu Kyokai Gakujutsu Ronbunshi-Journal of the Ceramic Society of Japan*, 1988, **96,** 831-836.
143. Y. Seki, S. Kose, T. Kodama, M. Kadota, T. Ogura, K. Tanimoto, and I. Matsubara: *Nippon Seramikkusu Kyokai Gakujutsu Ronbunshi-Journal of the Ceramic Society of Japan*, 1988, **96,** 920-924.
144. Z. Matamoros-Veloza, K. Yanangisawa, J.C. Rendon-Angeles, S. Oishi, and M.A. Cisneros-Guerrero: *Solid State Ion.*, 2004, **172,** 597-600.
145. H. Hojaji: *Materials Research Society Symposium Proceedings*, 1989, **136,** 185-206.
146. H. Abe, H. Seki, A. Fukunaga, and M. Egashira: *Journal of the Ceramic Society of Japan*, 1992, **100,** 33-37.
147. R. Sarkar and S.K. Das: *Tile & Brick International*, 2003, **19,** 24-27.

148. E. Bernardo, G. Scarinci, and S. Hreglich: *Glass Science and Technology*, 2005, **78,**
149. A.V. Gorokhovsky, J.I. Escalante-Garcia, J. Mendez-Nonell, V.A. Gorokhovsky, and D.V. Mescheryakov: *Glass Science and Technology*, 2002, **75,** 259-262.
150. J.P. Wu, A.R. Boccaccini, P.D. Lee, M.J. Kershaw, and R.D. Rawlings: *Adv. Appl. Ceram.*, 2006, **105,** 32-39.
151. F. Mear, P. Yot, M. Cambon, and M. Ribes: *Adv. Appl. Ceram.*, 2005, **104,** 123-130.
152. D. Liu: *Journal of Materials Science Letters*, 1996, **15,** 419-421.
153. L. Vaz, A.B. Lopes, and M. Almeida: *Journal of Materials Science: Materials in Medicine*, 1999, **10,** 239-242.
154. T. Hayashi, S. Sugihara, and K. Okazaki: *Japanese Journal of Applied Physics*, 1991, **30,** 2243-2246.
155. E. Gregorova, W. Pabst, and I. Bohacenko: *Journal of the European Ceramic Society*, 2006, **26,** 1301-1309.
156. J.G. Kim, Y.J. Kwon, J.H. Oh, W.S. Cho, N.H. Cho, C.M. Whang, and Y.C. Yoo: *Materials chemistry and physics*, 2004, **83,** 217-221.
157. C. Vitale-Brovarone, S. Di Nunzio, O. Bretcanu, and E. Verne: *Journal of Materials Science: Materials in Medicine*, 2004, **15,** 209-217.
158. O. Lyckfeldt and J.M.F. Ferreira: *Journal of the European Ceramic Society*, 1998, **18,** 131-140.
159. N.M. Bobkova, N.I. Zayats, T.V. Kolontaeva, G.N. Pun'ko, and G.B. Zakharevich: *Glass Ceram.*, 2000, **57,** 412-414.
160. E. Sousa, C.B. Silveira, T. Fey, P. Greil, D. Hotza, and A.P.N. de Oliveira: *Adv. Appl. Ceram.*, 2005, **104,** 22-29.
161. P. Colombo, J.R. Hellmann, and D.L. Shelleman: *Journal of the American Ceramic Society*, 2002, **85,** 2306-2312.
162. J.M. Villora, P. Callejas, and F. Barba, *Processing of highly porous hydroxyapatite from waste raw materials*, in *Euro Ceramics Vii, Pt 1-3*. 2002. p. 895-898.
163. E. Fidancevska, B. Mangutova, D. Milosevski, M. Milosevski, and J. Bossert: *Sci. Sinter.*, 2003, **35,** 85-91.
164. Y.W. Kim, S.H. Kim, X. Xu, C.H. Choi, C.B. Park, and H.D. Kim: *Journal of Materials Science Letters*, 2002, **21,** 1667-1669.
165. V. Shapovalov: *Materials Research Society Bulletin*, 1994, **April,** 24-28.
166. J.P. Wu, *Unpublished work*, in *Production of glass-ceramic materials from industrial silicate wastes*. 2005, Imperial College London: London.
167. C.J. Brinker: *Journal of membrane science*, 1994, **94,** 85-102.
168. E.P. Santos, C.V. Santilli, and S.H. Pulcinelli: *Journal of Non-Crystalline Solids*, 2002, **304,** 143-150.
169. T. Kokubu and M. Yamane: *Journal of Materials Science*, 1985, **20,** 4309-4316.
170. K. Yamamoto, T. Kasuga, and Y. Abe: *Journal of the American Ceramic Society*, 1997, **80,** 822-824.
171. T. Nakamura: *Journal of the American Ceramic Society*, 2000, **83,** 578-584.
172. A. Devasenapathi: *Journal of materials science*, 2005, **40,** 5463-5473.
173. A.R. Boccaccini, P. Veronesi, and C. Leonelli: *Journal of the European Ceramic Society*, 2001, **21,** 1073-1080.

174. A.R. Boccaccini, P. Veronesi, C. Siligardi, and C. Leonelli. *Porous Molybdenum Particle Reinforced Glass Matrix Composites Fabricated by Microwave Processing.* in *7th Conference & Exhibition of the European Ceramic Society.* 2001. Brugge, Belgium: Trans Tech Publications.
175. D. Bernard, D. Gendron, J.-M. Heintz, S. Bordere, and J. Etourneau: *Acta Materialia*, 2005, **53,** 121-128.
176. R.C. Atwood, J.R. Jones, P.D. Lee, and L.L. Hench: *Scr. Mater.*, 2004, **51,** 1029-1033.
177. Y. Nakashima, T. Nakano, K. Nakamura, K. Uesugi, A. Tsuchiyama, and S. Ikeda: *J. Contam. Hydrol.*, 2004, **74,** 253-264.
178. I.G. Watson, P.D. Lee, R.J. Dashwood, and P. Young: *Metallurgical and materials transactions. A, Physical metallurgy and materials science*, 2006, **37A,** 551-558.
179. J.H. Hubbell and S.M. Seltzer, Tables of X-ray mass attenuation coefficients and mass energy-absorption coefficients, https://physics.nist.gov/PhysRefData/XrayMassCoef/cover.html, 27th March, 2006
180. *Coal and coke - Analysis and testing, Part 21.1.1: Higher rank coal and coke - relative density - analysis*, in *AS 1038.21.* 2002, Standards Australia International Ltd.: Sydney.
181. *Specification for clay bricks*, in *BS 3921:1985.* 1985. p. 30.
182. *EMOD Program for Elasticity modulus calculation, version 9.12, User's Guide*, J.W. Lemmens Elektronika N.V.: Leuven. p. 57-60.
183. C.B. Ponton and R.D. Rawlings: *Materials Science and Technology*, 1989, **5,** 865-872.
184. G.R. Anstis, P. Chantikul, B.R. Lawn, and D.B. Marshall: *Journal of the American Ceramic Society*, 1981, **64,** 533-538.
185. A.R. Boccaccini, R.D. Rawlings, and I. Dlouhy: *Materials Science and Engineering A*, 2003, **347,** 102-108.
186. I. Dlouhy, M. Holzmann, and J. Man: *Kovove Materialy*, 1994, **32,** 3-13.
187. J.W. Wright, *Experiment 5: Thermal conductivity of refractory and insulating materials*, in *Undergraduate Lab Experiments*, Department of Materials, Imperial College London: London.
188. L. Gruner, *Chemical Durability of Silceram Glass-Ceramics.* 2000, Imperial College London: London.
189. T. Klupsch, E. Steinbeiss, R. Muller, C. Ulbrich, W. Schuppel, H. Steinmetz, and T. Hoche: *Journal of Magnetism and Magnetic Materials*, 1999, **196-197,** 264-265.
190. N. Rezlescu, L. Rezlescu, M.L. Craus, and E. Rezlescu: *Journal of Magnetism and Magnetic Materials*, 1999, **196-197,** 463-464.
191. L.W. Finger and Y. Ohashi: *American Mineralogist*, 1976, **61,** 303-310.
192. J.K. Winter, S. Ghose, and F.P. Okamura: *American Mineralogist*, 1977, **62,** 921-931.
193. R.M. Weston and P.S. Rogers: *Mineralogical Magazine*, 1976, **40,** 649-651.
194. R.S. Carmichael, *CRC Handbook of Physical Properties of Rocks.* Vol. 2. 1981, Boca Raton, Fla.: CRC Press.
195. C. Aksel and P.D. Warren: *Journal of the European Ceramic Society*, 2003, **23,** 301-308.
196. T.J. Lu and N.A. Fleck: *Acta Materialia*, 1998, **46,** 4755-4768.
197. T.W. Cheng and Y.S. Chen: *Chemosphere*, 2003, **51,** 817-824.

198. C. Fredericci, E.D. Zanotto, and E.C. Ziemath: *Journal of Non-Crystalline Solids*, 2000, **273,** 64-75.
199. T. Ota, I. Yamai, and S. Zhang: *Nippon Seramikkusu Kyokai Gakujutsu Ronbunshi-Journal of the Ceramic Society of Japan*, 1992, **100,** 1361-1365.
200. C.J. Ball, G.J. Thorogood, and E.R. Vance: *Journal of Nuclear Materials*, 1992, **190,** 298-301.
201. G. Bayer: *Journal of the Less-Common Metals*, 1971, **24,** 129-&.
202. K.K. Chawla, *Ceramic Matrix Composites*. 1993, London: Chapman & Hall. 291-.
203. J.J. Brennan and K.M. Prewo: *Journal of Materials Science*, 1982, **17,** 2371-2383.
204. A.R. Studart, U.T. Gonzenbach, E. Tervoort, and L.J. Gauckler: *Journal of the American Ceramic Society*, 2006, **89,** 1771-1789.
205. G. Bayer and S. Koese: *Riv. Staz. Sper. Vetro.*, 1979, **9,** 310-320.
206. G. Bayer: *Journal of Non-Crystalline Solids*, 1980, **38-9,** 855-860.
207. E.M.M. Ewais, M.I. Al-Wakeel, N. Khalil, and Y.M.Z. Ahmed: *Journal of the Ceramic Society of Japan*, 2004, **112,** 428-433.
208. N. Gao, K. Watari, S. Kume, Y. Ando, S. Ryo, and H. Itoh: *Journal of the European Ceramic Society*

Proceedings of the International Symposium on Inorganic and Environmental Materials, Eindhoven, NL, October 2004 - ISIEM (2004), 2006, **26,** 837-842.
209. Abrasive Grit Corporation at www.geocities.com/grit_za/aboutus.html, 20 April, 2006
210. PRE Abrasives & Refractories Recycling Exchange Listings - pacific.recycle.net, 25 April, 2005
211. Waste Matchers - www.waste-matchers.co.uk, 15 November, 2005
212. A.R. Boccaccini: *Journal of Materials Research*, 1998, **13,** 1693-1697.
213. Leach, A G: *Journal of physics. D, applied physics*, 1993, **26,** 733-739.
214. L.J. Gibson and M.F. Ashby, *Cellular Solids: Structure and Properties*. 2nd ed. 1999, Cambridge: Cambridge University Press.
215. F. Oliveira: *Materials science forum*, 2004, **455-456,** 172-176.
216. *Metals Handbook*. 9th ed. Vol. 8. 1985: American Society of Metals.
217. http://www-materials.eng.cam.ac.uk/mpsite/interactive_charts/spec-spec/IEChart.html, 04/07/2006,
218. D.P.H. Hasselman: *Journal of the American Ceramic Society*, 1969, **52,** 600-604.
219. E. Lucchinetti, *Composite models of bone properties*, in *Bone Mechanics Handbook*, S.C. Cowin, Editor. 2001, CRC Press: London.
220. K. Piekarski: *International Journal of Engineering Science*, 1973, **11,** 557-558.